

Plunging Breakers Impact Loading on Offshore Structures



**PhD thesis submission for the fulfilment for
Doctor of Philosophy in Offshore Engineering**

Supervisors

**Lloyd's Register Chair Professor
Newcastle University in Singapore
Newcastle University in Singapore
Newcastle University
Lloyd's Register Singapore Pte Ltd**

**Professor Longbin Tao
Associate Professor Arun Dev
Assistant Professor Xin Wang
Dr. Yongchang Pu
Mr. Anand**

Student Candidate

Chia De Wang (A9590023)

Kept Intentionally Blank

Content

Nomenclature

Contents

1. Introduction	15
2. Literature Review	19
2.1 Stability of Waves.....	19
2.2 Geometric of breaking waves	19
2.2.1 Crest-front Steepness	19
2.2.2 Crest-rear Steepness.....	21
2.2.3 Vertical wave symmetry ratio	21
2.2.4 Horizontal wave symmetry ratio.....	22
2.3 Kinematic breaking criteria	25
2.4 Dynamic breaking criteria	26
2.5 Generation of breaking waves	27
2.5.1 Stability of different focusing methods	29
2.6 Simulation of breaking waves	30
2.7 Factors affecting Slamming load force/pressure	32
2.7.1 Stages of Plunging Breakers	33
2.7.2 Rise Time	34
2.7.3 Geometrical cross sections of structure	35
2.7.4 Properties of Mediums	35
2.7.5 Measurement of Breaking wave kinematics.....	35
3. Design Breaking Wave, Novelty	37
3.1 Semi-Empirical Kinematics study (De Wang C, 2018)	37
3.2 Experimental Research on Kinematics of Breaking Waves.....	42
3.3 Review Kinematic Breaking Criteria	45
3.4 Review Geometric Breaking Criteria	46
3.5 Review Slamming Load Coefficient Calculation	50
4. Experiment Set up.....	51
4.1 Creating Breaking Waves in Newcastle University	51
4.2 Equipment and Calibration	52
4.3 Wave Parameters.....	57
4.4 Test Cases.....	60
4.5 Post Processing	61
5. Experiment preliminary Results.....	64

5.1 Kinematic results.....	64
5.2 Loadings results.....	65
5.3 Coefficient results	69
5.3.1 Wave Amplification Factor and Inertia Coefficient.....	72
5.3.2 Coefficient of vertical contributions	74
5.3.3 Maximum Slamming Coefficient.....	75
6. Numerical Simulation.....	80
6.1 Governing equations & Wave theory	80
6.2 Volume of Fluid	81
6.3 Courant Number	83
6.4 Numerical Calibrations Mesh set up and Sensitivity Test	83
6.4.1 Convergence study for x-direction.....	84
6.4.2 Convergence study for y-direction.....	89
6.5 Relaxation Zone	94
6.6 Wave Set ups.....	95
6.7 Mesh Set ups.....	95
6.8 Simulation cases.....	96
7 Results and discussions.....	97
7.1 Simulations Results	97
7.2 Simulation Kinematic Findings	98
7.2.1 Possible buffed body diffraction effects on wave kinematics	102
7.2.2 Kinematic comparison between experimental and numerical work.....	103
7.3 Comparison between experimental and simulation	105
7.4 Simulation Loadings Findings.....	106
7.4.1 Square Cylinders with Angle of Twist (θ).....	107
7.5 Slamming Load	109
7.6 Decaying.....	112
8. Conclusion.....	114
9. Acknowledgements.....	117
Bibliography	118
Appendix	122
A.1 Experimental work in National University of Singapore.....	122
A.1.1 Strokes Signal Calculation	124
A.1.2 Strokes Signal Modification	125
A.2 Post-processing.....	129

Nomenclature

β	Vertical wave crest asymmetry (-)
c	Phase celerity (m.s ⁻¹)
C	Courant Number (-)
C_B	Breaking wave celerity (m.s ⁻¹)
C_D	Drag coefficient (-)
C_M	Mass coefficient (-)
C_S	Slamming coefficient (-)
C_w	Waterplane area coefficient (-)
d	Water depth (m)
D	Cylinder Diameter (m)
E	Error (-)
ε	Crest-front Steepness (-)
f	Frequency (s ⁻¹)
f_c	Central frequency (s ⁻¹)
F	Total Force (N)
F_{Drag}	Drag Force (N)
F_{Inertia}	Inertia Force (N)
F_{Slamming}	Slamming Force (N)
g	Gravitational acceleration (m.s ⁻²)
H	Wave height (m)
H_B	Height of breaking wave (m)
H_i	Incident wave amplitude (m)
H_r	Reflected wave amplitude (m)
h	Water depth (m)
J	Volume ratio (-)
k	Wave number (rad.s ⁻¹)
θ	Angle of twist (deg)
ρ_w	Density of seawater (kg.m ⁻³)

R	Rate of Rise (m.s^{-1})
S	Stroke (m)
t_r	Rise time (s)
δ	Crest-rear Steepness (-)
u	Horizontal wave particle velocity (m.s^{-1})
$\frac{u}{c}$	Kinematic Breaking Criteria (-)
μ	Horizontal wave crest asymmetry (-)
λ	Wavelength (m)
ω	Oscillating frequency (rad.s^{-1})
ω_R	Relaxation weight (-)
ζ	Wave elevation (m)
ζ_a	Wave amplitude (m)
ζ_b	Breaking wave elevation (m)

List of Figures

Figure 1 – ‘The tube’, plunging breakers popularly chased by surfers	15
Figure 2 Wave parameters definition	20
Figure 3 Crest-front steepness, (Bonmarin, 1989).....	21
Figure 4 Vertical Asymmetry ratio, (Bonmarin, 1989) (red line indicate just prior to breaking, and purple lines indicate post-breaking)	22
Figure 5 breaking wave steepness analysis, [-],[+],[x], represents data extracted from (Babanin, 2007), (Wu, 2004), (Chan E.S L. Y., 1997) respectively	24
Figure 6 Piston wave-maker theory, (Dean, 1984)	28
Figure 7 H/S ratios for both Piston and Flap type wave-maker (Dean, 1984)	29
Figure 8 – Different stages of breaking wave impact zone by (Chan E.S W. M., 1988).....	34
Figure 9 Video Lagrangian method for tracking wave celerity	38
Figure 10 Wave profile of a propagating wave (crest denoted by a star, Jet’s nose denoted by a circle).....	39
Figure 11 ‘ U_L/U_E ’ values for different breaking intensities	39
Figure 12 Plunging Jet overtopping	40
Figure 13 ‘ c_L/c_E ’ ratios for different peak frequencies (breaking wave intensities)	40
Figure 14 ‘ c_L/c_3 ’ values for different non-dimensional breaking intensities ‘ T_z/T_p ’, using 3 rd order Stokes theory	41
Figure 15 Calculation of the rise-up of a breaking wave via a tracker.....	42
Figure 16 Comparison of pre-jet celerity obtained via the 3 methodologies.....	43
Figure 17 Comparison of $c_{L,p}$ and $c_{L,p'}$ against $c_{L,v,b}$	44
Figure 18 Comparison of celerity, adjusted for the rise of elevation against 3 rd -order linear celerity in the pre-jet case	44
Figure 19 Wave profile showcasing the formation of the plunging jet, $f_p = 0.5\text{Hz}$	45
Figure 20 Comparison of wave celerity before and after jet formation.....	45
Figure 21 U/c ratios for different wave-breaking intensities.....	46
Figure 22 Comparison of different crest-front steepness for plunging breakers with past researchers (Bonmarin, 1989) (Kjeldsen M. , 1979) (She.K, 1997)).....	48
Figure 23 Comparison of different crest-front steepness ratios	49
Figure 24 Newcastle University Wind Wave and Current Tank.....	51
Figure 25 Plan view layout of wave tank, cylinder will be placed at $x= 8.25\text{m}$, square denotes the GoPro 6 cameras, wave probes denoted by the blue transverse lines at $x= 7.75\text{m}$, 8m , and 8.25m ..	52
Figure 26 Regular wave elevation recorded at $x= 9\text{m}$	52
Figure 27 JONSWAP focused spectrum, $f_p= 0.65\text{Hz}$, $x= 9\text{m}$	53
Figure 28 Placement of ADVs as denoted by red stars	54
Figure 29 Average Peak Force for different spatial location of ADV as indicated in Figure 34	55
Figure 30 Average Peak velocity for different spatial location of ADV as indicated in Figure 32.....	55
Figure 31 Engineering drawing of 200mm diameter circular cylinder	56
Figure 32 Engineering drawing of square cylinder	56
Figure 33 Definition of characteristic diameter for diamond cylinder (Veritas D. N., 2010).....	56
Figure 34 Calculation of characteristic length for the diamond cylinder	57
Figure 35 Input and Output Phase differences of arbitrary wave components at Newcastle University Wind Wave and Current Tank.....	57
Figure 36 JONSWAP waves input.....	58
Figure 37 Spectra moment vs Peak Frequencies	58
Figure 38 Wave kinematics and time force history at $z= -80\text{mm}$, $f_p = 0.5\text{ Hz}$	61

Figure 39 Work flow to determine slamming load coefficient	62
Figure 40 Test cases set ups	63
Figure 41 Coefficient of waterplane of circular cylinder (De Wang Chia, Slamming Force Contribution Due to Plunging Breakers on Circular, Square and Diamond Cylinders, 2019)	63
Figure 42 Velocity profile for differing elevation for $0.47\text{Hz} \leq f_p \leq 0.5\text{Hz}$	64
Figure 43 Velocity profile for differing elevation for $0.47\text{Hz} \leq f_p \leq 0.5\text{Hz}$, using $f_p = 0.5\text{Hz}$ as a datum	65
Figure 44 Peak force for cylinder with diameter of 200mm	65
Figure 45 Peak force for diamond cylinder	66
Figure 46 Peak force for square cylinder	66
Figure 47 Force increment sensitivity	67
Figure 48 Force readings of 3 different cylinders, during post-jet breaking (for $x_B = 8.8\text{m}$), jet formation (for $x_B = 9\text{m}$), and pre-jet formation (for $x_B = 9.2\text{m}$)	67
Figure 49 Plunging wave impact on diamond cylinder	68
Figure 50 (Force/ ρD) analysis of the 3 cylinders, during post-jet breaking (for $x_B = 8.8\text{m}$), jet formation (for $x_B = 9\text{m}$), and pre-jet formation (for $x_B = 9.2\text{m}$)	68
Figure 51 Fixed boundary influence on drag coefficient (Veritas D. N., 2010)	69
Figure 52 Drag coefficient for fixed circular cylinder for steady flow with function of Reynolds Number (Veritas D. N., 2010)	70
Figure 53 Drag coefficient for 'rectangle with thin splitter plate' for steady flow state (Veritas D. N., 2010)	70
Figure 54 Rebounding effects for estimating drag coefficient multiplier for square cylinder ($L/D = 1$) (Veritas D. , 2011)	71
Figure 55 Drag coefficient for a diamond cylinder $L_0/D_0 = 1$ (Veritas D. , 2011)	71
Figure 56 Sway drag coefficient for different cylinders (1- 200mm circular cylinder, 2- 315mm circular cylinder, 3- 400mm circular cylinder, 4- square cylinder, 5- diamond cylinder) for irregular waves ..	71
Figure 57 Wake Amplification factors comparison (irregular waves only) with previous literature review by (Veritas D. , 2011)	72
Figure 58 Relation between ' C_D/C_{DS} ' and KC number, for all cylinders in this experimental work, involving both regular and irregular waves.	73
Figure 59 Sway Inertia Coefficient (or inline inertia coefficient) for different cylinders (1- 200mm Circular Cylinder, 2- 315mm circular cylinder, 3- 400mm circular cylinder, 4- Square Cylinder, 5- Diamond Cylinder)	73
Figure 60 Horizontal and vertical force time history during onset of plunging jet, for 200mm circular cylinder	74
Figure 61 Heave inertia coefficient (vertical axial direction) for different cylinders (1- 200mm Circular Cylinder, 2- 315mm circular cylinder, 3- 400mm circular cylinder, 4- Square Cylinder, 5- Diamond Cylinder)	75
Figure 62 Velocity Field	75
Figure 63 Maximum inline slamming coefficient of 5 cylinders test cases, with varying breaking intensities (1- 200mm circular cylinder, 2- 315mm circular cylinder, 3- 400mm circular cylinder, 4- square cylinder, 5- diamond cylinder)	76
Figure 64 Angle of contact (Denoted by the spread of coloured lines) for cylinders with different geometries cross section and circular cylinders with different diameters	76
Figure 65 Diffraction wave for the 400mm circular cylinder case. Wave propagated from right to left.	77
Figure 66 Maximum inline slamming coefficient for cylindrical structures with different Waterplane Area Coefficient during onset of breaking	77

Figure 67 Rise time for different breaking wave intensities. (1- 200mm circular cylinder, 2- 315mm circular cylinder, 3- 400mm circular cylinder, 4- square cylinder, 5- diamond cylinder)	78
Figure 68 Maximum Slamming Force ratio vs Rise Time ratio comparison.....	78
Figure 69 Maximum Inline Slamming Coefficient ratio vs Rise Time ratio comparisons.....	79
Figure 70 Stoke wave theory (Le Méhauté, 1976).....	81
Figure 71 Comparison of surface elevation at the focal point, between 2 methodologies	82
Figure 72 x-y plane of the numerical wave tank, modelled after NUS wave tank	83
Figure 73 Comparison of crest elevation between simulations and analytical methods, for x-meshes	85
Figure 74 Comparison of averaged crest elevation between simulations and analytical methods, for different amount of x-meshes per wavelength	86
Figure 75 Comparison of trough elevation between simulations and analytical methods, for x-meshes	87
Figure 76 Comparison of averaged trough elevation between simulations and analytical methods, for different amount of x-meshes per wavelength	87
Figure 77 Comparison of wave height between simulations and analytical methods for x-meshes ...	88
Figure 78 Comparison of averaged wave height between simulations and analytical methods, for different amount of x-meshes per wavelength	88
Figure 79 Error margin mesh sensitivity test for different x-axis mesh simulations	89
Figure 80 Comparison of crest elevation between simulations and analytical methods, for different amount of y-meshes per wave height	90
Figure 81 Comparison of averaged wave crest between simulations and analytical methods, for different amount of y-meshes per wavelength	90
Figure 82 Comparison of trough elevation between simulations and analytical methods, for y-meshes	91
Figure 83 Comparison of averaged trough elevation between simulations and analytical methods, for different amount of y-meshes per wavelength	91
Figure 84 Comparison of wave height elevation between simulations and analytical methods, for y-meshes	92
Figure 85 Comparison of averaged wave height between simulations and analytical methods, for different amount of y-meshes per wavelength	93
Figure 86 Error margin mesh sensitivity test for different y-axis mesh simulations	93
Figure 87 x-y plane of numerical tank with outlet relaxation zone	94
Figure 88 Comparison of simulation and analytical results, waveprobes located at $x = 0.7\text{m}$	94
Figure 89 Comparison of simulation and analytical results, waveprobes located at $x = 12.7\text{m}$	95
Figure 90 Early Jet formation at $t = 34.5\text{s}$, $f_p = 0.5\text{Hz}$ (wave propagation from right to left)	97
Figure 91 Early indication of formation of jet (using α_{water} representation), a red rectangle box is placed at $x = 9\text{m}$ for visualisation purpose.....	97
Figure 92 Early jet formation, with vectors	98
Figure 93 Velocity vectors.....	98
Figure 94 Placement of probes for square cylinder simulation case.....	99
Figure 95 Initial impact of plunging breaker on square cylinder – simulation	99
Figure 96 initial impact of plunging breaker on square cylinder – experimental.....	100
Figure 97 Plunging wave kinematic profile at $x = 8.99\text{m}$, horizontal wave kinematics	100
Figure 98 Plunging wave kinematic profile at $x = 8.99\text{m}$, vertical wave kinematics.....	101
Figure 99 Wave profile kinematic at $x = 8.74\text{m}$, $t = 34.7\text{s}$	101
Figure 100 Characteristic length for different angle of twist.....	102

Figure 101 Wave profile kinematic for $\theta = 15, 30, 45$ degrees, at $x = 8.74\text{m}$, $t = 34.7\text{s}$	102
Figure 102 tri-axial representation of kinematics. Horizontal axis (-0.08m to 0.19m) representing surface elevation, Transverse axis (34.75s to 34.9s) representing time, Vertical axis (-0.5ms^{-1} to 1ms^{-1}) representing velocity (experimental data)	103
Figure 103 tri-axial representation of kinematics. Horizontal axis (-0.1m to 0.23m) representing surface elevation, Transverse axis (34.75s to 34.9s) representing time, Vertical axis (-0.5ms^{-1} to 1ms^{-1}) representing velocity (simulation data)	104
Figure 104 Wave kinematic comparison at focal point (x_B, t_B), experiment vs simulation	104
Figure 105 Comparison of wave profile at focal point (x_B, t_B), experiment vs simulation.....	105
Figure 106 Wave amplitude contribution as a function of frequency, with peak frequency $f_p = 0.5$ Hz	106
Figure 107 Total Force time history on 315mm circular cylinder during plunging impact, experimental vs simulation case	106
Figure 108 bi-axial Force time history on square cylinders with different θ , simulation case	107
Figure 109 Transverse force contribution (Contributing transverse force indicated by red arrows)	107
Figure 110 transverse axial force for square and diamond cylinder, experimental and simulation work	108
Figure 111 Inline force during plunging, for varying θ , simulation cases	108
Figure 112 Slamming force time history on circular cylinder, square cylinders with different θ , simulation case	110
Figure 113 Placements of square cylinder ($\theta = 0, 45$ degrees)	110
Figure 114 Maximum slamming load co-efficient for 5 cylinders, simulation case (1- square cylinder, 2- square cylinder with $\theta = 15\text{deg}$, 3- square cylinder with $\theta = 30$ deg, 4- square cylinder with $\theta = 45$ deg, 315mm circular cylinder)	111
Figure 115 Maximum slamming load co-efficient for 3 cylinders, experimental & simulation case (1- square cylinder, 4- square cylinder with $\theta = 45$ deg, 315mm circular cylinder	111
Figure 116 Comparison of time histories of the slamming coefficient ($t = \text{time}$, $R = \text{cylinder radius}$, $V = \text{velocity}$) [(von Karman, 1929) (Wienke, 2001) (Wagner, 1932) (Goda, 1966) (Fabula, 1957) (Cointe, 1989) (De Wang Chia, Laboratory Investigation of Slamming Load Contribution of Plunging Breaker, 2019)]	112

List of Tables

Table 1 Past literature survey results for 2D waves, [1]- (Bonmarin, 1989) 2D focusing waves, [2]- (Kjeldsen M. , 1979) 2D wave-wave interaction, [3]- (Wu, 2004) 2D focusing waves.....	24
Table 2 Past literature survey results for 3D waves, [1]- (She.K, 1997) 3D wave angular focusing, [2]- (She.K, 1997) 3D wave multifrequency focusing [3]- (Wu, 2004) 3D diffracting waves, [4] (Wu, 2004) 3D focusing waves.....	24
Table 3 Wave Celerity	43
Table 4 Crest-front steepness comparison table	48
Table 5 Wave Parameters	60
Table 6 Comparison of wave crest elevation, for wave probes located from $6.09m < x < 24.15m$, for x-meshes ranging from 38 to 152 per wavelength	85
Table 7 Comparison of wave trough elevation, for wave probes located from $6.09m < x < 24.15m$, for x-meshes ranging from 38 to 152 per wavelength	86
Table 8 Comparison of wave crest elevation, for wave probes located from $6.09m < x < 24.15m$, for y-meshes ranging from 10 to 50 per wavelength	89
Table 9 Comparison of wave trough elevation, for wave probes located from $6.09m < x < 24.15m$, for y-meshes ranging from 10 to 50 per wave height	91
Table 10 Comparison of wave height elevation, for wave probes located from $6.09m < x < 24.15m$, for y-meshes ranging from 10 to 50 per wave height	92
Table 11 Wave Package parameter	95
Table 12 Kinematic of plunging waves during breaking, by elevation. Experimentally obtained values at $x = 8.99m$	103
Table 13 Resultant drag co-efficient for all 5 individual simulation cases.....	109

List of Equations

Equation 1 Morison's Equation for non-breaking wave force.....	Error! Bookmark not defined.
Equation 2 Drag force formula.....	Error! Bookmark not defined.
Equation 3 Inertia force formula	Error! Bookmark not defined.
Equation 4 Morison's Equation for breaking wave force	Error! Bookmark not defined.
Equation 5 Slamming force formula	Error! Bookmark not defined.
Equation 6 Crest-front steepness	Error! Bookmark not defined.
Equation 7 Stokes 1st order wave celerity	Error! Bookmark not defined.
Equation 8 Crest-rear Steepness.....	Error! Bookmark not defined.
Equation 9 Vertical wave crest length asymmetry	Error! Bookmark not defined.
Equation 10 Horizontal wave crest asymmetry	Error! Bookmark not defined.
Equation 11 Rate of Rise	Error! Bookmark not defined.
Equation 12 Stokes Second Order Phase Velocity	Error! Bookmark not defined.
Equation 13 Free surface elevation formula.....	Error! Bookmark not defined.
Equation 14 Phase Shift	Error! Bookmark not defined.
Equation 15 Volume of water	Error! Bookmark not defined.
Equation 16 Stroke displacement time history.....	Error! Bookmark not defined.
Equation 17 Change of Volume of Fluid per time step (Johan Roenby, 2016)	Error! Bookmark not defined.
defined.	
Equation 18 Slamming load time history formula - (Goda, 1966)	Error! Bookmark not defined.
Equation 19 Lagrangian formula for wave celerity.....	Error! Bookmark not defined.
Equation 20 Time calculation.....	Error! Bookmark not defined.
Equation 21 Eulerian formula for wave crest velocity.....	Error! Bookmark not defined.
Equation 22 Stokes 3 rd order wave celerity	Error! Bookmark not defined.
Equation 23 Semi-empirical breaking wave celerity.....	Error! Bookmark not defined.
Equation 24 Crest-front steepness (ϵ_1)	Error! Bookmark not defined.
Equation 25 Crest-front steepness (ϵ_2)	Error! Bookmark not defined.
Equation 26 Crest-front steepness (ϵ_3)	Error! Bookmark not defined.
Equation 27 phase shift, time adjustment.....	Error! Bookmark not defined.
Equation 28 Excel Function to account for zero initial condition for a wave tank .	Error! Bookmark not defined.
defined.	
Equation 29 adjusted wave amplitude with considering phase lag inputs	Error! Bookmark not defined.
defined.	
Equation 30 Individual Strokes Displacement-time history.....	Error! Bookmark not defined.
Equation 31 Conversion of cosine function to sine function.....	Error! Bookmark not defined.
Equation 32 New amplitude formula, sine function.....	Error! Bookmark not defined.
Equation 33 Excel function for wave amplitude generation, for sine function.....	Error! Bookmark not defined.
defined.	
Equation 34 Surface elevation involving rebounding waves	Error! Bookmark not defined.
Equation 35 Energy absorption formula.....	Error! Bookmark not defined.
Equation 36 JONSWAP Spectrum formula.....	Error! Bookmark not defined.
Equation 37 Spectra zeroth moment.....	Error! Bookmark not defined.
Equation 38 Frequency Formula.....	Error! Bookmark not defined.
Equation 39 Number of wave components	Error! Bookmark not defined.
Equation 40 Individual wave component maximum amplitude.....	Error! Bookmark not defined.
Equation 41 Wave harmonic motion	Error! Bookmark not defined.
Equation 42 Horizontal wave particle acceleration	Error! Bookmark not defined.
Equation 43 Submerged length formula.....	Error! Bookmark not defined.

Equation 44 Submerged half-width formula	Error! Bookmark not defined.
Equation 45 Drag Coefficient formula	Error! Bookmark not defined.
Equation 46 Keulegan Carpenter Number Formula	Error! Bookmark not defined.
Equation 47 Horizontal kinematics formula	Error! Bookmark not defined.
Equation 48 Conservation of Momentum Equation.....	Error! Bookmark not defined.
Equation 49 Conservation of Momentum at x-axis	Error! Bookmark not defined.
Equation 50 Conservation of Momentum at y-axis	Error! Bookmark not defined.
Equation 51 Conservation of Momentum at z-axis	Error! Bookmark not defined.
Equation 52 Conservation of mass	Error! Bookmark not defined.
Equation 53 Stoke's 4 th order free surface elevation theory (Fenton, 1983)	Error! Bookmark not defined.
Equation 54 Viscosity formulation for VOF.....	Error! Bookmark not defined.
Equation 55 Density formulation for VOF.....	Error! Bookmark not defined.
Equation 56 VOF boundary condition.....	Error! Bookmark not defined.
Equation 57 Courant Number	Error! Bookmark not defined.
Equation 58 Simple Grading formula.....	Error! Bookmark not defined.
Equation 59 2 nd order Stokes Wave Theory for surface elevation	Error! Bookmark not defined.
Equation 60 2 nd order Stokes Wave Theory for crest	Error! Bookmark not defined.
Equation 61 2 nd order Stokes Wave Theory for trough	Error! Bookmark not defined.
Equation 62 Explicit relaxation zone formula	Error! Bookmark not defined.

Abstract

A plunging wave induces slamming impact forces due to its collapsing jet. Linear wave theory would not be applicable for slamming load prediction. This is also one of the most devastating force that an offshore structure could experience in its operational lifespan. There are design guidelines to predict the resultant design slamming load contribution as a function of the breaking wave celerity.

Hence it is important to investigate and understand the factors that would have an impact of the slamming load contribution. Current industry design guideline for the slamming load coefficient doesn't take into account for different cylinders geometries, cylinders cross-sections, wave parameters, impact rise time, types of mediums used. Instead, the recommended slamming load coefficient is based on a 'smooth cylinder'. This would potentially give rise to scenarios where the design breaking wave load would be overly conservative, thus leading to unnecessary added construction cost and time wastage.

The aim of this project is to investigate this slamming load coefficient to different geometries and wave parameters. Besides the traditional circular cylinder, squared cylinder will also be analysed and compared. A circular cylinder of different diameters, coupled with different breaking wave signals of varying intensities would be used in this case, with the main objective of establishing a semi-empirical relation between the slamming load coefficient and the wave kinematics.

This PhD project also aims to establish a separate breaking wave design guidelines for 2 other geometrical cylinders; the square cylinder and the square cylinder with a 45-degree shift. These project will also investigate the sensitivity of different plunging jet maturity.

It was found that the geometric cross-section of the offshore structure has a direct influence on the slamming load distribution and coefficient. De Wang Chia, found that the fullness (C_w) of the offshore structure relative to the breaking wave propagation direction, has a direct correlation with the slamming load and slamming coefficient contribution. The fullness of the offshore structure would affect the air entrapment capability during the plunging jet contacting with the offshore structure. (De Wang Chia, 2019) concluded that the diamond-shaped cylinder that has the lowest fullness, would give the lowest slamming load and slamming coefficient, and with the square (flat wall) cylinder having the highest slamming load and coefficient contribution. For the circular cylinders, a larger radial cylinder would also have higher fullness and associated slamming contributions, with a larger radial cylinder starting to exhibit behaviour closer to a square (flat wall) cylinder.

De Wang Chia tries to investigate past researchers (P.A Blackmore., 1984) & (Chan E.S W. M., 1988) conclusion that the impact rise time would have a negative correlation with the slamming load. Breaking wave signals of varying breaking intensities were used for the purpose of achieving different rise times. It was shown that a lower rise time is indeed associated with higher slamming load contribution. However, it does not automatically equate to a higher slamming load contribution. This is due to the higher breaking wave intensities associated with higher wave celerity. The increased slamming load contribution derived from higher wave kinematics and not from the slamming load coefficient. It was concluded that the slamming load coefficient is not affected by the breaking wave intensities and rise time.

1. Introduction

Breaking wave is a naturally occurring phenomenon, and there are 4 types of breaking wave; spilling wave, collapsing wave, plunging wave and the surging wave. A surging wave would typically occur at the beach, mainly caused by low steepness and longer period of waves, having its base of the wave overrunning the wave crest, causing the wave crest to disappear. A plunging breaker could occur primarily due to 2 reasons. It could occur due to coastal effects; a rapid decrease of seabed depth, causing the wave energy/spectra to focus on the decreasing wavelength, and increasing wave height until it reaches a critical height (or instability) and finally collapsed.



Figure 1 – ‘The tube’, plunging breakers popularly chased by surfers

Surfers love to surf along these coastal plunging jet; otherwise known to surfers as ‘the tube’ (Figure 1). A plunging breaker could also occur in the deep-sea. Imagine the sea state as a sea condition whereby it actually made up of maybe 1,000 regular waves with varying oscillating frequencies, wave kinematics, amplitudes. And if one were to roll the dice infinite amount of times, one day, it just so happen that on the at the ‘wrong’ space and time $[\cos(kx - \omega t)]$, there is a rogue wave that occurs due to the superposition of sufficient regular waves, causing the rogue wave to reach a critical amplitude encouraging instability and finally to break. This allows the formation of a protruding jet and eventually crushing down with the aid of gravity. A spilling breaker could be described as a mini plunging breaker that does not form a mature jet; instead, the spilling breaker could just spill from its crest, instead of a violent jet overturning like its stronger cousin, the plunging wave. A collapsing wave would be a hybrid between spilling and a surging wave, having the breaking occurring near the base of the wave.

A plunging breaker induces the most devastating type of breaking wave; as compared to the 3 weaker breaking waves mentioned earlier. A rogue wave, upon breaking, is that of the plunging breaker. Rogue waves are oftenly associated with one of the extreme events occuring at deep sea. Hence, these are of course considered during the design stages. The impact of extreme events on both fixed and floating structures are essential factors in both designs as well as life extension analysis. Presently, there is the ability to perform an extreme event analysis based on steep waves, but the effect of plunging waves is not yet well understood; there is a lack of practical and accurate estimation of the impact caused by plunging breaker. There should be more experimental and numerical works to be done revolving plunging breaker impact loadings, specifically exploring

different test case set ups, wave parameters, or even different scalings. However, offshore structures are also susceptible to plunging wave forces at sea. Understanding the kinematics and mechanics these waves impose would be of great benefit to the shipbuilding and the oil and gas industry. Human errors, extreme weather conditions are one of the main culprit responsible for most of the structural damage or even loss of life during the offshore structure's useful life at sea. Hence, naval architects are required to design an offshore structure that would be capable of withstanding extreme conditions. Extreme weather conditions would include rogue wave, tsunami, earthquake etc. This project would focus more on plunging breakers that arise due to instability arises from rogue wave reaching a critical amplitude, causing the crest to topple over and crushing down with the assistance of gravitational force. During the instances of the plunging jet came crashing down, this phenomenon would exert a sharp spike of slamming pressure onto the impacted structure and is one of the most devastating force that an offshore structure could experience in its operational life.

Morison's Equation describe the wave force excluding the diffraction force, and only a slender body would not be affected by the diffraction force to make Morison's Equation applicable. A non-breaking wave ($\frac{D}{\lambda} < 0.2$) would impose mainly drag and inertia force on a slender offshore structure (Equation 1, Equation 2, Equation 3).

$$F = F_{Inertia} + F_{Drag} \quad (1)$$

$$F_{Drag} = 0.5 * \rho_w * C_D * A * u * |u| \quad (2)$$

A = Reference area plane perpendicular to the wave propagation direction. In this case, $A = H_B * D$

$$F_{Inertia} = \int_{-d}^{\zeta_b} C_M * \rho_w * \frac{\pi * D^2}{4} * \frac{\partial u(z)}{\partial t} * dz \quad (3)$$

But a plunging wave would impose additional slamming force due to its collapsing jet (Equation 4). This imposed slamming force is the strongest impact force that an offshore structure could encounter in its operational lifecycle. Understanding the mechanics behind the slamming force (Equation 5) induced by the plunging jet would be beneficial for reviewing the design of offshore structures.

$$F = F_{Inertia} + F_{Drag} + F_{Slamming} \quad (4)$$

$$F_S = 0.5 * \rho_w * C_S * D * C_b^2 * \lambda_C * \zeta_b \quad (5)$$

λ_C is the curling factor; a ratio of breaking wave impact height on structure over the breaking wave height (-).

ζ_b is the breaking wave height (m)

ρ_w is the density of the medium (kg.m^{-3})

D is the characteristic diameter of the impacted structure (m)

C_S is the slamming load coefficient (-)

C_b is the breaking wave celerity (m.s^{-1})

According to classification society design rulebook, there are guidelines on estimating the inertia, drag and slamming coefficient of the offshore structure. The inertia and drag coefficient were affected by few parameters; surface roughness, Keulegan Carpenter Number and geometrical shape.

However, the maximum slamming load coefficient had a one-size fit all value; a maximum slamming coefficient of $C_s = 5.15$ at the point of initial jet contact with the offshore structure. Also, the kinematics of breaking wave is a tricky parameter to estimate. Hence, current industry design guidelines calls for assuming the breaking wave celerity to be 120% of the 'most probable' breaking wave celerity. These above assumptions might give rise to the possibility of an inaccurate design criteria.

The amount of slamming load contribution is significantly dependant on the amount of air entrapment during the onset of breaking (Chan E.S W. M., 1988). A higher air entrapment is associated with higher impact pressure and associated slamming force. The amount of air entrapment could be affected by several factors. The cross-sectional area of impact structure would directly influence how the initial air pocket created by the curling of the plunging jet would disperse upon contact with the offshore structure. The plunging wave intensity; local steepness of plunging wave, would also yield different wave parameters. It is shown by (Chan E.S W. M., 1988) and (P.A Blackmore., 1984) that the impact rise time (t_i) would have a negative correlation with the resulting impact pressure. Wave kinematics or Keulegan-Carpenter number would affect the total contributing force on a structure. For a lower Keulegan-Carpenter number, the inertia force forms the bulk of the non-breaking force contribution, and for the higher Keulegan-Carpenter number, the drag coefficient is the dominant non-breaking force contribution. (Manual) stated that for design purpose, the contributing slamming load could be 250% of the drag component.

The maturity of the plunging jet would have a direct impact on the initial air entrainment and resultant air entrapment during the contact between the plunging jet and the offshore structure. (Chan E.S W. M., 1988) did experimental work investigating the slamming pressure contribution of plunging breakers of 3 varying maturities (Figure 8). The first stage is 'pre-jet' formation, whereby the wave have not shown signs of breaking, instead behaves more of a highly non-linear non-breaking wave. Second stage is the 'pre-mature jet' formation, this phase involving the earliest formation of a protruding jet. The last stage is the 'mature jet' formation, where one could clearly see the 'tongue' or 'the tube' of plunging wave jet. Figure 19 clearly illustrates the different stages of breaking wave via 'Tracker' programme; a video imagery processing programme.

He concluded that for a premature jet, there would be lower air entrainment, however, at the point of contact with the offshore structure, the premature jet would induce the most air entrapment dynamics on the offshore structure resulting in the highest slamming contribution of the 3 plunging breaker cases.

This motivates the crux of this PhD is to launch an investigation in the two knowledge gaps of the breaking wave industry design guidelines;

- 1) Kinematics of plunging breaker
- 2) Slamming load coefficient contribution of structures with different geometrical cross sections

It was concluded that the commonly used Eulerian method for predicting breaking wave kinematics would not be an accurate methodology. The breaking wave kinematics measured via Lagrangian method via video image processing, is found to surpass the kinematic values obtained by the Eulerian Method by up to 24%.

De Wang Chia researched on the impact of the slamming force contribution amongst circular cylinders, square cylinder and diamond cylinder. The slamming force contribution was estimated (Equation 2, Equation 3 & Equation 4) with known wave kinematics (celerity and acceleration) obtained via vectrinos. De Wang Chia concluded that the higher area (fullness) coefficient of the structure (datum plane taken perpendicular to the wave propagation direction), the lesser avenues available for the entrapped air to escape, hence inducing a higher slamming contribution. The square cylinder obtains a maximum slamming coefficient of 6.7, exceeds classification recommendation of 5.15 to 6.28. However, classification regulations assumed the maximum slamming coefficient for the case of a circular cylinder. It was noted in the experimental work that, the square cylinder had a higher area coefficient as compared with the circular cylinders, and hence the associated higher maximum slamming coefficient. On the contrary, when a plunging breaker hits a square cylinder with a 45-degree rotation from the vertical axis, the square cylinder becomes a diamond cylinder case. The diamond cylinder case would have the lowest fullness coefficient and lowest associated maximum slamming coefficient.

The use of structures with different geometrical cross section, perpendicular to the propagating wave axis, have a higher impact on the maximum slamming load coefficient. It was found that for a plate flat facing, square cylindrical structure, the maximum slamming load coefficient was measured to be as high as 8.52; a value exceeding the recommended maximum slamming load coefficient of 5.15 as proposed (Veritas D. N., 2010). Hence, the author would recommend a review of the maximum slamming load coefficient for a square cylinder offshore structure, proposing a maximum slamming load coefficient of 9.0.

2. Literature Review

2.1 Stability of Waves

Research on wave breaking had come a long way. Wave breaks due to instability and in the earlier days, (Benjamin, 1967) developed and studied on the condition of instability for 2-dimensional waves and created wave trains (similar wavelength in a parallel propagating direction) and argued that a 2D (with no propagating angle) Stokes wave train of a certain non-dimensional depth (kh) is unstable. (McLean J.W, 1981), advanced on the field of the modulational instability by the progressive study on the instability of 3D waves. In the following year, (WK, 1982) research revealed that the occurrence of breaking waves is not coincidental but was in the culmination of the two distinct systems of Benjamin-Feir and Mclean. For lower wave steepness, the 3D breaking effect was mild, and the breaking phenomenon was attributed to the 2D Benjamin-Feir instability. At higher wave steepness, the breaking phenomenon was dominated by the 3D Benjamin-Feir instability. (WK, 1982) revelation was through the association between breaking waves and the resistance of a hydrofoil that created the waves.

Many researchers (Kjeldsen M. , 1979) (Kjeldsen, 1981) (Bonmarin, 1989) (Schultz W.W, 1994) (G.I, 1971), had proposed few criteria for the prediction of wave breaking. There are three main widely discussed criteria; which will be discussed in details below. There are the geometry breaking criteria, which focus on the local wave shape and the global wave steepness. The kinematic breaking criteria, which focus on the ratio of the horizontal wave particle velocity and the phase celerity. The dynamic breaking criteria, which are based on the acceleration of the horizontal particle velocity, and the rate of growth of the wave steepness and the rate of change of wave energy.

2.2 Geometric of breaking waves

2.2.1 Crest-front Steepness

More than a century ago, (Stokes, 1880) introduced the first geometric breaking criterion, ($\frac{H}{\lambda} = \frac{1}{7}$).

This equation gives the maximum non-breaking wave steepness, as $\zeta_a k = 0.4488$ ($\zeta_a = 0.5H$)($k = 2\pi/\lambda$)

(Kjeldsen M. , 1979) (SP, 1984) noted that wave breaking does not undergo symmetrical behaviour whilst undergoing breaking. The crest of the breaking wave is usually more than half of the wave height (H), and the crest-front length of the wave is less than a quarter of the wavelength (λ). It was concluded that the use of the wave steepness parameter ($\zeta_a k$) wouldn't be an accurate parameter; as it doesn't takes into account the asymmetrical properties of the breaking wave. Hence, instead of using wave steepness ($\zeta_a k$), a new geometric wave breaking criterion that accounts for the non-symmetric behaviour of the breaking wavefront was introduced.

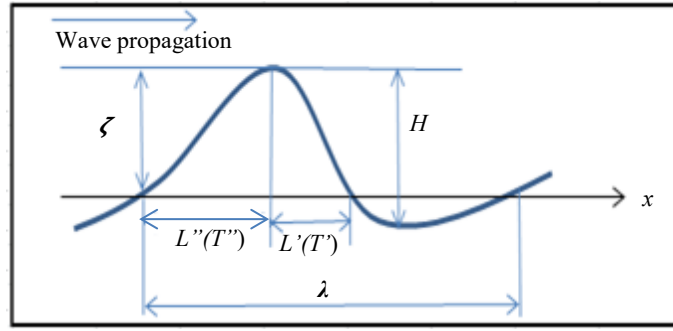


Figure 2 Wave parameters definition

$$\varepsilon = \frac{\zeta}{L'} \quad (6)$$

$L' = \left(\frac{g}{2\pi} * T_z * T'\right)$ is the crest-front length as shown in the above Figure 1.

$$c_{E1} = \frac{g * T_z}{2\pi} \quad (7)$$

T' , is the time taken for the wave propagating from the free surface to the crest, measured via wave probes,

Equation 6 & Equation 7 is relating the crest-front length as a function of both Stokes celerity and wave rise time. Kjeldsen uses the zero down-crossing method; which involves extracting the time taken for a single wave. This method involves taking a first reference point at a still water surface level after the wave crest. This important wave parameter defined here is termed as T_z , down-crossing wave period. This down-crossing wave period method would be a more accurate methodology as compared to extracting the time taken for 2 successive crests to occur. There are difficulties of capturing the exact time occurrence of the crest due to the crest smoothness, potentially affecting accuracy. Hence, the zero-down crossing method would be used to calculate the wave celerity and wavelength respectively (Equation 7)

(Bonmarin, 1989), on the other hand, conducts the experiment with a wave tank having a length, breadth and a constant depth of 40m, 3.2m, and 1, respectively. Deepwater conditions were used, and breaking waves were created with 2 different modes. The first mode is by modulational instability; which induces the Benjamin-Feir instabilities, which is achieved by constantly decreasing the frequency of the wave, giving a different wave phase speed. The second mode creates breaker via a focusing method, which involves superposition of several dozen regular waves.

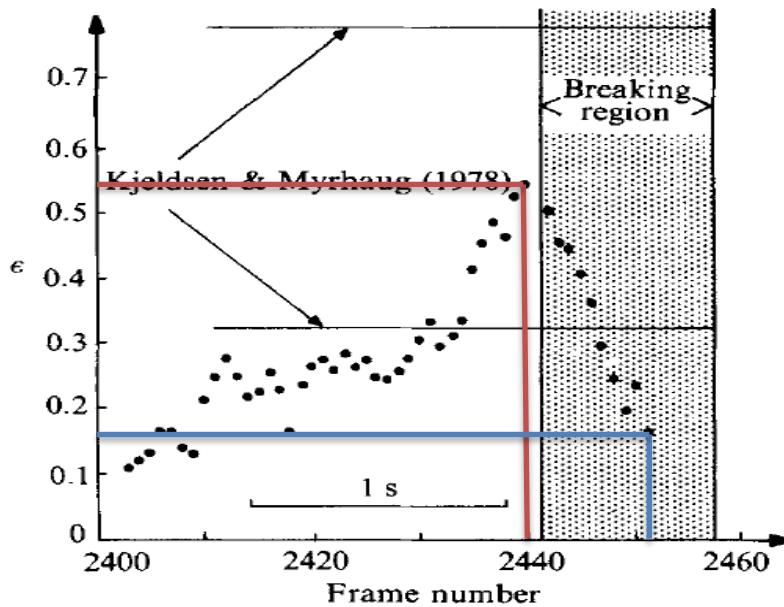


Figure 3 Crest-front steepness, (Bonmarin, 1989)

Bonmarin showed a steady increase in ϵ , to 0.55 prior to breaking (Figure 2), for a case of plunging breaker. After breaking, the ϵ decreased steadily to 0.15 after 10 frames (0.4 seconds). He also concluded an average $\epsilon = 0.38$ for spilling breakers, and an average $\epsilon = 0.61$ for plunging breakers. This clearly shows a relationship of plunging breaker being closely associated with higher crest-front steepness.

2.2.2 Crest-rear Steepness

(Kjeldsen M. , 1979) concluded the decrease in wavelength leading up to breaking. Giving different L' and L'' values. Coupled with varying wave crest values, the resultant ' ϵ ' and ' δ ' would be analysed to understand the behaviour during an onset of breakers.

$$\delta = \frac{\text{wave crest}}{\text{crest-rear length}} \text{ (applicable for Particle Image Velocimetry users)} \quad (8)$$

$$\delta = \frac{\zeta}{\frac{g}{2\pi} * T'' * T_z} \text{ (applicable for wave probe users)}$$

$$\text{Note- crest-rear length} = \frac{g}{2\pi} * T_z * T''$$

T'' , the time taken for the wave at wave crest, travel to free surface

However, (Bonmarin, 1989) did not show the behaviour of δ , leading to breaking. However he showed a range of values of $0.26 < \delta < 0.48$ with an average value of $\delta = 0.33$ for spilling breakers, and values of $0.24 < \delta < 0.33$ and an average value of $\delta = 0.29$ for plunging breakers. This doesn't give a distinct relation between the types of breakers and the crest-rear steepness value, unlike the crest-front steepness. This shows inconclusive crest-rear steepness with the intensity of breakers and their occurrence.

2.2.3 Vertical wave symmetry ratio

In comparison, (Kjeldsen M. , 1979) also extended the geometric wave breaking criteria to include ' β ' & ' μ ', which were used to describe vertical and horizontal wave crest asymmetry.

$$\beta = \frac{\text{crest-rear length}}{\text{crest-front length}} \text{ (Applicable for PIV users)} \quad (9)$$

$$\beta = \frac{T''}{T'} \text{ (Applicable for wave probe users)}$$

Or β (Equation 9) could also be expressed ε/δ . The phase speed used for calculating both crest-front length and crest-rear length was assumed to be uniform or inconclusive as discussed in (2.2.2 Crest-rear Steepness). (She.K, 1997) (Bonmarin, 1989) (Kjeldsen M. , 1979)

It is noted that for symmetrical waves, the value of $L' = L''$, giving a ' β ' of 1. However, as the wave approaches breaking, the wave crest will lean towards the direction of propagation, giving $L' < L''$. Hence, prior to the onset of breaking, the vertical wave crest asymmetry factor will have a higher value. Both (Bonmarin, 1989) & (Kjeldsen M. , 1979) concluded an upper limit vertical asymmetry value of 2.2 prior to the onset of breaking.

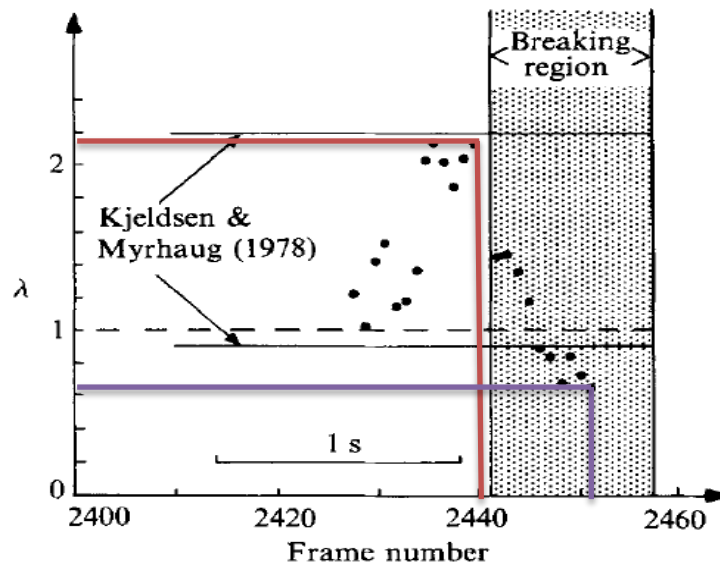


Figure 4 Vertical Asymmetry ratio, (Bonmarin, 1989) (red line indicate just prior to breaking, and purple lines indicate post-breaking)

Bonmarin also showed the behaviour of β , which shows β raising gradually till a peak of 2.2, and dropping as much as 70% to a low β value of 0.6 (and having the crest-front length overtaking the crest-rear length) in just 10 frames (0.4 seconds) after breaking. (as indicated in above Figure 3)

2.2.4 Horizontal wave symmetry ratio

$$\mu = \frac{\text{wave crest}}{\text{wave height}} \quad (10)$$

Waves with low steepness would have similar wave crest and wave trough values, indicating a symmetrical wave with a horizontal wave crest symmetry factor, μ of 0.5. As the wave approaches higher steepness and till the onset of breaking, the wave crest would be greater than the half of the wave height and at the same time, the depth of wave trough will decrease. Also, recalling higher order of Stokes theory (Equation 60) that for a higher order crest, 'substitute $(kx) = 0$ in Equation 46', the higher order crest is higher than the 1st order Stokes theory. On the other hand, for a higher order trough, 'substitute $\cos(kx) = -\pi$ in Equation 61', the higher order trough is shallower than what the 1st order Stokes theory would describe it to be. Hence the Stokes higher order theory and this formula take into account of the asymmetric features of the wave crest and trough prior to breaking. (Bonmarin, 1989) had shown a mean μ value of 0.69 for spilling breakers, and a mean μ value of 0.77 for plunging breakers; compared to a symmetrical μ value of 0.5 for regular waves. These varying

Horizontal wave symmetry values for plunging, spilling and regular waves, seems to hint that a higher wave steepness would generate a higher μ value.

(She.K, 1997) expanded on earlier two-dimensional research work done (Kjeldsen M. , 1979) & (Bonmarin, 1989) by generating three-dimensional breakers. The experiment was conducted at Edinburgh University with a wave basin that had length, breadth and a constant depth of 12m, 27m and 1.2m respectively. Plunging breakers were generated using two different methodologies; the single frequency method and multi-frequencies method. The single frequency method involved 360 wavefronts and with different angular properties. The phase shifts of these fronts were calculated such that this would yield the maximum crest at a pre-determined point. The multi-frequencies method used 1,000 wavefronts with different frequencies, but these wavefronts had a constant angular property, or a 2D breaking wave.

(She.K, 1997) then used wave gauges to record the elevation time history. These data were used to calculate the 4 geometric wave breaking criteria; ϵ , δ , β and μ . The wave period, T , was calculated using the zero-down crossing method, similar to earlier researchers. (She.K, 1997) experiment yielded higher ϵ and δ values as compared to two-dimensional breaking waves, especially for single-frequency focusing wave recording ϵ and δ values doubling those of a two-dimensional breaking wave from previous studies. It appears that single frequency three-dimensional multi-directional focusing waves, able to get a higher concentration of energy as compared to focusing methods which use singular directional of wave generation with varying frequencies.

(Duncan, 1983) did an experiment on breaking waves using a towed hydrofoil in a tank that had length, breadth and a constant depth of 24m, 0.61m and 0.61m respectively. The water of the tank was dyed with a fluorescent dye and a light-slit generator was installed to create a beam of light. When the lights are switched on, the camera would be able to capture surface displacement. He concluded that the corresponding wave breaking limiting steepness was 0.31. (Rapp, 1990) did several experimental works on breaking waves, using a range of wave steepness (ζ_{ak}) and different group frequency bandwidth ($\frac{\Delta f}{f_c}$). Breaking waves were generated in a wave tank having length, breadth and depth of 25m, 0.7m and 0.6m respectively, via focusing method. The tank was filled with low-density dye particles that would float at the surface. During the onset of the breaking wave, the affected free surface would undergo mixing and the breaking phenomenon will be captured by a camera. They showed that wave breaking could also occur at lower wave steepness of $0.15 < \zeta_{ak} < 0.22$, at a wave group's frequency bandwidth of $(0.4 < \frac{\Delta f}{f_c} < 0.6)$, although the recorded loss of energy correlates to the steepness of the wave group, and is lower in this case of breaking. (Wu, 2004) went on to further (Rapp, 1990) research by using a range of wave group's frequency bandwidth ranging from $0.1 < \frac{\Delta f}{f_c} < 1.4$. They concluded that breaking wave's geometric properties could be affected by the wave group's frequency bandwidth and presented data showing a negative correlation between wave group's frequency bandwidth and breaking waves' geometric properties. Although recorded breaking wave steepness could be as low as 0.15 (when $\frac{\Delta f}{f_c} = 1.4$), which matched (Rapp, 1990) research. However, this focused wave was achieved using the constant amplitude method; a method which was shown by (Chan E.S L. Y., 1997) to produce lower wave stability and causing the focused wave to break at lower wave steepness. (Babanin, 2007) conduct experimental work at an air-sea wave tank which is also capable of simulating wind flow. (Babanin, 2007) discussed the limits for wave steepness that for wave steepness, $\zeta_{ak} > 0.44$, wave breaking occurs almost immediately within a wavelength; agreeing well with Stokes breaking the limit of $\frac{H}{\lambda} =$

$\frac{1}{7}$ or $\zeta_{ak} = 0.4488$. At wave steepness, $\zeta_{ak} < 0.08$, wave breaking would not occur unless with the interference with the wind. (Babanin, 2007) studies also established that as long as the wave steepness is within the range of the two limits, $0.08 < \zeta_{ak} < 0.44$, it will eventually lead to breaking.

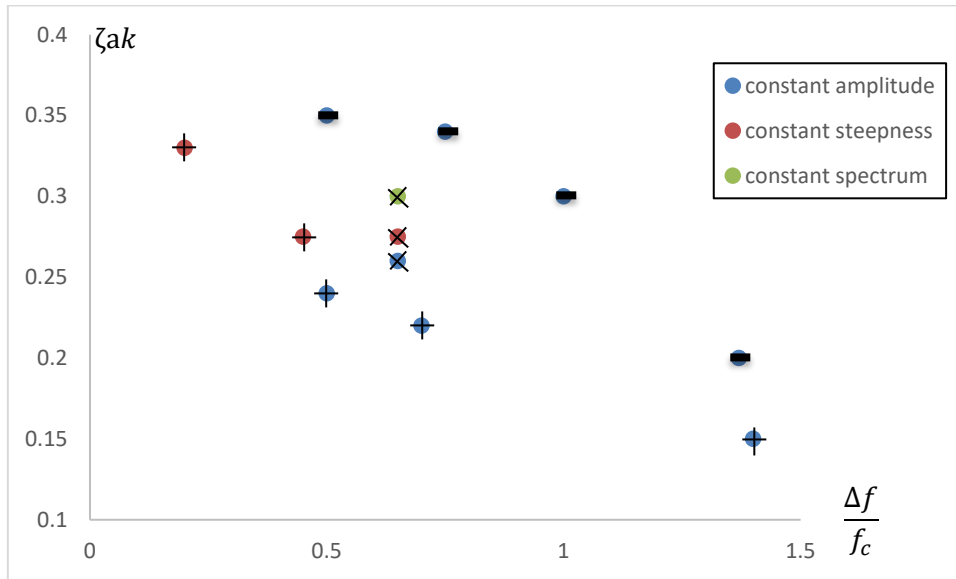


Figure 5 breaking wave steepness analysis, [-],[+],[x], represents data extracted from (Babanin, 2007), (Wu, 2004), (Chan E.S L. Y., 1997) respectively

(Note: The constant amplitude values given by (Babanin, 2007) appears to be inflated as he uses ζ_{ak_c} for the wave steepness parameter instead of ζ_{ak} .) (Babanin, 2007) pegs each wave components to the central frequency (f_c) instead of the wave individual frequency (f).

A negative correlation between the wave spectrum bandwidth and the wave breaking steepness parameter can be established. (Wu, 2004) experimental data agrees with (Chan E.S L. Y., 1997) that the constant amplitude method would yield a lower wave breaking steepness parameter as compared to the constant steepness method.

2D waves	[1]	[2]	[3]
ϵ	0.85	0.78	0.84
δ	0.33	0.39	0.41
β	3.09	2.18	2
μ	0.93	0.95	0.82

Table 1 Past literature survey results for 2D waves, [1]- (Bonmarin, 1989) 2D focusing waves, [2]- (Kjeldsen M. , 1979) 2D wave-wave interaction, [3]- (Wu, 2004) 2D focusing waves

3D waves	[1]	[2]	[3]	[4]
ϵ	1.52	1.02	0.84	1.26
δ	0.96	0.68	0.45	0.52
β	1.68	2.25	1.8	2.6
μ	0.65	0.67	0.8	0.86

Table 2 Past literature survey results for 3D waves, [1]- (She.K, 1997) 3D wave angular focusing, [2]- (She.K, 1997) 3D wave multifrequency focusing [3]- (Wu, 2004) 3D diffracting waves, [4] (Wu, 2004) 3D focusing waves

From the above wave breaking parameters (Table 1 & Table 2), it is shown that from higher β values that there is longer crest-rear length as compared to the crest-front length before the onset of breaking. Also, a μ value of > 0.5 , would validate (Kjeldsen M. , 1979) theory that the local crest height is more than half of the overall wave height.

However, the higher crest-rear length and local crest height value would lead to a cancellation effect on the δ , resulting in having inconclusive local crest-rear steepness for the onset of breaking waves. On the other hand, the crest-front steepness ϵ , shown to be a better wave breaking geometry parameter due to its consideration of the local wave asymmetric geometries; higher crest height and the lower crest-front length. As such, this research work will focus on the most distinctive and widely used geometric breaking criterion; the crest-front steepness.

2.3 Kinematic breaking criteria

Breaking waves could also be evaluated by analysing the kinematics criteria. Many comparisons were done between the horizontal wave particle velocity and the wave phase speed.

In approaching shallow water, the shallow water dispersion relationship, $c = (gd)^{0.5}$ is applied. The value of wave phase speed will decrease together with decreasing depth, d . However, the horizontal wave particle velocity remains relatively the same. Hence at a point, the horizontal wave particle velocity will finally surpass the decreasing wave phase speed, and breaking will occur. (Chang K.A, 1998) simulated breaking waves in intermediate water ($\lambda=121\text{cm}$, $H= 20\text{cm}$, $H/\lambda = 0.165$) and observed that the wave particle velocity near the overturning jet is 1.5 to 2 times the phase velocity which reasons well with the common relationship understanding between the wave particle velocity and phase velocity.

However, in deep water, the phase speed does not reduce due to shoaling effects. Breakers still occur due to the horizontal wave particle velocity reaching a critical level; exceeding the phase velocity. In (Rapp, 1990) experimental work, there is a phase speed reduction right before the onset of plunging.

(Perlin .M, 1996) created breaking waves via dispersive focusing, which involved using a range of wave frequencies to simulate breaking waves. PIV (Particle Image Velocimetry) and PTV (Particle tracking velocimetry) were used to determine the fluid's particle velocity. He went on and generated the plunging breaker and found that the wavelength prior to breaking is 0.7m, which gave a phase speed of 1.05m/s, according to linear wave theory. His measured phase speed of 1.08m/s, matched a close approximation to the calculated value.

(Perlin .M, 1996) found out that the PIV-measured ' u' ' was 0.8m/s, which was approximately 25% lower than the measured phase velocity. However, his PTV-measured ' u' ', was actually showing signs of the horizontal wave particle velocity surpassing the phase speed. He concluded that the discrepancies could be due to possible lack of sufficient resolution at the air-water interface. (Perlin .M, 1996) went on and concluded that prior to breaking, the crest front becomes nearly vertical and the wave particle at the crest starts to accelerate horizontally.

(Stansell. Paul, 2002) performed experiments of plunging breaker and spilling breaker to observe the ' u/c' ' ratio upon breaking. They found out that the ' u/c' ' recorded for plunging and spilling breakers were 0.81 and 0.95 respectively which were less than 1. This confirms that the common understanding of ' $u/c' > 1$ ' for breaking waves, isn't a necessary kinematics parameter, but more of a sufficient kinematics parameter.

However, there are studies conducted by (Baldock T.E, 1996) which consider that the crest velocity could have been underestimated, whilst using linear theory. As wave breaks at higher wave steepness, the use of linear wave theory to predict crest velocity may not be suitable. In (Baldock T.E, 1996) research, it was found out that the phase velocity might be calculated to be 3% higher than the value calculated using linear theory, which seems to agree with linear theory. However, Baldock concluded that the near-surface calculated velocity was higher than the calculated velocity using linear theory. (De Wang C, 2018) created plunging breakers and investigated the kinematics of breaking waves, and concluded that the kinematics of breaking wave could vary by 7 – 24% higher (dependant on the intensities of breaking wave) than otherwise obtained by the linear theory.

(Longuet-Higgins MS S. N., 1983) introduced a new parameter, R , the rate of rise Equation 11.

$$R = \frac{\Delta\zeta}{\Delta t} \quad (11)$$

It describes the rate of change in elevation. Taking c , as the ratio of change in horizontal displacement divided by time. R is reformulated as, $R = c * \frac{\Delta\zeta}{\Delta x}$. Taking that the slope of the plunging wave (α), taking the horizontal axis as a datum, $\alpha = \tan\left(\frac{\Delta\zeta}{\Delta x}\right)$, giving the resulting expression for $R = c * \tan(\alpha)$.

An earlier research had been done, (Longuet-Higgins MS F. , 1977) to determine the maximum value of the slope (α). The value of α was calculated using the analytical method by extrapolating the maximum steepness of gravity waves and a maximum value of $\tan(\alpha) = 0.586$ was obtained. Substitute the critical slope value into R , which finally gives $R = 0.586 * c$. Meaning any vertical velocity surpassing 0.586 of phase speed, will exceed the critical slope of a wave, giving rise to instability causing the wave to break. However, (Longuet-Higgins MS F. , 1977) had assumed an average phase speed while calculating the critical rise rate, which cast doubts on the accuracy of the equation as wave breaking involves dynamic changes prior to breaking. (Xu Delun, 1986) improved the critical rise rate formula by changing the phase velocity to include second-order function (Equation 12).

$$c = \frac{gT}{2\pi} * \left(1 + \left(k * \frac{h}{2}\right)^2\right) \quad (12)$$

This method of using the critical rate of rise to predict the onset of breaking waves differs from the other methods of using wave kinematics as described earlier. For the other wave kinematic prediction method that uses horizontal particle velocity at the wave crest, need PIV to record readings. However, the critical rise rate could be calculated using $\Delta\zeta, \Delta x, \Delta t$ which would be calculated using just wave probes using high frequencies recording capabilities for improved accuracy.

2.4 Dynamic breaking criteria

Normally, breakers ((Schultz W.W, 1994), (Michael L Banner, 1998) (Tian Z.G, 2010)) are predicted via a noticeable drop in wave energy or a deceleration (slowing) of the wave crest velocity; kinematic results post breaking would be shown in Simulations and Experimental results discussion) would be . On the contrary, several researchers are proposing a solution to predict breaking criteria based on local energy growth rate. Schultz relate the large energy input rate with large plunging waves. The severity of the breaking wave is related to the energy input rate. Michael Banner consider not only the local energy growth rate, and as well as the momentum densities. Tian concluded that at the lower frequency spectra, before wave breaking, change of energy is due to the nonlinear energy

transfers (Note: $E = 0.5 * \rho * g * \zeta^2$); a 50% reduction in wave elevation would mean a 75% change of energy. For higher frequencies spectra, within breaking zone, the change of energy is primarily due to the wave breaking. Tian further related the range of the rate of change of energy to the intensities of wave breaking.

Not only limited to the rate of energy growth, but there are also numerous researches that researched on the rate of acceleration of wave crest. (G.I, 1971) stated that when the wave crests acceleration reaches g (earth-gravitational acceleration 9.81m/s^2), the wave crest will grow to become unstable. This would eventually lead to breaking, and the loss of energy and deceleration of the wave, and ultimately restoring the stability. (Snyder, 1983) did an experimental study and found a value of $0.5g$ for the wave crest acceleration to produce whitecap breaking wave. (Snyder, 1983) further concluded that the study isn't definitive due to the limitations of the frequency of the spectral peak that was considered. (Longuet-Higgins, Accelerations in Steep Gravity Waves, 1985) discussed 2 different methods to obtain the vertical acceleration components. The 'apparent' method obtains the acceleration via a fixed wave probe (the double differentiation of the elevation by time), and the 'real' method or Lagrangian method obtains the acceleration via using a surface buoy to obtain the change in surface kinematics. (Longuet-Higgins, Accelerations in Steep Gravity Waves, 1985) suggested that any dynamic wave breaking criterion should be based on the upwards acceleration values at the wave trough, rather than the downwards acceleration at the crest. This is due to the tendency of the acceleration values to suffer a sharper negative spike at the wave crest as compared to the upwards acceleration values taken from the trough of the wave crest that is shown to be more uniformly distributed; in the form of a smooth sinusoidal curve. (Longuet-Higgins, Accelerations in Steep Gravity Waves, 1985) also states that for a wave steepness of $\zeta ak = 0.35$, an upward acceleration of $0.28g$ could be observed, as compared to a downwards acceleration of $-1.28g$ at the wave crest. (Shemer L, 2013) expanded the research on the horizontal particle acceleration into 3rd order having wave steepness of 0.3 , which is on the verge of breaking and concluded that an extension of the particle acceleration to the 3rd order is comparable with 2nd order analysis, is also beneficial to the prediction of the wave breaking criterion. (Shemer L, 2013) creates breaking wave with $\zeta ak = 0.3$, and noted that for both Eulerian and Lagrangian 3rd order vertical acceleration values exceeds $-0.5g$, agreeing with (Snyder, 1983).

2.5 Generation of breaking waves

Appropriate experimental setups are essential for the data recording and post-processing to obtain an accurate output and conclusion. Breaking wave experimental works are not the usual wave experimental work that had been done. Breaking wave experimental works are more demanding, due to the fact that it involves high non-linearity in terms of surface elevation, impact pressures, phase velocity and so on.

Breaking waves could be generated by focusing methods or shoaling effects. Generating breaking waves via shoaling effects tend to occur at coastal area, and mainly bounded by the gradient of the seabed. Whereas on the other hand, the art of generating breaking wave by the focusing method is not that straightforward.

(Chan E.S L. Y., 1997) introduces 3 methods of creating focusing waves at the National University of Singapore. The 3 methods are constant steepness method, constant amplitude method and the constant spectrum distribution method. 28 regular waves of varying frequencies $0.56 \text{ Hz} \leq f \leq 1.1 \text{ Hz}$ were chosen for his experimental work. The constant steepness method consisted of 28 regular wave components with a constant steepness with respect to the individual wave

component's parameters. The constant amplitude method uses a constant amplitude of 0.01m for each of its individual 28 regular wave components. The spectrum distribution method distributes the individual wave component's amplitude according to the individual wave components frequency.

$$\zeta(x, t) = \sum_{n=1}^N \zeta_{a,n} * \cos(k_n x - \omega_n t + \phi_n) \quad (13)$$

By setting the equation of each individual waves, $\cos(k_n x_b - \omega_n t_b - \phi_n) = 1$. The maximum potential of each individual wave component was achieved at the intended focal point.

x_b (m) = distance from the wave generating paddle to the location of breaking waves

t_b (s) = time taken for the breaking waves to occur

k_n (rad.m⁻¹)= individual wave number, (which is fixed for each individual regular waves)

ω_n =(rad.s⁻¹)= individual wave angular frequency, (which is fixed for each individual regular waves)

$$\phi_n = k_n x - \omega_n t \pm 2\pi * m \quad (14)$$

Where $m = (0,1,2,...)$

There are few types of wave-makers in the industry, of which, the piston type wave-maker and the flap type wave-maker are commonly used. The proposed theory for this wave-maker is based on the assumption that the amount of water displaced by the wave-maker is equivalent to the amount of fluid in a wave crest.

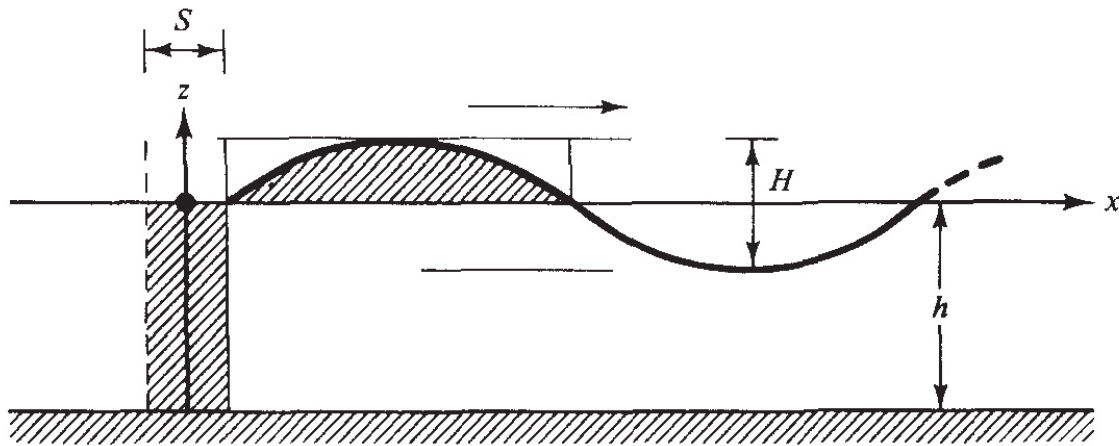


Figure 6 Piston wave-maker theory, (Dean, 1984)

Above (Figure 5), illustrated the water displacement by the wave piston; indicated with shaded areas. The Stroke of the piston wave-maker (S), multiply by the working depth (d) of the water, would equate to the water displaced for the formation of the wave crest (Equation 15); which are the shaded components in the above figure.

$$S * d = \int_0^{\lambda/2} \left(\frac{H}{2}\right) * \sin(kx) . dx \quad (15)$$

$$S * d = -\left(\frac{H}{2k}\right) * \left[\cos\left(\frac{k\lambda}{2}\right) - \cos 0\right] , \left(k = \frac{2\pi}{\lambda}\right)$$

$$S * d = -\left(\frac{H}{2k}\right) * (-1 - 1)$$

$$S * d = \left(\frac{H}{k}\right)$$

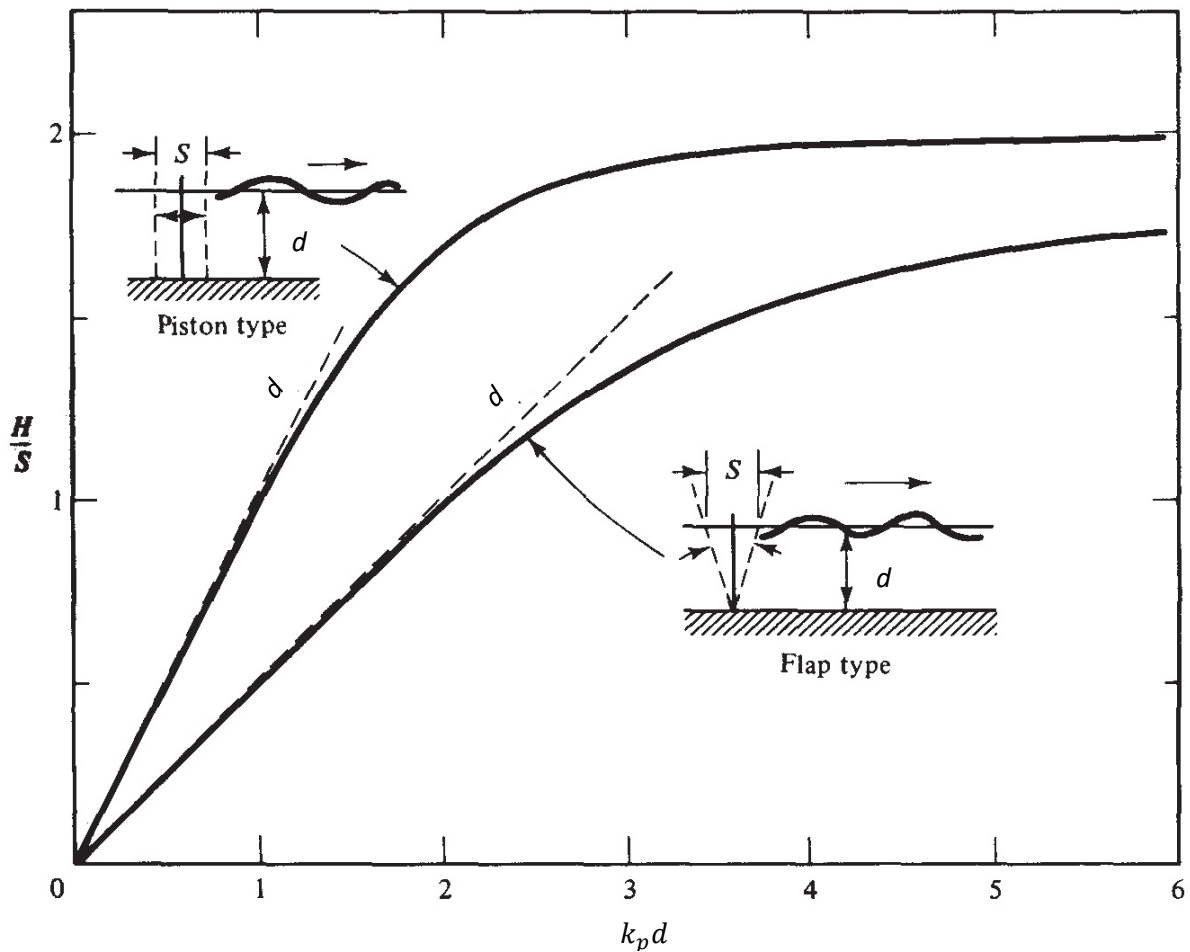


Figure 7 H/S ratios for both Piston and Flap type wave-maker (Dean, 1984)

(Chan E.S L. Y., 1997) set up the experiment on an experimental wave flume, measuring 35.22m, 2m, 1.3m, length, width and height respectively, and with a constant water depth of 0.8m. The details of the 28 regular waves, of varying frequencies, wave number and phase shift, were then inputted to obtain the wave height-time history (Equation 13 & Equation 14). Subsequently, using the individual wave number (k) and constant working water depth (d), the individual contribution of H/S ratio is established.

With the use of individual wave component and parameter and the above (Figure 6) appropriate H/S ratio to use, the piston stroke displacement time-history requirement from each individual wave component could be established. (Figure 6 & Equation 13)

$$S(t) = \sum_{n=1}^N S_n * \cos(-\omega_n t + \phi_n) \quad (16)$$

The space domain function (Equation 16) was removed, as at the wave piston position, $x=0m$.

The above mathematics could be used for all 3 wave focusing methods that (Chan E.S L. Y., 1997) introduced.

2.5.1 Stability of different focusing methods

Most researchers ((Bonmarin, 1989), (Kjeldsen S., 1984), (She.K, 1997), (Wu, 2004)) use the focal spectrum method for creating plunging breaker. This method involving assuming the sea state,

although that of irregular waves. It is assumed that these irregular waves are made up of many (hundreds, or even thousands) or regular waves with varying frequencies. These regular waves will then superposition to elevate the amplitude past a critical value, inducing instability causing a breaker. However, (Chan E.S L. Y., 1997) introduced 3 focusing methods; constant amplitude, constant steepness and focal spectrum method. Prof Chan concluded his findings that, the constant steepness distribution method has the greatest stability prior to breaking due to the fact that the wave amplitude in the higher frequencies was relatively smaller as compared to the lower frequencies, allowing the wave crest to build up more energy which allows a higher wave crest before breaking. Subsequently, for the constant amplitude method, wave amplitude in the higher frequencies was as high as the lower frequencies. Wave amplitude itself, should not pose a problem. However, constant wave amplitude in the higher frequencies would mean a higher wave steepness which would contribute to a highly unstable wave crest. This results in the wave crest breaking at smaller amplitude for the constant amplitude method. Whereas the spectrum distribution had wave amplitude in between the previous two methods, hence the results were shown to be less stable than the constant steepness method and more stable than the constant amplitude method.

2.6 Simulation of breaking waves

An accurate description of the free surface behaviour and evolution is essential for the study of breaking wave. (F.H. Harlow, 1965) were the pioneer in establishing a method to track free surface, solving the Navier-Stokes equation. They used a method; namely the 'marker and cell method'. This method places a large number of massless markers on the free surface to track fluid motion. However, this method was proved to be futile when it comes to problems which involved breaking waves, or other problems with high nonlinearity. As the deformation of the wave gets too huge, a massive amount of markers are needed, complicating the tracking procedures. The marker and cell method have problems accounting for the air bubbles in waves while dealing with breaking waves.

(C.W. Hirt, 1981) devised a method, known as the Volume of Fluid (VOF) method which is a two-phase surface tracking method. This method involves using a volume ratio function, ' J ' to mark each mesh's cell. With value of ' $J = 1$ ', indicating that the mesh is fully occupied by fluid, and with value of ' $J = 0$ ', indicating that the mesh is only occupied by air. When there is two-phase involvement in a single mesh cell, a value of J would be given as a percentage of the mesh cell being filled with fluid. With a determined ' J ' value, the density and viscosity could be calculated as a direct function of ' J '.

(Gang Chen, 1999) simulated plunging breaker and extends the Volume of Fluid method by using the Piecewise Linear Interface Construction Method (known as PLIC). As the VOF method for free surface tracking might be prone to error for problems involving high non-linearity. The PLIC method involves estimating a ' J ' value for each individual cell and re-calculates the free surface velocity and giving a new ' J ' value, significantly reducing the error of margin for the position of the interface.

As compared to the marker and cell methods, where massless markers are placed along the free surface, VOF can also indicate the free surface by tracking the location whereby the ' J ' value undergoes changes. The ' J ' value could be set as 0.5 to pre-define the interface, and this setting is valid even for extreme wave events and breaking waves. However, in such VOF based simulations, it is important to take note of the size of the grids. (Li Xiaoyi, 2010) did a simulation using the 'Coupled Level Set and Volume of Fluid' method (CLSVOF) for two-phase flow problem involving fuel jets. The level-set method involves using a level set function (let's call it γ), a value of $\gamma = 0$, defining the interface. Imagine looking at an ice berg surrounded by water, in plan view. The layer which the ice berg having contact with the water is the interface. And this interface will evolve, as the ice melts or

freezes. The level-set method interface will be time dependant, allowing to track changes of interface as function of time. As some under-sized bubbles would not be accounted for due to the coarseness of the grids, there would be an error on the VOF interface, if the size of the bubbles generated by the breaking waves matches the grid. It is always advisable to have the grid size finer than the size of bubbles created. (Li Xiaoyi, 2010) pointed out that the interface of the two phases was crucial and went on to refine the mesh at the interface area until convergence. Their findings concluded a more accurate experimental comparison for a simulation with a finer grid. Simulations with a finer grid also detect a higher volume percentage of bubbles, which would have gone undetected for simulations with coarser grids.

(Zhaoyuan Wang, 2012) employ a second order accuracy for the volume of fluid (VOF) method to track demanding sharp interface interactions. The interface was evaluated using a second order accuracy distance function. This involves a distance function scheme to reconstruct the interface. This method is proven to be more efficient than the CLSVOF methods in terms of surface interface treatment. The error of margin that this new VOF method gives is similar to the CLSVOF method. However, this new VOF method requires much lower computational resources as compared to the CLSVOF method, making it arguably being more time-efficient.

Smoothed Particle Hydrodynamics (SPH) of late, is a hot favourite for modelling waves of high non-linearity. SPH is able to track free surface with ease and is suitable to track breaking waves, flow separation. SPH has its own share of limitations; commonly involving some viscosity problem which would ultimately affect the shear force in fluid. (Dalrymple. R.A, 2006) introduced a sub-particle scaling (SPS) technique and change the viscous formula to improve the turbulence problem. For using a slightly compressible SPH, there would be some physical irregularities observed at the free surface, due to the density variations. The SPS method which is used by (Dalrymple. R.A, 2006) averaged out the densities and perform such filtration on regular time steps interval to maintain a smoothed density of the water particle.

The accurate simulation and generation of wave breaking garner much interest of late. This is the most fundamental step before moving into the simulation of breaking wave's impact loading. The predicted breaking wave loading would be meaningless if the inputted wave simulations are not accurate. Breaking waves could be generated by shoaling effect, superposition of waves or due to strong winds. (Wu N.T, 1994) simulated breaking wave impacts on vertical walls. However, for the case of breaking wave impact with substantial amount of entrapped air, they were unable to compute the accurate magnitude of the breaking wave impacts due to the lack of the current model to account for the compressibility of air. (Bredmose H, 2011) did breaking wave simulations on offshore wind turbine foundations, using a different focal point. They concluded the same findings as (Chan E.S L. Y., 1997) that the more developed breaking waves, give a lower peak force. However, (Bredmose H, 2011) using the simulated wave breaking impact force output to compare with analytical Morison's Equation (Equation 1); that doesn't account for the slamming force contribution from the breaking wave impact, which explains the apparent overestimation of the peak force of the simulated breaking wave.

(Johan Roenby, 2016) further expanded the two-phase VOF surface tracking method, and came out with a new numerical method; now known as isoAdvect. There are 2 additional steps to the older VOF method that is commonly used for free surface tracking. The first step is to reconstruct a geometric surface within a given cell. From the transported properties through a face of the cell, it is possible to track the change of volume within a cell.

$$\Delta V_j(t, \Delta t) = \int_t^{t+\Delta t} \int_{F_j} H(x, \tau) u(x, \tau) \cdot dS \cdot d\tau \quad (17)$$

'H' in the above equation refers to a non-dimensional indicative field that is a function of different mediums density, and a function of spatial location. If most of the fluid is coming from local distribution of say, Fluid A, then 'H' would be 1, and if all of its fluid, say Fluid B derived from another neighbouring face, then 'H' would be 0. 'u' is the velocity registered at the given face of the cell, and 'S' is the surface area.

In the traditional VOF method, the velocity is calculated based on the averaged cell values. Hence any 'sharp' local distribution phenomenon, wouldn't be accurately represented. In isoAdvector, an additional step is introduced which would be highly based on the local distribution of the both fluid A & B, effectively reconstructing the interface within a given cell. Integrating this newly reconstructed area to obtain the more accurate change of VOF over a specific time step.

2.7 Factors affecting Slamming load force/pressure

(von Karman, 1929) was the first to investigate the value of slamming load coefficient. He did an experimental study of the maximum slamming impact of seaplane floats, allows the seaplane float to freefall into the water. He determined the maximum slamming load coefficient to be the value of π upon initial impact.

(Wagner, 1932) expanded von Karman's theory to consider the shape deformation of the water while in contact with the cylinder structure. He noted a pile-up deformation effect on the water during initial contact with the structure. Due to this pile-up effect, taking into consideration the rise of free surface level, this increases the consideration of the wetted surface area. Therefore a maximum slamming coefficient of 2π was recommended, double the value of von Karman's theory.

(Fabula, 1957) expand (Wagner, 1932) theory by introducing the slamming pressure as a function of time. He uses an ellipse fitting method to calculate the increased wetted surface area due to the deformation of the water (pile-up effects). (Fabula, 1957) concluded his findings with the slamming coefficient peaking at 2π upon initial contact, however, with a rapid decaying slamming coefficient after initial contact. (Goda, 1966) introduced an additional force term to be added to the original Morison Equation to account for the additional slamming load induced by the plunging breaker (Equation 4). The maximum slamming load upon contact is described by Equation 5.

$$F_S(t) = 0.5 * \rho_w * \pi * D * C_b^2 * \lambda_c * \zeta_b * \left(1 - \frac{C_b}{R} t\right) \quad (18)$$

t , describes the impact duration. $t = 0$ during initial impact.

R = Cylinder characteristic radius (m)

(Goda, 1966) also attempts to describe the entire slamming load contribution as a function of time, and uses a slamming coefficient of π and Equation 5 is calculated when $t = 0$, during initial impact. As Goda suggested (Equation 18), upon initial slamming (when $t = 0$), the slamming load contribution starts to encounter a linear decaying phenomenon (Figure 123), until the breaking wave propagates through the cylinder.

(R. Cointe, 1986) did a correction to the cylindrical shape to account for the pile-up effects, and describes the wetted cylinder boundary as a parabolic shape. As compared to (Fabula, 1957), (R. Cointe, 1986) concluded a more gradual decaying phenomenon. (J. Wienke, 2005) did experimental

work on the breaking wave impact force. Pressure gauges were placed on different elevations of the cylinders and also along the circumference of the cylinder. Force transducers were placed on both ends of the cylinder to capture the total reaction force. The deformation of the water while in contact with the cylinder, known as 'pile-up' effects was taken into consideration for their experimental study. (J. Wienke, 2005) derived slamming co-efficient is time variable, with the initial max slamming co-efficient is $= 2\pi$, and then decaying shape within agreement with (R. Cointe, 1986), albeit with a steeper decaying towards the latter part of the slamming impact.

(J. Wienke, 2005) create a breaking wave focal point after the cylinder spatial location, to capture only the quasi-static loading acting on the cylinder and subtract the obtained quasi-static loading to other loading condition which involved plunging wave slamming jet loads; to obtain the contributing slamming loads. Next, using the obtained pressure values, they analysis the slamming pressure spreading along the circumference of the cylinder. Recalling Equation 5, the difference between a two-dimensional and three-dimensional force analysis is the inclusion of the curling factor (expressed as a ratio of less than 1, λ). The derived maximum curling factor achieved was consistent with Goda's description of a typical curling factor value of 0.4 to 0.5.

The research on wave breaking impact loads on offshore structures gained significant interests in the past few decades. It is widely understood that the wave breaking impact loads are more significant than non-impact loads.

Under normal circumstances, while considering hydrodynamic force acting on a slender cylinder, the Morison's Equation is being used to consider such wave forces affecting slender structures (4.4.1 Assumptions for Morison's Equation). However, while considering hydrodynamic forces that are of highly non-linearity in nature, like breaking waves force, the Morison equations, together with commonly used potential theory, will be rendered invalid in such situations. There were many types of research that came up with new theories and proposals to try to have a better prediction of highly non-linear breaking wave loadings and more research and understanding are needed to improve on this area of uncertainty.

In this research, we would be focusing on the Morison's Equation that accounts for the inclusion of the non-linear slamming force loading (Equation 4 Morison's Equation for breaking wave force).

2.7.1 Stages of Plunging Breakers

(Chan E.S W. M., 1988) conduct plunging wave experiments on walls and cylinder, to assess the effects of plunging breaker. Plunger breaker was created using superposition of 32 regular waves of varying frequencies, via the constant amplitude method. 6 Pressure transducers were mounted on the structure of interest, with a low response time of $1\mu s$ and a pressure recording capability of $21,000 \text{ kN/m}^2$. For the recording of wave breaking force contribution, the structure of interest was attached to a vertical supporting frame and 2 force blocks were attached on the horizontal axis of the rail. Wave breaking force will be impacting on the vertical support frame, which will, in turn, create a shear reaction on the horizontal axis. This shear force will then be recorded by the 2 force blocks.

They discussed that both walls and cylinder have similar reading comparable to each other. However, they also noted that the wall structure would have a greater influence on the dynamic pressure impact. In other words, motion-based contribution to the dynamic pressure load is more significant in the wall structure, as compared to cylindrical. (Chan E.S W. M., 1988) researched on the slamming pressure induced by the plunging breakers at 3 different stages. He classified breaking

wave impact to 3 different regions; the breaking wave impact, the transition zone, and the broken wave impact (as shown in below Figure)

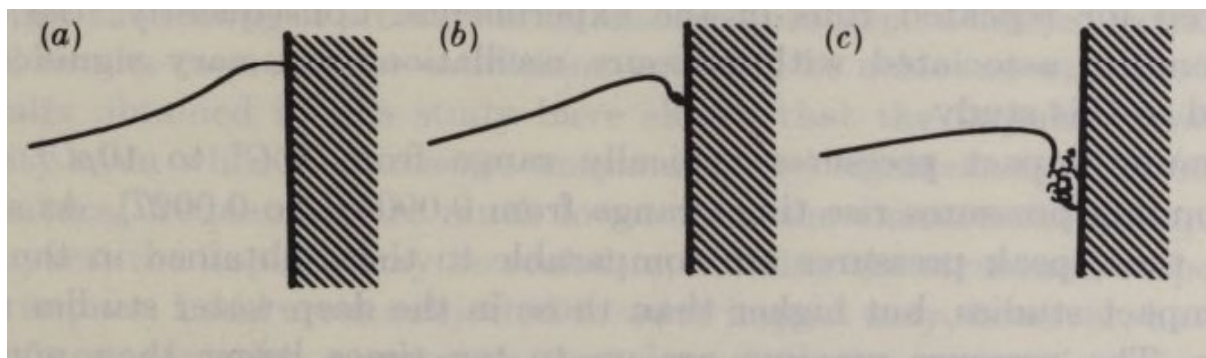


Figure 8 – Different stages of breaking wave impact zone by (Chan E.S W. M., 1988)

The breaking wave impact zone is defined by an immature form of plunging breaker, with an immature jet forming at the crest. The transition zone is characterized by a more mature jet with higher air entrainment; curl of jet. Finally, the broken wave impact is the final form of the plunging jet, with the mature jet starting to collapse downwards onto the vertical wall. (Chan E.S W. M., 1988) concluded that the slamming pressure maxima occur during the breaking wave impact zone; with an immature jet impacting onto the vertical structure. Although there is lesser air entrainment (air bubbles generated during breaking) at this breaking wave impact zone, however, there is more air entrapment (air bubbles trapped, during plunging impact with structures) during the impact of the immature plunging jet. On the other hand, the early stage of the plunging breaker, during its initial impact, as there is a lack of air entrainment and entrapment, there is lesser slamming pressure recorded by the experimental work.

This research work would not be seeking to further revalidate knowledge that has been contributed by Chan. This research would focus on the worst-case scenario to further research on the maximum potential of the plunging wave impact loading, and hence, would be focusing on the transition zone of plunging breakers.

2.7.2 Rise Time

(P.A Blackmore., 1984) investigated the slamming pressure on beach walls at different locations in England. Pressure sensors were placed on different locations of the walls that were impacted by these coastal induced plunging waves. The pressure sensors record the pressure-time history and they concluded that a lower pressure rise time (t_r), would result in the highest slamming pressure, and vice versa. (Chan E.S W. M., 1988) created plunging breakers using the focused wave method, involving the superposition of a few dozens of regular waves with varying oscillating frequencies. The experimental tank that was used to conduct the experimental work has a constant depth, to eliminate the coastal effects. He researched the impact breakers using the 3 different regions (2.7.1 Stages of Plunging Breakers) involving different maturity of plunging breakers and their associated impact loading. These 3 different experimental case studies, that use different maturity of plunging breakers would give different impact rise time. Meaning to say, Chan controls the impact rise time via different maturity of plunging breakers. (Chan E.S W. M., 1988), agreeing with (P.A Blackmore., 1984), also associated the critical slamming pressure with lower rise time.

In this research, attempts to tweak the impact rise time, would be done via using different intensities of breaker signals; would be discussed in further details in 4.3 Wave Parameters.

2.7.3 Geometrical cross sections of structure

From the above chapter (2.7.1 Stages of Plunging Breakers), it was concluded that the air entrapment during the onset of breaking does play a significant role in the amplitude of slamming load contribution. Hence there is a hypothesis (from the author) that offshore structures of different geometrical cross sections would have a direct impact on the air entrapment properties. However, at the point of writing, there is no articles researching on slamming load contribution of offshore structures of different geometrical cross sections (besides the author's publications)

2.7.4 Properties of Mediums

(Chan E.S L. Y., 1997) relate the slamming load contribution to the amount of air entrapment between the structure and the collapsing plunging jet. (David E.S, 1999) research on the effects of bubbles formation in both freshwater and seawater. They concluded that seawater will give an increased amount of air bubbles as compared to freshwater, due to higher viscosity properties. And the temperature of the water has a direct relationship with the viscosity properties of the water. They also found that a reduction of temperature of the seawater from 20 degrees to 3 degrees will increase bubbles production by 50%, which would have a direct impact on breaking waves slamming load. The impact of a slamming force has a direct correlation with the amount of entrapped air between the curl of the jet and the impacted surface of the structure. This would be an interesting point to take note while carrying out experimental works on breaking waves impact loads. (A.H. Techet, 2005) uses both distilled water and alcohol-water solution. The alcohol-water solution was mixed using isopropyl. Compared with using distilled water, a breaker produced with 3% alcoholic solution shows having a more defined breaking and more air entrainment. Further experiment tests revealed that solutions with higher alcohol percentage would have a reduced surface tension. The above literature reviews show that the use of different mediums (having different surface tension, specific gravity, etc) would create different surface profiles and possibly different air entrapment capabilities upon initial impact of plunging breakers. Whilst there were researches on creating plunging breakers with different mediums (saltwater, fresh water and distilled water with alcoholic solution), however, there is no known research on the effects of the plunging breaking impact loadings.

2.7.5 Measurement of Breaking wave kinematics

(Xu Delun, 1986) introduced to incorporate Stokes Second Order theory (Equation 12) for calculating the kinematic breaking criteria. (Perlin .M, 1996) also showed that the actual kinematics of the wave is slightly larger than the estimated celerity derived using a linear method. (Baldock T.E, 1996) showed that during the onset of breaking, the kinematics of breaking wave does not behave linearly (as compared to linear wave theory, celerity proportionates to period (T), Equation 7).

The kinematic behaviour of the plunging breaker is an important parameter, as it is widely used to calculate the geometric breaking criterion and as well as predicting the design slamming load.

Several researchers ((Kjeldsen M. , 1979), (She.K, 1997) (Yanfei Deng, 2016)) that uses wave probe for measuring the geometrical breaking criterion had assumed a constant velocity throughout the entire phase of the breaking wave by using Equation 6.

Current classification society rules (Veritas D. N., 2010) stated that while estimating the kinematics of breaking waves for calculating the design slamming load. The kinematics of the breaking wave is assumed to be '120% of the most probable breaking celerity'. The above classification guidelines that give a conservative estimate of the kinematics of breaking waves (relating Design Slamming load to c^2 , Equation 5); Equation 5 shows, over-estimating the kinematics would have an

exponential over-estimation of the design slamming force. The high breaking wave celerity safety factor imposed by classification society rules shows that during the onset of a plunging breaker, the kinematic behaviour of the plunging breaker is erratic.

(Cui Cheng, 2013) did research on the behaviour of the kinematics of non-breaking freak waves; a non-linear phenomenon. He found out that the kinematics of the freak waves tend to deviate even more from the linear theory for waves with a higher steepness (ak) value. (De Wang C, 2018) expanded Cui Cheng's research to focus on the kinematics of breaking waves just before plunging. Various intensities of plunging breaker were created by adjusting the peak frequencies of the focused JONSWAP spectrum (4.4 Wave Parameters), creating different focused wave packages with different wave kinematics and profiles. De Wang C found similar findings to Cui Cheng; he found that the actual wave celerity could be about 7-24% higher than the value obtained from the linear method.

The above literature review provokes the following questions

- a) What would be a good methodology to obtain the breaking wave kinematics?
- b) How does offshore structures with different geometric cross sections contributes to the slamming load force or/and slamming load coefficient?
- c) Could the geometric breaking criteria be better calculated? Not using linear wave theory?
- d) How would different breaking wave intensities affects the kinematics of breaking waves, and ultimately, if the breaking wave intensities play a crucial role in the slamming load coefficient?

3. Design Breaking Wave, Novelty

After going through detailed literature review, and identifying the potential gaps in knowledge pertaining to the kinematics, breaking criteria, slamming load contributions. This chapter would provide a detail insight of the attempt to solve the above questions.

Plunging breaker were created at Newcastle University Wind Wave and Current (WWC) Tank. Plunging breakers of several intensities (detailed technicalities explained in Chapter 4.4); $0.47 \leq f_p \leq 0.52$ were used for the kinematic study.

3.1 Semi-Empirical Kinematics study (De Wang C, 2018)

Kinematics of breaking wave is a complicated parameter to solve. The kinematics of breaking wave is tightly correlated to the induced loadings, kinematic breaking criterion and geometric breaking criterion. Depending on the methodologies to estimate celerity, different celerity values could be established for the same experimental work. (Bonmarin, 1989) noted a possible 3 to 11% underestimation of the breaking wavelength using a constant celerity formula. As discussed briefly earlier (2.3 Kinematic breaking criteria), both (Perlin .M, 1996) & (Stansell. Paul, 2002) used PIV to measure the particle velocity u . Perlin predicted wave celerity by extracting the wavelength via video. With the known wavelength, the wave celerity could be obtained via linear wave theory. (Stansell. Paul, 2002) used 3 different methodologies to derive the values of the phase celerity. First is the linear phase speed approximation (Equation 7). The second method is to employ the Hilbert transform to recalculate the local wavenumber and angular frequency. However, this method, as admitted by (Stansell. Paul, 2002), is controversial and not suitable for irregular waves with a wide spectrum. The third method is to consider the spatial distance travelled within a certain time period. (Equation 19). (Baldock T.E, 1996) uses laser beams to track the wave kinematics, similar method to Stansell's 3rd method, however, Baldock uses laser beams, whereas Stansell uses video processing. (De Wang C, 2018) did experimental work at Newcastle University. Plunging breakers were created using the focused JONSWAP method. Plunging breakers of various intensities were created (to be discussed in details in Chapter 4.2, Equation 36). The value of the horizontal crest particle velocity and wave celerity was measured by wave probes and high-speed cameras respectively. The value of the horizontal crest velocity could be approximated using Figure 10, tracking the maximum value of the wave elevation. However, that runs a huge risk, as the actual ' U ' that we are interested in, is the jet nose as denoted by star in Figure 10. The wave probe reading is unable to track the jet of the plunging wave. Using both wave probe (Eulerian method) and high-speed camera (Lagrangian method) of recording capability of 240fps, horizontal crest particle velocity and wave celerity just before breaking were measured and compared.

$$c_L = \frac{(x_2 - x_1)}{(t_2 - t_1)} \quad (19)$$

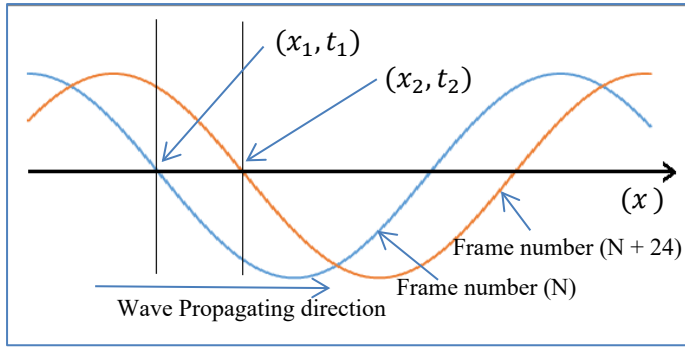


Figure 9 Video Lagrangian method for tracking wave celerity

Where $(x_2 - x_1)$ is the spatial distance travelled between 2 spatial locations (m);

$(t_2 - t_1)$ is the time taken to travel from x_1 to x_2 (s).

The methodology measured the Lagrangian wave celerity by taking a fixed elevation point at a free surface ($z = 0$), and tracking the spatial horizontal distance propagated by the wave and the celerity is calculated (Equation 19). Figure 7 illustrates two-wave profiles that were 24 frames apart. The time difference between the two wave profiles can be calculated as (Equation 20)

$$\Delta t = t_2 - t_1 = \frac{\text{Frame}(N_2) - \text{Frame}(N_1)}{\text{fps of the camera}} \quad (20)$$

In this experimental work, the frame-number difference is fixed at 24 frames, and the camera used, has a recording capability of 240fps. Thus, $\Delta t = 0.1\text{s}$.

The Lagrangian wave crest velocity was measured using the same methodology, with the elevation point of interest being at the crest level. Wave celerity can be measured by the zero down-crossing method via using wave probes, known as the Eulerian Wave celerity (Equation 7). The horizontal crest velocities were estimated by the time needed for the crest to travel to the succeeding wave probes.

$$U_E = \frac{x_{N+1} - x_N}{t_{\text{Crest},N+1} - t_{\text{Crest},N}} \quad (21)$$

Where x_N is the spatial distance of the first wave probe encountered by propagating wave from the wave piston position (m);

x_{N+1} is the spatial distance of the succeeding wave probe from the wave piston position (m);

$t_{\text{Crest},N}$ is the total time taken for the crest to reach probe N (s);

$t_{\text{Crest},N+1}$ is the total time taken for the crest to reach the successive probe (s).

However, the above Eulerian method did not account for the dynamic changes of the kinematics of the breaking wave; before breaking. This Eulerian method assumed constant wave celerity during the entire breaking wave period, which contributed a level of inaccuracy. Each wave packages are repeated 10 times and the mean celerity of the data were used. It is noted that there is a deviation of about 3.2% for the celerity. (It is noted in the latter chapters that, the kinematics of the plunging breaker have higher deviation, as compared to the loadings deviation of only about 0.5%). As shown in below Figure 10, for the Lagrangian method, that involves video imagery processing, the crest is

denoted by the blue and red circles. However, if a user were to use purely fixed wave probe to analyse the crest celerity, the user would be unable to calculate the jet celerity. The wave probe users would usually assume the highest elevation point of to be the incident crest.

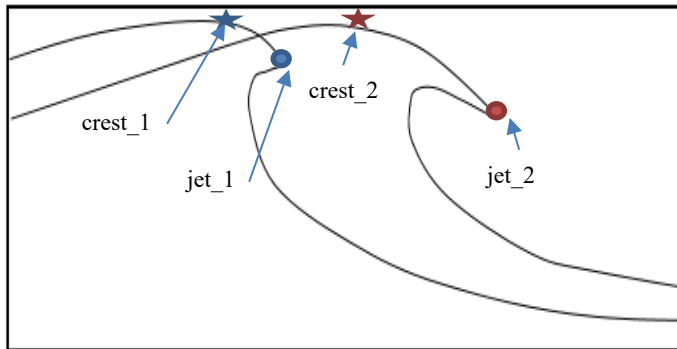


Figure 10 Wave profile of a propagating wave (crest denoted by a star, Jet's nose denoted by a circle)

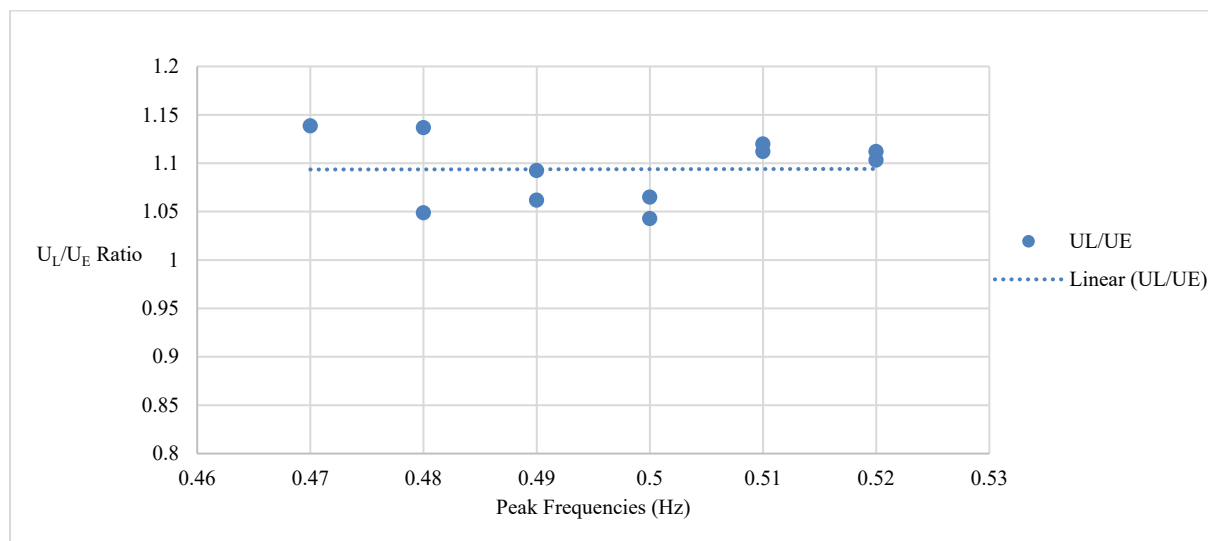


Figure 11 ' U_L/U_E ' values for different breaking intensities

The use of the maximum crest values for wave probes with different spatial, would not necessarily accurately describe the actual horizontal crest velocity, as the jet does not occur at the maximum crest value during collapsing (Figure 10). This is one reason why wave probes are never used for calculating the associated breaking wave kinematics in both experimental and numerical works. Hence, high-speed camera of 240fps was used to determine the wave celerity and the jet velocity, simply using dx/dt . The ' U_L/U_E ' appears to be ranging 1.04 to 1.14, and not affected by the breaking wave intensities (note: higher breaking wave intensities correlating to steepness (αk), unlike the phenomenon observed by (Cui Cheng, 2013). It is also concluded that the use of wave probe is not a suitable methodology (U_E) to determine:

- a) Breaking wave kinematics
- b) Kinematic breaking criterion

It is also interesting to note that for the Peak Frequency, $f_p = 0.48\text{Hz}$, there is a wider range of $1.05\text{m}\cdot\text{s}^{-1}$ to $1.14\text{m}\cdot\text{s}^{-1}$, with a deviation of 3.9%. For the rest of the frequency range, the standard deviations are negligible.

(Cui Cheng, 2013) noted that there would be greater disparities amongst the kinematics obtained via Lagrangian and Eulerian method for non-breaking waves with higher nonlinearity. In the experimental work done by (De Wang C, 2018), he created plunging breakers (Figure 10) of varying breaking intensities by adjusting the peak frequency of the JONSWAP spectrum (would be explained in details in 4.4 Wave Parameters)(Equation 36).



Figure 12 Plunging Jet overtopping

The obtained wave celerity via the Lagrangian method, during the rise of the crest before collapsing as shown below,

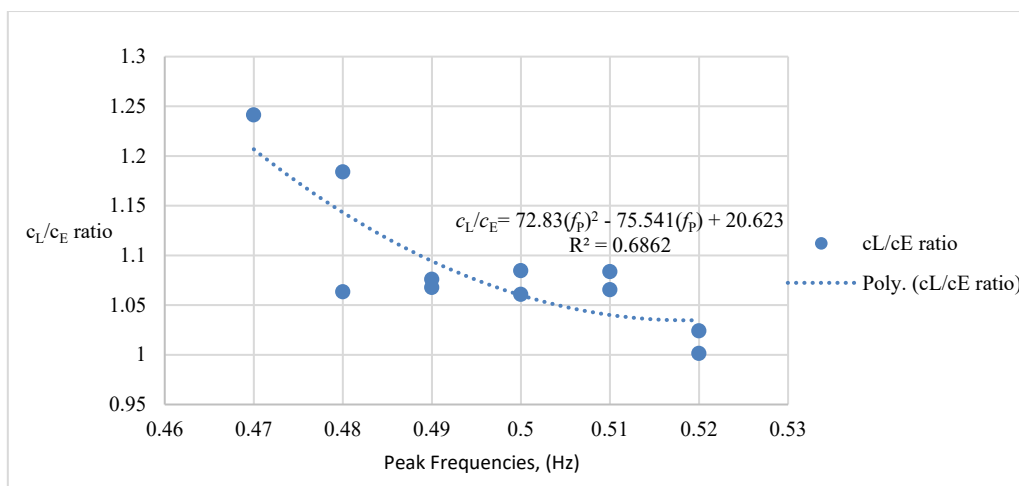


Figure 13 'c_L/c_E' ratios for different peak frequencies (breaking wave intensities)

The 'c_L/c_E' ratios range from a value of 1 to 1.24 (Figure 13). Showing the same phenomenon as (Cui Cheng, 2013) research that the disparities between the c_L and c_E widen more with higher breaking intensities (lower peak frequencies would create higher breaking intensities Equation 36)

The wave celerity based on the 3rd order Stokes theory can be written as (Equation 22)

$$c_3 = \frac{g * T_z}{2\pi} * ((1 + 0.5(ak)^2) + O(ak)^4) \quad (22)$$

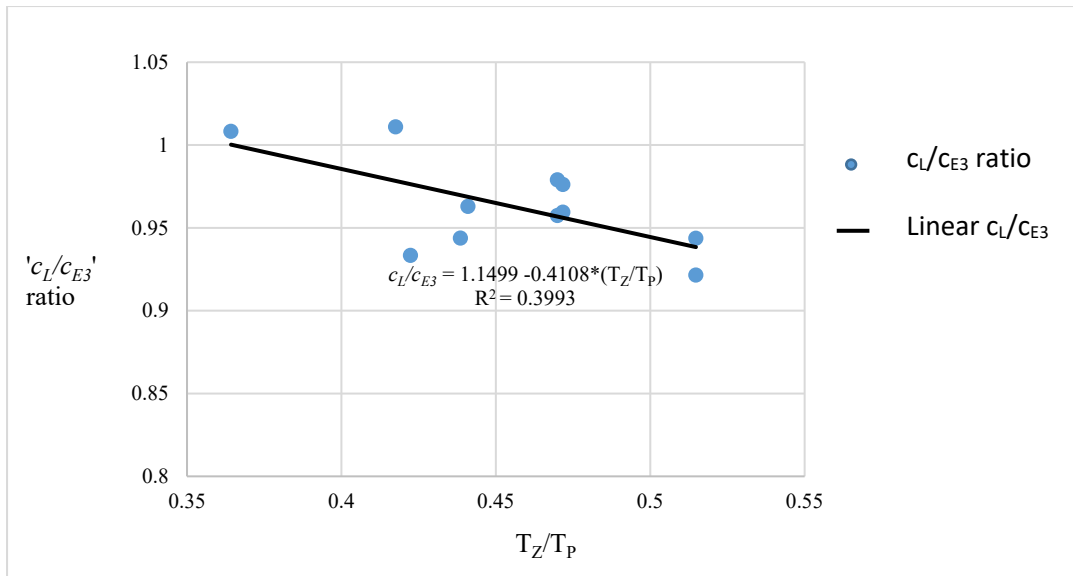


Figure 14 ' c_L/c_3 ' values for different non-dimensional breaking intensities ' T_z/T_p ', using 3rd order Stokes theory

Comparing the ' c_L/c_3 ' ratio against the non-dimensional breaking intensities ' T_z/T_p '; in which a lower ' T_z/T_p ' represents higher breaking intensities, a regression analysis of the parameters is shown as above (Figure 14).

Hence the semi-empirical breaking wave celerity is formulated as below

$$c_L = \frac{g * T_z}{2\pi} * ((1 + 0.5(ak)^2) * (1.1499 - 0.4108 * (\frac{T_z}{T_p}))) \quad (23)$$

The above equation gives a semi-empirical estimation of the Lagrangian wave celerity just by inputting variables obtainable by the wave probes (T_z , a). As Figure 13 suggested, the value of ' c_L ' tends to be 7 – 24% greater than the Eulerian wave celerity. However, while comparing against Stokes 3rd order wave celerity and taking the Lagrangian wave celerity as a comparative datum, it seems that for lower breaking wave intensity (higher T_z/T_p ratio), Eulerian 3rd order Stokes celerity (Equation 22) seems to be overestimating the celerity. For higher breaking wave intensity, 3rd order Stokes celerity seems to be a closer approximation of the Lagrangian wave celerity.

(De Wang C, 2018) concluded that, whilst it is convenient to use the Eulerian method to measure wave celerity. However, for highly nonlinear waves like the plunging breakers, this method proved to be questionable. Breaking waves with varying breaking intensities were generated, and a semi-empirical relation of the breaking wave celerity was established as above. There is a negative correlation amongst ' c_L ' and ' T_z/T_p ' ratio, meaning that the predicted breaking wave celerity increases with increasing wave breaking intensities. Equation 23 would not hold for non-breaking waves or waves with higher ' T_z/T_p ' ratios; as only breaking waves of differing intensities were used in this research. For weakly nonlinear waves, the traditional and convenient Eulerian method could still use used (due to negligible deviations between the methods). There might be occasion during the design stage, whereby there is a lack of luxury of 'time consuming and resource intensive', video processing method to obtain the Lagrangian celerity. Hence it was suggested, with using few fixed wave probes, and with the semi-empirical solution as obtained in above (Equation 23), we could obtain a better curve fitting approximation for estimating the 'most probable breaking wave kinematics' as compared to purely Eulerian method.

In this experimental work, wave celerity at two locations are being investigated: $x = 7.75\text{m}$ and $x = 8\text{m}$. As explained above, the generated wave starts exhibiting signs of breaking at about $x = 7.75\text{m}$. Therefore, the wave celerity before jet formation is obtained at $x = 7.75\text{m}$, and the one during jet formation is obtained at $x = 8\text{m}$.

3.2 Experimental Research on Kinematics of Breaking Waves

A total of 3 methods have been used to estimate wave celerity from laboratory-test results to obtain the celerity from both spatial locations of interest.

The earlier method discussed is the use of the zero down-crossing period T_z , to estimate the 3rd Order Stokes Celerity (Equation 22). 2nd method which is a Lagrangian method is the use of 2 wave probes to track the celerity via Equation 19; the use of multiple wave probes pre-determine the space domain, and the differential in time for the pre-defined elevation point of interest between the two probes forms the solution to Equation 19. A problem one may encounter when applying this method is that the free surface may rise up before wave breaking ((Longuet-Higgins, Accelerations in Steep Gravity Waves, 1985)). The values obtained via a fixed wave probe are known to be the apparent celerity (Eulerian method). This method of obtaining the Lagrangian wave celerity via wave probes would be known as c_{LP} .



Figure 15 Calculation of the rise-up of a breaking wave via a tracker

Figure 15 shows a wave profile before breaking obtained from the experiment. The blue horizontal line indicates the initial undisturbed free-surface level, and it can be seen that the trough before the wave jet is above the initial water level at this instant due to the rise-up effect. The rise-up effect will directly influence the identification of the zero-cross point and therefore the estimated wave celerity. With the assistance of video images, the rise-up effect can be corrected by shifting the initial water level accordingly. In the above Figure 15, the black horizontal line right above the blue horizontal line is the corrected for the rise-up effect. The distance of the corrected distance could be easily derived from the 'Tracker' software; taking reference to spatial points within the video. With the known corrected surface elevation, the Lagrangian wave celerity would be derived from the wave probes (Equation 19). This method of estimating the wave celerity using wave probes via the Lagrangian method with corrected free surface elevation is hereby known as $c_{LP'}$.

The third method is similar with the second method, however, instead of using two fixed wave probes, it uses a video for post-processing; had been discussed in detail in 3.1 Semi-Empirical Kinematics study (Equation 19 & Equation 20, Figure 9). The Lagrangian wave celerity derived from the third method would hereby be known as c_{LV} . Celerity obtained at $x = 7.75\text{m}$ is denoted by additional subscript 'before'; implying before jet formation. Celerity obtained at $x = 8\text{m}$ is denoted by additional subscript 'jet'; implying a jet formation.

Table 3 Wave Celerity

f_p	T_p	$C_{E,before}$	$C_{E,jet}$	$C_{3,before}$	$C_{3,jet}$	$C_{L,p}$	$C_{L,p'}$	$C_{L,v,before}$	$C_{L,v,jet}$
0.47	2.127	1.483	1.202	1.739	1.505	2.940	1.724	2.030	2.100
0.47	2.127	1.514	1.272	1.775	1.593	4.160	1.786	1.820	2.000
0.47	2.127	1.499	1.233	1.757	1.543	6.250	1.724	1.875	2.143
0.48	2.083	1.545	1.374	1.763	1.569	2.273	1.690	1.929	2.000
0.48	2.083	1.553	1.358	1.779	1.594	2.174	n.a	n.a	n.a
0.48	2.083	1.584	1.280	1.814	1.466	2.630	1.754	1.875	2.143
0.48	2.083	1.538	1.358	1.762	1.556	2.630	1.773	1.875	2.000
0.49	2.040	1.608	1.397	1.801	1.577	2.083	1.612	2.000	2.067
0.49	2.040	1.577	1.335	1.766	1.495	2.000	1.563	1.820	2.069
0.49	2.040	1.600	1.342	1.792	1.503	2.174	1.572	1.875	2.000
0.5	2.000	1.686	1.467	1.850	1.619	1.786	1.740	2.020	2.000
0.5	2.000	1.701	1.459	1.861	1.609	1.786	1.605	2.099	2.050
0.5	2.000	1.639	1.350	1.793	1.474	1.852	1.533	1.935	1.940
0.51	1.960	1.717	1.444	1.869	1.603	1.667	1.623	2.080	1.960
0.51	1.960	1.709	1.451	1.863	1.611	1.724	1.633	1.960	2.060
0.52	1.923	1.732	1.545	1.876	1.678	1.667	1.623	1.915	2.100
0.52	1.923	1.741	1.538	1.866	1.669	1.667	1.667	1.835	2.000

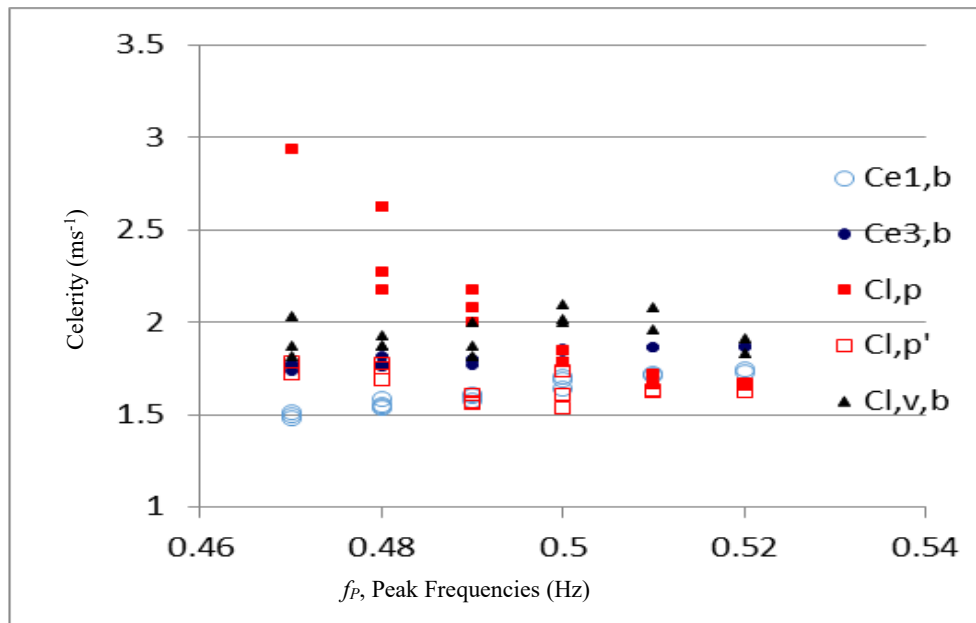


Figure 16 Comparison of pre-jet celerity obtained via the 3 methodologies

Figure 16 shows the values of celerity obtained via different methodology with varying breaking wave peak frequency values. It is assumed that the Lagrangian value measured by the video imagery processing should give the most accurate of all results; as this method captures the real time spatial shifts. It shows that the Lagrangian value measured by the wave probe ($C_{L,p}$) was found to show inconsistent results as wave breaking intensified. The value of $C_{L,p}$ had the widest range from 1.667ms^{-1} to 6.25ms^{-1} . This is due to there being a higher elevation rise with higher associated wave-breaking intensities. To reduce the rise-up effect, the elevation of the celerity calculation will take

account of the rise. It is also evident from above Figure 16 that a higher intensity breaking wave is associated with having higher celerity disparity amongst the different methodology.

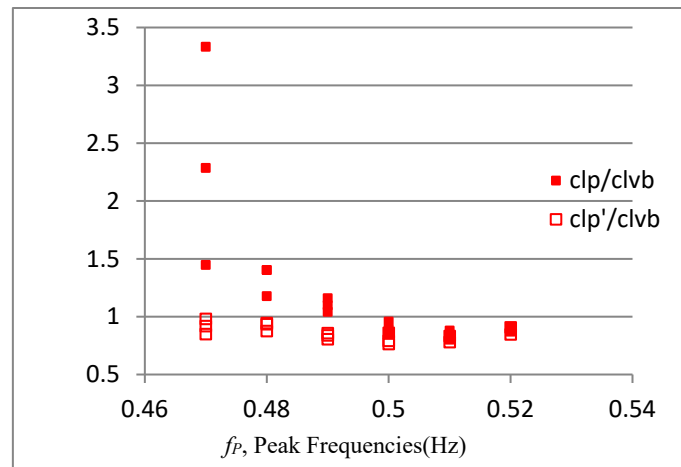


Figure 17 Comparison of $c_{L,p}$ and $c_{L,p}'$ against $c_{L,v,b}$

Figure 17 is a comparison of both $C_{L,p}$ and $C_{L,p}'$ against $C_{L,v}$, with the main motive of comparing the accuracy of the modified $C_{L,p}'$. It is evident that the improved $C_{L,p}'$ showed better agreement with $C_{L,v}$ as compared with $C_{L,p}$. Otherwise, the zero down-crossing period would be underestimated due to the rise-up effects, resulting in an overly inflated celerity value for breaking waves with higher intensities ($f_p \leq 0.48$ Hz); higher breaking wave intensity been associated with higher rise-up effects due to their higher non-linearity nature, further reiterating the need of this correction.

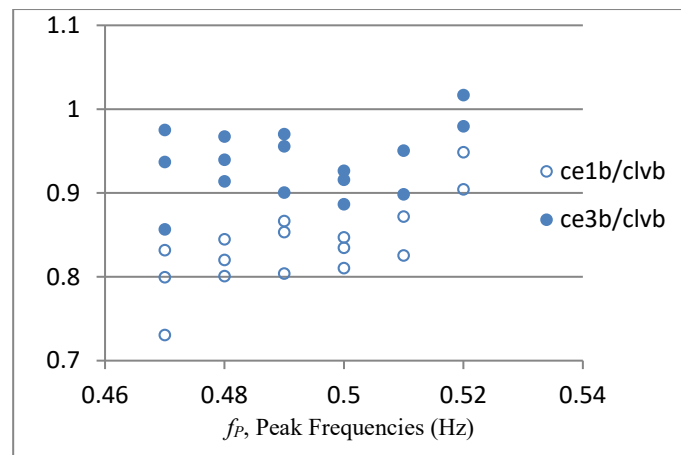


Figure 18 Comparison of celerity, adjusted for the rise of elevation against 3rd-order linear celerity in the pre-jet case

From Figure 18, C_{E3} could be observed to be more effective at estimating wave celerity than C_{E1} , probably because it accounts for the higher-order effects of the breaking wave (which is a highly nonlinear phenomenon). Equation 23 shows that the wave celerity for higher breaking wave intensity would gradually be closer to C_{E3} . This also shows that C_{E3} tends to overestimate the breaking-wave celerity for lower breaking intensities (Higher $\frac{T_Z}{T_P}$).

Comparing Figure 17 & Figure 18, both $C_{L,p}'$ and $C_{L,v}$ showed agreement amongst different wave breaking intensities. Both $C_{L,p}'/C_{L,v}$ and $C_{E3}/C_{L,v}$ had a stable ratio ranging from 0.8 to 1. However, the $C_{L,p}'/C_{L,v}$ showed lower variance as compared with $C_{E3}/C_{L,v}$, implying a more homogenous set of data.

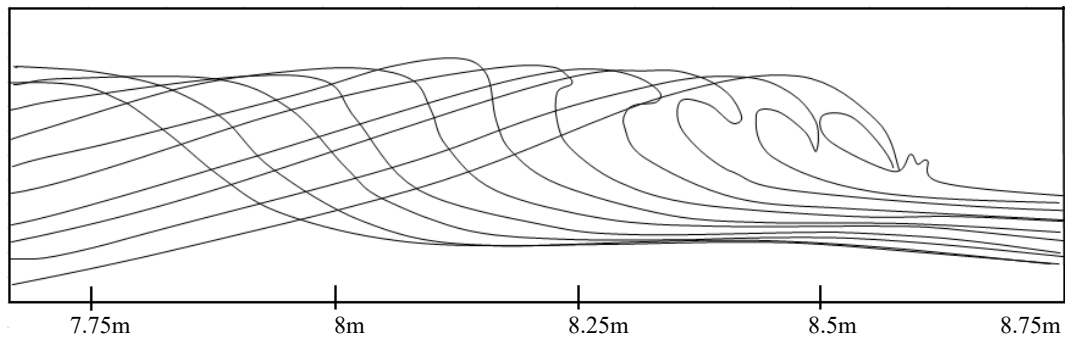


Figure 19 Wave profile showcasing the formation of the plunging jet, $f_p = 0.5\text{Hz}$

Figure 19 shows an example of a breaking-wave profile obtained in this study; extracted via video imagery processing programme “Tracker”. It can be seen that the vertical wavefront starts to form at $x = 8\text{ m}$, and therefore nonlinear wave geometry was recorded at this location. For celerities readings taking via wave probes at the breaking zone, will incur higher error margin due to the breaking phenomenon.

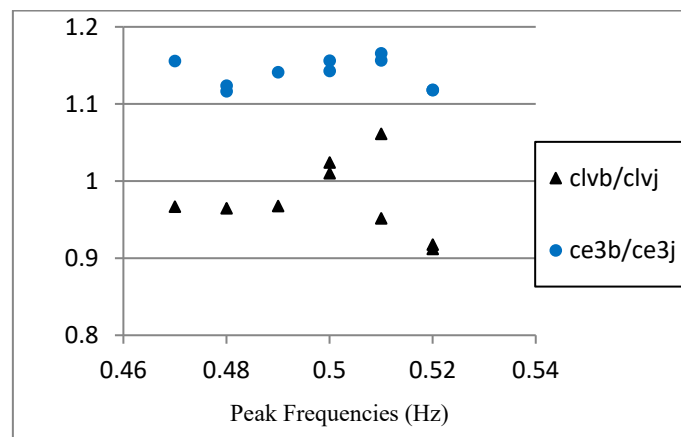


Figure 20 Comparison of wave celerity before and after jet formation

According to Figure 18, and using the celerity values extracted via video method as a comparative datum. Comparing celerities before and during jet formation, there is some agreement between $c_{l,v,b}$ and $c_{l,v,j}$. This shows that there are not much disparities of the actual celerities before jet formation and during breaking. However, there were greater disparities between $c_{E3,b}$ and $c_{E3,j}$; obtained via wave probes. This shows that the use of probes for the estimation of wave celerity may not be suitable for calculating wave geometry/kinematics; especially for a breaking wave.

3.3 Review Kinematic Breaking Criteria

As discussed earlier (2.3 Kinematic breaking criteria), the most commonly used kinematic breaking criterion is the $\frac{U}{c}$ ratio. A breaking kinematic ratio of more than 1, would implies the crest velocity exceeding the wave celerity, allowing a protruding jet to be formed and eventually breaking with the aid of gravity. (De Wang C, 2018) has explored the dynamic nature of wave leading to breaking. It was found that leading up to wave breaking, the wave celerity decreases and allowing the horizontal crest velocity to exceed, forming a jet which finally leads to breaking.

The values of the horizontal wave-particle velocity (u) were investigated using both the Lagrangian and Eulerian method, as in earlier discussions (Equation 21).

The u , which is measured by the Lagrangian method from video processing, is 4% to 14% greater than the method measured via two-wave probes (Figure 9). The U_L/U_E ratio tends to be hovering about 110% and is independent of the breaking intensities.

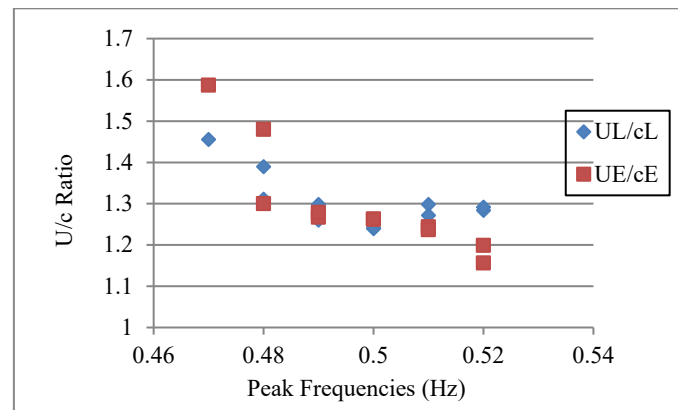


Figure 21 U/c ratios for different wave-breaking intensities

Figure 21 shows that the kinematic breaking ratio (U_E/c_E) appears to be lower than its Lagrangian counterparts (U_L/c_L) for wave signals with higher peak frequencies (or lower breaking wave intensities), and higher kinematic ratio for higher breaking wave intensities. This is mainly due to the findings as mentioned by earlier findings that the U_L and U_E ratio was independent of the breaking wave intensities; however, the c_L and c_E ratio was dependent on the breaking wave intensities, recording higher c_L values for the higher breaking wave intensities. Coupling both phenomena of higher c_L/c_E ratios during higher breaking intensities and constant U_L/U_E ratios regardless of the breaking intensities, a higher (U_L/c_L) was recorded for the higher breaking wave intensities and vice versa.

It is noted that the use of both methods; Lagrangian and Eulerian, both yielded kinematic ratios above the upper limit of 1. A kinematic ratio of > 1 would have indicated that the velocity of the horizontal wave particle exceeding the wave celerity, inducing a jet to form and ultimately collapsing with the aid of gravity.

3.4 Review Geometric Breaking Criteria

In this current experimental work uses crest-front steepness that is derived via various methodologies and revisit past literature regarding geometry breaking criteria. Crest-front length could be obtained via few methods; visual method via video post-processing or expressed as a function of celerity. Expressing it as a function of celerity could be tricky as proven in above sub-chapter (3.1 Semi-Empirical Kinematics study (First Journal Publication)).

Both Geometric Breaking Criteria and Kinematic Breaking Criteria replies heavily on the estimation of Kinematics of Breaking Wave. The Geometric Breaking Criterion that is the most widely used, the crest-front steepness (Equation 24), replies on the estimation of the wave celerity to calculate the crest-front length, in a bid to derive the steepness. On the other hand, the kinematic breaking criterion that is most widely used, the " $\frac{U}{c}$ ratio' also relies dominantly on the wave kinematics.

Past literature survey ((Kjeldsen M. , 1979), (Kjeldsen S. , 1984) (Bonmarin, 1989), (She.K, 1997)) that uses Equation 7 assumes constant wave celerity throughout the entire wave celerity, would have underestimated the crest-front length and overestimated the geometry breaking criteria by a significant margin depending on the breaking intensities.

This would cast doubt on the crest-front steepness limiting value for a breaking wave. In this research, attempts were made using different methodologies to estimate the crest-front length; which will affect the crest-front steepness estimation (Equation 6). In this experimental work, the plunging wave was undergoing breaking as early as $x=7.75\text{m}$ and eventually collapsing at $x=9\text{m}$. Even though the designated spatial focal point was at $x=9\text{m}$, however, due to the non-linearities phenomenon of the breaking wave mechanics, it is not uncommon for the breaking wave to start undergoing breaking earlier than stipulated ((Rapp, 1990)).

In this research, values of crest-front steepness were obtained via various methodologies and are presented and discussed below.

ε_1 , ε_2 and ε_3 were obtained as a function of wave celerity (Equation 6, Equation 7, 2.2.1 Crest-front Steepness). ε_4 is estimated by extracting the crest-front length via the video image processing tool.

Earlier discussions have shown that 3rd-order Stokes theory yields better estimates (3.2 Review Kinematic Breaking Criteria) for highly nonlinear phenomena such as breaking waves. Hence, recalling Equation 22, Equation 24 replaces the wave celerity with 3rd-order Stokes theory.

$$\varepsilon_1 = \frac{\eta}{L'} = \frac{\eta}{\frac{g}{2\pi} * T_z * ((1 + 0.5(ak)^2) + O(ak)^4) * T'} \quad (24)$$

ε_2 uses the Lagrangian celerity obtained via video processing. (Equation 19 & Figure 7).

$$\varepsilon_2 = \frac{\eta}{c_{L,v} * T'} \quad (25)$$

ε_3 uses the Lagrangian celerity, obtained via the modified wave probe method (As discussed earlier in Chapter 3.2).

$$\varepsilon_3 = \frac{\eta}{c_{L,p} * T'} \quad (26)$$

ε_4 simply uses Equation 6, derives the crest-front length from picture images; obtained via a video processing software known as "Tracker". However, the crest elevation (η) were obtained via wave probes, this goes the same for previous equations (Equation 24, Equation 25 & Equation 26).

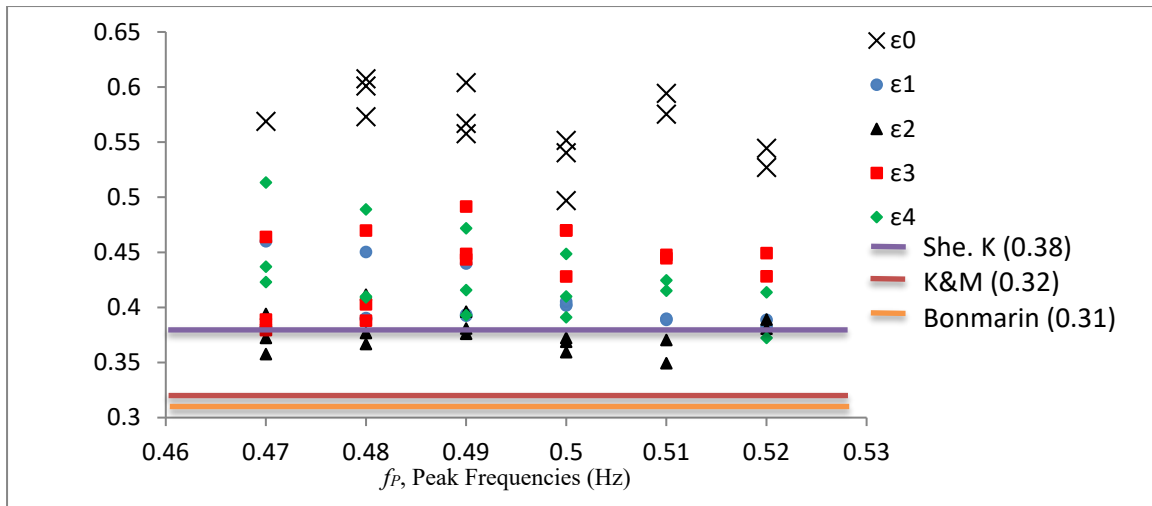


Figure 22 Comparison of different crest-front steepness for plunging breakers with past researchers (Bonmarin, 1989) (Kjeldsen M. , 1979) (She.K, 1997))

Taking the ‘traditional’ method of determining crest-front steepness as ϵ_0 (Equation 6), this method uses Stokes 1st-order wave theory to calculate the crest-front steepness. The 2D focused spectrum-breaking waves were generated and compared with the results of past studies, (She.K, 1997) (Kjeldsen M. , 1979) (Bonmarin, 1989) (Figure 22). The 5 crest-front steepness (ϵ_0 , ϵ_1 , ϵ_2 , ϵ_3 and ϵ_4) were used to compare with previous researchers.

Table 4 Crest-front steepness comparison table

Researcher	Methodology	ϵ	waves
(S.P. Kjeldsen 1984)	video	0.32	Plunging; constant steepness
(Bonmarin, 1989)	wave probe	0.31	Plunging;
(Bonmarin, 1989)	wave probe	0.24	Spilling;
(She. K et al., 1994)	wave probe	0.38	Plunging; angular spreading
(Chan. E.S. et al., 1998)	Photo	0.304	Plunging; constant spectrum
Present	Video & wave probes	0.22	Spilling; constant spectrum
Present	Video & wave probes	0.32	Plunging; constant spectrum

Referring to Table 4 & Figure 22, researchers have been using two main methods to derive the crest-front steepness; One is using a video to obtain the crest-front length and crest elevation (similar to ϵ_4); the other is the ‘traditional method’ derived via the use of wave probes (similar to ϵ_0). The above data ‘Present’, indicates the values indicating the lower limit of the crest-front steepness for spilling/plunging breaker to occur in this research work.

A past literature survey (Bonmarin, 1989) has shown that the wave celerity calculated using the traditional linear method via a wave probe tends to be a conservative estimate (as discussed in 3.1 Semi-Empirical Kinematics study (First Journal Publication)). Such an estimate would in return yield a short crest-front length, resulting in an inflated crest-front steepness value. ϵ_0 could be seen hovering at a range of 0.49 to 0.61 for a range of wave breaking intensities as compared to 0.35 to 0.51.

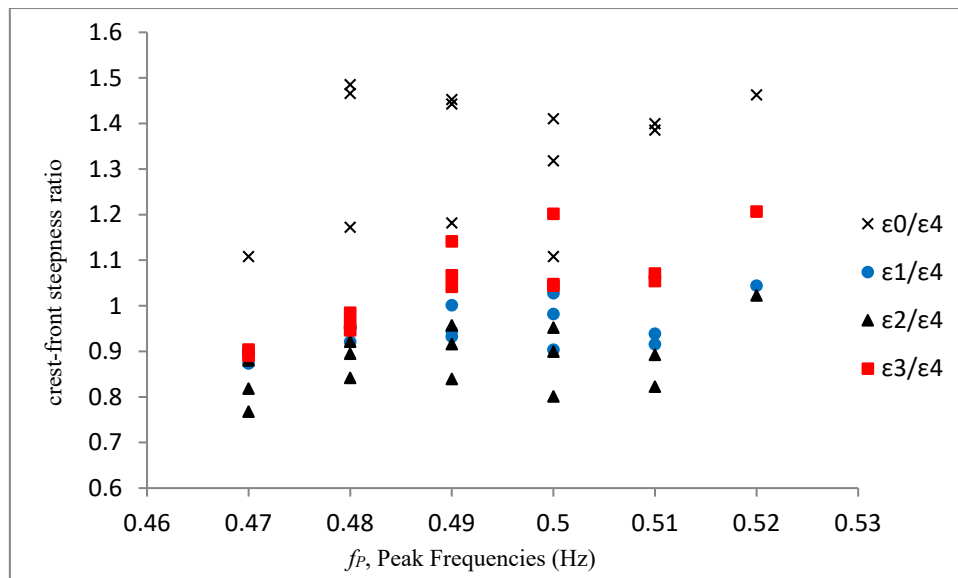


Figure 23 Comparison of different crest-front steepness ratios

Figure 21, ϵ_4 was used as a datum for comparison. ϵ_4 which was obtained via video post-processing was assumed to be the most accurate method of all.

As discussed in Chapter 3.2 “It is assumed that the Lagrangian value measured by the video imagery processing should give the most accurate of all results; as this method captures the real time spatial shifts”.

After which, the primary purpose of Figure 28 would be to compare and discuss the results of different methodologies. Agreeing with previous Figure 20, the ϵ_0/ϵ_4 gave the most overly conservative estimation of the geometric breaking criterion. It gives a range ϵ_0/ϵ_4 ratio of 1.1 to 1.5, the highest ratio amongst the 5 methodologies. ϵ_1 is based on the 3rd-order Stokes theory and can be observed to have a steepness coefficient ratio (ϵ_1/ϵ_4) ranging from 0.9 to 1.04.

ϵ_2 tracks for a time interval of 0.1 s (24 frames) during breaking, and yields the largest deviation as compared to ϵ_4 . ϵ_1 was observed to closely agree with ϵ_2 . Both ϵ_1 and ϵ_2 tend to have higher disparities for the stronger plunging case. This goes to show that breaking is a very dynamic phenomenon during which the breaking wave kinematics undergoes great changes.

ϵ_3 uses the adjusted $C_{L,p}$ value, which takes account of the rise height, thereby minimising the effects of the rise-up phenomenon and providing the best agreement with ϵ_4 .

This section compares the different methods for estimating the geometric breaking criterion and has the following concluding remarks

- Commonly used Eulerian method tends to underestimate wave celerity, leading to overestimation of the geometric wave-breaking criteria
- 3rd-order Stokes theory is an improved and convenient method to predict both the wave kinematics and crest-front steepness of a breaking wave.
- ϵ_3 provides one of the best agreement with ϵ_4 . However, the rise-up effect, still need to be captured by video processing.

3.5 Review Slamming Load Coefficient Calculation

There are few hypothesises that would be of novelty and contribution to the knowledge pool of breaking wave design.

- 1) As mentioned in earlier (3.1 Semi-Empirical Kinematics study), the later chapters experimental work would extract the kinematics profile as a function of elevation from impacted cylinders elevation to review the slamming load coefficient, instead of using DNV breaking wave kinematics guidelines.
- 2) The maximum slamming load coefficient calculation could relate it as a function of breaking wave intensities, and/or associated crest rise time
- 3) The use of cylindrical structures with different cross section area, riding on the lack of the availability of relevant literature findings regarding such topic, allowing the current design slamming load coefficient to deem fit for all cylindrical shape.

4. Experiment Set up

The aim of this chapter and experimental set up is to investigate the hypothesis that were described in end of Chapter 3.5. To investigate the hypothesis laid out as above, different set ups were designed in place.

- 1) Test equipment - Cylinders with different geometrical cross sections, Circular cylinders with different radius. This is specifically to test the effect the different cylinder has on the slamming load coefficient.
- 2) Wave parameters/wave intensities (Describe in details in Chapter 4.3) – Each cylindrical will be subjected to different wave packages, with the intention of testing the ‘sensitivity’ of how different cylinders behave while subjected to intensified plunging breakers. Are there any distinctive relationship if a certain test case cylinder would behave much favourability in certain wave conditions?

4.1 Creating Breaking Waves in Newcastle University

Breaking waves were generated at Newcastle University, in the Wind, Wave and Current Tank (Figure 28), measuring 11m by 1.8m by 2m, length, width and height respectively, via the focused spectrum method. This wave tank uses a piston-type wave maker. A constant depth was used to eliminate the effects of shoaling. The sidewalls of the WWC Tank are fitted with glass panels, allowing a clear profile view of the propagating wave. Furthermore, nearing the opposite end of the wave tank, there would be a feature to dissipate the wave as much as possible to minimise the amount of rebounding waves. At Newcastle University, the wave relaxation zone near the end of the wave tank is fitted with semi-porous wave absorption. It is also not uncommon for wave tank to have artificial raising seabed towards the end of the wave tank, to encourage propagating wave to break via shoaling effects.



Figure 24 Newcastle University Wind Wave and Current Tank

4.2 Equipment and Calibration

Equipment used

- 2 "GoPro Hero 6" cameras with a recording frequency of 240fps. These 2 cameras were placed at the side of the Wind Wave and Current tank, overseeing the profile view of the breaking waves.
- 1 Sony RV100 camera with a recording frequency of 1000fps. This camera is used for the recording of the wave splash up. This splash up phenomenon could be as short as 40ms. Hence having a high-speed camera would be beneficial.
- 2 Acoustic Doppler Velocimeter (ADV) having a recording frequency of 200fps.
- Cylinders with 3 different cross-sections, discussed in details below
- Force transducer with a recording capacity of 250N in each 3 axial directions, with a recording frequency of 200fps.
- 3 wave probes with a recording frequency of 200fps.
- Experiment Post Processing Methodology

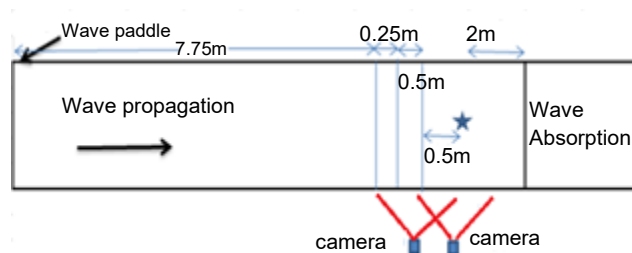


Figure 25 Plan view layout of wave tank, cylinder will be placed at $x = 8.25\text{m}$, square denotes the GoPro 6 cameras, wave probes denoted by the blue transverse lines at $x = 7.75\text{m}$, 8m , and 8.25m

Wave Tank Energy Absorption

A single regular non-breaking wave was generated with wave probes installed at $x = 9\text{m}$. The purpose of this experimental run is to judge if the said location is suitable to be the focal point and if it is vulnerable to rebounding waves.

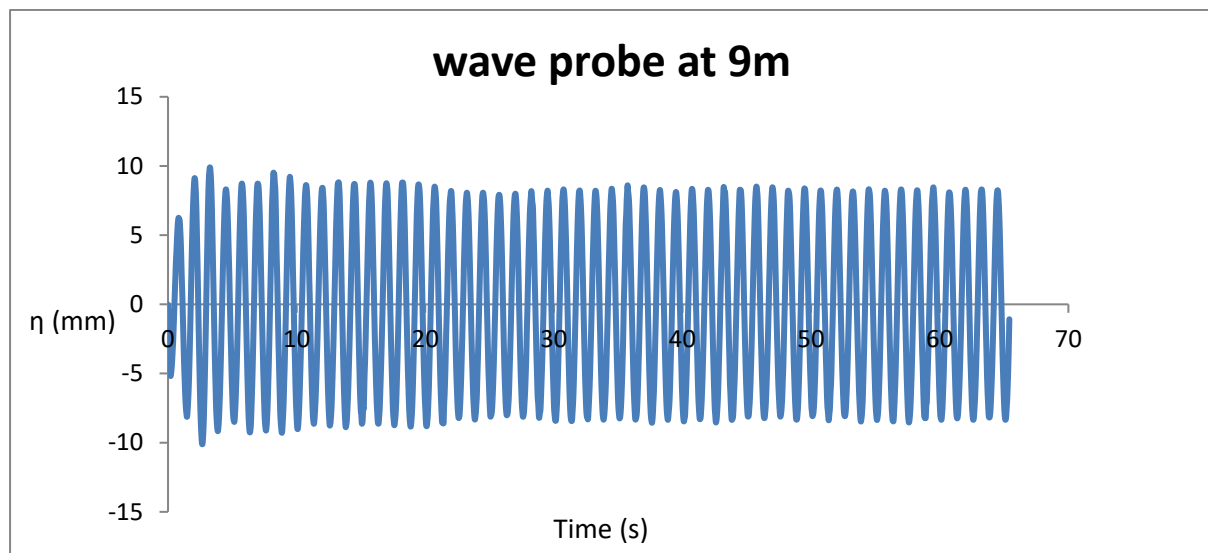


Figure 26 Regular wave elevation recorded at $x = 9\text{m}$

Regular wave with an amplitude of 10mm, having a period of 1.25s were generated, and in the initial 5 wave crest recordings did show no signs of rebounding waves effects. However, later wave crests showed an average amplitude of 8.753mm, showing signs of rebounding wave effects.

$$\eta = H_i * \cos(kx - \omega t + \theta) + H_r * \cos(kx + \omega t + \theta) \quad (27)$$

Taking that $H_i = 10\text{mm}$, $\eta = 8.753\text{mm}$,

$$8.753\text{mm} = 10\text{mm} * \cos(9 * k - \omega t) + H_r * \cos(-2 * k + \omega t - 11k)$$

The reflected wave amplitude is 1.948mm;

$$\Delta E = \rho * g * (H_i^2 - H_r^2) \quad (28)$$

Based on the above findings, the WWC tank's semi-porous wave absorption has an energy absorption rate of 96.2%.

Further attempts to create a focused wave were made using the adjusted peak frequencies, $f_p = 0.65\text{Hz}$. A higher peak frequency is chosen so that a near breaking wave would be generated.

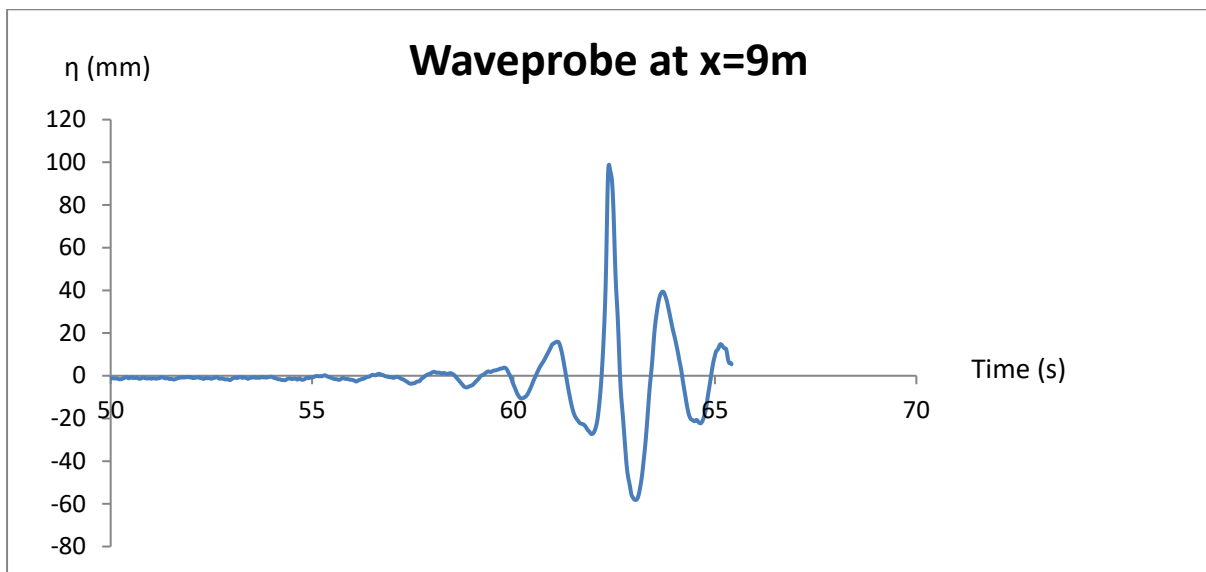


Figure 27 JONSWAP focused spectrum, $f_p = 0.65\text{Hz}$, $x = 9\text{m}$

A focused non-breaking wave was generated at the desired focal point. The threat of rebounding waves are not a concern as the largest incident wave that would affect the focal point has an amplitude of just 3.6mm, $t = 59.74\text{s}$, (The incident wave just before the focused wave, $t = 61.04\text{s}$ wouldn't in time to propagate to the wave absorption and back to impact the actual focal point). Hence the threat of rebounding wave affecting the focused wave would be negligible.

Calibration of Acoustic Doppler Velocimeter (ADV) positioning

There were concerns for the placement of Acoustic Doppler Velocimeters (ADV), causing a potential disturbance to the force transducer measurements.

Assuming a 2-dimensional propagating wave, the y-axis placement of the ADVs could induce a fluid-structure interaction (FSI) and creating diffraction effect and affecting the actual breaking wave impact loading and velocity profile reading.

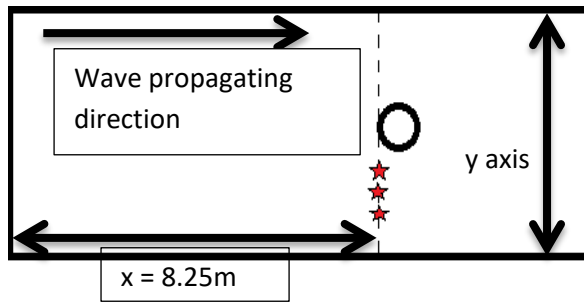


Figure 28 Placement of ADVs as denoted by red stars

The original designated spatial focal point is at $x = 9\text{m}$. However, this value would only hold for linear wave or the most, a weakly non-linear wave. For waves with higher non-linearity, (Longuet-Higgins, *Breaking Waves - in deep or shallow water*, 1974) it is known that the intended focal point is brought earlier. This non-linear phenomenon is due to an increase in phase speed (Yuen, 1982), which occurred during wave-wave interaction such that linear theory assumption would be underestimating the actual phase speed. The wave group starts exhibiting signs of breaking as early as $x = 8\text{m}$, with the onset of jet starts forming and finally collapsing at $x = 9\text{m}$. Hence, taking cue from earlier literature review (Chan E.S W. M., 1988), (2.7.1 Stages of Plunging Breakers), the breaking wave slamming loading would be the most destructive during the stage 2; the transition phase whereby the plunging breaker would be in a more mature form, with its jet being protruding and starts to curl. Hence the cylinder would be placed slightly after the initial signs of breaking, at $x = 8.25\text{m}$, and the ADV would also be placed at the same parallel x -axis, albeit with varying y -axial placements (Figure 28)

The ADV would be placed at $y = -0.5\text{m}$ away from the cylinder, and be allowed to run 10 times. Subsequently, the ADV would be offset to differing y -axial location, $y = -0.2\text{m}$, -0.3m . The mean and variance of the maximum resultant force resulting from the 3 different y -axial placements of the ADVs would be compared with the results of the default case.

The velocity-time history recordings of the ADVs would also be compared amongst the 3 different case studies. This is to gauge if there is much kinematics deviation with respect to further offset placement of the ADV. For the kinematics study, the ADV that was placed furthest from the cylinder; $y = -0.5\text{m}$ in this case, would be the basis of comparative study. The experiment case with ADV was run a total of 20 times using the JONSWAP spectrum, with a peak frequency of 0.5 Hz and a gain factor of 1.2 . The 200mm diameter cylinder was used and yielded an average peak inline force of 68.76N , with a low standard deviation of 0.336N and a variance of 0.112N .

A typical wave force-time history is shown on the Chapter 5.2 Loading results (Figure 66). Tri-axis force transducer were used for the recording of the force-time history, and the average of the peak force were presented in the Figure 35 below. Plunging breaker were generated with the above mentioned calibration test case as denoted by Figure 34. For each calibration test case, 10 runs were generated and with the Peak force for each case being recorded. The resultant average of these 10 runs for each calibration test case were then presented in Figure 35 below.

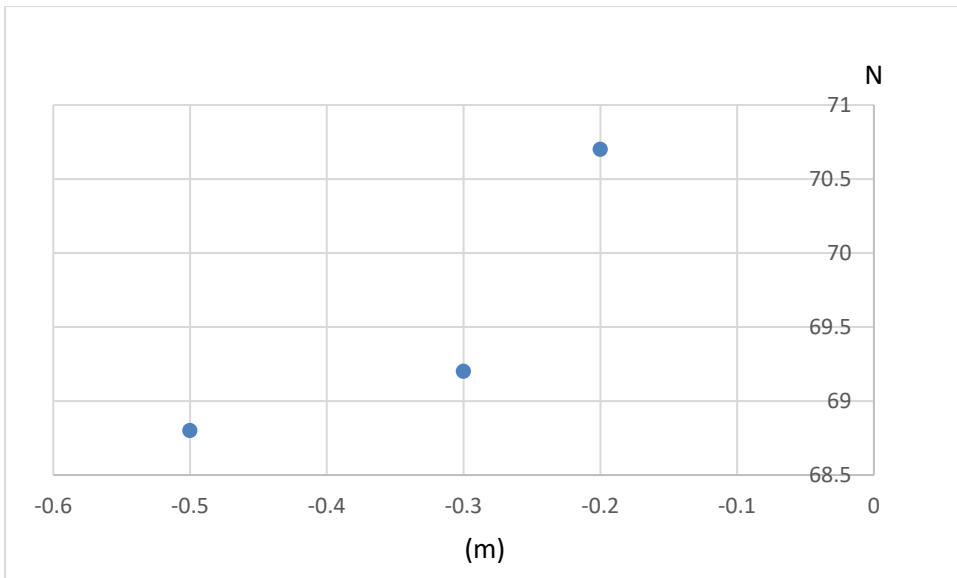


Figure 29 Average Peak Force for different spatial location of ADV as indicated in Figure 34

Figure 29 seems to indicate that the peak force does get affected by the placement of the Acoustic Doppler Velocimeter (ADV). The closer the ADV is placed to the cylinder, the higher the average peak force is. The average peak force when the ADV is the closest to the cylinder; at a 0.2m shift from the transverse axis, was 70.76N, a 3% increase as compared to the reading measured when the ADV was placed 0.5m away from the cylinder. This seems to hint that the introduction of ADV might create some fluid-structure interactions that would have a direct interference with the resultant force.

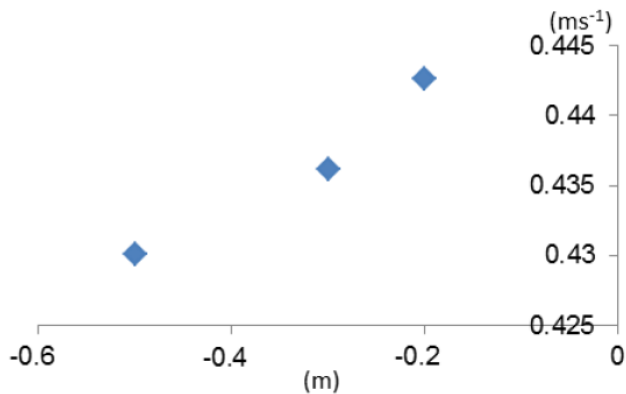


Figure 30 Average Peak velocity for different spatial location of ADV as indicated in Figure 32

Figure 30 shows a similar phenomenon as Figure 29, seeming to agree that the average peak velocity also experienced a marginal increment for ADVs that were placed closer to the cylinder. The average peak velocity at 0.2m away from the cylinder was 0.443m/s, a 3% increase over the achieved kinematics when the ADV was placed 0.5m away.

In this research, 3 different types of cross-sectional cylinders (circular cylinder, square cylinder and diamond cylinder) would be used for this experimental work. Circular cylinders with a diameter of 200mm (Figure 31), 315mm, and 400mm were used for the experiment.

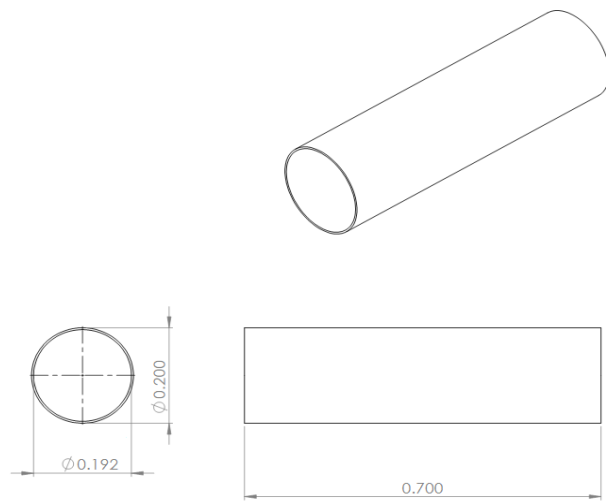


Figure 31 Engineering drawing of 200mm diameter circular cylinder

A square cylinder with an aspect ratio of 0.1 (filleted diameter over plate width) and a width of 200mm was used.

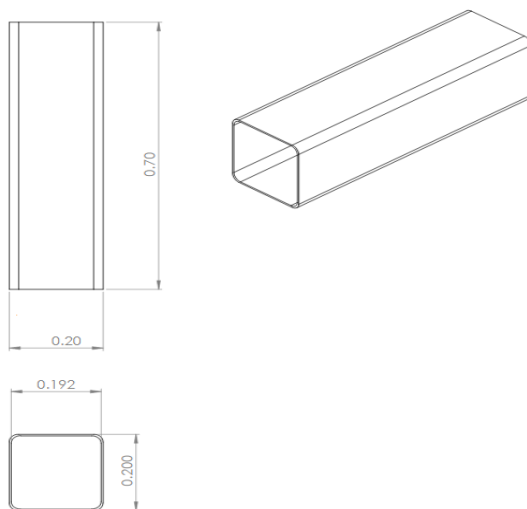


Figure 32 Engineering drawing of square cylinder

Twisting the above structure (Figure 32) by 45 degrees along the vertical axis would portray as a diamond-shaped cylinder, yielding a total of 5-cylinder cases

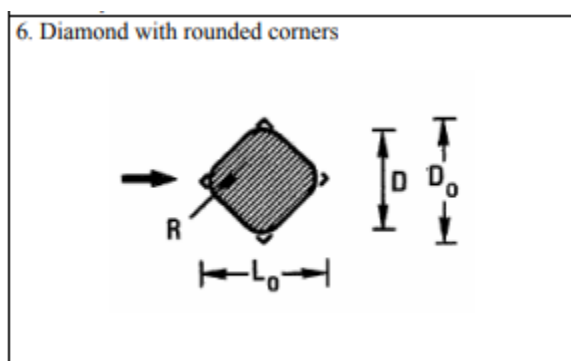


Figure 33 Definition of characteristic diameter for diamond cylinder (Veritas D. N., 2010)

According to Figure 33, for a propagating wave direction as directed above, the characteristic length/diameter would be the perpendicular distance from the wave propagation direction.

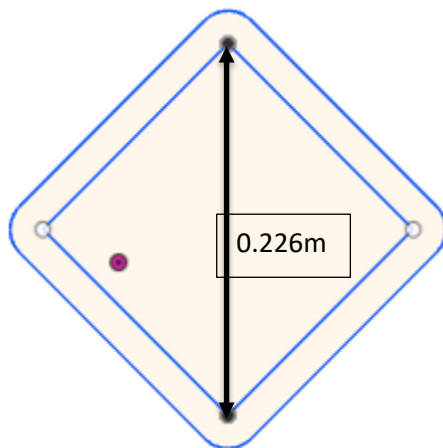


Figure 34 Calculation of characteristic length for the diamond cylinder

Taking into consideration of an aspect ratio of 0.1 (Fillet radius vs Cylinder diameter). Given the diameter of the cylinder is 0.2m, fillet radius of 0.02m. The inner square has a dimension of 0.226m (Figure 34) and adding the fillet radius would give a characteristic length/diameter of 0.266m.

4.3 Wave Parameters

Initial attempts were made to duplicate the exact input of the wave signal derived at NUS (A.1 Experimental work in National University of Singapore), a wave package with 19 regular wave components with an input phase lag ranging from, $\pi < \theta_n < 25\pi$. However, the system recognizes it as 19 separate regular wave components instead of a single wave group. Hence, the system recognizing and adjusting all individual wave components with phase input more than 2π radian, to less than 2π .

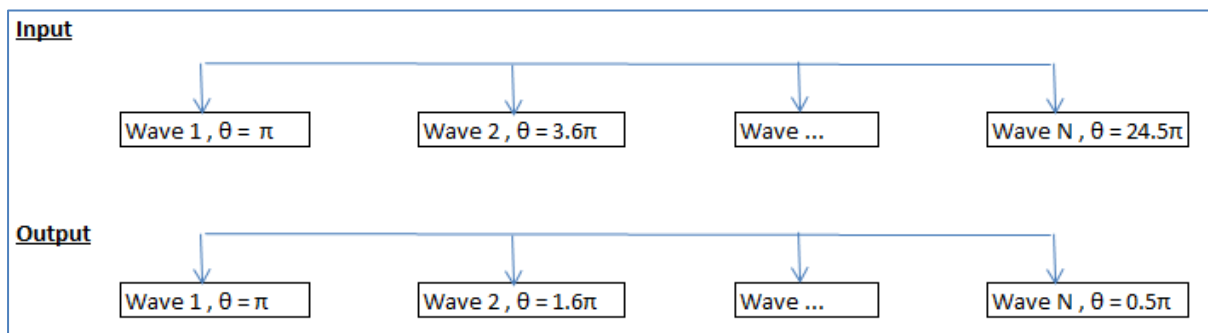


Figure 35 Input and Output Phase differences of arbitrary wave components at Newcastle University Wind Wave and Current Tank

Recognising $\cos(2\pi * m + \theta) = \cos(\theta)$; $m = 1,2,3, \dots$,

The system was unable to induce more than 2π radian phase shift for an individual wave component. A phase shift of more than 2π radian is crucial for enabling the faster wave components to sync with the slower propagating wave components. And for a wide wave frequency range as mentioned earlier, the kinematic spread of the wave components would be huge enough to command a phase shift of as high as $20-30\pi$ radians to aid superposition. Alternatives to create plunging breaker would be left with 2 more options, Shoaling/Coastal effects (via a gradient slope seabed) or via focused spectrum. However breaking waves constructed via shoaling/coastal effects are more relevant to shallow water, and might not be in alignment with the current scope of work.

Hence, JONSWAP spectrum was used for creating focused wave; plunging breakers in this experiment. (Equation 29)

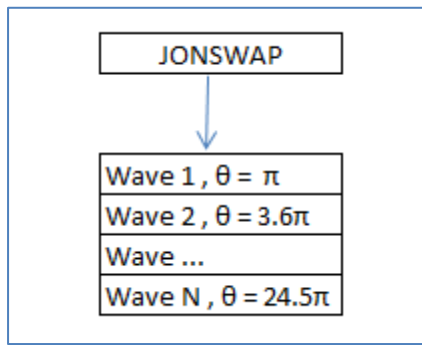


Figure 36 JONSWAP waves input

The system recognises the JONSWAP contributing wave components as a single wave group (Figure 36), eliminating the phase lag problem encountered earlier.

$$S_j(\omega) = \frac{\alpha * g^2}{\omega^5} * \exp \left[-1.25 * \left(\frac{\omega_p}{\omega} \right)^4 \right] * \gamma^r \quad (29)$$

where $\alpha = 0.0081$,

$g = 9.81 \text{ m.s}^{-2}$

$\gamma = 1$

The peak angular frequency (ω_p) was adjusted to create different intensities of breaking wave. A lower ω_p gave a stronger plunging breaker. However, caution should be exercised when adjusting the peak angular frequency, the peak angular frequency (ω_p) should not be lowered such that there are breaking occurring even before the intended focal point.

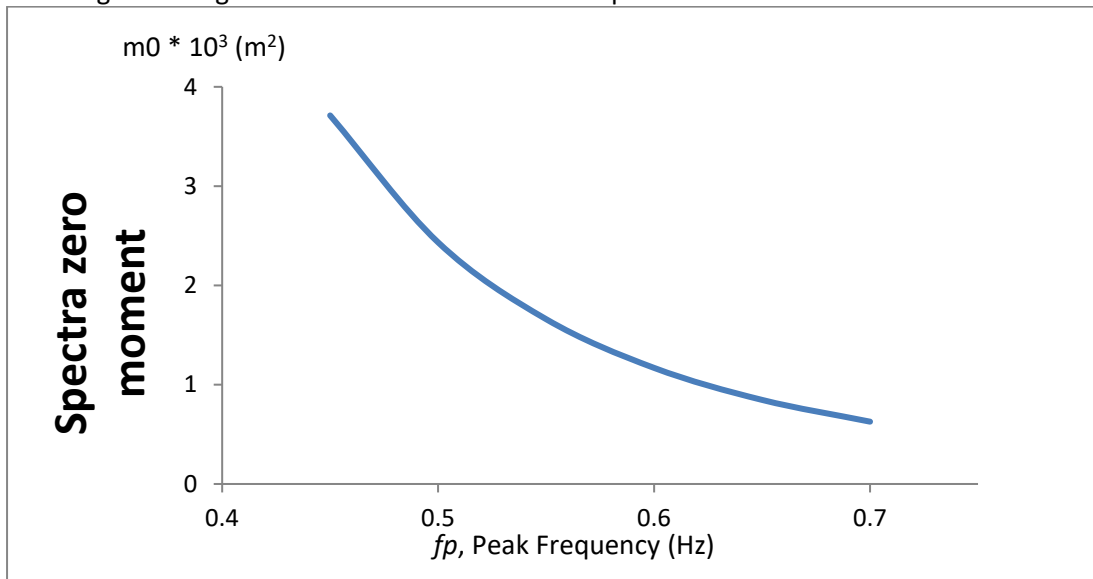


Figure 37 Spectra moment vs Peak Frequencies

Subsequently, the peak frequencies of the wave packages were reduced gradually to create stronger plunging breakers which would be explained in greater details in 4.3 Wave Parameters, (Equation 29), whereby the peak frequencies have a negative correlation with the energy spectrum (Figure 37) & (Equation 37).

$$m_0 = \int_0^{\infty} f^0 * s(f) * df \quad (30)$$

Signs of breaking waves from the focusing JONSWAP spectrum, start showing for $f_p \leq 0.65\text{Hz}$. Spilling breaking waves were observed for $0.53 \leq f_p \leq 0.6$, and plunging breaker were observed for $f_p \leq 0.52$. Plunging breakers of 4 different intensities were generated in this research project, having a range of peak frequencies, $0.47 \leq f_p \leq 0.5$, with the same frequency range of $0.25 \leq f \leq 2$.

$$f = \omega/2\pi \quad (31)$$

The frequency range for generating various regular waves was chosen from $0.25\text{Hz} \leq f \leq 2\text{Hz}$. The step frequency (Δf) is 2^{-6}Hz . The total count of wave components (N), is determined by

$$N = 1 + ((f_{\max} - f_{\min}) * 2^6) \quad (32)$$

There were initial attempts that failed to generate a focus breaker, for the same peak frequencies. Initially, the frequency range was $0.25 \leq f \leq 1.25$, and although the spectrum contribution from $1.25 \leq f \leq 2$ is marginal, but it aids the generation of breaker through instability. Both tail ends of the frequency spectrum, $f \rightarrow f_{\max}$ and $f \rightarrow f_{\min}$, have little contribution to the amplitude of the wave signals, but a wide range of frequency spectrum is associated with modulation instability that would aid the breaking of wave (Chan E.S W. M., 1988). Subsequently, the step oscillating angular frequency ($\Delta\omega$) could be determined via the aid of N that is derived via Equation 32.

$$\zeta_n = \sqrt{2 * S(\omega) * \Delta\omega} \quad (33)$$

The individual wave components contribution could be calculated via Equation 40.

The value of the wave amplitude is bounded by the space (x) and time-domain (t) (Equation 13). The spatial location of breaking (x_B) and the time of breaking and the time of breaking (t_B) had been pre-determined. To generate a breaking wave, the amplitude could be superposition until it reaches critical amplitude and finally breaks due to instability.

Next, to determine the value of (t_B), it must not be at such a low value whereby, there is insufficient time allowed for the slowest wave in the wave package to reach the desired breaking location. Considering the slowest wave components, based on the highest frequency component, the slowest wave component would be 0.78ms^{-1} . Taking into considering the desired breaking location (x_B) = 9m, it would take at least 12 seconds, and excluding phase lag for the highest frequency wave to reach the desired focal point. The wave piston of the wave tank requires starting with relatively low motion. Therefore it would need more time to allow full propagation of the entire wave signal.

$$\cos(k_n x_B - \omega_n t_B + \phi_n) = 1 \quad (34)$$

After determining x_B and t_B , and the individual wave components parameters k_n and ω_n . The phase shift (ϕ_n) of each wave component is programmed in such a way that it satisfies Equation 41, to ensure all the wave components would superposition at the pre-determined spatial location to allow the resultant wave to reach critical amplitude for breaking.

The diameter (D) of the cylinder and the characteristic wavelength (λ) should be $D/\lambda < 0.2$; to fulfill the Morison's Equation boundary condition for the slenderness ratio.

The wavelength of the incoming propagating wave was estimated via wave probe. (Ying Tu, 2017) estimated the wavelength by using the zero-crossing analysis method. It was known that the use of capacitance type wave probes was prone to white noise. And also assuming that the spatial evolution

of the propagating wavelength could be approximated from the temporary evolution, the wavelength could be estimated.

The wave probes reading were first post-processed to eliminate any non-zero mean surface elevation. Next, the elevation readings on the wave probes were smoothed using a 1-second moving average to remove any white noises. The obtained zero-crossing period was then extracted from this data and be used to estimate the wavelength of the breaking wave.

Table 5 Wave Parameters

f_p	T_z	λ	D/λ
0.47	1.096	1.875	0.107
0.48	1.080	1.821	0.109
0.49	1.062	1.760	0.114
0.5	1.025	1.641	0.122

30 readings each were taken for the analytic of the wave parameters. The wavelength is calculated using the averaged of the zero-crossing period analysis. The (D/λ) is computed using a diameter of 0.2m. The above table shows that stronger wave breaking intensities (or lower peak frequency), would create lengthier wavelength before breaking.

For this experiment, cylinder diameters ranging from 200mm to 400mm were used. This would have meant that the research work revolves having (D/λ) ratio of 0.106 to 0.244. Regular waves were constructed and the time history of the wave kinematics was recorded using the ADV with a recording frequency of 200 Hz. The force transducer is mounted at the top of the cylinder and allows the cylinder to be on a fixed-free position. The waves are propagated in a 2D direction. Even though tri-directional wave kinematics and forces were recorded in the experiment, however y-axial kinematics and forces are negligible.

4.4 Test Cases

Non-breaking case 1

JONSWAP focused spectrum. Focal point = 9m, $F_{\min} = 0.25\text{Hz}$, $F_{\max} = 2.0\text{Hz}$, $f_p = 1\text{Hz}$.

A non-breaking wave case would be made and as the peak frequency is higher than the breaking wave case; creating a weaker spectrum and a lower focused height.

Non-breaking case 2

Regular wave. $T = 1\text{s}$, $\zeta = 40\text{mm}$

Non-breaking wave cases with varying kinematics are generated to observe and post process the drag behaviour for varying kinematics.

Test Case 1

JONSWAP focused spectrum, Focal point = 9m, $F_{\min} = 0.25\text{Hz}$, $F_{\max} = 2.0\text{Hz}$, $F_p = 0.5\text{ Hz}$

Test Case 2

JONSWAP focused spectrum, Focal point = 9m, $F_{\min} = 0.25\text{Hz}$, $F_{\max} = 2.0\text{Hz}$, $F_p = 0.49\text{ Hz}$

Test Case 3

JONSWAP focused spectrum, Focal point = 9m, $F_{\min} = 0.25\text{Hz}$, $F_{\max} = 2.0\text{Hz}$, $F_p = 0.48\text{ Hz}$

Test Case 4

JONSWAP focused spectrum, Focal point = 9m, $F_{\min} = 0.25\text{Hz}$, $F_{\max} = 2.0\text{Hz}$, $F_p = 0.47\text{ Hz}$

Test Case 5

JONSWAP focused spectrum, Focal point = 8.8m, $F_{\min} = 0.25\text{Hz}$, $F_{\max} = 2.0\text{Hz}$, $F_p = 0.5\text{ Hz}$

This test case, the plunging wave focal point is deliberately brought forward, so that, during the impact of the initial contact with the cylindrical structure, $x = x_B + 0.2\text{m}$, it would be of a mature plunging jet with a fully formed collapsing jet.

Test Case 6

JONSWAP focused spectrum, Focal point = 9.2m, $F_{\min} = 0.25\text{Hz}$, $F_{\max} = 2.0\text{Hz}$, $F_p = 0.5\text{ Hz}$

Test case 6 is just the opposite with its predecessor. With the aim of creating an immature plunging jet upon initial contact with the cylindrical structure at $x = x_B - 0.2\text{m}$.

Test case 1, 2, 3 & 4 would be compared to analyse for the contributing effects of using plunging wave breakers with varying breaking intensities.

Test case 1, 5 & 6 would be compared to analyse the effects of the different maturity of plunging breakers.

4.5 Post Processing

$$\frac{\partial u}{\partial t} = \zeta_a * g * k * \frac{\cosh k(z+h)}{\sinh(k*h)} * \sin(kx - \omega t) \quad (35)$$

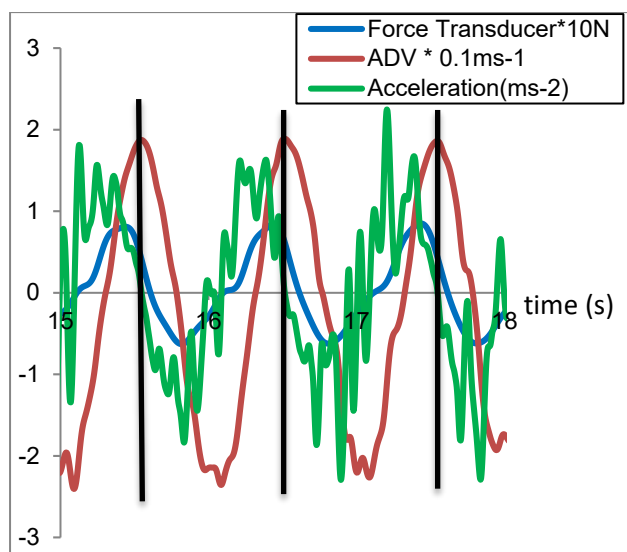


Figure 38 Wave kinematics and time force history at $z = -80\text{mm}$, $f_p = 0.5\text{ Hz}$

Figure 38 shows the reading of the wave horizontal particle velocity time history recorded by the ADV, which will be placed at different elevations, to capture the wave kinematics behaviour with the

function of elevation. Each surface elevation ($\Delta z = 30\text{mm}$) wave kinematics for both non-breaking and breaking cases would be captured 10 times each. The acceleration time history was extracted using Equation 35; differentiating the obtained velocity-time history as recorded by the ADV. It is noted that the derived acceleration-time history was not a smooth curve, this is due to the ADV functioning at 200fps, equates to a very short time step, $\Delta t = 0.005\text{second}$. Differentiating the changing kinematics over a very short time step would give a much 'sensitive' data of the derived acceleration-time history, as shown in the above Figure 38, indicated by the green line.

As shown in the above Figure 38, a vertical black line was constructed at each time step when the acceleration is 0. On above Figure 38, the vertical line that passes through the force-time history, shown to be dominated by wave horizontal velocity due to 0 acceleration. This is due to the relationship between the wave horizontal velocity and wave horizontal acceleration, that the wave horizontal acceleration is a derivative of the wave horizontal velocity resulting in different sine and cosine terms. With the known drag force and kinematics of the regular wave, the drag coefficient of the cylinder could be derived.

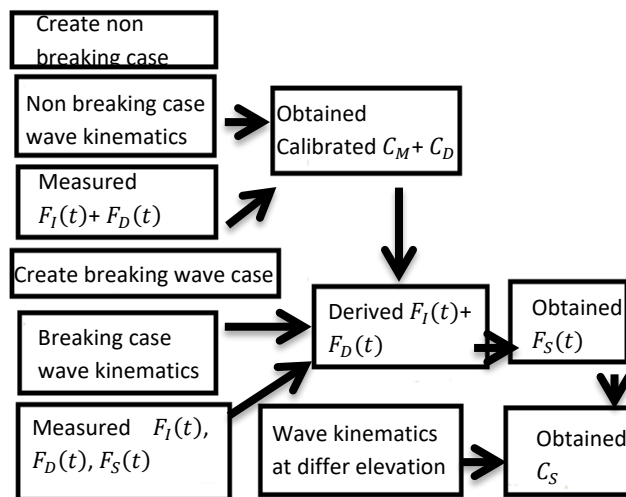


Figure 39 Work flow to determine slamming load coefficient

As explained in the above Figure 39. A regular wave case will be run 10 times per test cylinder. The force transducer having a recording frequency of 200Hz will be used to record the force-time history. The non-breaking coefficient, namely the drag coefficient and mass coefficient would be estimated from the non-breaking wave case. Recalling initial force component formula (Equation 3) and drag force component formula (Equation 2), the initial force is a function of $\frac{\partial u(z)}{\partial t}$, and the drag force is a function of $u(z)$. Applying the relationship of $\frac{\partial u(z)}{\partial t}$ & $u(z)$, when $\frac{\partial u(z)}{\partial t} = \text{maximum}$, $u(z) = \text{zero}$, and vice versa. The drag force component (Equation 2) of the regular wave case could be extracted directly from the total force for a non-breaking case, when $\frac{\partial u(z)}{\partial t}$ and inertia force are negligible. Likewise, the inertia force component could also be approximated from the total force for a non-breaking case when $u(z)$ and drag force is negligible. With the known contributions of the drag and inertia force, the non-breaking coefficient, drag coefficient and mass coefficient could be derived.

Next (as shown in Figure 40), for each of the 5 test cylinder cases, 4 breaking wave cases, having $0.47\text{Hz} \leq f_p \leq 0.5\text{Hz}$ were generated. After estimating the non-breaking coefficients, the drag and inertia force components of the breaking wave case could be approximated with the known

kinematics of the incoming breaking waves. Subsequently, the slamming force contribution and the slamming coefficient could be derived (Equation 4 & Equation 5).

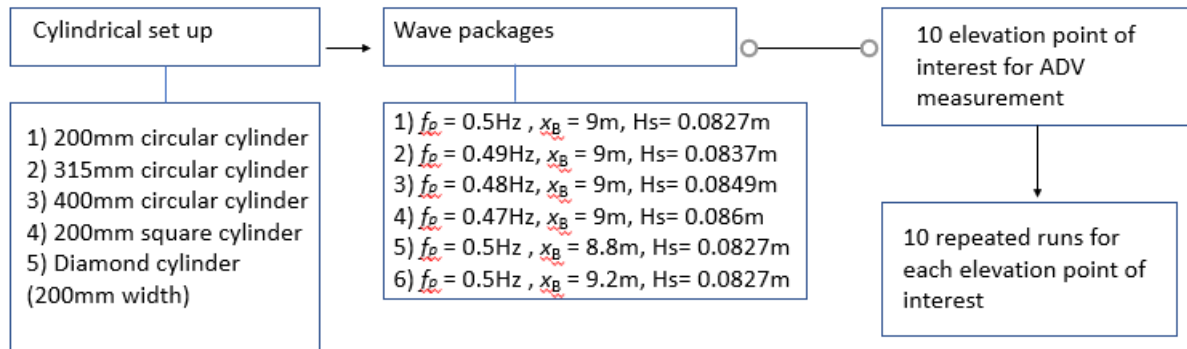


Figure 40 Test cases set ups

For each of the wave signals, at least 10 sets of peak wave force values, drag force and their associated wave kinematics (velocity), and inertia force were recorded and analysed. The acceleration values were approximated by the time derivative of the obtained wave particle velocity.

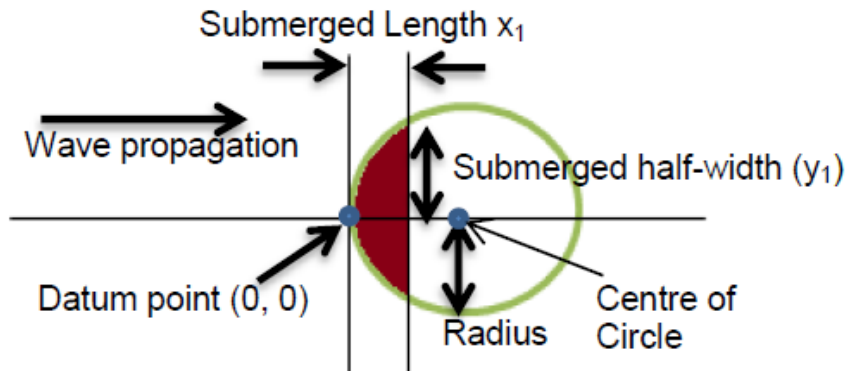


Figure 41 Coefficient of waterplane of circular cylinder (De Wang Chia, Slamming Force Contribution Due to Plunging Breakers on Circular, Square and Diamond Cylinders, 2019)

$$x_1 = t_i * C_b \quad (36)$$

$$y_1^2 = r^2 - (r - x_1)^2 \quad (37)$$

$$y_1 = \sqrt{2 * x_1 * r - x_1^2}$$

The geometrical cross-sections of the cylinders are expected to have a direct influence over the slamming coefficient because it affects the air entrapment between the cylindrical structure and the plunging jet. With the known submerged length and width of the cylindrical structures (Figure 41, Equation 36 & Equation 37), the coefficient of the waterplane area (C_w) could be established.

5. Experiment preliminary Results

5.1 Kinematic results

Raw data derived from the Newcastle University Wind Wave and Current tank were processed and analysed. The kinematic readings were only extracted after the first few waves; to minimize the influence of the evanescent wave generated by the wavemakers.

The wave kinematics registered the lowest sample variances of $4.192 \times 10^{-5} \text{m.s}^{-1}$ when the ADV was placed at a lower elevation, $z = -80 \text{mm}$, with a mean velocity of 0.186m.s^{-1} . The highest velocity sample variance of $1.9 \times 10^{-3} \text{m.s}^{-1}$ is recorded at the higher elevation, $z = 40 \text{mm}$ with a mean velocity of 0.337m.s^{-1} . The variance-to-mean ratio (VMR) for the recorded wave kinematics even at the highest sample variance was only 0.57% (at $z = 40 \text{mm}$), giving a relatively constant output. The average breaking wave height recorded from an average of 10 repeated runs for differing values of f_p of 0.47 – 0.5Hz were 203mm, 208.5mm, 214.5mm and 217mm respectively.

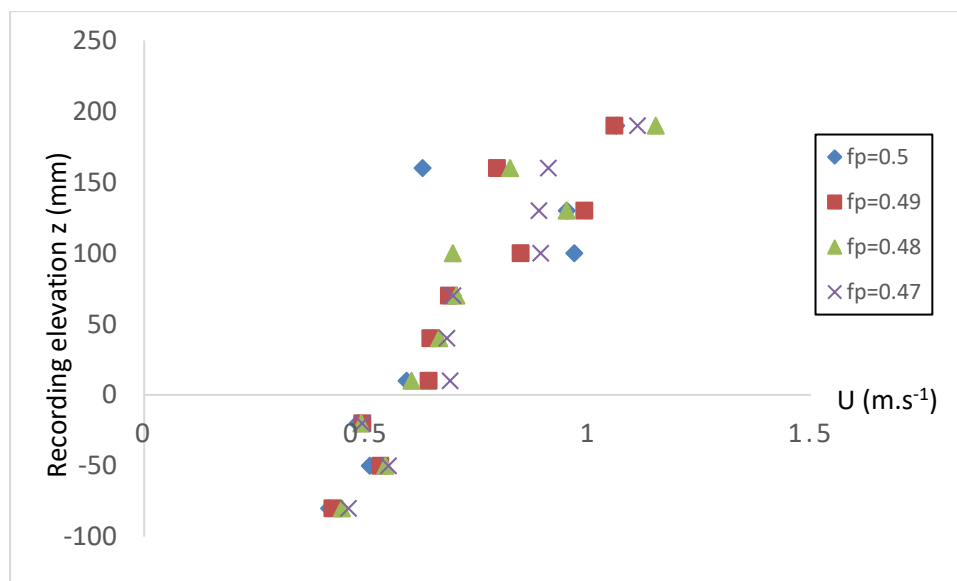


Figure 42 Velocity profile for differing elevation for $0.47 \text{Hz} \leq f_p \leq 0.5 \text{Hz}$

Figure 42 shows the velocity profile at the focal point. There is a correlation between the elevation measure point and the measured velocity. It could be seen that the highest horizontal particle velocity occurs towards the crest of the plunging breaker. The higher velocity nearer to the crest is often associated with aiding the formation of the protruding jet that eventually allows the protruding jet to collapse with the aid of gravity.

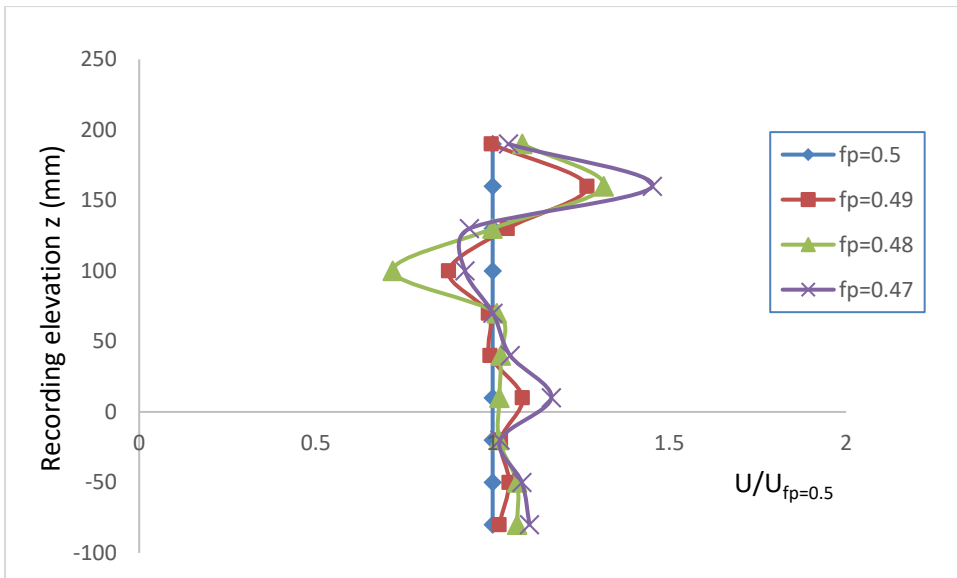


Figure 43 Velocity profile for differing elevation for $0.47\text{Hz} \leq f_p \leq 0.5\text{Hz}$, using $f_p = 0.5\text{Hz}$ as a datum

Figure 43 shows the relationship between the velocity amongst the 4 breaking intensities across all recorded elevations. A horizontal value ($U/U_{f_p=0.5}$) > 1 would have meant there, the measured kinematics for the specified wave intensities is higher at that datum point of interest ($f_p = 0.5\text{Hz}$), and vice versa. It is shown that at the top surface elevation, at the occurrence of the jet formation, higher breaking intensities experiences higher horizontal inline velocity. However, for the surface elevation just below the jet formation ($100\text{mm} \leq z \leq 130\text{mm}$), the higher intensities plunger shows a reduction in the horizontal inline velocity. The above-mentioned phenomenon, coupled with a higher horizontal velocity at the jet formation, would give rise to a more protruding jet formation with a steeper curl below the jet formation (Figure 49).

Having different curl of the plunging breaker, would also give rise to different slamming load contribution, and would be discussed in detail in later chapters.

5.2 Loadings results

Initial comparison of force analysis was made for the cylinders with different geometry cross-sections, amongst with different breaking intensities.

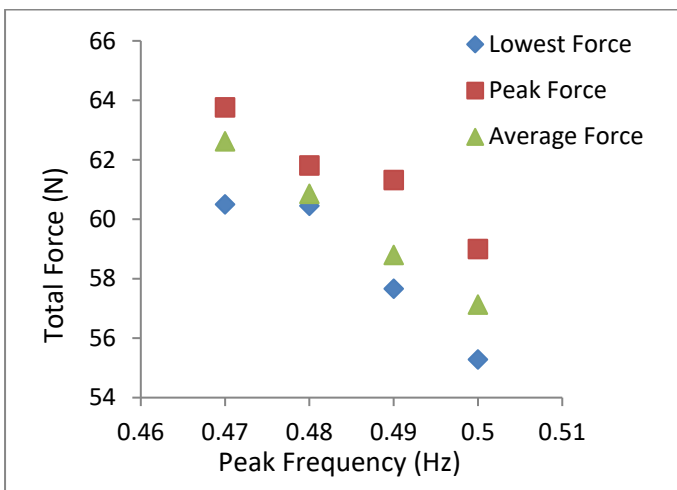


Figure 44 Peak force for cylinder with diameter of 200mm

Focused waves were constructed using the JONSWAP spectrum with a fixed frequency range $0.25\text{Hz} \leq f \leq 2\text{Hz}$ for all cases. However, the peak frequency of the spectrum was as Figure 44. Each peak frequencies test case were allowed to run for 10 times. Subsequently, the average peak force, lowest peak force, and the highest peak force of the 10 runs were plotted in the above Figure 44. A distinctive negative correlation could be observed between the induced force and the peak frequency of the spectrum.

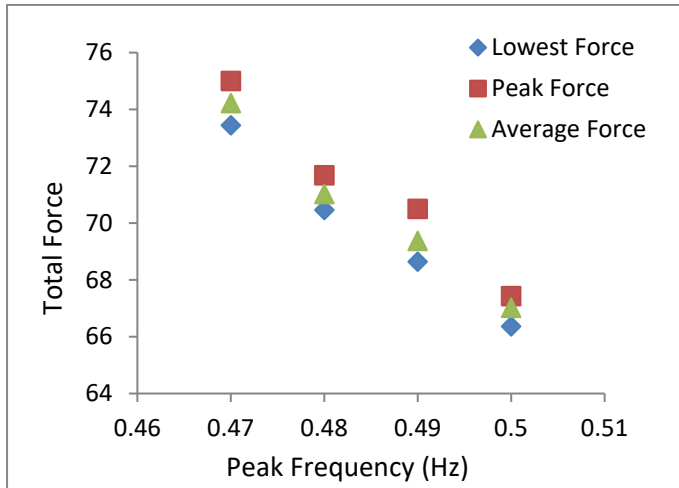


Figure 45 Peak force for diamond cylinder

The diamond cylinder having similar traits with the previous circular cylinder (Figure 45), higher forces reading was registered due to the diamond cylinder's wider effective diameter as explained earlier in 4.2 Equipment and Calibration.

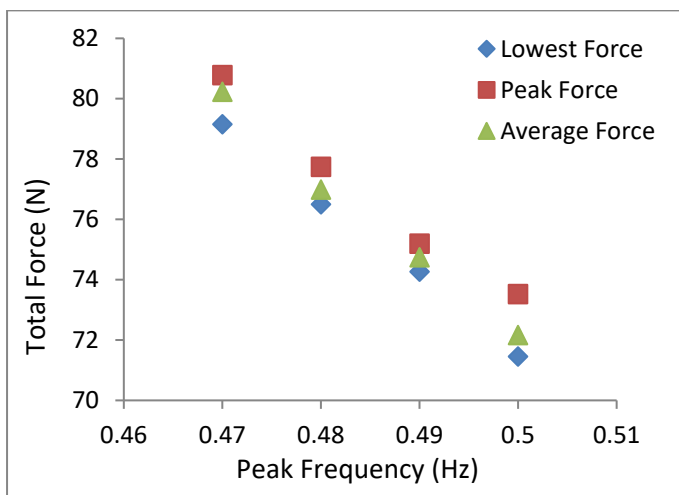


Figure 46 Peak force for square cylinder

Although both the square and circular cylinder shared the same diameter. However, it is obvious that the square cylinder had a 20%+ higher peak force than the circular cylinder. In-depth analysis would be done in the latter chapter, to break these forces down to determine the actual contribution for the increment of peak force.

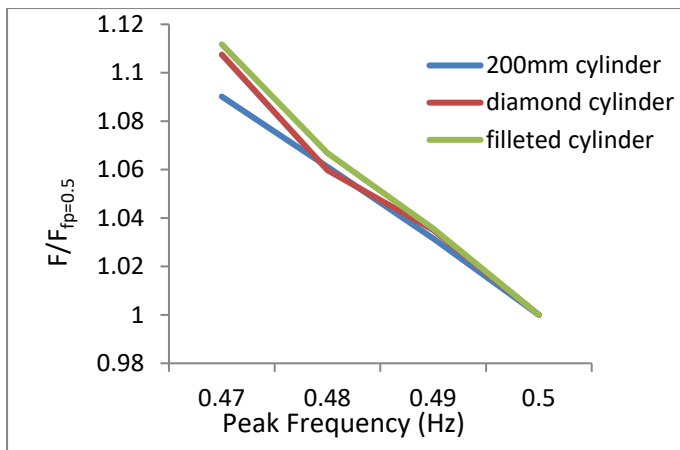


Figure 47 Force increment sensitivity

Taking the force obtained for each cylinder at $f_p = 0.5 \text{ Hz}$ as a datum point of comparison, Figure 51 established the sensitivity of the force increment encountered by each cylinder with respect to increasing wave intensity. This important analysis shows that the percentage increment of breaking wave force is also affected by the geometric cross-section of the cylinder. The force increment experienced by the commonly researched circular cylinder, recorded a spike of 9% when stronger plunging wave of $f_p = 0.47 \text{ Hz}$ was launched on the cylinder. On the other hand, the square cylinder recorded a higher of 11.1% under the conditions.

The square cylinder, having a flat plate perpendicular to the inline wave propagation, was shown to have the greatest impact force as compared to the circular cylinder. The square cylinder could have an increased air entrainment capability at the flat plate section of the square (filleted edge) cylinder.

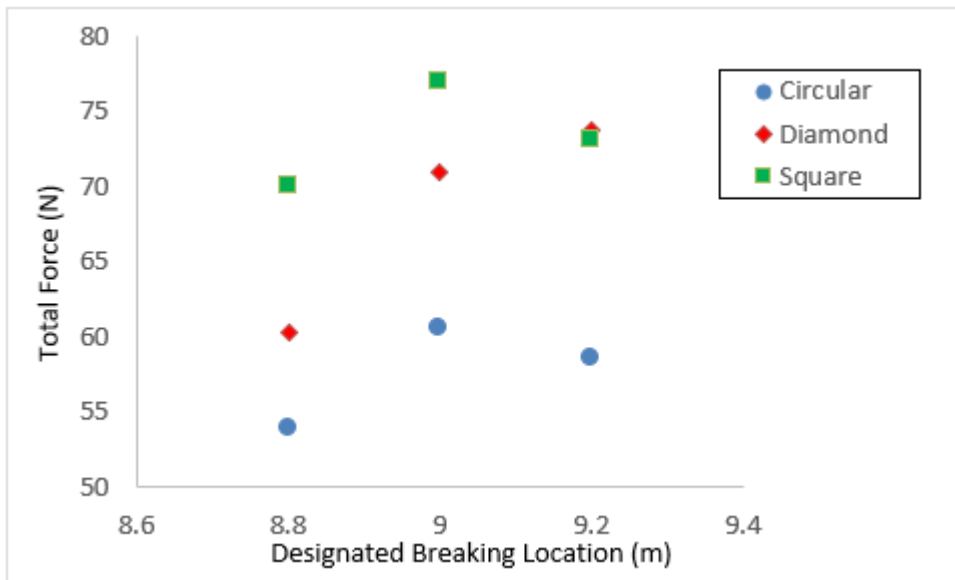


Figure 48 Force readings of 3 different cylinders, during post-jet breaking (for $x_B = 8.8\text{m}$), jet formation (for $x_B = 9\text{m}$), and pre-jet formation (for $x_B = 9.2\text{m}$)

(Chan E.S W. M., 1988) did plunging wave experiments on a vertical wall, and split the wave breaking into 3 regions. The pre-jet formation, during jet formation, and the post jet formation which is the collapsing of the plunging jet. The spatial location of these 3 cylinders was fixed at $x = 8.25\text{m}$ (with $x = 0\text{m}$ being the location of the wave piston). By adjusting the designated breaking location (x_B) of the plunging wave, the above 3 regions could be analysed. The cylinders would be experiencing a post

jet breaking if the defined $x_B = 8.8\text{m}$, a jet formation for x_B defined as 9m , and a pre-jet formation for x_B defined as 9.2m .

(Chan E.S W. M., 1988) experiment concluded that there were the highest impact pressures during the 2nd region of breaking; jet formation stage. This is mainly attributed to the air entrainment due to the curling of the jet on the vertical wall. Figure 52 agrees with Chan E.S to a certain extent. The circular cylinder and the square cylinder experienced the highest impact force during jet formation. However, the diamond-shaped cylinder experienced peak force during pre-jet formation.



Figure 49 Plunging wave impact on diamond cylinder

Figure 49 shows that the diamond-shaped cylinder doesn't have the same amount of air entrainment as compared to the 2 other cylinders during breaking, this phenomenon would ultimately lead to having lower slamming co-efficient. However, due to the higher kinematics associated with the pre-jet formation (3.1 Semi-Empirical Kinematics study), the pre-jet kinematics, coupled with the diamond cylinder wider characteristic diameter, contributed to a higher post-jet plunging force.

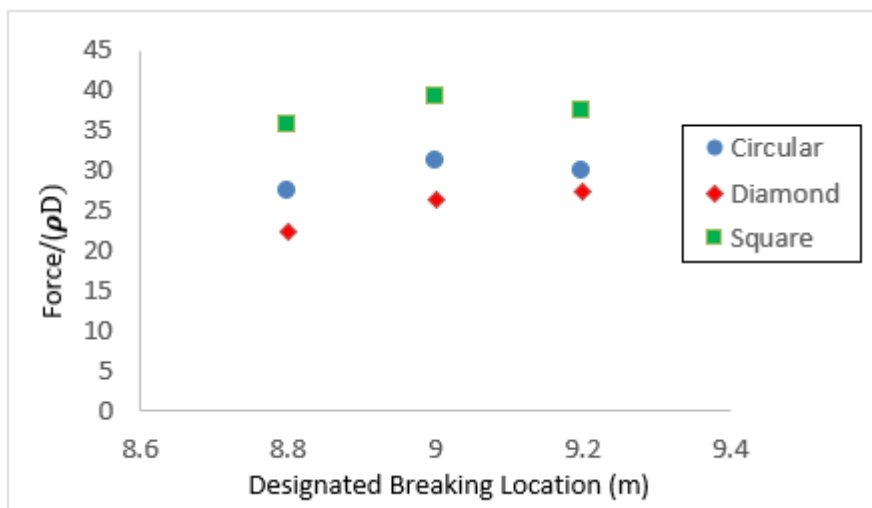


Figure 50 (Force/ρD) analysis of the 3 cylinders, during post-jet breaking (for $x_B = 8.8\text{m}$), jet formation (for $x_B = 9\text{m}$), and pre-jet formation (for $x_B = 9.2\text{m}$)

Figure 50 portrays the 'Force/ρD', taking into account the characteristic diameter of the cylinders. Both the circular and the square cylinder has a diameter of 0.2m ; however, the diamond cylinder has a characteristic diameter of 0.266m (Chapter 4.2, Figure 34) perpendicular to the wave propagation

direction. Figure 48 merely suggested that in the current experiment setups, the diamond cylinder has the highest force due to the increased characteristic diameter.

Taking into consideration of the characteristic diameter of the diamond cylinder, preliminary results showed that the square cylinder had had the highest slamming coefficient and the diamond cylinder with the lowest slamming coefficient.

5.3 Coefficient results

According to DNV rulebook (Veritas D. N., 2010) Chapter 6.7, Page 55, the value of the drag coefficient is affected by the surface roughness and Keulegan Carpenter number.

$$C_D = C_{DS}(\Delta) * \Psi(KC) \quad (38)$$

Ψ = wake amplification factor

$$KC = \pi * \frac{H}{D} \quad (39)$$

H , wave height (m)

D , structural diameter (m)

KC is Keulegan Carpenter formula to be used for structure in the wave zone.

$$\Psi = 1.3 + 0.1(KC - 12) \quad 2 < KC < 12$$

$$\Psi = 0.3 \quad 0.75 < KC < 2$$

$$\Psi = 0.3 - 2(KC - 0.75) \quad KC \leq 0.75$$

From the regular wave case, the ADV was placed at 5 differing surface elevation, yielding maximum velocity reading ranging from 0.2m.s^{-1} to 0.6m.s^{-1} . Equation 38 stated that the oscillatory drag coefficient for cylinder could be approximated from the steady-state drag coefficient for the cylinder. The oscillatory drag coefficient can be estimated by multiplying the wake amplification factor; which is a function of the Keulegan Carpenter Number. For the non-breaking wave case, the KC would be ranging from 0.75 to 1.5, giving a wake amplification factor of 0.3.

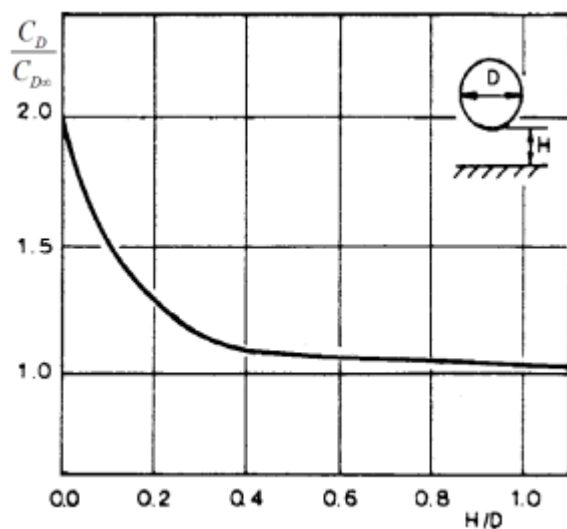


Figure 51 Fixed boundary influence on drag coefficient (Veritas D. N., 2010)

According to Figure 51, 'H' relates to the clearance from the boundary to the structure. The clearance 'H' could be calculated by deducting the radius of the cylinder from the half-width of the wave tank. Considering the half-width of the wave tank to be 0.9m, and radius of cylinders ranging from 0.1m to 0.2m, the 200mm diameter cylinder would have negligible rebounding effects as compared to the 400mm diameter cylinder. Figure 56 would have shown the higher associated drag coefficient due to this rebounding effect multiplier.

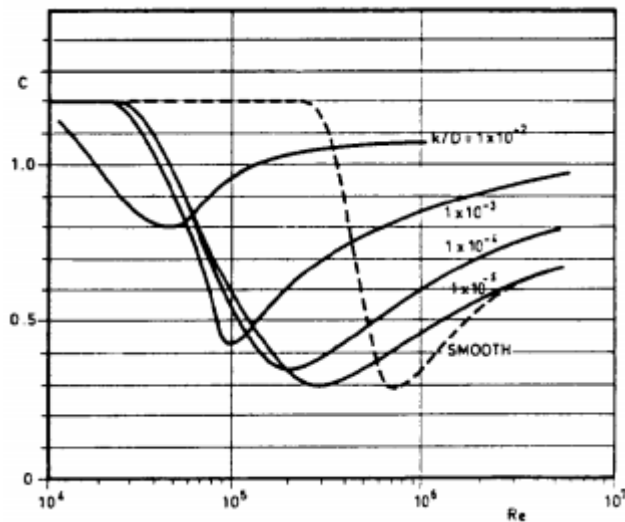


Figure 52 Drag coefficient for fixed circular cylinder for steady flow with function of Reynolds Number (Veritas D. N., 2010)

The Reynold's Number for the 5 test cylinder would be ranging from 9×10^4 to 1.8×10^5 . According to Figure 52, this would steady flow drag coefficient C_{DS} of 1.2 for the 3 circular test cylinder. According to Equation 38, C_{DS} would be a function of Reynold's Number and the wave amplification factor is a function of KC number.

2. Rectangle with thin splitter plate	L/D	T/D			
		0	5	10	
	0.1	1.9	1.4	1.38	
	0.2	2.1	1.4	1.43	
	0.4	2.35	1.39	1.46	
	0.6	1.8	1.38	1.48	
	0.8	2.3	1.36	1.47	
	1.0	2.0	1.33	1.45	
	1.5	1.8	1.30	1.40	
	2.0	1.6	-	1.33	
	$Re \sim 5 \times 10^4$				

Figure 53 Drag coefficient for 'rectangle with thin splitter plate' for steady flow state (Veritas D. N., 2010)

The C_{DS} of a square cylinder could be estimated by assuming $\frac{T}{D}$ ratio = 0; indicating the absence of a splitter plate. The shape of the square could be represented by a $\frac{L}{D}$ ratio of 1. This would give a C_{DS} of 2.

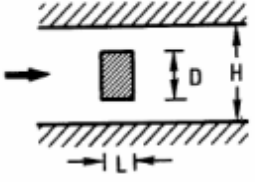
<p>4. Rectangle in a channel</p> 	$C_{DS} = (1-D/H)^{-n} C_D \mid H = \infty \text{ for } 0 < D/H < 0.25$					
	L/D	0.1	0.25	0.50	1.0	2.0
	n	2.3	2.2	2.1	1.2	0.4
$Re > 10^3$						

Figure 54 Rebounding effects for estimating drag coefficient multiplier for square cylinder ($L/D = 1$) (Veritas D. , 2011)

For cylinder case 4; the square cylinder, considering that the $D = 0.315\text{m}$, H (width of wave tank) = 1.8m , attaining a $\frac{D}{H}$ ratio of ≈ 0.2 . According to Figure 54, this would mean that the wall boundary effects could be neglected.

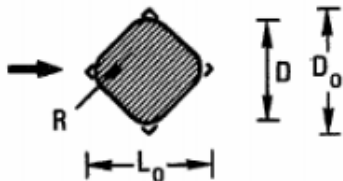
<p>7. Diamond with rounded corners</p> 	L_0/D_0	R/D_0	C_{DS}	
	0.5	0.021	1.8	Fore and aft corners not rounded
		0.083	1.7	
		0.167	1.7	
	1.0	0.015	1.5	
0.118		1.5		
0.235		1.5		
2.0	0.040	1.1	Lateral corners not rounded	
	0.167	1.1		
	0.335	1.1		
$Re \sim 10^5$				

Figure 55 Drag coefficient for a diamond cylinder $L_0/D_0 = 1$ (Veritas D. , 2011)

For cylinder case 5; the diamond cylinder, considering the body as symmetrical along the horizontal and vertical axis, ' $L_0/D_0 = 1$ '. For a ' R/D_0 ' of 0.075 and a ' $L_0/D_0 = 1$ ', the C_{DS} of the diamond cylinder could be assumed to be 1.5 .

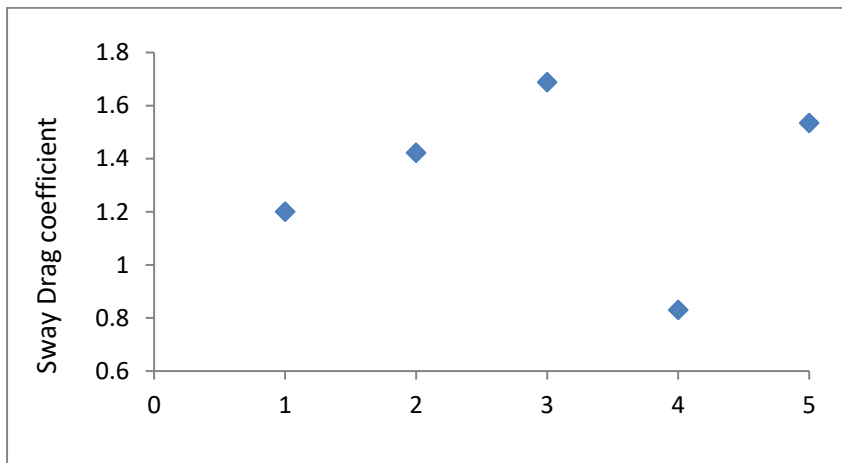


Figure 56 Sway drag coefficient for different cylinders (1- 200mm circular cylinder, 2- 315mm circular cylinder, 3- 400mm circular cylinder, 4- square cylinder, 5- diamond cylinder) for irregular waves

Figure 56 showed the 5 cylinders sway hydrodynamic coefficient values derived from experimental works and from DNV rulebook (Veritas D. N., 2010) (Veritas D. , 2011). Comparing amongst the first 3 cylindrical cases, it seemed to hint at a larger boundary wall effects as suggested by the theoretical relation suggested by DNV (Figure 51), or it could also be due to different resultant wake amplification factor due to differing KC value. As according to Figure 39 (explained in details in Chapter 4.5 Post Processing), the force transducer would record the total force-time history.

Obtaining the non-breaking coefficients and with the obtained kinematics of breaking wave. The time history for the inertia and drag force component could be subtracted from the total force time history, yielding the slamming load time history.

5.3.1 Wave Amplification Factor and Inertia Coefficient

The wave amplification factor $\Psi(KC) = \frac{C_D}{C_{DS}}$, is crucial for determining the value of C_D . There have only been experimental work done by past researchers and including this current PhD work to relate the relationship between the wave amplification factor and KC number.

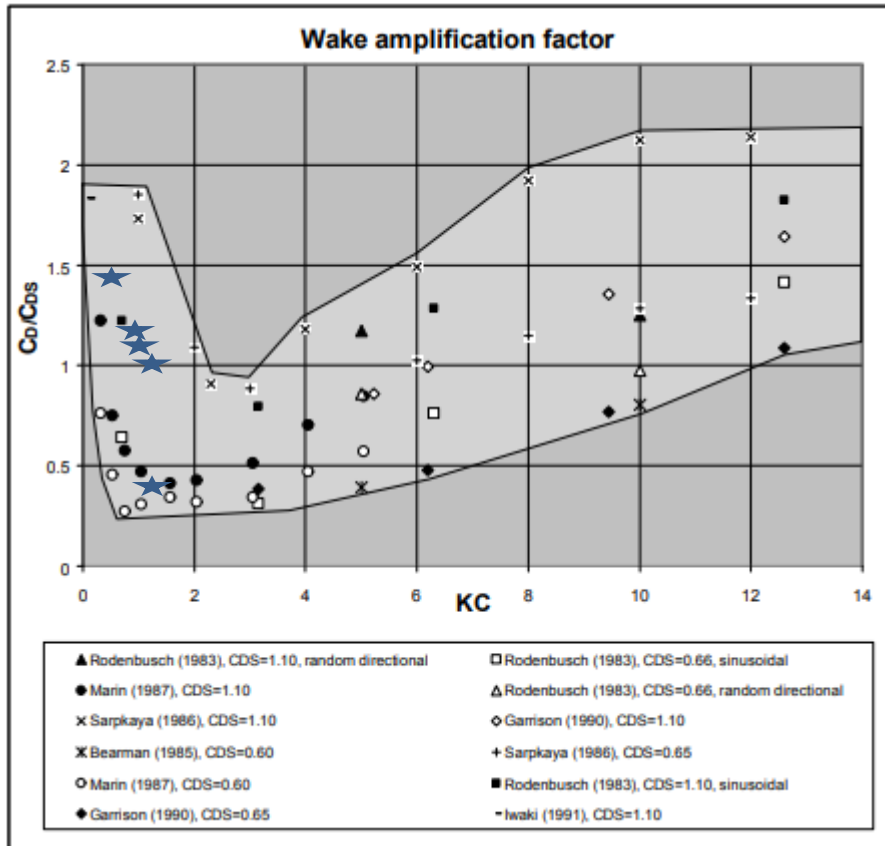


Figure 57 Wake Amplification factors comparison (irregular waves only) with previous literature review by (Veritas D. , 2011)

Figure 57 shows past literature review of the wake amplification factor from various studies and there is an obvious initial downtrend of the KC number and the Wake amplification factor; a phenomenon that is observed in this experimental work involving only irregular waves (denoted by blue stars in the above figure)

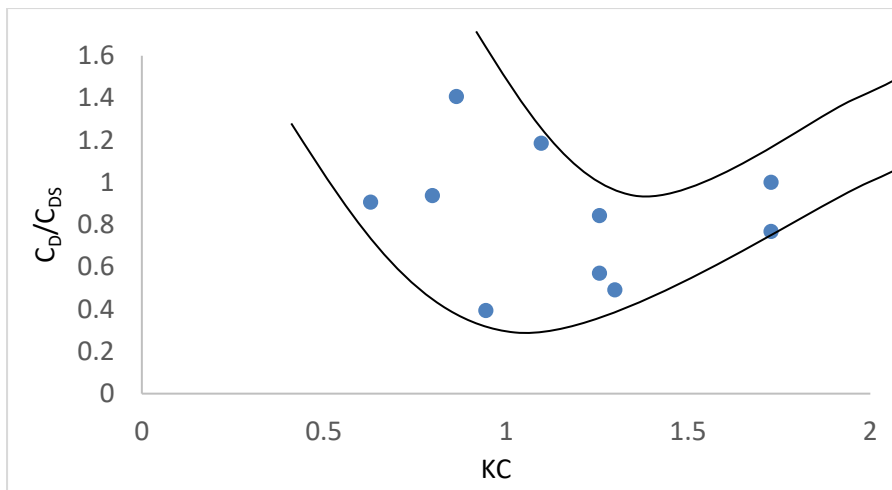


Figure 58 Relation between ' C_D/C_{D_s} ' and KC number, for all cylinders in this experimental work, involving both regular and irregular waves.

A C_{D_s} of 1.2 was assumed for the above case. Figure 58 showed obvious similar trends as compared to previous literature reviews as shown in the previous figure (Figure 57). The wake amplification factor started off on a higher scale and started sliding and bottoming out when it approaches $KC=1$; a phenomenon commonly seen amongst literature reviews. As the KC number increases and deviates away from 1, it started forming an uptrend. The wake amplification factor seems to bottom at 0.393, when $KC = 0.945$.

Using the above figure that was derived from current non-breaking experimental work, with the known KC number of the breaking wave case, the wake amplification could be approximated to derive the drag coefficient and the contributed drag force.

The above step was repeated and plotted when the wave horizontal velocity is negligible; when wave horizontal acceleration is at the maximum, neglecting the drag force component. Applying Equation 3 and having the known $\frac{\partial u(z)}{\partial t}$, the mass coefficient could be approximated. The obtained drag and mass coefficient are then cross verified with the average maximum force incurred by the regular wave force.

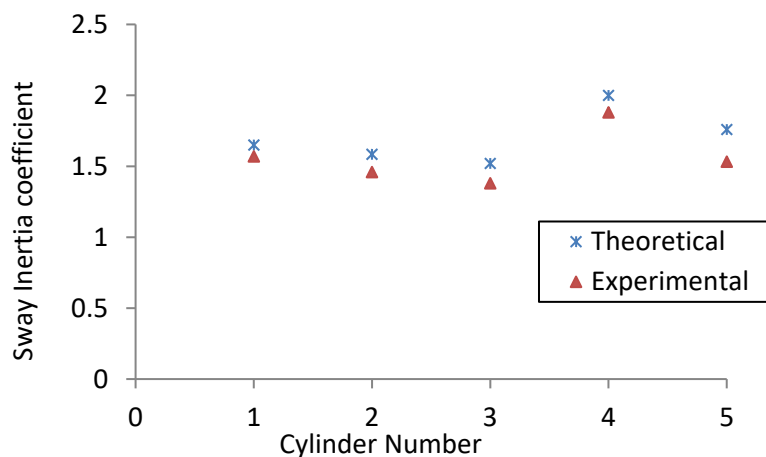


Figure 59 Sway Inertia Coefficient (or inline inertia coefficient) for different cylinders (1- 200mm Circular Cylinder, 2- 315mm circular cylinder, 3- 400mm circular cylinder, 4- Square Cylinder, 5- Diamond Cylinder)

(Tarik Sabuncu, 1981) investigated the inertia coefficient for vertical cylinder non-dimensional sizes amongst sway and heave responses. The impact on the coefficients was plotted as a function of different non-dimensional parameters; $\frac{\text{water depth}}{\text{radius of cylinder}}$, $\frac{\text{submerged cylinder depth}}{\text{radius of cylinder}}$, & $\frac{\omega^2 * \text{radius}}{g}$. Taking ($C_M = 1 + C_A$), the inertia coefficient is plotted amongst the theoretical and experimental values (Figure 63). The theoretical values of cylinder 2 (315mm diameter cylinder) was estimated via the theoretical values of cylinder 1 and 3, via straight-line interpolation (200mm and 400mm diameter cylinder). The non-circular inertia coefficient theoretical values were obtained from (Veritas D. , 2011). It could be observed from Figure 63 that the current Sway Inertia coefficient derived from this present experimental work is slightly lower than the theoretical values, however, overall it shows a good agreement between the theoretical and experimental values for the Sway inertia coefficient.

5.3.2 Coefficient of vertical contributions

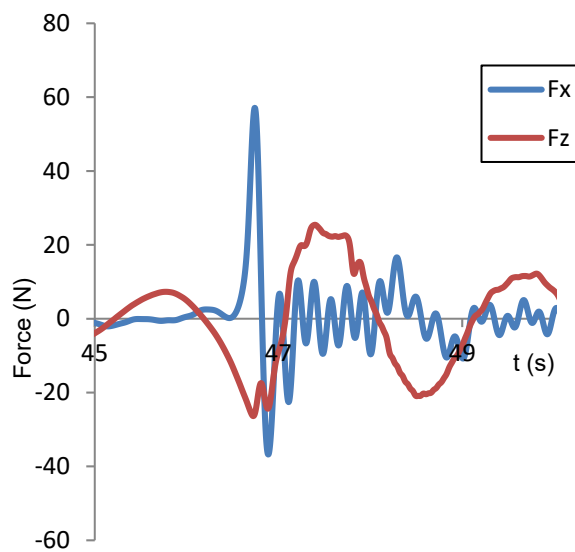


Figure 60 Horizontal and vertical force time history during onset of plunging jet, for 200mm circular cylinder

During the onset of the plunging breaker (Figure 60), at $t = 46.75s$, the inline force maxima coincide with the vertical force minima. This goes to show that during plunging breaking, on top of an inline slamming contribution, there is a relatively large vertical non-slamming contribution.

In the z-direction, the structure would encounter heave added mass force, and as well as lift force. This lift force could be a result from, unsymmetrical geometry, vortex shedding, wake effects or wall effects (structure being too near to the boundary). However, in this experiment, the lift force will only occur due to wall effects. The lift force due to unsymmetrical geometry is negligible as symmetrical structures were used in this experimental work. Wake effects induced lifting force isn't applicable as there wasn't a disturbed flow before breaking. And finally, in this experimental setup, operates at a maximum KC Number of ~ 7 ; in which shedding effects could be neglected; (Veritas D. N., 2010) calls for a critical minimum KC Number of 10. There would also be negligible wall induced lifting force for a gap ratio ($\frac{\text{gap between cylinder and wall}}{\text{cylindrical diameter}}$) > 0.5 . Hence the lift force in this experimental work would be negligible.

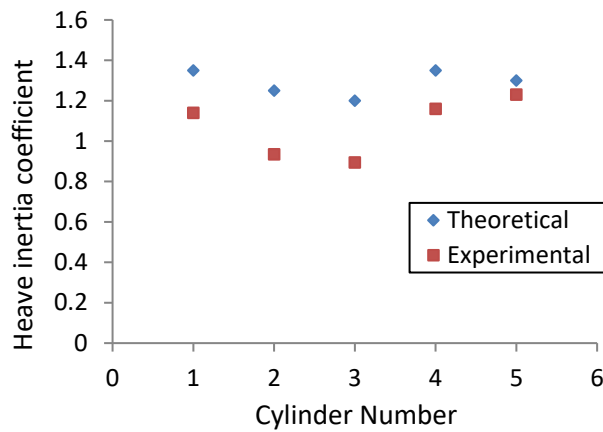


Figure 61 Heave inertia coefficient (vertical axial direction) for different cylinders (1- 200mm Circular Cylinder, 2- 315mm circular cylinder, 3- 400mm circular cylinder, 4- Square Cylinder, 5- Diamond Cylinder)

According to (Tarik Sabuncu, 1981), the theoretical heave added mass coefficient (vertical axial direction) would be ranging from 1.05 to 1.35 for this experimental work. According to Figure 61, the experimental yielded a slightly lower coefficient than the empirical values.

5.3.3 Maximum Slamming Coefficient

The drag and slamming force components are related to the associated squared velocity. The drag force component is spanned across from the amplitude of the wave profile to the bottom of the cylinder. Whereas for the slamming load component, only the elevations from the curl of the jet till the crest is considered.

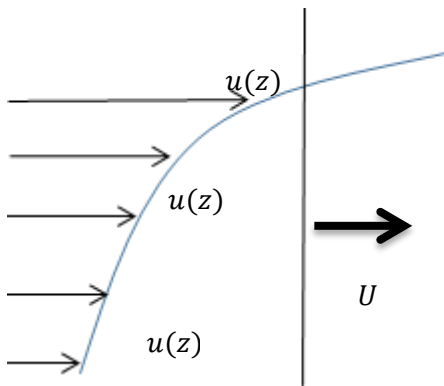


Figure 62 Velocity Field

Above Figure 62 shows the typical wave kinematics profile; with a stronger kinematic profile at the higher elevations.

$$U^2 = \sum_{z=-0.1m}^{z=\zeta} \frac{u(z)^2}{N} \quad (40)$$

The wave kinematics were measured at each elevation profile to obtain kinematics associated with each elevation. Recalling Equation 5, the slamming force is proportioned to the square of breaking wave celerity. Estimating the resultant slamming coefficient from the derived slamming force would need the value of the 'average squared velocity $(\frac{u(z)^2}{N})$ ' and not the 'squared average velocity $(\frac{u(z)}{N})^2$ '. Using strip theory, each recorded kinematics at varying elevations were squared and averaged, to get the average squared velocity (Equation 40). As the cylinder is submerged till $z = -$

0.1m, that forms the lower limit of the strip theory's elevation point of interest. After obtaining the average squared velocity, with the estimated drag coefficient obtained from 5.3 Coefficient results, the drag force-time history could be approximated. As explained in detail in 4.5 Post Processing, the slamming load component could finally be computed.

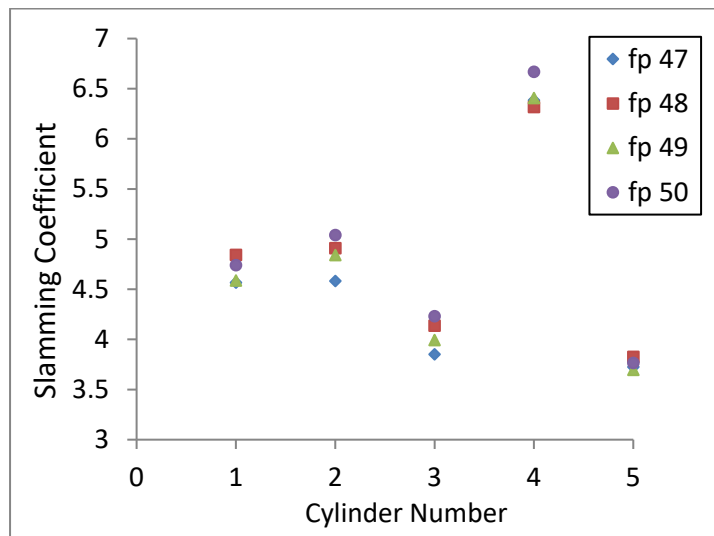


Figure 63 Maximum inline slamming coefficient of 5 cylinders test cases, with varying breaking intensities (1- 200mm circular cylinder, 2- 315mm circular cylinder, 3- 400mm circular cylinder, 4- square cylinder, 5- diamond cylinder)

The maximum slamming coefficients seem to hover at a range of 3.85 to 5.04 for circular cylinders (Figure 63), agreeable with earlier literature review findings of a maximum slamming coefficient value of 5.15 (Campbell, 1980). However, it seems that for a square cylinder, with its frontal flat plate perpendicular to the breaking wave propagation direction, will have the highest maximum inline slamming coefficient of as high as 6.7 in this present experimental work (higher than 5.15 (Campbell, 1980)). However, when the breaking wave plunge on the square cylinder from a contact angle of 45 degrees, effectively rendering the test case into a diamond cylinder, the maximum inline slamming coefficient drops about 45% to a range of 3.7 to 3.82, the lowest of the 5 test cylinders. It is interesting to note that cylinder 3 (the 400mm diameter cylinder), has a lower maximum inline slamming coefficient than the other 2 smaller cylinders.

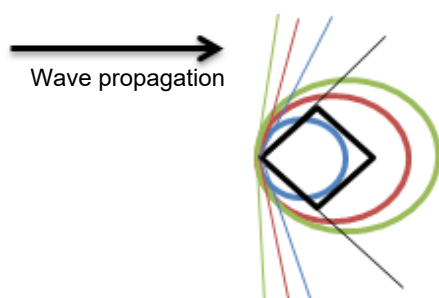


Figure 64 Angle of contact (Denoted by the spread of coloured lines) for cylinders with different geometries cross section and circular cylinders with different diameters.

Figure 64 shows that the angle of contact amongst the 3 circular cylinders and the diamond cylinder. The larger diameter circular cylinder would have an angle of contact closer to 180 degrees (denoted by green lines); almost equivalent of that to an angle of contact for a square cylinder. This means that for a large diameter circular cylinder, the slamming load phenomenon could be assumed to be similar to that of a flat plate wall; a square cylinder. On the other hand, the small-diameter circular cylinder would have a larger angle of contact, however not as large as the angle of contact of a diamond cylinder; this explains the associated slamming load contribution.

The maximum inline slamming load coefficient contribution for a 400mm circular cylinder would have expected to be in between a 315mm circular cylinder and the square cylinder (Figure 64). However, as shown in above Figure 63, the inline maximum slamming coefficient for the 400mm cylinder lies between 3.85 to 4.23, even lesser than the 200mm cylinder. One reason for this deviation is, the 400mm cylinder was deliberately included in the experimental work, as the only cylinder that did not satisfy the boundary condition of the Morison Equation; ($\frac{D}{\lambda} < 0.2$).

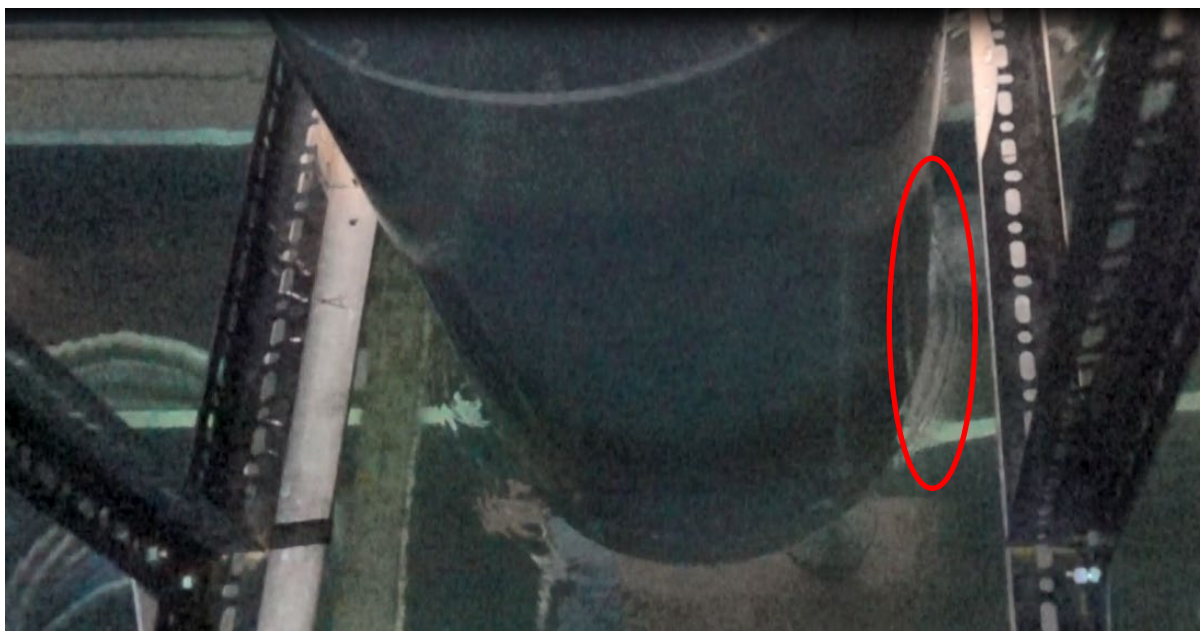


Figure 65 Diffraction wave for the 400mm circular cylinder case. Wave propagated from right to left.

The 400mm circular cylinder would be the only test piece that would be subjected to diffraction effects (Figure 65). This diffraction effects would have produce diffraction waves upon interaction with the buff body structure, altering the impact of actual breaking wave impact on the buff structure as shown in Figure 63. For the sake of consistency to focus on the slamming coefficient of slender structures, the 400mm circular cylinder would be excluded in the latter discussion.

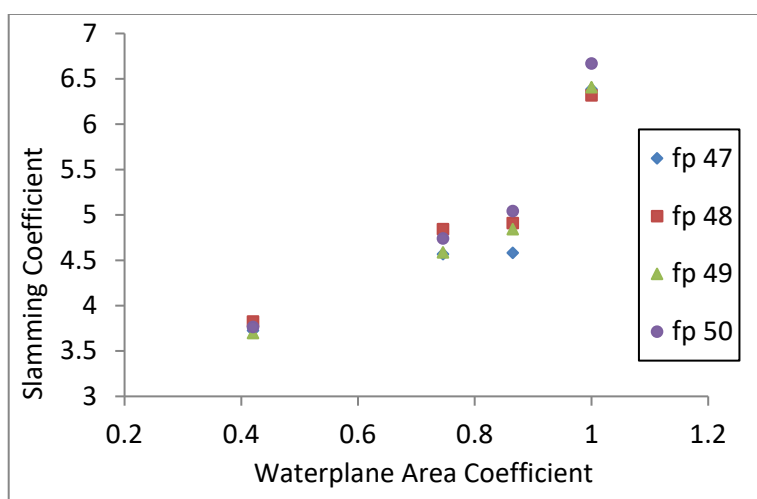


Figure 66 Maximum inline slamming coefficient for cylindrical structures with different Waterplane Area Coefficient during onset of breaking

The purpose of the above Figure 66 is to investigate the impacts of the cross-section geometry of the cylinder has on the resultant maximum inline slamming coefficient. As (Chan E.S W. M., 1988)

pointed out that the air entrapment between the structure and the curl of the plunging jet would have direct implications on the resultant maximum slamming force. Figure 65 concluded a positive correlation between the Waterplane Area Coefficient and the maximum inline slamming coefficient could be observed. With this PhD thesis, a method to predict maximum wave slamming load for different section for different section shape of structure should be proposed.

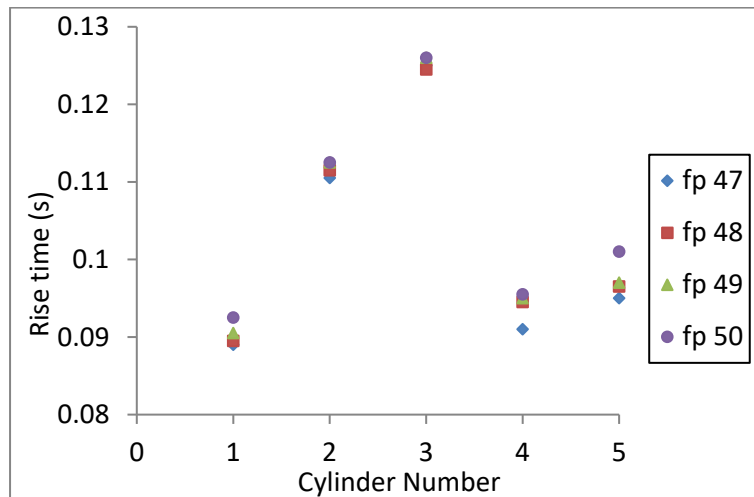


Figure 67 Rise time for different breaking wave intensities. (1- 200mm circular cylinder, 2- 315mm circular cylinder, 3- 400mm circular cylinder, 4- square cylinder, 5- diamond cylinder)

(Chan E.S W. M., 1988) & (P.A Blackmore., 1984) concluded that the rise time does have a negative correlation with the slamming pressure. (Chan E.S W. M., 1988) try to create different rise time by shifting the spatial location of the cylinder, in order to track the associated slamming pressure amongst different maturity of the plunging breaker. In this experimental work, the rise time was adjusted based on different intensities of the plunging breaker (Figure 67, Equation 29). It is shown on the above figure that a lower rise time could be observed for the higher breaking intensity breakers. The rise time at $f_p = 0.47$ Hz, could be observed to be up to 5% lower than at $f_p = 0.5$ Hz. For Cylinder-1, the rise time is shown to be ranging from 0.089s to 0.0925s. For Cylinder-2, the rise time is shown to be ranging from 0.111s to 0.112s. For Cylinder-3, the rise time is 0.1245s to 0.126s. Cylinder-4 rise time is 0.091s to 0.095s. Cylinder-5 rise time is 0.095s to 0.101s.

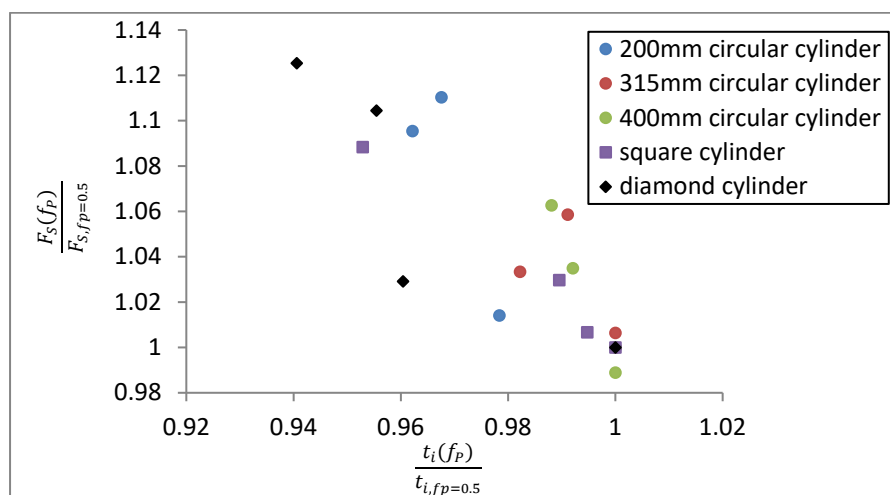


Figure 68 Maximum Slamming Force ratio vs Rise Time ratio comparison

Taking rise time and maximum slamming force at the weakest plunging breaker ($f_p = 0.5 \text{ Hz}$) as a datum. The maximum slamming force ratio is plotted against the change in rise time ratio (Figure 68). The above findings gave a similar conclusion with (Chan E.S W. M., 1988) & (P.A Blackmore., 1984) that a lower rise time would lead to a higher maximum slamming force contribution.

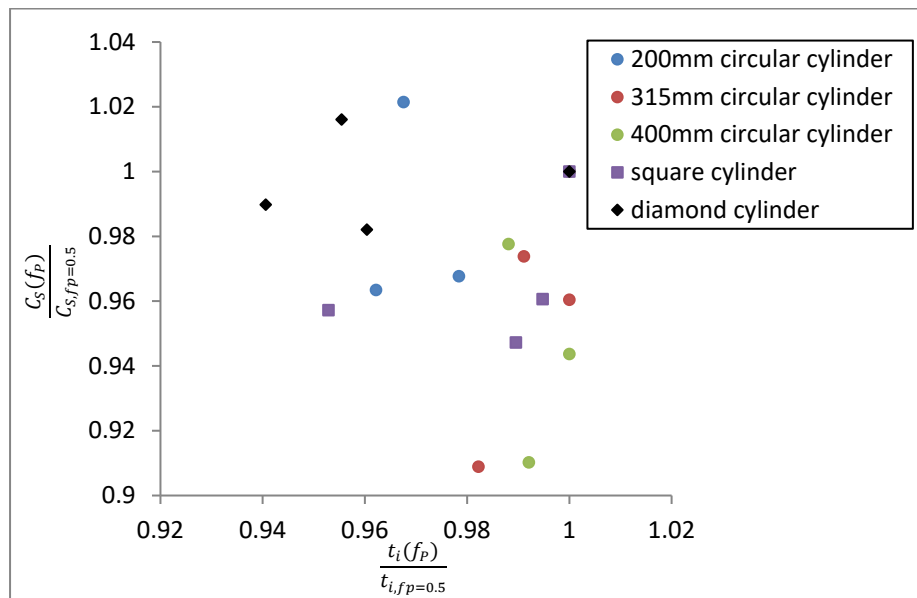


Figure 69 Maximum Inline Slamming Coefficient ratio vs Rise Time ratio comparisons

Applying Equation 5, the maximum inline slamming coefficient is obtained from the derived maximum slamming load. Although there is higher maximum slamming load relation as shown in Figure 68, however, due to the higher associated kinematics of the stronger plunging breakers, the increase in the maximum slamming load is offset by the increased breaking wave kinematics. This resulted in having no distinct correlation between the maximum inline slamming coefficient and the rise time (Figure 69), for the same plunging breaking maturity. These results seem to suggest that the lower rise time that is resulted due to different breaking wave intensity (f_p) does not affect the slamming coefficient.

This chapter concludes that

- 1) Higher breaking intensities would equate to higher breaking wave kinematics, except for at an elevation point ($z= 100\text{mm}$) as noted in Figure 43.
- 2) The higher breaking intensities did translate into higher associate slamming load. However, there is no distinctive relations between the slamming load coefficient and breaking intensities, due being offset by the higher breaking wave kinematics (Equation 5).
- 3) The force rise time did give a higher slamming load contribution, but it does not necessary translate into a higher maximum slamming coefficient as shown in Figure 68.
- 4) The squared cylinder has the highest maximum slamming load contribution, and breaking wave design guidelines should account for the squared cylinder; as it is a not an uncommon design in the offshore industry.

6. Numerical Simulation

Numerical simulations were performed to simulate plunging breakers. Initially, the numerical set-ups were designed to mimic the actual experimental set-ups, solely for cross validation. Next, few numerical simulation test cases were set up to solve some hypothesis that were not address in the experimental phase.

- 1) What is the critical angle of twist for the square cylinder?
- 2) What is the transverse force behaviour for varying angle of twist for the square cylinder?
- 3) Does the transverse force ever exceed the horizontal inline force to be of a design concern?

6.1 Governing equations & Wave theory

Open-source Field Operation And Manipulation, (hereafter known as OpenFOAM) uses Navier-Stokes Equations as the governing equation, which could be described as follows: (Equation 41). The below equation assumed for an incompressible fluid.

$$\rho \left(\frac{\partial V}{\partial t} + (V \cdot \nabla)V \right) = -\nabla p + \rho g + \mu \nabla^2 V \quad (41)$$

And further expanded to x-y-z directions, (Equation 42 & Equation 43 & Equation 44)

$$\rho \left(\frac{\partial u}{\partial t} + u \frac{\partial u}{\partial x} + v \frac{\partial u}{\partial y} + w \frac{\partial u}{\partial z} \right) = -\frac{\partial p}{\partial x} + \mu \left(\frac{\partial^2 u}{\partial x^2} + \frac{\partial^2 u}{\partial y^2} + \frac{\partial^2 u}{\partial z^2} \right) + \rho g_x \quad (42)$$

$$\rho \left(\frac{\partial v}{\partial t} + u \frac{\partial v}{\partial x} + v \frac{\partial v}{\partial y} + w \frac{\partial v}{\partial z} \right) = -\frac{\partial p}{\partial y} + \mu \left(\frac{\partial^2 v}{\partial x^2} + \frac{\partial^2 v}{\partial y^2} + \frac{\partial^2 v}{\partial z^2} \right) + \rho g_y \quad (43)$$

$$\rho \left(\frac{\partial w}{\partial t} + u \frac{\partial w}{\partial x} + v \frac{\partial w}{\partial y} + w \frac{\partial w}{\partial z} \right) = -\frac{\partial p}{\partial z} + \mu \left(\frac{\partial^2 w}{\partial x^2} + \frac{\partial^2 w}{\partial y^2} + \frac{\partial^2 w}{\partial z^2} \right) + \rho g_z \quad (44)$$

ρ is the density, μ is the dynamic viscosity, ' u ', ' v ' & ' w ' represents the velocity in the x, y and z directions respectively.

$\rho = \text{constant}$, for fluid assuming to be incompressible.

Hence the conservation of mass equation to be satisfied is re-written as below, (Equation 45)

$$\frac{\partial u}{\partial x} + \frac{\partial v}{\partial y} + \frac{\partial w}{\partial z} = 0 \quad (45)$$

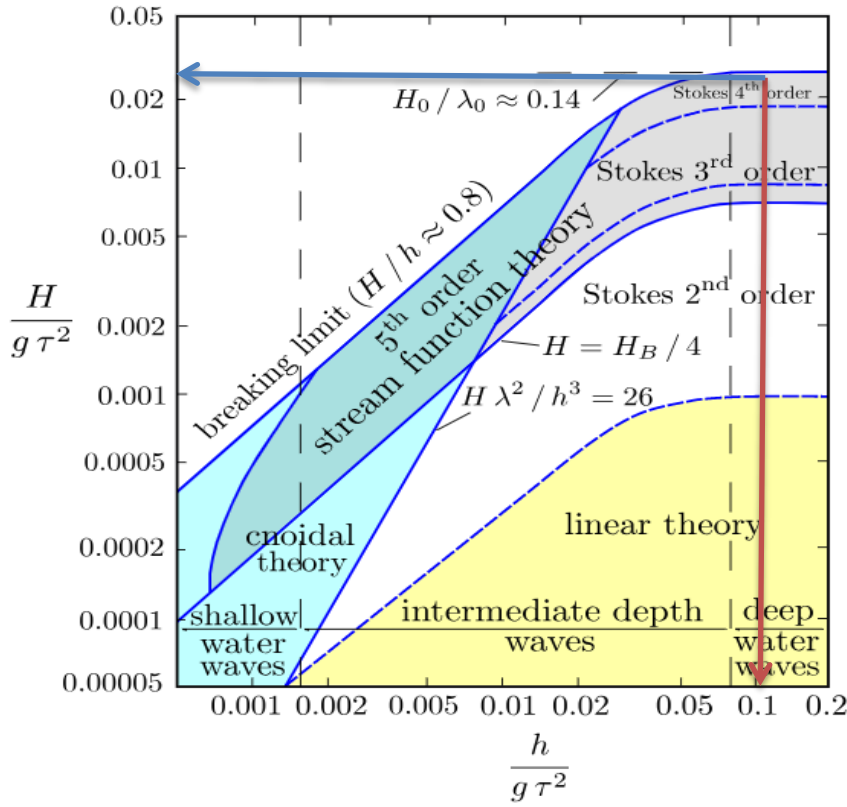


Figure 70 Stoke wave theory (Le Méhauté, 1976)

According to the experimental work that was done in this PhD project ((De Wang C, 2018), (De Wang Chia, Slamming Force Contribution Due to Plunging Breakers on Circular, Square and Diamond Cylinders, 2019)), the experiments yielded a zero-down crossing period of approximate 1s, Breaking wave height of approximate 0.25m, on an operating constant depth of 1m. The experimental output would have given a $(\frac{h}{g\tau^2})$ of approximately 0.1, and a corresponding $(\frac{H}{g\tau^2})$ of 0.025. This would mean a Stokes 4th order wave theory upon breaking and is very close to the Stokes geometric breaking limit as shown (Figure 70).

$$k\eta(x) = kd + (ak) \cos(kx) + (ak)^2 B_{22} \cos(2kx) + (ak)^3 B_{31} (\cos(kx) - \cos(3kx)) + (ak)^4 (B_{42} \cos(2kx) + B_{44} \cos(4kx)) + O(ak)^5 \quad (46)$$

$$B_{22} = \coth(kd)(1 + 2S)/[2(1 - S)]$$

$$B_{31} = -3(1 + 3S + 3S^2 + 2S^3)/[8(1 - S)^3]$$

$$B_{42} = \coth(kd)(6 - 26S - 182S^2 - 204S^3 - 25S^4 + 26S^5)/[6(3 + 2S)(1 - S)^4]$$

$$B_{44} = \coth(kd)(24 + 92S + 122S^2 + 66S^3 + 67S^4 + 34S^5)/[24(3 + 2S)(1 - S)^4]$$

$$S = \operatorname{sech}(2kd)$$

6.2 Volume of Fluid

The surface between the two-phase air and water were tracked using the Volume of Fluid method. This method uses a fraction (J) to describe each cell. If a cell is completely filled by water, $J = 1$, and if the cell is completely filled by air, $J = 0$. If the cell is filled with a mixture of air and water, the value will range $0 < J < 1$.

The properties of each cell could be estimated by the following explicit formula (Equation 47 & Equation 48)

$$\mu = J \mu_w + (1 - J) \mu_a \quad (47)$$

$$\rho = J \rho_w + (1 - J) \rho_a \quad (48)$$

$$\frac{\partial J}{\partial t} + u \frac{\partial J}{\partial x} + v \frac{\partial J}{\partial y} = 0 \quad (49)$$

This equation (Equation 49) states that the 'J' value changes with the fluid. In Lagrangian mesh, where the motion is in tune with the fluid particles, 'J' will remain constant in each cell

Declaring J as an indicator field of the cell's face is a volumetric ratio of water over the volume of the cell. Using the inputs of the faces of the adjacent cells, the volume fraction could be derived via integrating between the faces of the cells. The change in volume fraction J for a defined time step could be established as a function of integrating and finding the change of the indicator field ratio for the cell with respect to the defined time step.

Earlier literature review (2.6 Simulation of breaking waves) introduced about isoAdvector, that introduces additional steps to account for the local distribution of properties within a given cell.

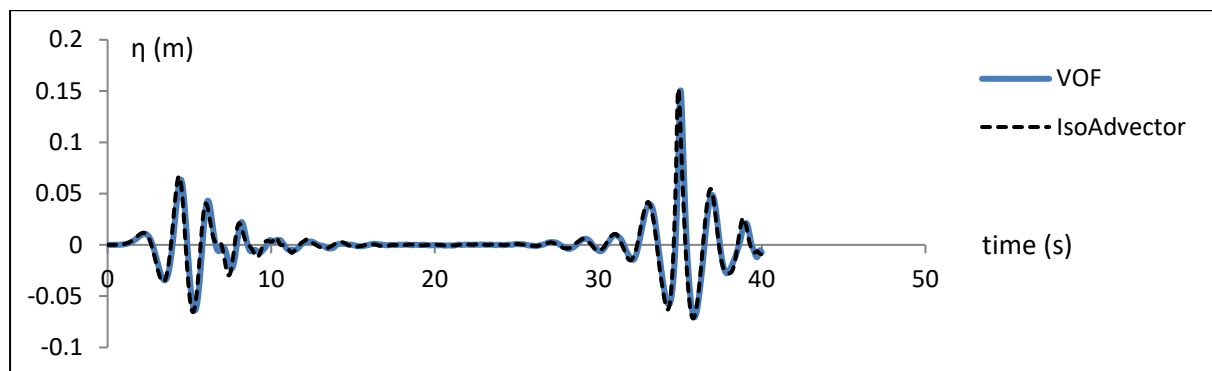


Figure 71 Comparison of surface elevation at the focal point, between 2 methodologies

Using the same wave inputs (focused wave), properties, meshing (6.7 Mesh Set ups) and all other setups unchanged, less for the surface tracking methodology. Comparisons were made between the 2 setups (Figure 71). The VOF scheme obtained a maximum crest elevation of 150.6mm and the isoAdvector scheme obtained a maximum elevation of 152.2mm (a small increment of 1.1%). The maximum elevation for the isoAdvector case occurs at $t = 34.898s$ and VOF scheme at $t = 35.031s$. A higher surface elevation and also an earlier focal time is an obvious result of increased non-linearity effects (Longuet-Higgins, Breaking Waves - in deep or shallow water, 1974). This PhD project will be taking advantage of isoAdvector for its capabilities to account for the local distribution of the two-phase within a given cell; an important boon for demanding numerical works that requires demanding interface representation, such as simulation of breaking wave.

6.3 Courant Number

Setting an ‘appropriate’ Courant Number is an essential step for solving the Navier-Stokes Equations.

$$C = \frac{U \cdot \Delta t}{\Delta x} \quad (50)$$

A lower Courant Number is associated with numerical simulation stability at the cost of slower simulation speed; due to lower associated time step (Equation 50). In OpenFOAM, an adjustable time step function is available for such purpose. For this current numerical work, the initial wave conditions were not as demanding as during wave breaking. Hence, for the initial wave conditions, a Courant Number of as high as 0.1 was used. In this case, a static (non-moving) mesh was used; hence the value of Δx is constant. However, as wave elevation gets amplified, due to the superposition of the regular waves and a higher nonlinear phenomenon and coupled with a higher horizontal particle velocity nearing the breaking zone, lower Courant Number would be needed to avoid having a convergence problem. In this current numerical work, a Courant Number as low as 0.005 could be used nearing the occurrence of the wave breaking zone; or else the simulation might encounter convergence problem; causing the entire simulation to run on a very negligible or zero time step.

6.4 Numerical Calibrations Mesh set up and Sensitivity Test

For a JONSWAP spectrum, both tail-ends components of the spectrum would contribute very negligible wave amplitude to the overall wave amplitude during superposition. However, it is not feasible to stick to the ‘traditional rules’ of ensuring 20-40 meshes per wave height (My Ha Dao, 2016), as this is almost impossible to achieve for both tail-ends components of the JONSWAP spectrum. For this mesh sensitivity test, a regular one wave, bi-chromatic waves, and 10 wave regular wave superposition were used for this convergence study.

Initial mesh convergence test was modelled after National University of Singapore (NUS) wave tank, having a dimension of 35.22m, 2m, and 1.3m (Length, width, height respectively). The piston wave paddle generates waves at $x = 0\text{m}$, and allows the wave to propagate till it reaches a slope at $x > 30\text{m}$, allowing the waves to disperse by breaking due to shoaling effects from $30\text{m} > x > 35.22\text{m}$.

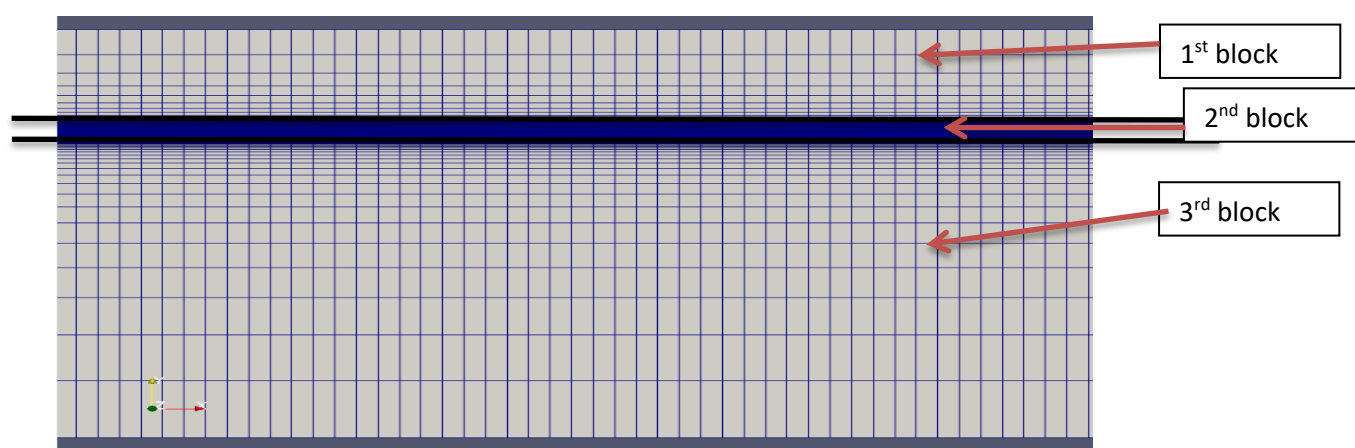


Figure 72 x-y plane of the numerical wave tank, modelled after NUS wave tank

The 2nd block as shown in above Figure 72, describes the free surface block of the numerical wave tank consisting of both air and water flow. This portion is the crux of the simulation and very fine mesh would be used in both x and y-axis for the numerical work. The 1st block describes the air flow phase, and the 3rd block describes the water phase.

The meshes at the extreme top and bottom of the wave tank are the coarsest and become finer while approaching the free surface of the wave tank. This is achieved by using the OpenFOAM command; 'simpleGrading'. If a simpleGrading co-efficient is less than 1, means the mesh size would be smaller as it moves down the axis of interest, and vice versa. A simpleGrading co-efficient of 0.25 means that the mesh at the end of the axis of interest of the block would be 0.25 times the size of the initial mesh at the start of the axis. It is important to note that the size of the meshing between the interface different blocks must be consistent; else it would lead to processing problems.

Hence it would be very crucial to determine the appropriate value of the SG (simpleGrading coefficient) to allow for the mesh to be gradually coarser as along both extreme ends in the vertical axis. With a known value of ' $\delta Z_{avg,1st-block}$ ' and ' $\delta Z_{avg,2nd-block}$ ' and assuming $\delta Z_{avg,2nd-block} < \delta Z_{avg,1st-block}$,

Balancing the 1st vertical mesh of the 1st block with 2nd block mesh will yield the below formula.

$$\left(\frac{1}{1+sg}\right) * 2 * \delta Z_{avg,1st-block} = \delta Z_{avg,2nd-block} \quad (51)$$

$$SG = ((2 * \delta Z_{avg,1st-block} - \delta Z_{avg,2nd-block}) / \delta Z_{avg,2nd-block})$$

A similar calculation would be done to determine the SG of the lower blocks.

1 regular wave component, having a wavelength of 3.78m, and amplitude of 18.9mm having a phase lag of 2.29 radians was used in this first mesh convergence study. Wave probes were placed across the horizontal x-axis of the numerical wave tank, at an interval of 1.29m; a third of the wavelength. Mesh convergence was tested in both x and y directions.

6.4.1 Convergence study for x-direction

Initially, for a 37.8mm wave height case, and applying Figure 69 inputs, for a given $\left(\frac{h}{g*T^2}\right)$ of approximately 0.1 ($f = 1$ Hz), 2nd order Stoke wave theory would be considered for analytical comparison.

$$\eta(x) = \frac{H}{2} [\cos(kx) + (ak)B_{22} \cos(2kx) + O(ak)^2] \quad (52)$$

$$B_{22} = \coth(kd) * \frac{1+2S}{[2(1-S)]}$$

$$S = \operatorname{sech}(2kd)$$

Equation 52 is the 2nd order Stokes theory for calculating elevation. The equation assumed a cosine wave function, with the initial condition starting at the wave crest.

$$\eta(x) = \frac{H}{2} [1 + (ak)B_{22} \cos(2kx)] \quad (53)$$

Replacing $kx = 2m*\pi$ ($m = 0,1,2,\dots$), to represent the spatial domain at the crest level (Equation 60). The 2nd order Stokes Wave Theory for crest elevation resulted in a higher crest elevation than the 1st order linear theory, due to a positive 2nd order Stokes Wave contribution on the right-hand side equation of Equation 53.

$$\eta(x) = \frac{H}{2} [-1 + (ak)B_{22} \cos(2kx)] \quad (54)$$

Replacing $kx = (2m-1)*\pi$ ($m = 0,1,2,\dots$), to represent the spatial domain at the trough level (Equation 54). The right-hand side of the above equation (2^{nd} order trough contribution) would result in a positive elevation contribution due to the multiplier effects of $2kx$. This would mean that the 2^{nd} order Stokes Wave Theory for trough elevation, would be shallower than the 1^{st} order Stokes Wave Theory for trough elevation.

Taking that the resultant wave height is the crest contribution (Equation 53) minus the trough contribution (Equation 54), the additional elevation gained from the second-order contribution for Equation 53 is offset by the shallower trough in Equation 61. This would ultimately give the same 1^{st} and 2^{nd} order wave height.

Initially, a coarse mesh was used arbitrary, $\Delta x = 100\text{mm}$. Considering the wavelength of 3780mm , that would equate to 38 meshes per wavelength. Then, the meshes were refined and subsequently, the amount of meshes per wave length was increased to 76, 100, 120, and 152. The amount of meshes per wave height is fixed at 30.

Table 6 Comparison of wave crest elevation, for wave probes located from $6.09\text{m} < x < 24.15\text{m}$, for x-meshes ranging from 38 to 152 per wavelength

probes(m)	6.09	7.38	8.67	9.96	11.25	12.54	13.83	15.12	16.41	17.7	18.99	20.28	21.57	22.86	24.15
mesh-x															
38	0.019492	0.018872	0.019208	0.018645	0.018608	0.018718	0.018038	0.018124	0.018308	0.017735	0.017832	0.018077	0.017595	0.017283	0.017578
76	0.019825	0.018754	0.019907	0.019241	0.019055	0.020266	0.018875	0.018871	0.020403	0.018744	0.019092	0.020264	0.018397	0.019259	0.019773
100	0.020025	0.018899	0.020198	0.019459	0.019025	0.020421	0.019032	0.018982	0.020515	0.018896	0.018982	0.020175	0.018897	0.019009	0.019695
120	0.020067	0.018882	0.020261	0.019465	0.01899	0.020565	0.019058	0.01904	0.0207	0.018911	0.019148	0.020422	0.018978	0.019172	0.019844
152	0.020086	0.01892	0.020321	0.019476	0.018991	0.020924	0.019077	0.018919	0.02101	0.019027	0.019104	0.020595	0.018964	0.01929	0.01994
crest 1st	0.018925	0.018925	0.018925	0.018925	0.018925	0.018925	0.018925	0.018925	0.018925	0.018925	0.018925	0.018925	0.018925	0.018925	0.018925
crest 2nd	0.019745	0.019745	0.019745	0.019745	0.019745	0.019745	0.019745	0.019745	0.019745	0.019745	0.019745	0.019745	0.019745	0.019745	0.019745

The 4^{th} to 13^{th} wave crest was taken at each probe locations (Table 7). These 10 wave profiles were then averaged and plotted with respect to space, for each individual simulation study. The 4^{th} to 13^{th} wave profile was chosen so that to eliminate any initial disturbance and to improve accuracy.

The average wave height for each simulation study was then calculated and plots against all other simulation studies and to compare with analytical results to determine mesh convergence.

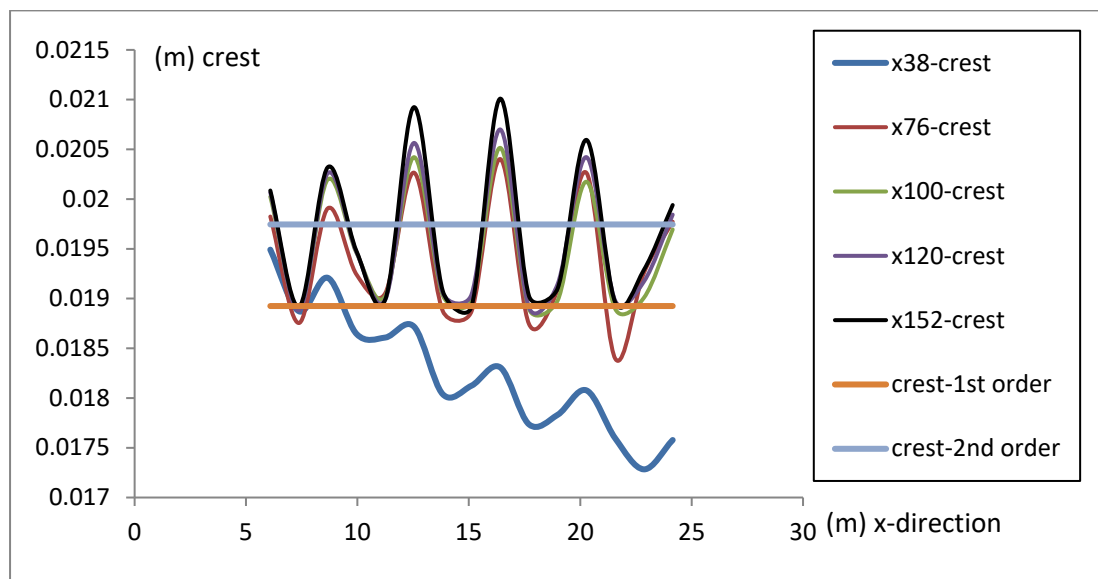


Figure 73 Comparison of crest elevation between simulations and analytical methods, for x-meshes

From Figure 73, there is an obvious numerical dissipation for the coarsest mesh, which describes the entire wavelength with only 38 cells. There is a numerical dissipation of approximately 5% over the 4 wave periods. However, when the coarse mesh size is halved, there is no obvious numerical dissipation observed.

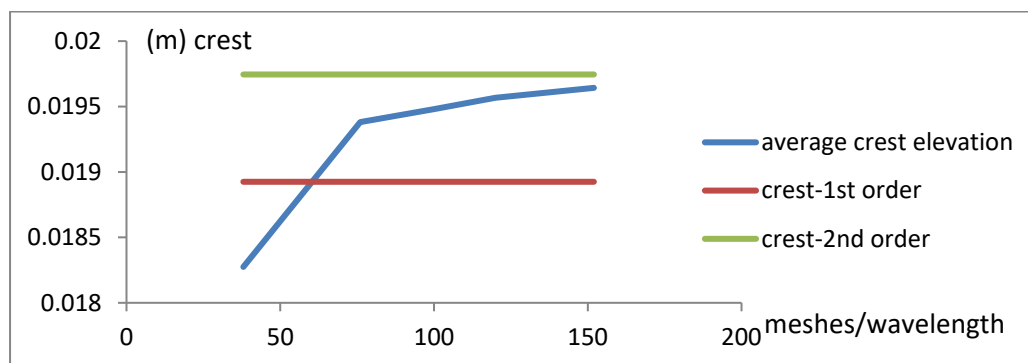


Figure 74 Comparison of averaged crest elevation between simulations and analytical methods, for different amount of x-meshes per wavelength

The effects of the harmonic motion of the wave were removed by averaging the elevation of the 15 wave probes located at different spatial (Figure 74). Above figure shows a steep increment of the average crest elevation till the numerical simulation reaches 100 meshes per wavelength. From 100 meshes per wavelength onwards, the curves start to plateau. At 120 meshes per wave length, the crest elevation has a 1% deviation from the 2nd order solution. At 152 meshes per wave length, it is only a shy 0.5% deviation from the 2nd order solution.

Table 7 Comparison of wave trough elevation, for wave probes located from 6.09m < x < 24.15m, for x-meshes ranging from 38 to 152 per wavelength

probes	6.09	7.38	8.67	9.96	11.25	12.54	13.83	15.12	16.41	17.7	18.99	20.28	21.57	22.86	24.15
mesh-x															
38	-0.01784	-0.01799	-0.01741	-0.01739	-0.01733	-0.01717	-0.01683	-0.01678	-0.01691	-0.01643	-0.01644	-0.01671	-0.01631	-0.01599	-0.01621
76	-0.01756	-0.01849	-0.01725	-0.01772	-0.01848	-0.01726	-0.01785	-0.01796	-0.01736	-0.01811	-0.01761	-0.01764	-0.01786	-0.01741	-0.01801
100	-0.01769	-0.01862	-0.0176	-0.01784	-0.01845	-0.01763	-0.01788	-0.01808	-0.01776	-0.01814	-0.01758	-0.01792	-0.01817	-0.01737	-0.01808
120	-0.01774	-0.01863	-0.01761	-0.01794	-0.01852	-0.01763	-0.018	-0.01815	-0.01775	-0.01825	-0.0176	-0.01801	-0.01832	-0.01733	-0.01824
152	-0.01769	-0.01873	-0.01765	-0.0179	-0.01859	-0.01776	-0.01806	-0.01809	-0.01784	-0.01843	-0.0176	-0.01809	-0.0185	-0.01732	-0.01838
trough 1st	-0.01893	-0.01893	-0.01893	-0.01893	-0.01893	-0.01893	-0.01893	-0.01893	-0.01893	-0.01893	-0.01893	-0.01893	-0.01893	-0.01893	-0.01893
trough 2nd	-0.0181	-0.0181	-0.0181	-0.0181	-0.0181	-0.0181	-0.0181	-0.0181	-0.0181	-0.0181	-0.0181	-0.0181	-0.0181	-0.0181	-0.0181

The exact same methodology previously used for the crest values extraction was used to extract the trough values for Table 8.

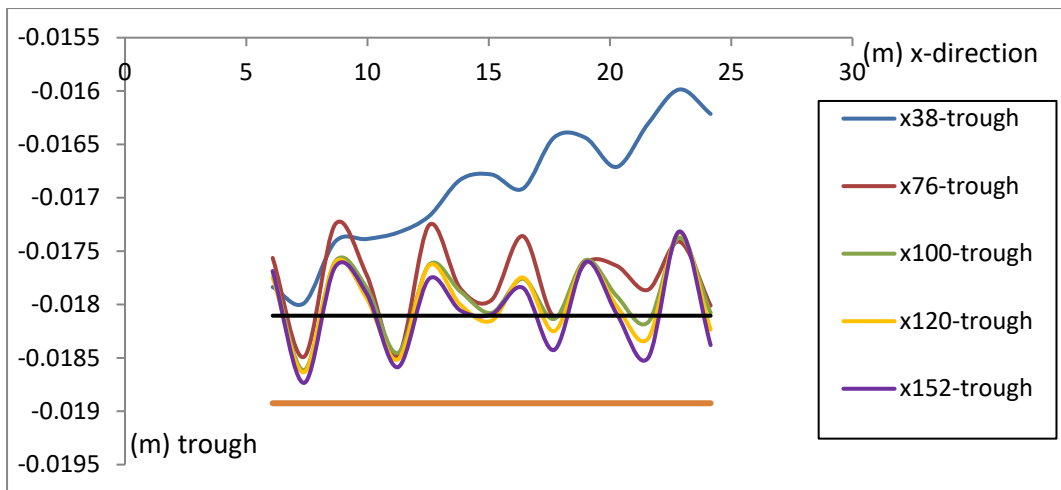


Figure 75 Comparison of trough elevation between simulations and analytical methods, for x-meshes

Showing a similar phenomenon as compared to Figure 73, Figure 75 shows that the coarsest numerical mesh also suffers numerical dissipation for the trough. As much as 8% for 3 wave periods.

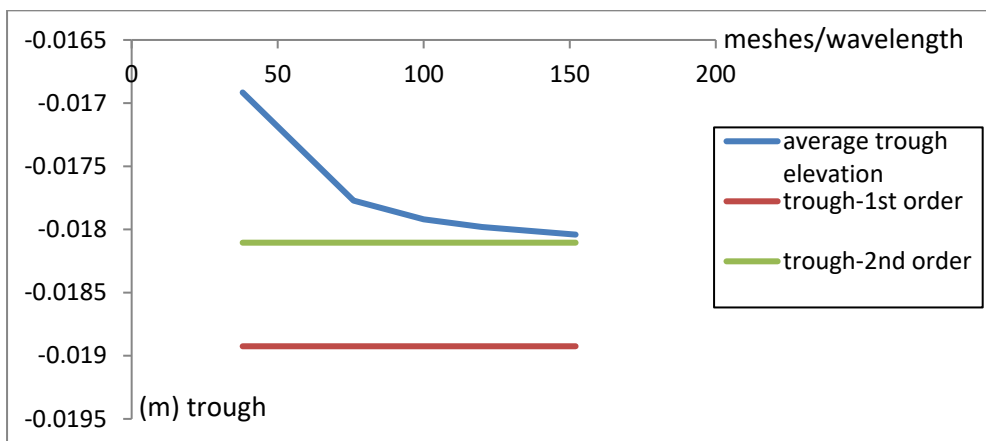


Figure 76 Comparison of averaged trough elevation between simulations and analytical methods, for different amount of x-meshes per wavelength

Presenting the same phenomenon with Figure 74, Figure 76 showed that the mesh convergence for 120 meshes per wave length. However, note that the 2nd order trough is shallower than the 1st order analytical solution as explained earlier (Equation 54). The finer meshing shows signs of converging with the 2nd order trough solution, capturing the higher orders effect. At 120 meshes per wavelength, the trough elevation has a 0.6% deviation from the 2nd order solution. At 152 meshes per wavelength, there is only a 0.3% deviation from the 2nd order solution.

It would be numerically draining to attempt to decrease the numerical dissipation further, as the crest elevation has reached a gentle slope and is close to convergence, even at 120 meshes per wavelength. Base on Equation 50, refining mesh by half, doubling the total amount of computational mesh, would also decrease the time step in order to maintain for the same Courant Number. Hence, if one were to further refine the meshes (considering only 1 axis refinement) and doubling the number of computational meshes, and also doubling the total amount of time steps (due to maintaining same Courant Number Equation 50), this would easily further quadruple the number of simulation resources needed.

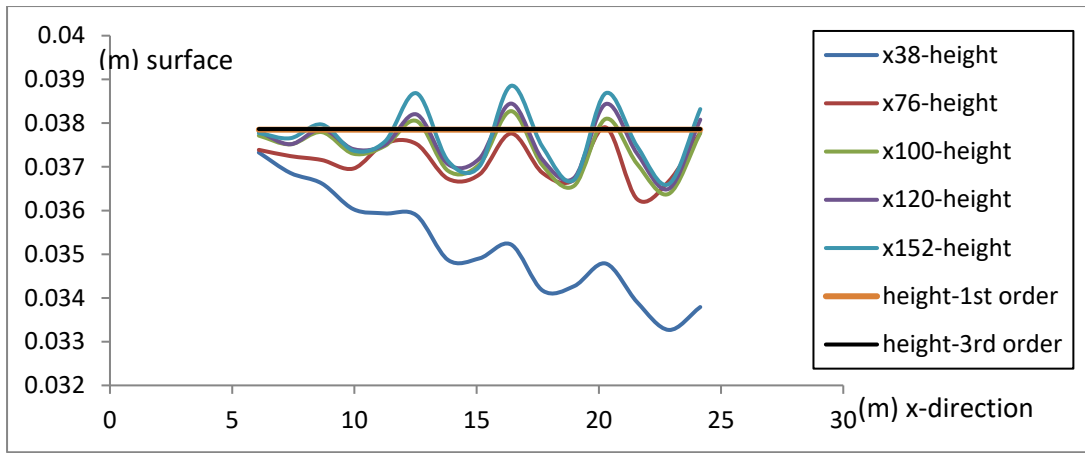


Figure 77 Comparison of wave height between simulations and analytical methods for x-meshes

Applying the sum of Equation 53 & Equation 54, the higher order of wave height could be estimated. Both the 38 meshes per wavelength and 76 meshes per wavelength (Figure 77), showed obvious numerical dissipations as the waves propagate down the axis.

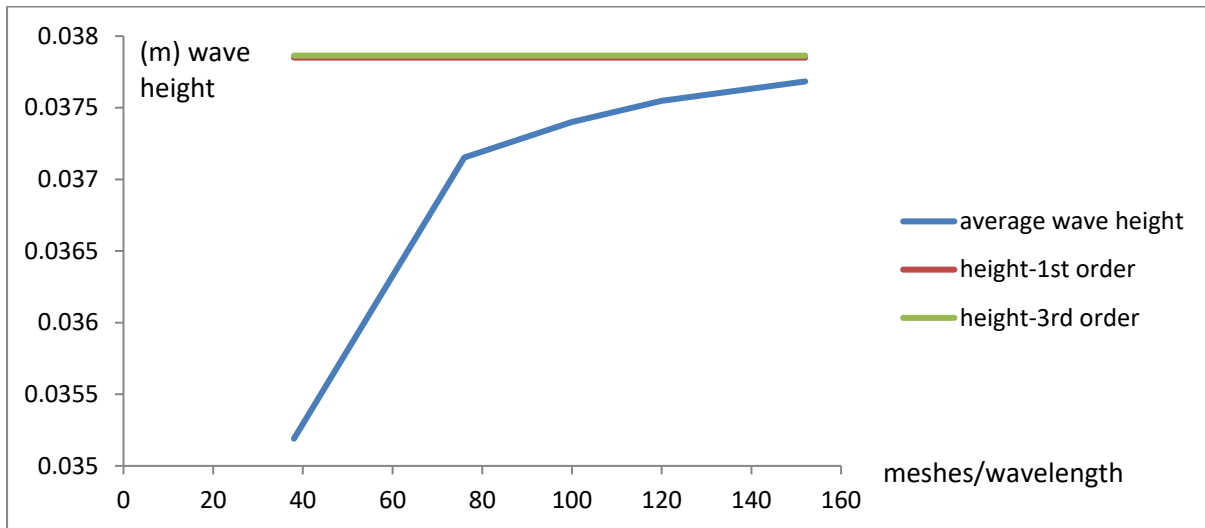


Figure 78 Comparison of averaged wave height between simulations and analytical methods, for different amount of x-meshes per wavelength

Figure 78 showed a similar phenomenon as the figures showing the crest and the trough readings (Figure 74 & Figure 76). Above figure also showed mesh convergence closer to 120 meshes per wave length, having an average wave height reading of 37.55mm as compared to the analytical expected reading of 37.86mm (Stokes 3rd order wave height), a 0.8% of numerical error. The 152 meshes per wave length numerical simulation produced an average wave height of 37.68mm, about 0.5% numerical error. For coarser mesh simulations, a steeper slope and a larger error margin of up to 2% could be observed. Hence using 120 meshes per wavelength would arguably be sufficient for the later simulation work.

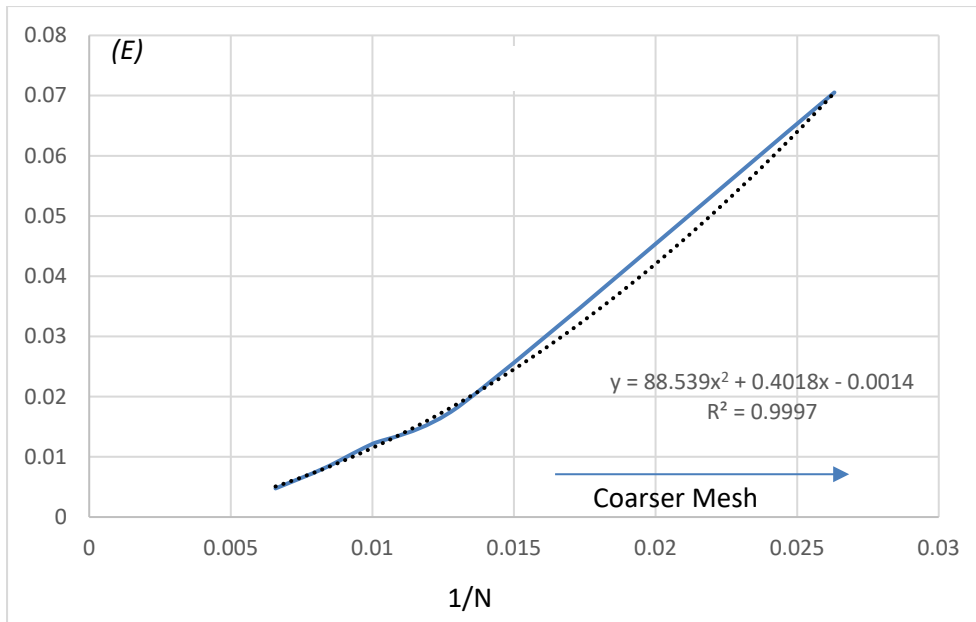


Figure 79 Error margin mesh sensitivity test for different x-axis mesh simulations

Figure 79 plots the relationship between mesh fineness and the error margin. The x-axis is plotted using $(1/N)$, where N is the number of meshes used to describe the wavelength, and E is the error margin between numerical and analytical solution. A $(1/N)$ value of 0 would have meant that an infinite amount of meshes were used, which is unrealistic in nature. Plotting for a polynomial trendline, there is an excellent agreement with the R^2 achieving a value of 0.9997, implying a perfect fit. According to the derived trendline equation, assuming an infinite amount of meshes were used for the numerical simulation, there would still be a numerical error of 0.47%. Hence, in this case, a 0.8% numerical error, for using 120 meshes per wave length would be used for future numerical work.

6.4.2 Convergence study for y-direction

In the y-direction (vertical axis), the free-surface block was defined as having a height of 40mm. The amount of meshes per wave length was fixed at 152. Initial simulation case, coarse meshes of only 10 meshes were used to describe the wave height. Then, the amount of vertical meshes was gradually increasing the amount of mesh in the vertical axis up to 50 meshes per wave height.

Table 8 Comparison of wave crest elevation, for wave probes located from $6.09m < x < 24.15m$, for y-meshes ranging from 10 to 50 per wavelength

probes (m)	6.09	7.38	8.67	9.96	11.25	12.54	13.83	15.12	16.41	17.7	18.99	20.28	21.57	22.86	24.15
mesh-y															
10	0.019758	0.018454	0.019696	0.018886	0.018883	0.0203	0.018443	0.018335	0.02066	0.018347	0.018593	0.020611	0.017775	0.018771	0.019956
15	0.019807	0.018924	0.020055	0.019211	0.019027	0.02017	0.018823	0.018907	0.020092	0.018812	0.018792	0.019696	0.01887	0.018736	0.019325
20	0.020065	0.018856	0.020048	0.019359	0.019131	0.020451	0.018914	0.019048	0.020652	0.018767	0.019226	0.020488	0.018557	0.019302	0.020004
30	0.020086	0.01892	0.020321	0.019476	0.018991	0.020924	0.019077	0.018919	0.02101	0.019027	0.019104	0.020595	0.018964	0.01929	0.01994
40	0.02023	0.019071	0.020322	0.019538	0.019266	0.020718	0.019016	0.019299	0.020934	0.018926	0.019169	0.020761	0.019244	0.019237	0.020082
50	0.020385	0.019137	0.020403	0.019614	0.019352	0.020838	0.019098	0.019322	0.021089	0.019006	0.019376	0.020908	0.019002	0.019501	0.020292
crest 1st	0.018925	0.018925	0.018925	0.018925	0.018925	0.018925	0.018925	0.018925	0.018925	0.018925	0.018925	0.018925	0.018925	0.018925	0.018925
crest 2nd	0.019745	0.019745	0.019745	0.019745	0.019745	0.019745	0.019745	0.019745	0.019745	0.019745	0.019745	0.019745	0.019745	0.019745	0.019745

Using a similar methodology with extracting the readings for the x-axis mesh sensitivity test, the 4th to 13th wave crest were taken at each probe locations (Table 9). These 10 wave profiles were then averaged and plotted with respect to space, for each individual simulation study. The 4th to 13th

wave profile was chosen so that to eliminate any initial disturbance (e.g. evanescence wave) and to improve accuracy.

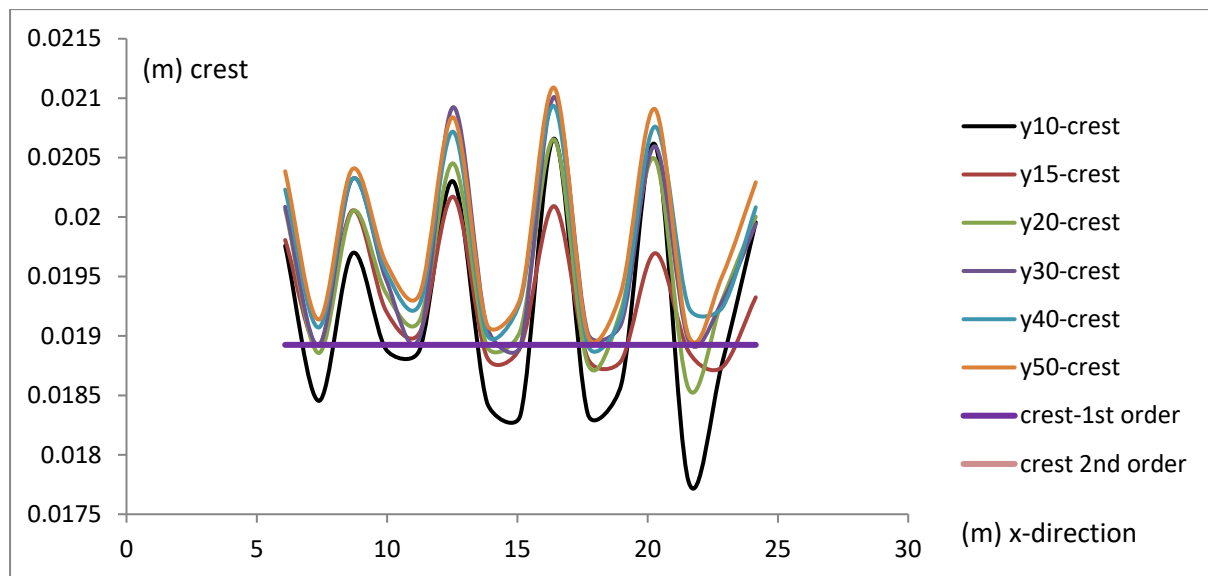


Figure 80 Comparison of crest elevation between simulations and analytical methods, for different amount of y-meshes per wave height

Figure 80 showed that even for the coarsest mesh used; 10 meshes per wave height, does not have that much of a severe numerical dissipation as compared to the coarsest mesh used for x-axis meshes. However, the numerical simulation seems to stabilise at 40 meshes per wave height.

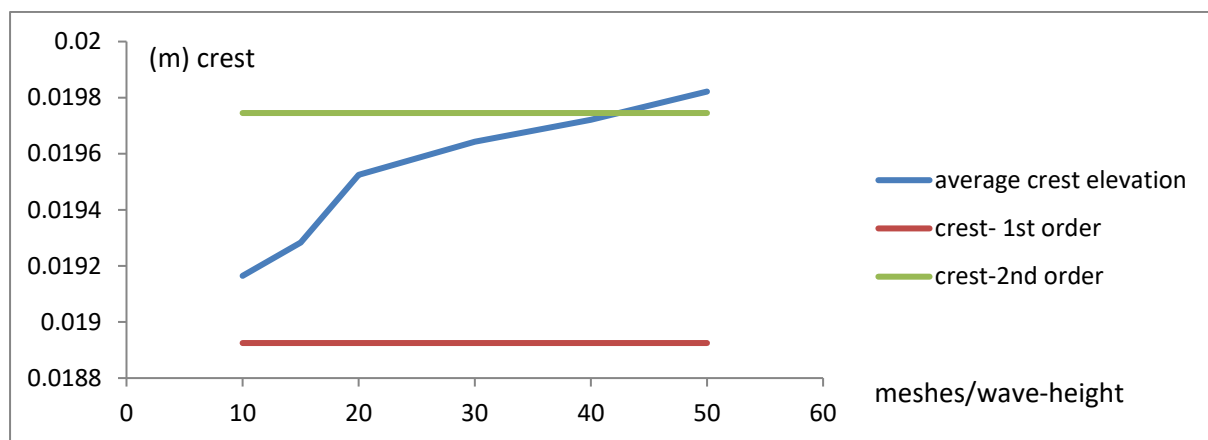


Figure 81 Comparison of averaged wave crest between simulations and analytical methods, for different amount of y-meshes per wavelength

There is a steep slope for coarser meshes leading up to 20 meshes per wave height (Figure 81), followed by a gentle slope. It is interesting to note that for the numerical simulation done using 50 meshes per wave height, exceeded the 2nd order crest elevation by 0.4%. This might mean that the finest mesh in this simulation case, managed to capture higher-order effects.

Table 9 Comparison of wave trough elevation, for wave probes located from 6.09m < x < 24.15m, for y-meshes ranging from 10 to 50 per wave height

probes (m)	6.09	7.38	8.67	9.96	11.25	12.54	13.83	15.12	16.41	17.7	18.99	20.28	21.57	22.86	24.15
mesh-y															
10	-0.01709	-0.01836	-0.01689	-0.01729	-0.01851	-0.01705	-0.01745	-0.01768	-0.0173	-0.01784	-0.0173	-0.01763	-0.01742	-0.01704	-0.01822
15	-0.01774	-0.01845	-0.01759	-0.01775	-0.01817	-0.01771	-0.01774	-0.01771	-0.01778	-0.01785	-0.01724	-0.01786	-0.0178	-0.01713	-0.01779
20	-0.01766	-0.01865	-0.01743	-0.0178	-0.01864	-0.01745	-0.01791	-0.01824	-0.01755	-0.01812	-0.01781	-0.01786	-0.01807	-0.01741	-0.0183
30	-0.01769	-0.01873	-0.01765	-0.0179	-0.01859	-0.01776	-0.01806	-0.01809	-0.01784	-0.01843	-0.0176	-0.01809	-0.0185	-0.01732	-0.01838
40	-0.01775	-0.01879	-0.01754	-0.01787	-0.01879	-0.01761	-0.01797	-0.01846	-0.0178	-0.01832	-0.01771	-0.01816	-0.01855	-0.01717	-0.01858
50	-0.01756	-0.01873	-0.01762	-0.01768	-0.01876	-0.01765	-0.01773	-0.01832	-0.01781	-0.01803	-0.0177	-0.01802	-0.01806	-0.01734	-0.01849
trough 1st	-0.01893	-0.01893	-0.01893	-0.01893	-0.01893	-0.01893	-0.01893	-0.01893	-0.01893	-0.01893	-0.01893	-0.01893	-0.01893	-0.01893	-0.01893
trough 2nd	-0.0181	-0.0181	-0.0181	-0.0181	-0.0181	-0.0181	-0.0181	-0.0181	-0.0181	-0.0181	-0.0181	-0.0181	-0.0181	-0.0181	-0.0181

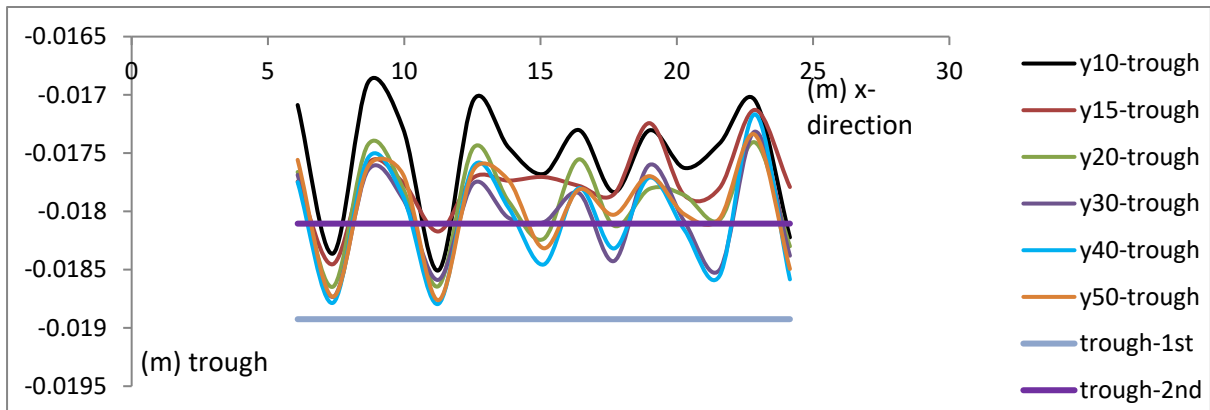


Figure 82 Comparison of trough elevation between simulations and analytical methods, for y-meshes

The coarser meshes (10 & 15 meshes per wave height), showed hints of numerical dissipation (Figure 82). Showing similar traits as the earlier Figure 80, the numerical simulation seems to stabilise finer mesh of at least 20 meshes per wave height.

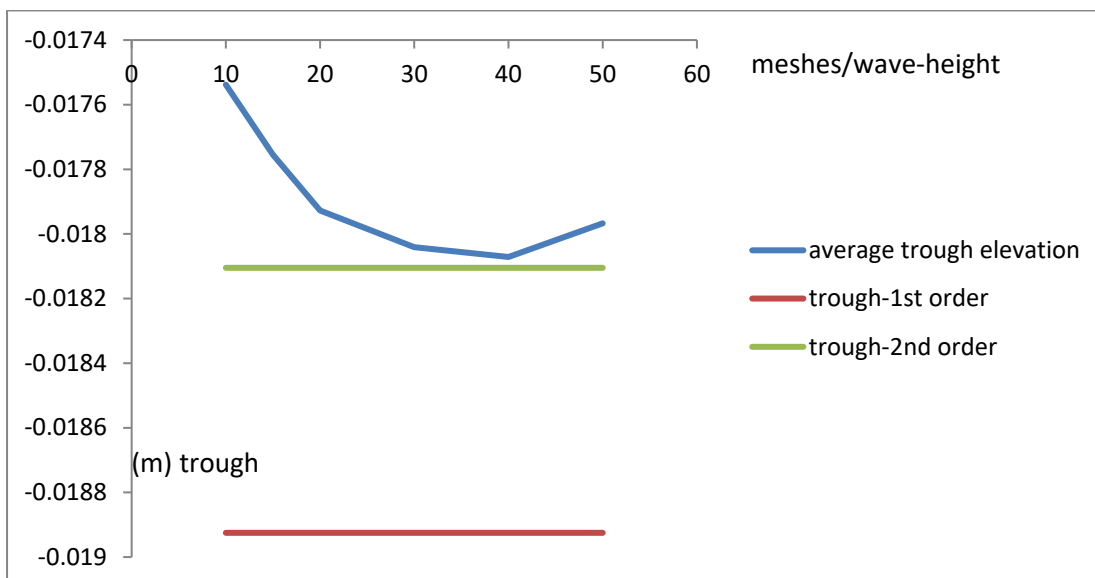


Figure 83 Comparison of averaged trough elevation between simulations and analytical methods, for different amount of y-meshes per wavelength

Numerical simulations of coarse mesh registered a steeper increment of trough depth; from 17.53mm to 17.92mm for 10meshes and 20meshes simulations. Subsequently, a much gentler increment till it reaches 18.07mm trough at 40meshes simulation, just a 0.15% simulation difference from the 2nd order effects. However, the finest mesh simulation; 50meshes, seemed to be recording

a shallower trough than the coarser mesh simulations (Figure 83). Crossing out increased numerical dissipation for the 50meshes simulation, it seems to suggest that this numerical simulation could be capturing higher order of trough elevations (higher-order Stokes Theory for trough is always associated with shallower trough). Capturing higher orders of Stokes Theory in the finest mesh simulation is also seen in previous Figure 81.

Table 10 Comparison of wave height elevation, for wave probes located from $6.09m < x < 24.15m$, for y-meshes ranging from 10 to 50 per wave height

probes	6.09	7.38	8.67	9.96	11.25	12.54	13.83	15.12	16.41	17.7	18.99	20.28	21.57	22.86	24.15
mesh-y															
10	0.036845	0.036817	0.036591	0.036177	0.03739	0.037346	0.035896	0.036013	0.037961	0.036182	0.035898	0.038238	0.035192	0.035815	0.03818
15	0.03755	0.037378	0.037644	0.036964	0.0372	0.037881	0.036559	0.036612	0.037872	0.036664	0.036034	0.037559	0.036669	0.035865	0.037115
20	0.037727	0.037503	0.037475	0.037163	0.037773	0.037904	0.036828	0.037283	0.038205	0.036891	0.037033	0.03835	0.03663	0.036709	0.038303
30	0.037773	0.037655	0.037967	0.037371	0.037579	0.038683	0.037133	0.037012	0.038853	0.037452	0.036706	0.038684	0.037465	0.036605	0.03832
40	0.037979	0.037856	0.037863	0.037409	0.038061	0.038329	0.036986	0.037754	0.038735	0.037244	0.036879	0.038921	0.037797	0.036404	0.038665
50	0.037943	0.03787	0.03802	0.037297	0.038114	0.038484	0.036832	0.037639	0.038901	0.037035	0.037074	0.038933	0.037064	0.036842	0.038786
height 1st	0.03785	0.03785	0.03785	0.03785	0.03785	0.03785	0.03785	0.03785	0.03785	0.03785	0.03785	0.03785	0.03785	0.03785	0.03785
height 2nd	0.03785	0.03785	0.03785	0.03785	0.03785	0.03785	0.03785	0.03785	0.03785	0.03785	0.03785	0.03785	0.03785	0.03785	0.03785
height 3rd	0.037864	0.037864	0.037864	0.037864	0.037864	0.037864	0.037864	0.037864	0.037864	0.037864	0.037864	0.037864	0.037864	0.037864	0.037864

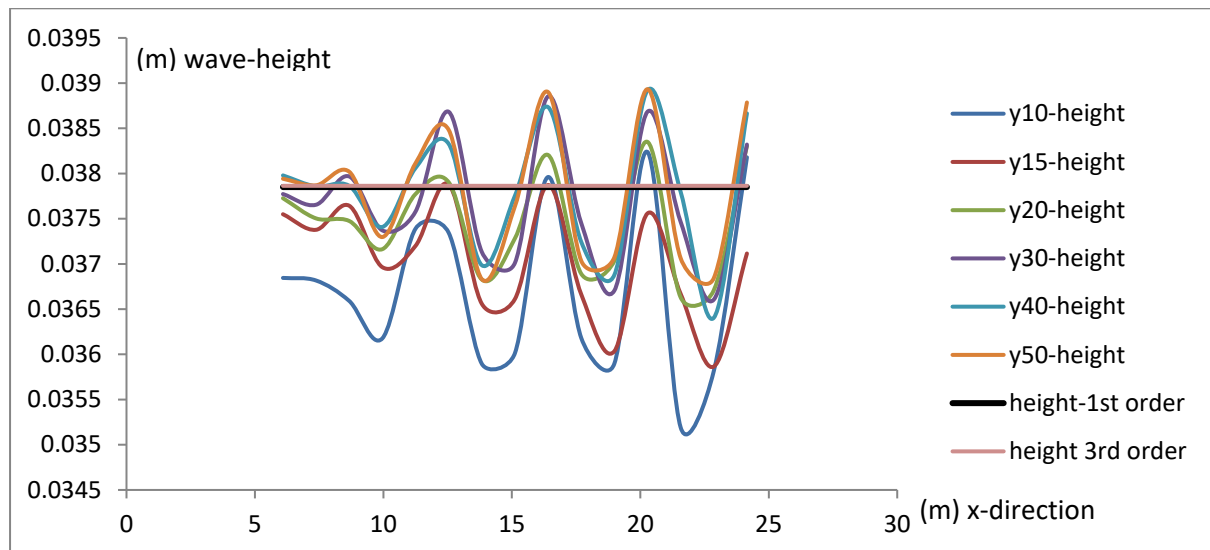


Figure 84 Comparison of wave height elevation between simulations and analytical methods, for y-meshes

Figure 84 shows obvious numerical dissipation for the coarser mesh simulations; 10meshes and 15meshes. The 30, 40 and 50meshes simulation seemed to be agreeing with each other, hinting a convergence at 30meshes per wave height.

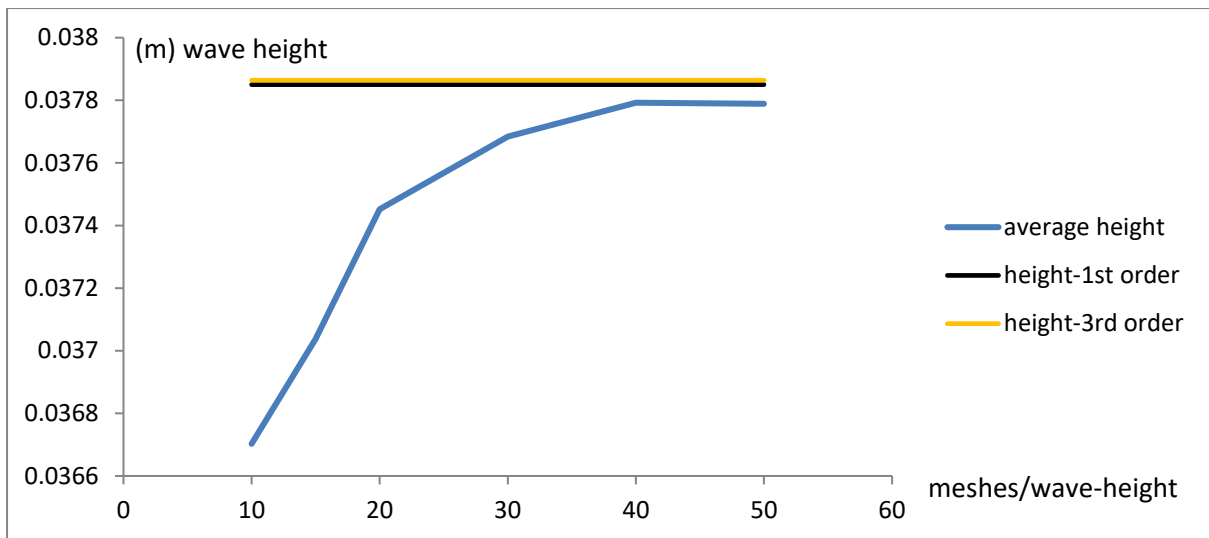


Figure 85 Comparison of averaged wave height between simulations and analytical methods, for different amount of y-meshes per wavelength

Echoing earlier findings (Figure 81 & Figure 83), the wave height experienced a relatively steeper slope increment from 36.7mm to 37.45mm; from a 10mesh to a 20mesh simulation. However, the wave height starts to experience a gentle slope increment from 37.45mm to 37.8mm; from a 20mesh to a 40mesh simulation, and plateau at the 40mesh simulation (Figure 85). Earlier higher-order effects; increased crest elevation and shallower trough(Figure 81 & Figure 83), cancels off each other higher-order contribution, resulting in the same wave height elevation for the 50mesh simulation.

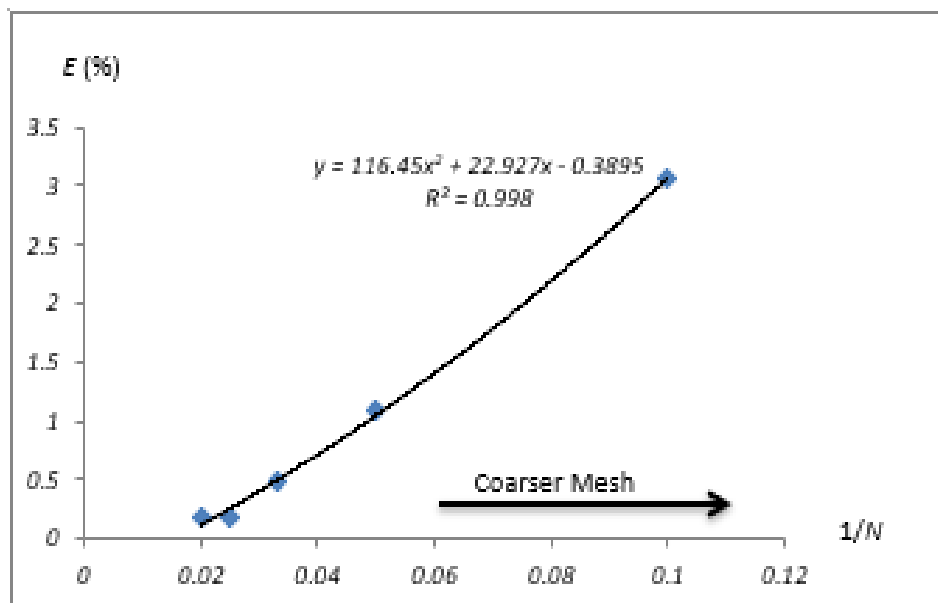


Figure 86 Error margin mesh sensitivity test for different y-axis mesh simulations

Figure 86 shows the numerical error between simulations and analytical reduces as the numerical meshes become finer. Simulation error starts converging from the 30mesh simulation, registering an error margin of about 0.5%.

6.5 Relaxation Zone

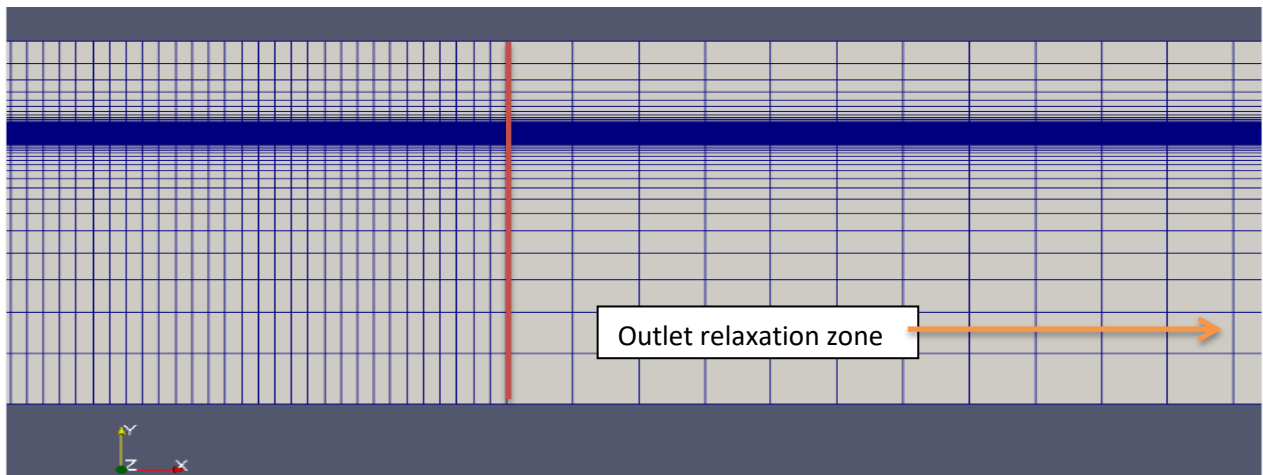


Figure 87 x-y plane of numerical tank with outlet relaxation zone

Outlet relaxation zone is set as $30\text{m} > x > 35.2\text{m}$ (Figure 87). This is 1.3 times the length of the longest wave. To aid the wave relaxation, coarser meshes were used in the outlet relaxation zone, enabling numerical dissipation. Also in the relaxation zone, an explicit relaxation approach is utilised (Niels Gjøøl Jacobsen, 2012);

$$\Psi = (1 - \omega R) * \Psi_{target} + \omega R * \Psi_{computed} \quad (55)$$

ωR is the weight distribution for the above Equation 55, is a function of the shape of the relaxation zone and their associated coordinates.

Bichromatic waves were simulated with the purpose to test for the effectiveness of the relaxation zone.

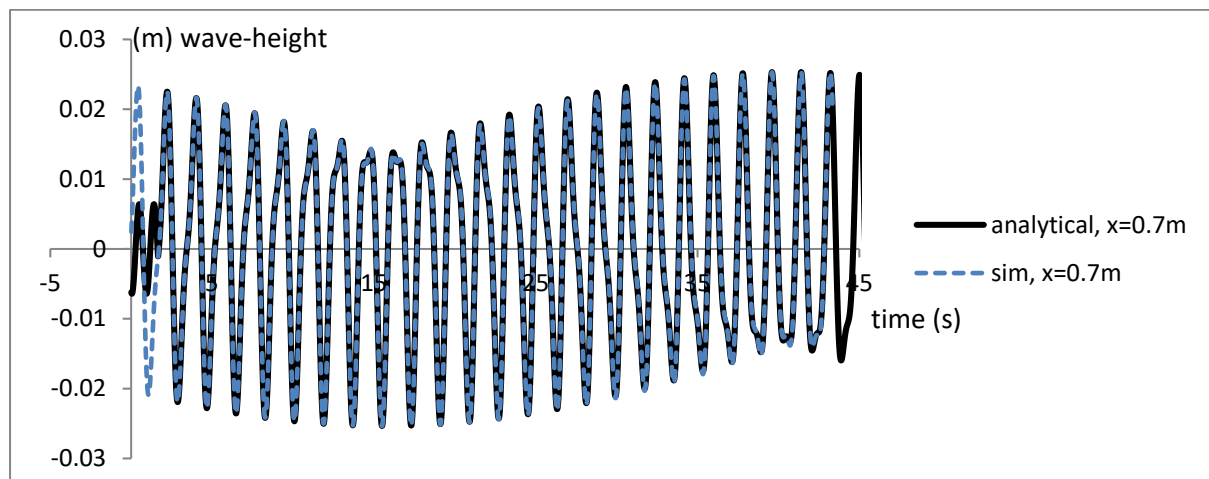


Figure 88 Comparison of simulation and analytical results, waveprobes located at $x = 0.7\text{m}$

Waveprobes were installed right after the wavemaker. The purpose of Figure 88 is to investigate the error margin of the wavemaker. Less the initial disturbance and generation of waves, involving the initial propagation of waves; a phenomenon not taken into consideration by the analytical solution, the error margin of both solutions is negligible.

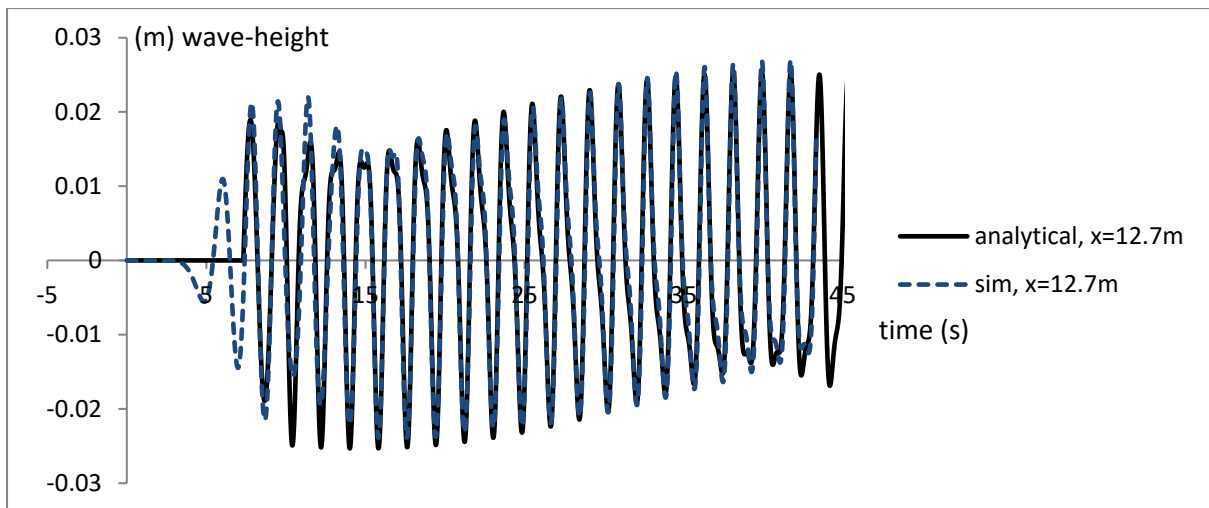


Figure 89 Comparison of simulation and analytical results, waveprobes located at $x = 12.7\text{m}$

Figure 89 shows the wave elevation time history at location $x = 12.7\text{m}$. The threat of rebounding waves is negligible from the above data. Hence, at the actual focal point of $x = 9\text{m}$, there is no threat of rebounding waves for the simulation study.

6.6 Wave Set ups

In the experimental work conducted at Newcastle University, Wind, Wave and Current tank. As explained in detail earlier (4.3 Wave Parameters), the simulation work would mimic the experimental wave parameters.

Table 11 Wave Package parameter

Wave type	Irregular
Spectrum	JONSWAP
N	113
T_p	2s
gamma	3.3
depth	1m
Phase method	Focusing Phase
Focus time	35s
Focusing point (m)	(9 0 0)
H_s	0.081m
f_{low}	0.25Hz
f_{high}	2Hz

Table 11 tries to mimic the actual wave conditions used in the experimental setups. Peak frequency was chosen as $f_p = 0.5\text{Hz}$; or in this case $T_p = 0.5\text{s}$. Focal location is set as $x = 9\text{m}$, same as described in the experimental setups.

6.7 Mesh Set ups

Meshes were modelled after the Wind, Wave and Current tank used in Newcastle University. The function 'snappyHexMesh' were used to aid the mesh generation and refinement. A 'refinement Box' was added, covering the span around the free surface to aid further mesh refinement. A 'refinement cylinder' was also placed surrounding the cylinder of interest. This 'refinement cylinder' would further refine meshes within a predefined radius from the cylinder midpoint.

Wave probes were placed from $5.49\text{m} < x < 8.99\text{m}$, with $\Delta x = 0.25\text{m}$.

60 cores were used for the simulation work. Instead of splitting the cores by the traditional 'simple method'; a method that allocates resources by dividing the 3 axes by the allocated numbers. A (2 2 1) input, would have divided the resources into 4 parts, 2 at the x-axis, 2 at the y-axis, and the z-axis to remain intact. One major flaw with the simple method is, it would slice the entire numerical tank spatially equally; e.g. for a numerical wave tank of 9m, to be cut into 3 sections would be cut equally at the 3m & 6m mark; regardless of the biasness of the mesh distribution.

In this numerical case, most of the meshes were concentrated near the cylindrical (at the x-axis), and near the free surface level (for the y-axis). Hence, using the simple method for this case would result in an uneven resource distribution; cores allocated near the free-surface might be dealing with too many meshes, and cores allocated near the numerical tank bottom might be dealing with possibly just a few hundreds of meshes.

The scotch method (Niels Gjøøl Jacobsen, 2012) is a more preferred method in this case, as it will split the cores accordingly to a similar amount of mesh to discretise, boosting efficiency.

6.8 Simulation cases

5 simulation cases were set up, mainly involving cylinders with 2 types of geometrical cross-section; 1 involving a 315mm diameter circular cylinder and another is a square cylinder as used in an experimental test case. For the square cylinder, 4 simulation cases were used. The default square cylinder case with no(0) angle of twist along the vertical axis, and with 3 other simulation cases, but with 15, 30, and 45-degree angle of twist. As discussed in earlier experimental work that the flat walled square cylinder (with no angle of twist) gave the highest impact slamming load, and the geometrical cross-section of the structures play a significant role in predicting the slamming load. It would be interesting to investigate the bi-directional slamming force contribution of these simulation cases.

7 Results and discussions

7.1 Simulations Results

The numerical simulations were post-processed. One key advantage that the numerical simulation post-processing has over the experimental work is the flexibility of the OpenFOAM to manipulate the representation of data. There is freedom to manipulate and define the 'alpha-water' or known as ' α ' as typically 0.5 to represent the free surface as shown in below Figure 91. There is also flexibility to present the visual data in forms of extremities ' α ' = 0 for air phase, and ' α ' = 1 for liquid phase as shown in Figure 92 or present the visual data in forms of vectors (Figure 93) from the OpenFOAM 'glyph' function. However, one of the main disadvantages of this data representation of OpenFOAM, especially for this PhD project or other projects that requires a very fine time step, is the vast amount of data storage space needed. For this PhD project, nearing the crucial time (t_b) and in order to capture the breaking wave kinematics, loadings, visualisations; a time step as low as $t = 0.005$ second was used. Easily few hundred gigabytes of data were stored for just one simulation case. It is highly advisable to separate purchase an external hard disk drive (HDD) for the simulation works.

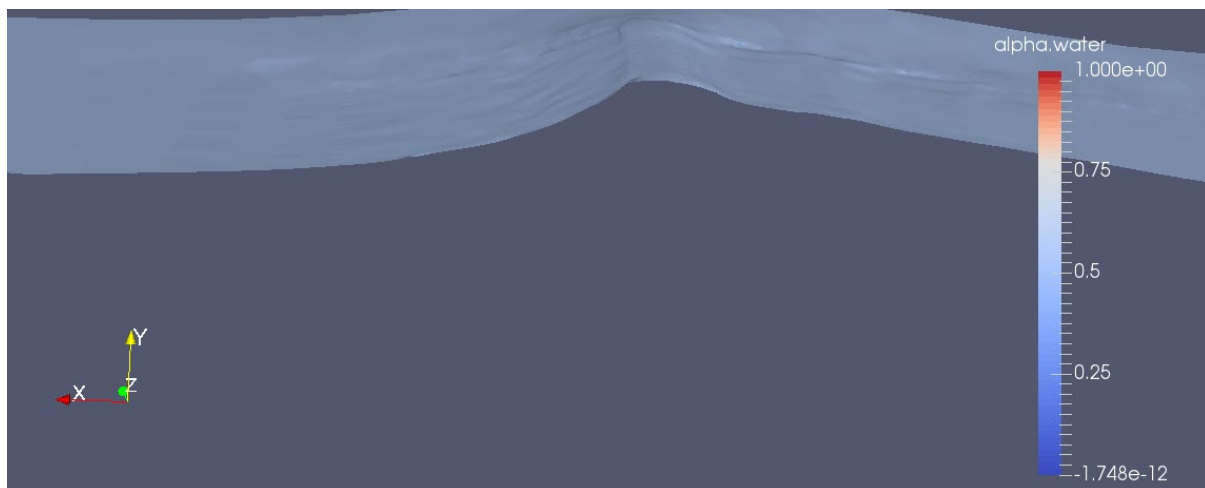


Figure 90 Early Jet formation at $t = 34.5s$, $f_p = 0.5Hz$ (wave propagation from right to left)

Figure 90 showed the early jet formation occurring at $t = 34.5s$, 0.5s before the actual focal point.



Figure 91 Early indication of formation of jet (using alpha_water representation), a red rectangle box is placed at $x = 9m$ for visualization purpose

White splash could be seen forming, approaching the focal point. This shows that the volume fraction near the crest level is between 0 to 1, indicating a two-phase mix at the white splash region.

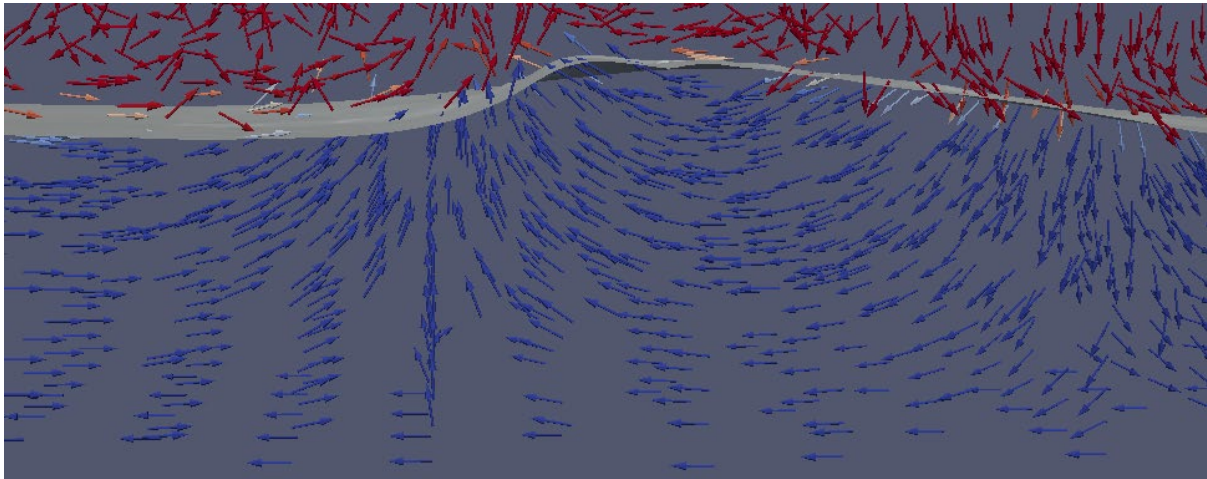


Figure 92 Early jet formation, with vectors

Figure 92 shows the vectors indicating the direction of the jet propagation. Above figure shows that the vectors were pointing slightly upwards before having a protruding jet and allowing it to collapse with the aid of gravity. Above figure also shows that nearing the focal point, there is a bi-axial flow leading towards breaking.

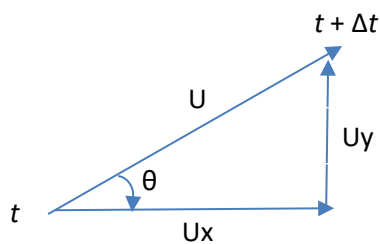


Figure 93 Velocity vectors

The wave profile leading towards breaking would have bi-axial direction kinematics (Figure 93), however, for the inline slamming load contribution, we would be keen in the inline wave kinematics.

7.2 Simulation Kinematic Findings

On the square cylinder, 10 probes were placed to record the 3-axis wave kinematics. The cylinder was placed at $x=9\text{m}$, with $x=0\text{m}$ located at the wave paddle. And probes were placed at 2 horizontal location, $x=8.74\text{m}$ and $x=8.99\text{m}$ respectively (Figure 99). Previously, the probes placed at $x=9\text{m}$, but weren't able to obtain a reading due to clashes with the cylindrical structure.

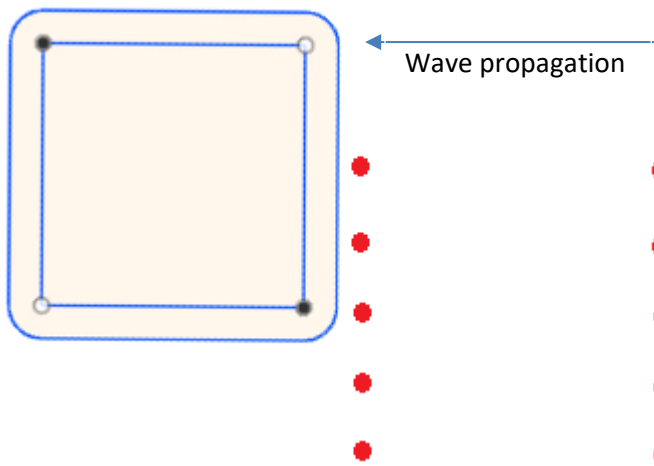


Figure 94 Placement of probes for square cylinder simulation case

The probe will also capture the Volume Ratio (J), also known as 'alpha_water' of the profile. Previous experimental work, unable to capture the plunging breaking kinematics upon impact due to the physical constraint of the ADV. It is also impossible to place ADV due to possible physical interference of the propagating wave.

OpenFOAM has been relatively advantageous in this aspect, allowing to place infinite (resource allowing) the number of probes for analytical purpose. 2 key contributions of the slamming force are both the inline plunging wave kinematics and also the impacted area of slamming on the cylinder (Figure 95 & Figure 96).

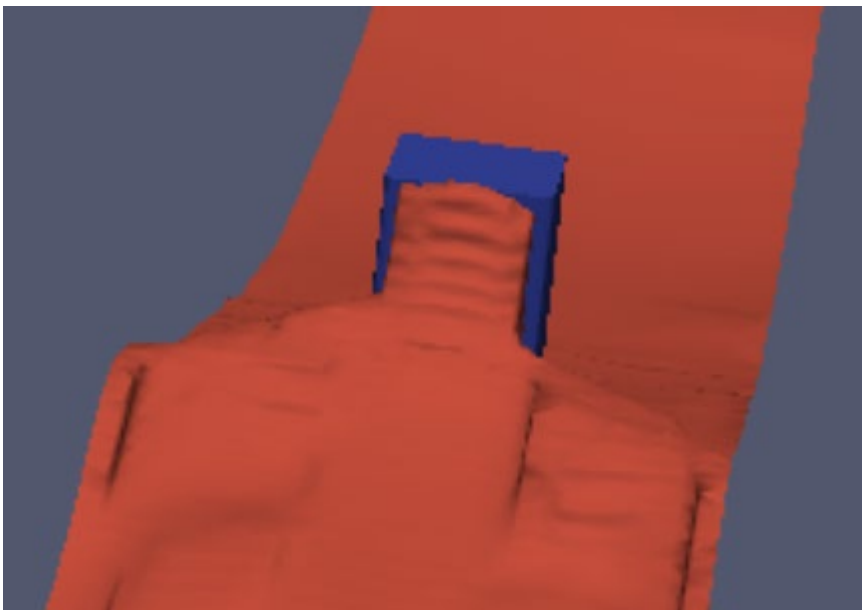


Figure 95 Initial impact of plunging breaker on square cylinder – simulation

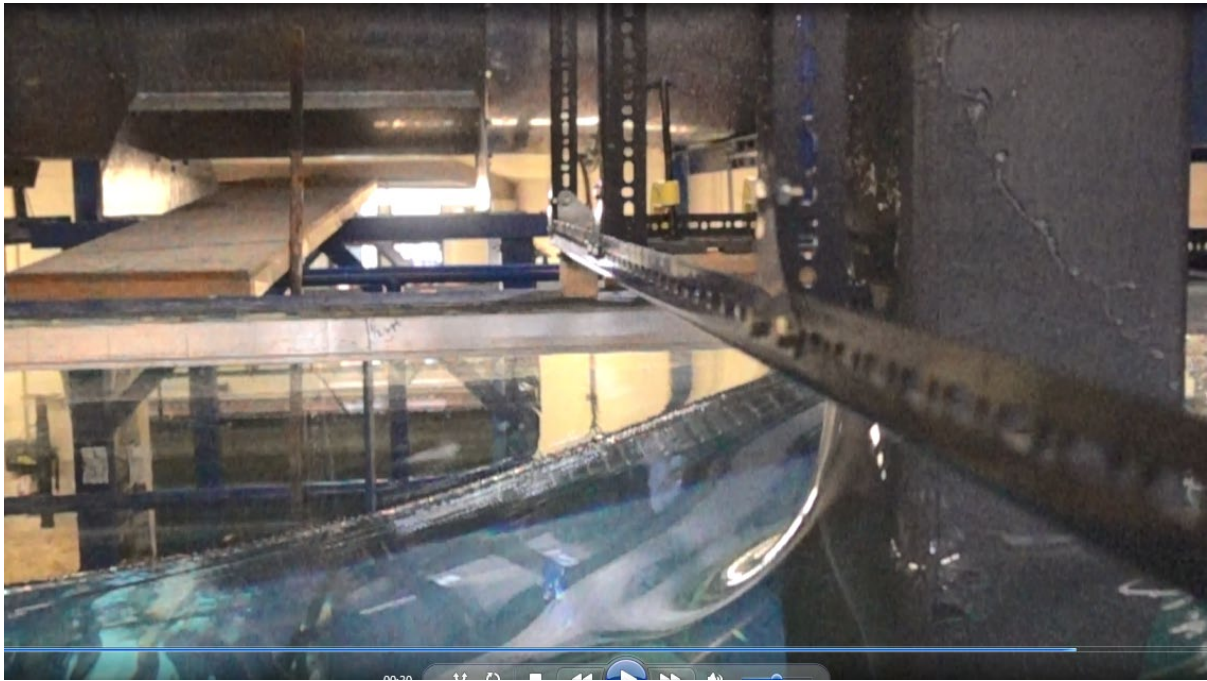


Figure 96 initial impact of plunging breaker on square cylinder – experimental

Plunging breaking kinematics at impact, derived from the simulations showed an inline kinematic of approximately 0.2m/s on the cylinder. This would have hinted that the contributory inline force of the plunging wave run-up is negligible, and with the entrainment of the air bubbles between the plunging jet nose and the re-entry of the free surface the main culprit of the slamming impact loadings.

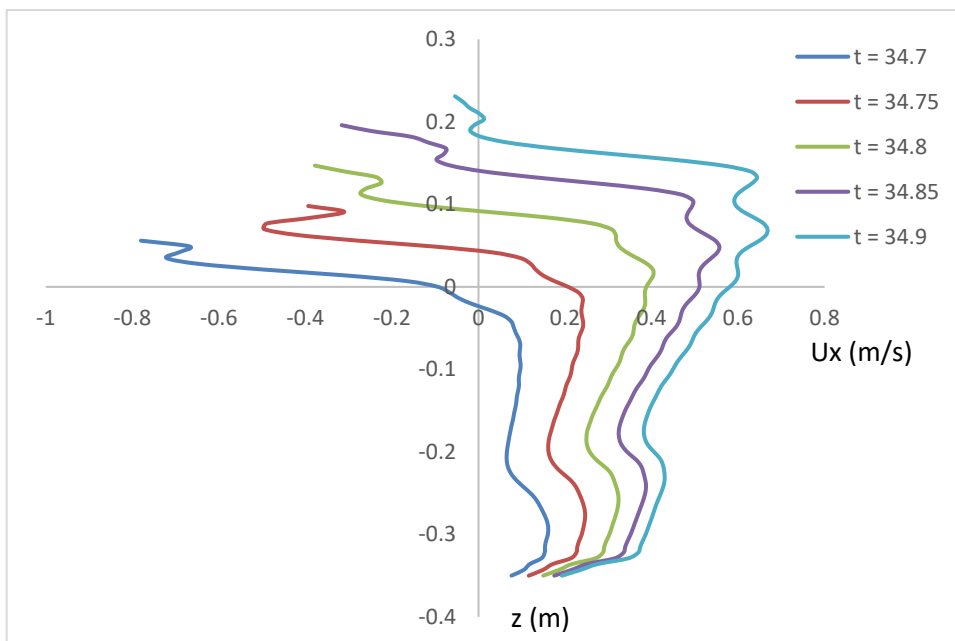


Figure 97 Plunging wave kinematic profile at $x = 8.99\text{m}$, horizontal wave kinematics

Figure 97 shows the horizontal wave kinematics leading to breaking at the intended focus time of $t = 34.9\text{s}$. With $z = 0\text{m}$ located at the free surface level, the above figure gives an insight into the wave kinematics at different elevations. From $t = 34.7\text{s}$ onwards, towards the crest, there is an increased horizontal wave velocity. As t approaches $t_B = 34.9\text{s}$, the differential of the kinematics from the crest of the wave profile, increased dramatically.

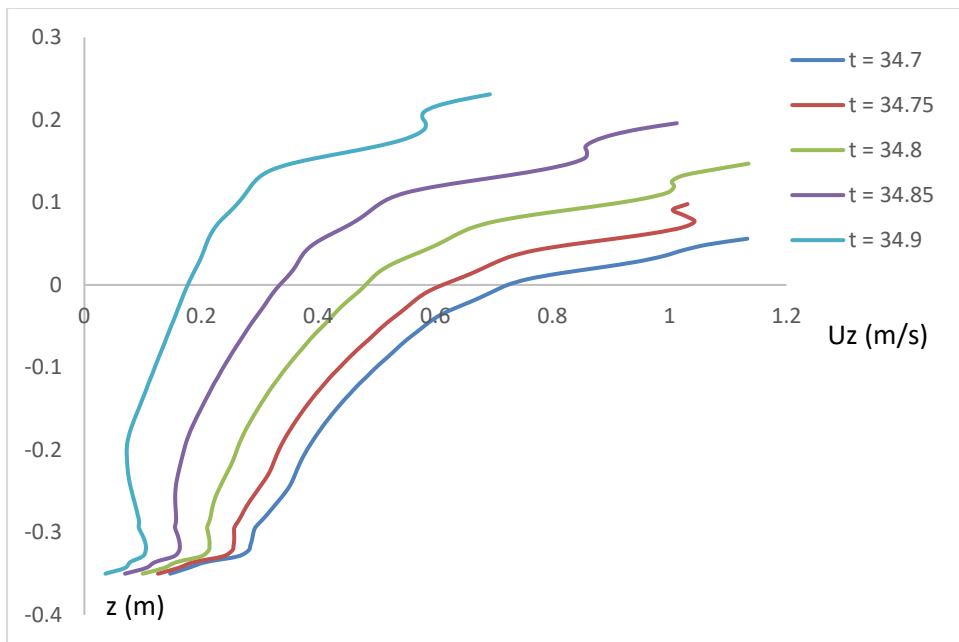


Figure 98 Plunging wave kinematic profile at $x = 8.99\text{m}$, vertical wave kinematics

In the early stages of plunging breaking, during the formation of the plunging jet nose, the jet nose kinematics were dominated by the downwards velocity (Figure 98). However, at $t = 34.9\text{s}$, the downwards velocity had greatly reduced to as low as 0.6m/s at the crest.

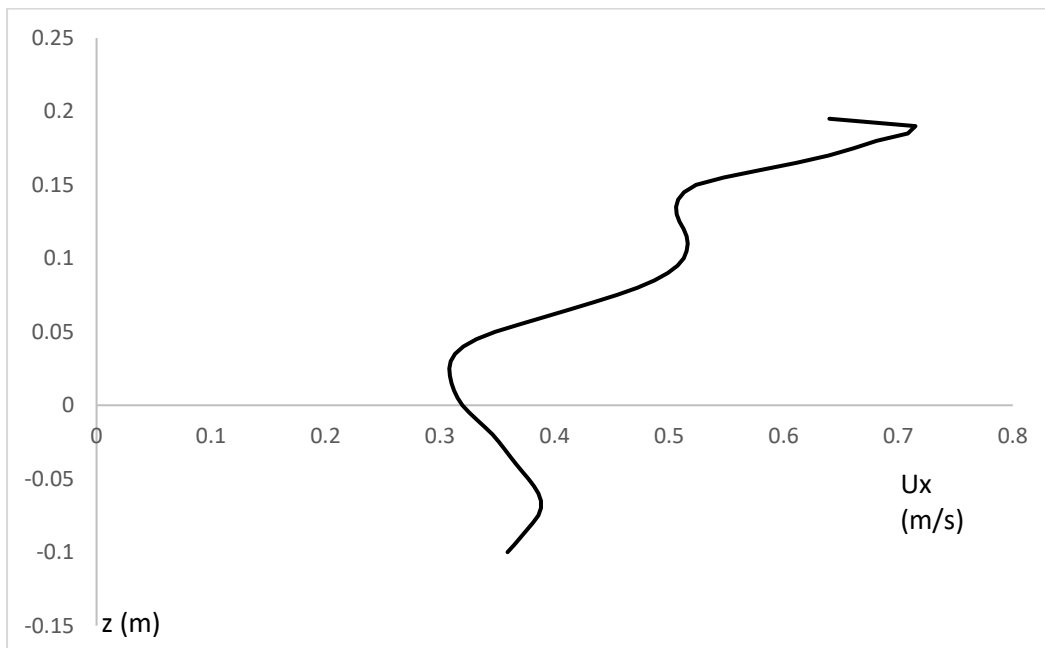


Figure 99 Wave profile kinematic at $x = 8.74\text{m}$, $t = 34.7\text{s}$

One of the common attributes of a plunging breaker is the formation of the plunging jet nose. Earlier chapters (2.3 Kinematic breaking criteria) discussed the kinematic breaking criterion, and that is one of the common understanding regarding the phenomenon leading up to breaking is, the formation of the plunging jet nose. Just before the stipulated focal point ($x_B = 9\text{m}$), Figure 99 shows early signs of wave breaking, and the above figure shows obvious discrepancies in kinematics near the crest and at elevations towards the free surface levels. This huge kinematic discrepancy aided the initial formation of the plunging jet nose near the crest and subsequently allowing the plunging jet nose to collapse with the aid of gravity.

7.2.1 Possible buffed body diffraction effects on wave kinematics

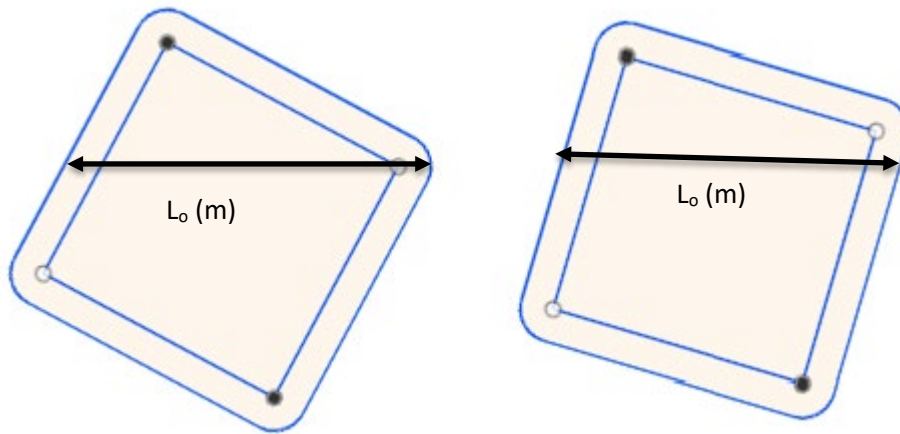


Figure 100 Characteristic length for different angle of twist

Cylinders with similar geometrical cross-sections, albeit with a different angle of twist, would give different characteristic length (L_o). This might in return, affect the kinematics leading up to plunging wave impact, in return, also affecting the slamming load contribution. For the square cylinder with 4 different angles of twist $0 \leq \theta \leq 45$. The characteristic length for the above cases ranges from as low as 200mm to 274.56mm for the cylinder case with $\theta = 45$ degrees.

Previous cases for the square cylinder with no angle of twist, the probes were deliberately placed 0.01m away from the cylinder at $x = 8.99\text{m}$ to attempt to capture the kinematics during impact. For the simulation cases involving $\theta = 15/30/45$ degrees, to imitate the similar setups used in earlier cases. The probes were also placed just 0.01m away from the twisted cylinder. However, for probes placed 'before' the impact zone, was unchanged at $x = 8.74\text{m}$ for all simulation test cases.

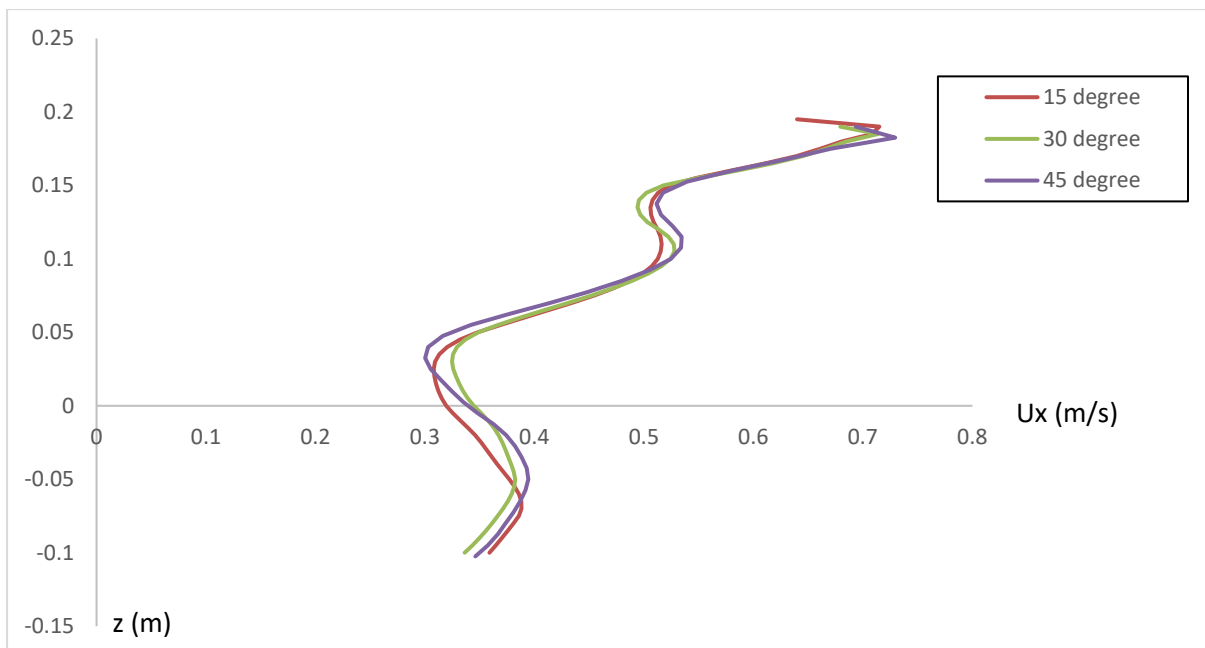


Figure 101 Wave profile kinematic for $\theta = 15, 30, 45$ degrees, at $x = 8.74\text{m}$, $t = 34.7\text{s}$

From earlier (Figure 101), it is shown that the second cylindrical case involving different angle of twist along its vertical axis. Above figure shows that the propagating breaking wave horizontal

velocity, just before impacting, $x = 8.74\text{m}$, $t = 34.7\text{s}$, exhibits very similar kinematics with all 3 cases. The maximum was registered at $z = 182.5\text{mm}$ to 190mm , registering a peak velocity of 0.7 to 0.72ms^{-1} . Such differential of horizontal wave kinematics between the crest and the lower region encourages the formation of a jet nose at the crest and finally forming a plunging breaker.

7.2.2 Kinematic comparison between experimental and numerical work

Table 12 Kinematic of plunging waves during breaking, by elevation. Experimentally obtained values at $x = 8.99\text{m}$

z/t	34.75	34.8	34.81	34.82	34.83	34.84	34.845	34.85	34.9	34.95
-0.08	0.307	0.361	0.372	0.384	0.394	0.401	0.405	0.408	0.415	0.381
-0.05	0.351	0.455	0.473	0.487	0.499	0.507	0.510	0.513	0.502	0.445
-0.02	0.300	0.399	0.412	0.427	0.445	0.464	0.473	0.480	0.476	0.414
0.01	0.316	0.432	0.414	0.394	0.392	0.392	0.393	0.399	0.609	0.543
0.04	0.303	0.488	0.529	0.566	0.601	0.635	0.649	0.660	0.592	0.499
0.07	0.270	0.584	0.612	0.631	0.646	0.660	0.666	0.669	0.602	0.542
0.1	-0.133	-0.099	0.270	0.610	0.854	0.978	0.999	0.998	0.726	0.354
0.13	0.044	0.450	0.634	0.796	0.909	0.961	0.967	0.960	0.690	0.019
0.16		-0.306	-0.299	-0.137	0.155	0.501	0.666	0.811	0.108	-0.427
0.19			0.086	0.210	0.279	0.269	0.233	0.180		

The above Table 12 shows the kinematic profiles leading to breaking and post-breaking for varying surface elevations. The leftmost most column indicates the z (m, free surface) and the top row indicates the t (s); the highlighted datum indicating the time of breaking, t_b . The above table shows that at the moment just before breaking, $t \rightarrow 34.85\text{s}$, $34.84\text{s} \leq t \leq 34.85\text{s}$, there were negligible change of velocity profiles at most surface elevation; less for the $z = 0.16\text{m}$ and $z = 0.19\text{m}$. This would further validate Figure 43 earlier findings and also the linear wave theory, that at the occurrence of maximum velocity, acceleration is 0, or negligible.

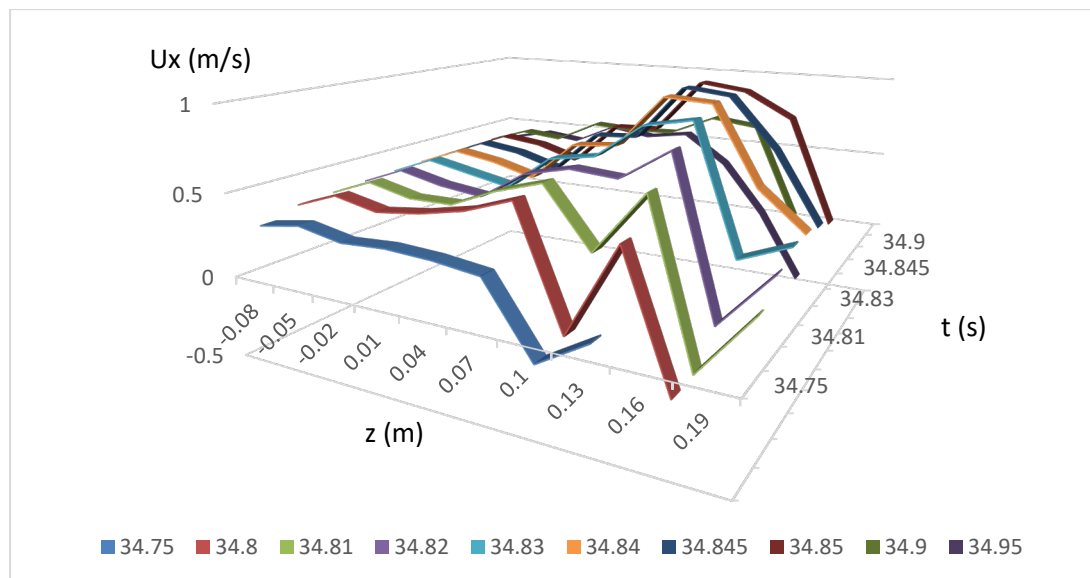


Figure 102 tri-axial representation of kinematics. Horizontal axis (-0.08m to 0.19m) representing surface elevation, Transverse axis (34.75s to 34.9s) representing time, Vertical axis (-0.5ms⁻¹ to 1ms⁻¹) representing velocity (experimental data)

Figure 102 shows a bird eye view of the kinematic behaviour with respect to both time and elevation. It is evident that the maximum inline velocity occurs towards the focal time ($t_b = 34.85\text{s}$)

and at an elevation just below the crest at $0.13\text{m} \leq x \leq 0.16\text{m}$. The ‘almost’ parallel curves shown by $34.84\text{s} \leq t \leq 34.85\text{s}$, indicate that the velocity remains relatively similar.

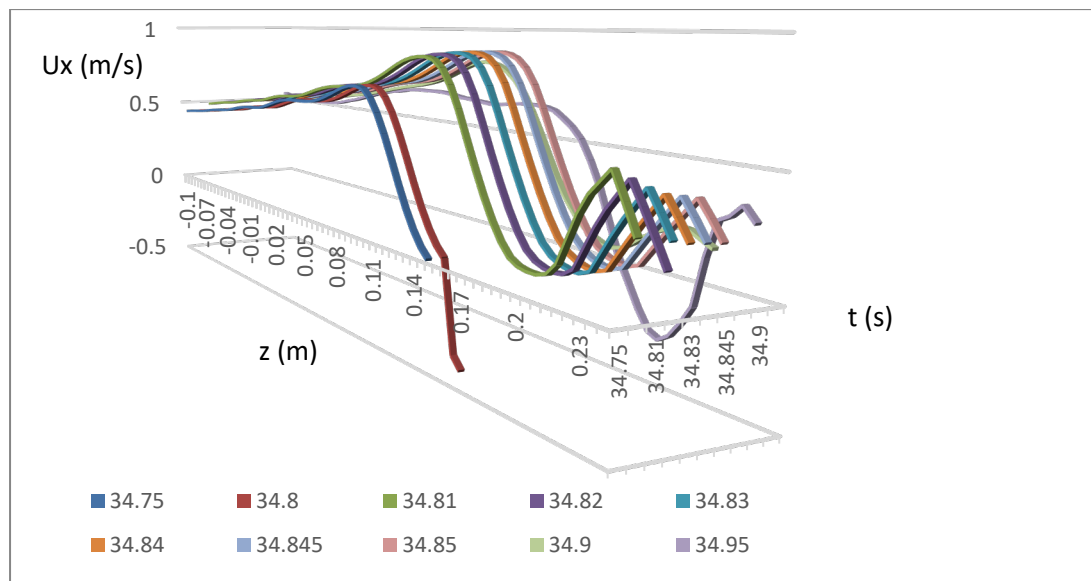


Figure 103 tri-axial representation of kinematics. Horizontal axis (-0.1m to 0.23m) representing surface elevation, Transverse axis (34.75s to 34.9s) representing time, Vertical axis (-0.5m/s^1 to 1m/s^1) representing velocity (simulation data)

Above Figure 103 trying to show similar kinematics wave profile, using numerical solution representation. The numerical solution strikes a good agreement with the experimental solution, such that, parallel fitting curves were observed for the few time step leading to the focal point, $t \rightarrow 34.85\text{s}$, suggesting that acceleration were minimal spanning across entire surface elevation recorded. In the experimental case, it could be seen that inline velocity was seen picking up till $t = 34.83\text{s}$, before plateauing from $34.83\text{s} \leq t = 34.85\text{s}$. For the numerical solution case, the inline velocity was picking up till $t = 34.81\text{s}$ and plateauing till the focal point, striking a good agreement.

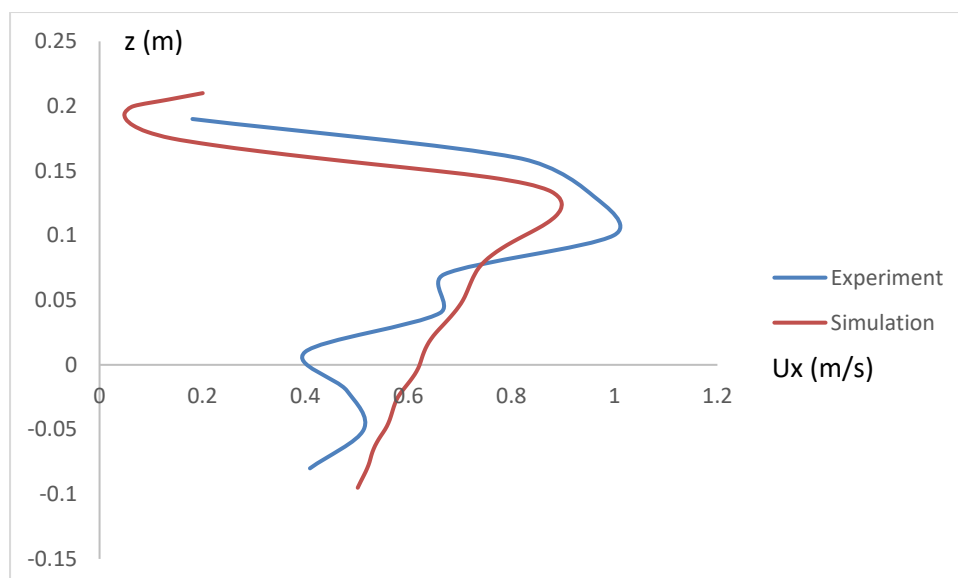


Figure 104 Wave kinematic comparison at focal point (x_B, t_B), experiment vs simulation

Other than a slight offset at the higher elevation level which is possibly the result of numerical errors (will be discussed in 7.3 Comparison between experimental and simulation), both experimental and numerical solutions pointing the maximum inline velocity occurring below the crest and at an

elevation of $z = 0.1$ to 0.12m (Note: The experimental kinematic values were measured having a Δz of 0.03m), and the experimental work recording a maximum inline velocity of 0.99ms^{-1} and the numerical solution recording a maximum inline velocity of 0.9ms^{-1} .

7.3 Comparison between experimental and simulation

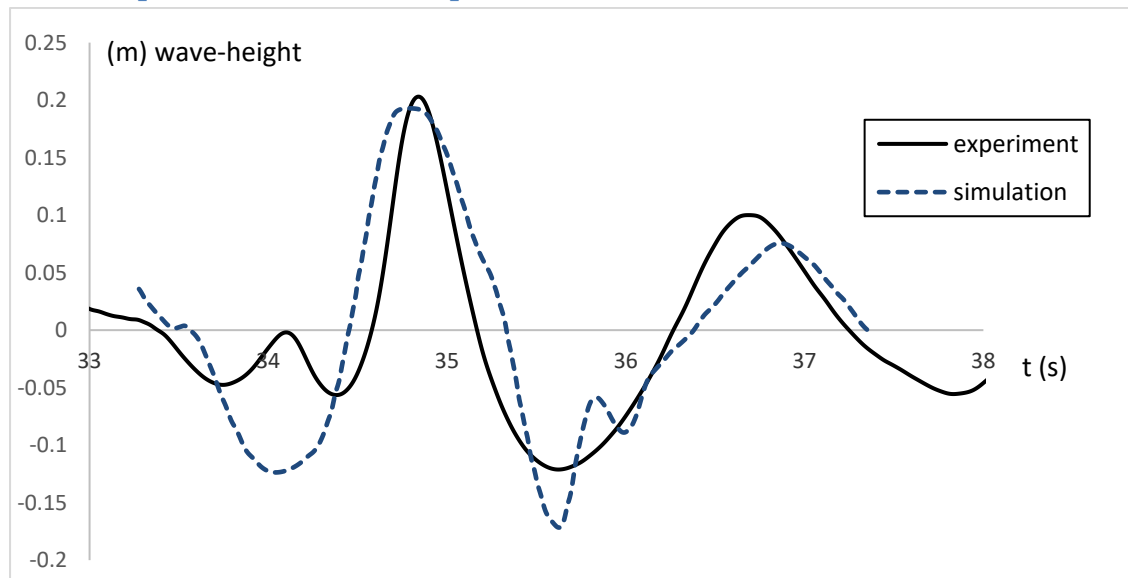


Figure 105 Comparison of wave profile at focal point (x_B, t_B) , experiment vs simulation

The stipulated breaking location (x_B) for both experimental and numerical simulations were indicated as $x_B = 9\text{m}$. As stated and explained earlier (4.2 Equipment and Calibration), the experimental case, would experience signs of breaking slightly before the stipulated focal location. However, this phenomenon of having the breaking wave occurring before the focal location is not repeated in the numerical work.

Above numerical case (Figure 105); with the same experimental setup, achieved an elevation of 192.87mm , as compared with the experimental case elevation of 203mm , a deviation of 4.99% . Previously (6.4 Numerical Calibrations Mesh set up and Sensitivity Test) was able to achieve an even relatively lower simulation error margin. However for this JONSWAP focused wave, (Equation 29 & Equation 33) illustrates both tail ends insignificant contributions to the wave spectra. Whilst it would have been numerically intensive, and resource impossible at this stage to abide by the mesh fineness (6.4 Numerical Calibrations Mesh set up and Sensitivity Test) at both tail ends of the spectrum; however, both tail ends of the spectrum is still essential for a wider spectrum frequency range; often associated with instability and breaking (4.3 Wave Parameters). Earlier experimental work using a lower range of frequency ranges $0.25 \leq f \leq 1.25 \text{ Hz}$, was unsuccessful in creating a breaker, even though, the tail-end of the frequency range from 1.25Hz to 2Hz , were accountable for a negligible amount of the spectra energy.

It is also noted that the trough of the plunging breaker deviates more in the experimental and numerical work; possibly due to the reason explained above. It is noted that the deviations in the trough of the plunging breaker would not be a cause of major concern as ultimately the impact of plunging breaker, the crest and formation of the plunging jet would be the phase of interest. Even though there were some deviations in results recorded between both experimental and numerical

work, however it is noted that the key results (kinematics, loading, crest elevations) have a comfortable low margin of error.

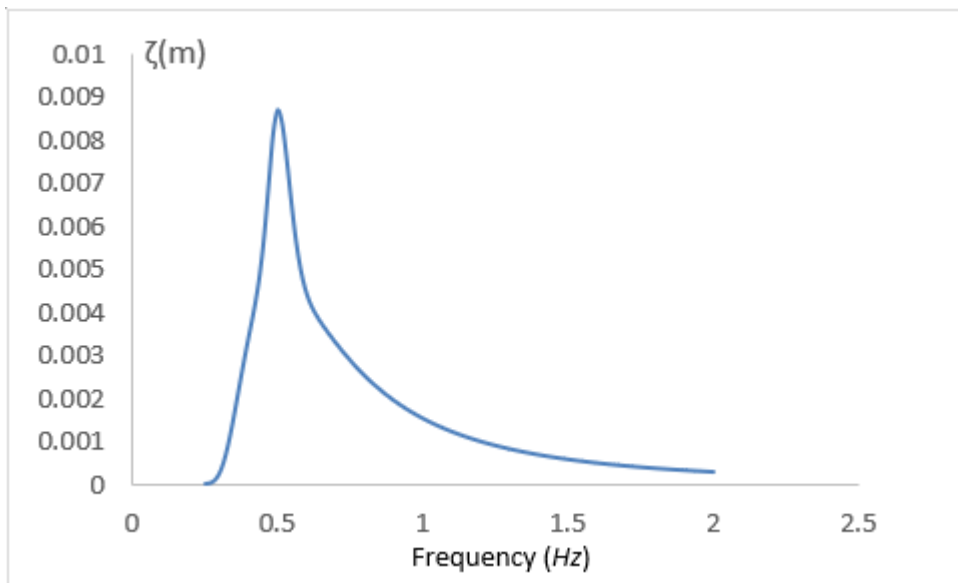


Figure 106 Wave amplitude contribution as a function of frequency, with peak frequency $f_p = 0.5$ Hz

Figure 106 shows the wave amplitude contribution for varying frequency. The summation of the above frequency components will amount to 200.4mm, this means that the experimental case gives a 1% higher total contribution at the focal point. Above figure would have demonstrated that it would be very resource-draining to use a fine mesh to capture the frequency contribution components for $f < 0.32$ Hz, and $f > 1.75$ Hz; or amplitude smaller than 0.5mm. Hence, the above mentioned both tail ends of the frequency spectrum would suffer from numerical dissipation due to the demanding simulation resources otherwise needed.

7.4 Simulation Loadings Findings

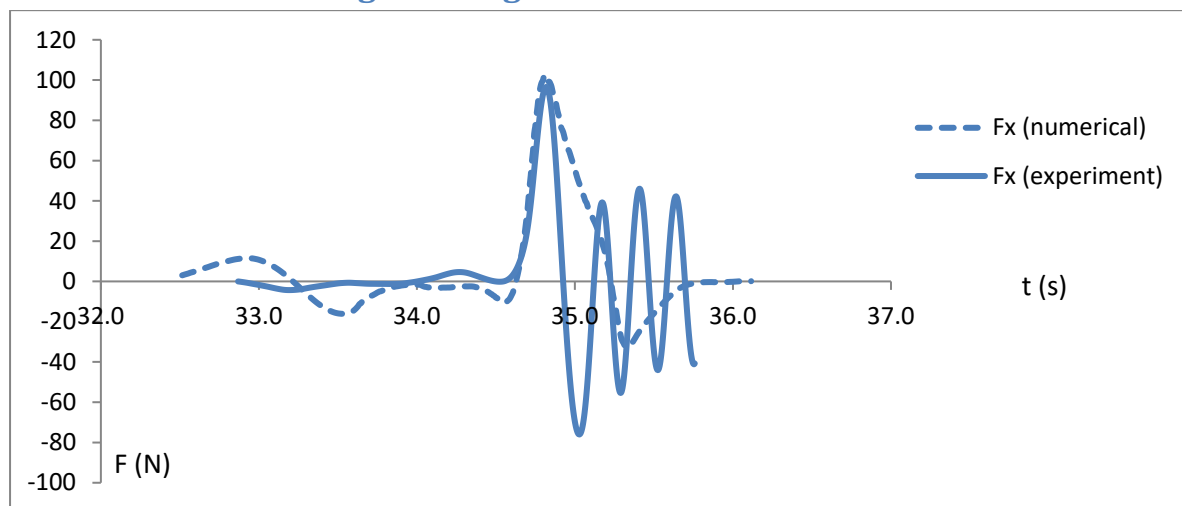


Figure 107 Total Force time history on 315mm circular cylinder during plunging impact, experimental vs simulation case

Both the numerical cases and experimental work seem to agree on the events leading to the actual plunging breaking impact (Figure 107). The numerical case has a force rise time of approximately 195ms, and the experimental work has a force rise time of 270ms. The numerical simulation recorded a peak inline force of 101.9N, a 5% higher than the 96.585N recorded by experimental work.

However, for the experimental work, there are ringing effects after plunging breaker initial impact; as explained in earlier 4.2 Equipment and Calibration, that the cylinder is assumed to be of a simple-free support cantilever on one end. Hence any plunging force decay analysis work, analytical work would have to have relied on numerical work output.

7.4.1 Square Cylinders with Angle of Twist (θ)

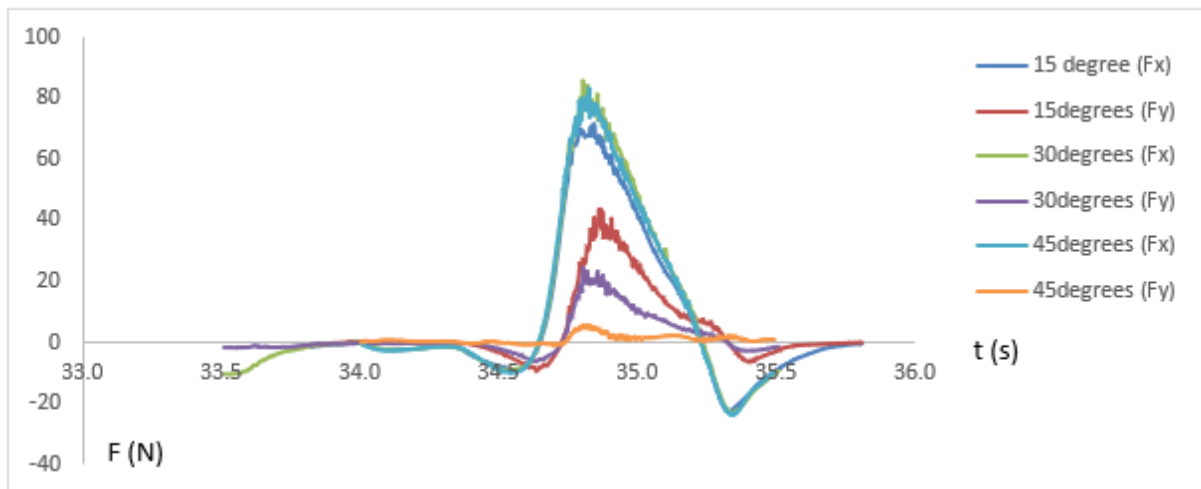


Figure 108 bi-axial Force time history on square cylinders with different θ , simulation case

Figure 108 shows the bi-axial force-time history for the different cylinder test case. It is interesting to note that the test case with a $\theta = 30, 45$ -degree, had the largest inline force. The 30-degree simulation cases registered the largest peak force of 83.71N, edging the 45-degree case by 1%. However, further detailed analysis in the later chapter will be done to account for the difference in impact angle, and different characteristic length/width of the twisted cylinders.

For the transverse force (F_y) axis, the 15-degree simulation case recorded the peak amongst the 3 cases, registering a peak transverse force of 42.8N, or 70% of its peak inline force for the same test case.

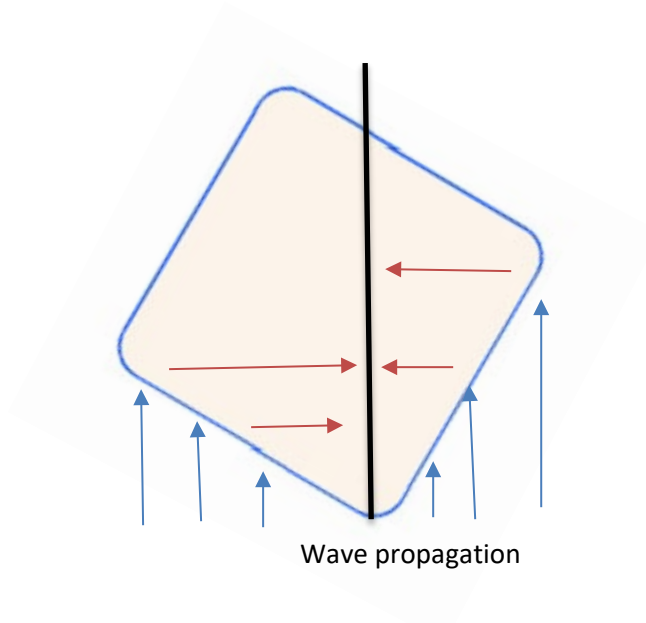


Figure 109 Transverse force contribution (Contributing transverse force indicated by red arrows)

Unlike the inline total force, the transverse force showed a negative correlation between the transverse force and the θ . This could be explained by above force vectors (Figure 109), that when $\theta \rightarrow 45$ degrees, the transverse force will tend to cancel out from both sides. However, it is noteworthy that none of the transverse reading exceeds the inline force to be recognised as a possible breaking wave design problem; as the inline slamming loads supersedes in these simulation cases.

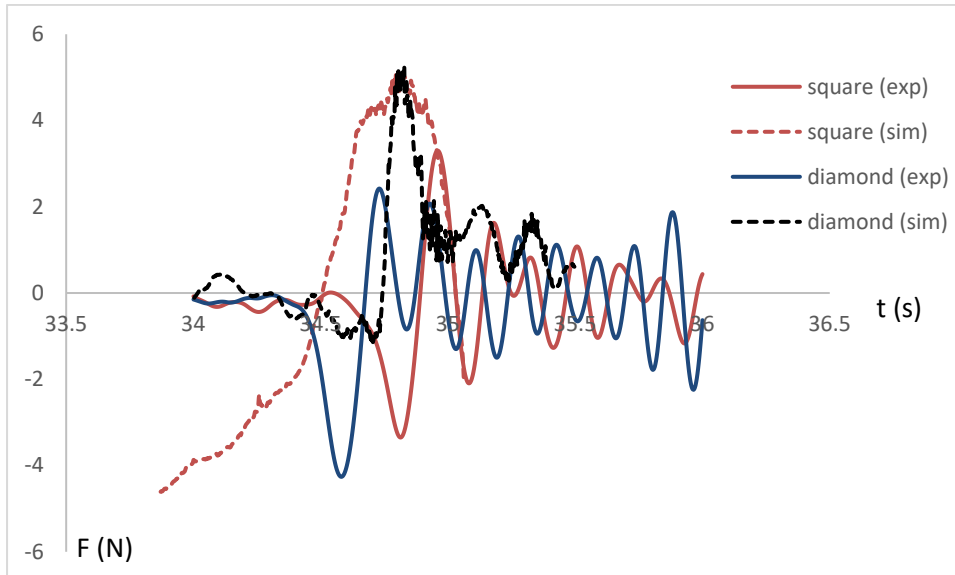


Figure 110 transverse axial force for square and diamond cylinder, experimental and simulation work

The transverse axial force was compared for both square and diamond cylinders for experimental and simulation work (Figure 110). It is shown that the transverse force during plunging impact is negligible as compared to the inline plunging breaking force. Both simulation and experimental cases showed a maximum transverse force of 4-5N, and decay 50% after 2 periods. However, the experimental cases showed prolonged ringing due to vibration effects.

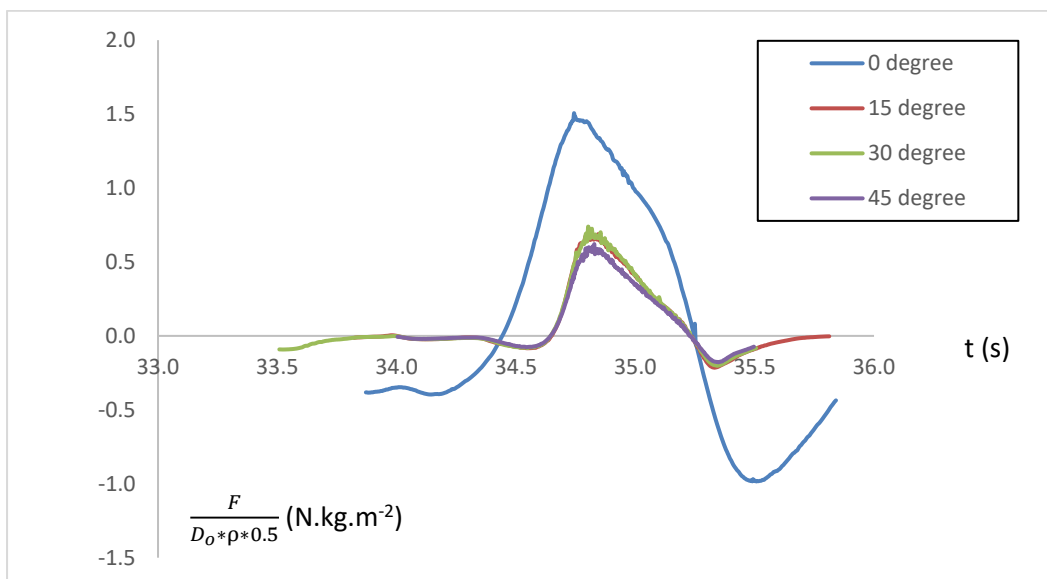


Figure 111 Inline force during plunging, for varying θ , simulation cases

As stated earlier, that even for the same cylinder with cross-sectional profiles, a different angle of twist will give rise to varying effective diameter (Figure 33 & Figure 100). Recalling the drag and

slamming force formula (Equation 2 & Equation 5), the above Figure 111 accounts for the effective width of each different simulation cases, and also the common factors of Equation 2 & Equation 5 were divided from the above figures for comparison purposes.

Taking a cue from earlier discussions (7.2.1 Possible buffed body diffraction effects on wave kinematics) that there are negligible FSI-induced kinematic effects from the above simulation cases with different angle of twist, above Figure 111 shows the resultant slamming impact time history for the different twisting angles.

It is evident that the square cylinder with no twisting suffered the highest maximum force (adjusted to account for effective width). The above figure showed that the square cylinder had a $(\frac{F}{D_o * \rho * 0.5})$ of 1.48, as compared to its nearest rival, both the 15-degree and 30-degree simulation cases of 0.692. The 45-degree simulation case was closely behind the pack with a $(\frac{F}{D_o * \rho * 0.5})$ of 0.568, having the weakest axial forces in both inline and transverse direction. This numerical work shows beyond a 15-degree twisting angle, the inline slamming force seems to plateau, suggesting that even a slight angle of twist, would probably reduce the slamming force by a big margin. Earlier experimental work involving different diameter of circular cylinders (5.2 Loadings results) shows a slight incremental slamming load co-efficient that for a larger diameter circular cylinder (315mm vs 200mm diameter); that has a slightly larger angle of contact (Figure 64). Likewise, for this numerical work, there are the same diminishing effects on using a wider angle of contact (15degree twist vs 45degree twist). It is plausible to derive an argument from both the simulation and experimental work that, a small angle of contact deviation from the 180-degree flat plate square cylinder, is enough to reduce the high-pressure two-phase entrainment during plunging impact. Both experimental and numerical work shows a reduction of 50-60% of the slamming load co-efficient between the square cylinder and the diamond cylinder (also known as, square cylinder with 45-degree angle of twist).

7.5 Slamming Load

Recalling Figure 39 & Figure 57, the wake amplification factor and drag co-efficient could be estimated with the known wave kinematics (respective Keulegan Carpenter number). Recalling Equation 46, the KC formula is a function of wave height (for wave zone, and extracting numerically obtained wave height from Figure 105 to be 315mm; wave height being the trough to the successive critical crest) and characteristic diameter of the cylinder as defined in Figure 55.

Table 13 Resultant drag co-efficient for all 5 individual simulation cases

test	cylinder	D_o	KC	C_D/C_{DS}	C_{DS}	C_D
1	315mm circular	0.315	3.142	0.414	1.2	0.538
2	200mm square	0.2	4.948	0.595	1.3	0.773
3	200mm square + 15 deg	0.2071	4.779	0.578	1.5	0.867
4	200mm square + 30 deg	0.2309	4.285	0.529	1.5	0.793
5	diamond cylinder	0.2663	3.716	0.472	1.5	0.707

The value of C_{DS} was extracted from (Veritas D. N., 2010) (Chapter 5.3)(Figure 52 ~ 55) and multiplied by the semi-empirical formula of the wake amplification factor $(\frac{C_D}{C_{DS}})$ (Equation 39) to obtain the resultant drag co-efficient (Table 13).

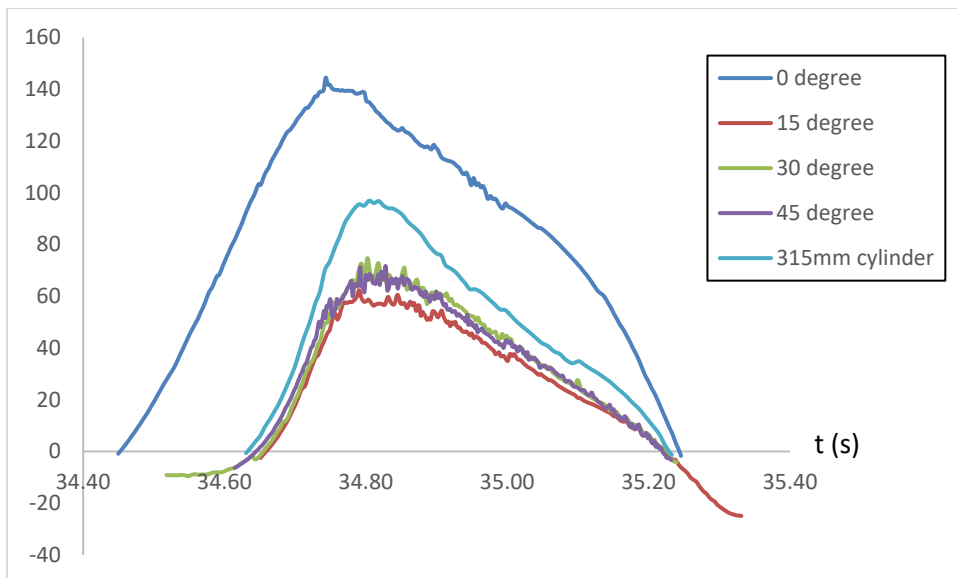


Figure 112 Slamming force time history on circular cylinder, square cylinders with different θ , simulation case

There are huge differences between the default square cylinder ($\theta = 0$ degree) and with other simulation cases involving varying θ . One key observation is the force rise time (from 0 slamming force to peak slamming force) as high as 0.3 seconds for the square cylinder case, and approximately 0.14 to 0.15 second for the latter 3 twisting square cylinders, and 0.18 second for the circular cylinder.

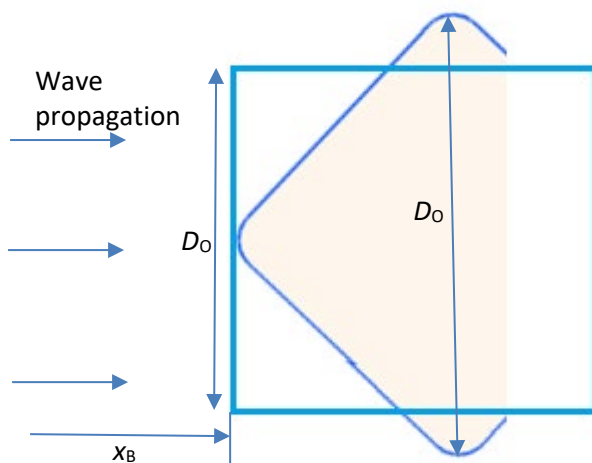


Figure 113 Placements of square cylinder ($\theta = 0, 45$ degrees)

Figure 113 showed the placement of the square cylinders. The initial point of contact of the cylinders is fixed at x_B . However, the contact area (plane perpendicular to the wave propagation axis) of the default square cylinder would already be at its peak during the initial plunging breaking impact. Likewise, the maximum contact area of the 3 square cylinders with twisting angle, will only hit maximum some 51mm to 141mm away. This could be a possible explanation the phenomenon encountered in Figure 112, whereby the square cylinders with varying θ , had their peak slamming force occurring approximately 50ms after the maxima occurred as compared with the default square cylinder case. It was also noted that as shown in Figure 112, that the rise time of the cylinders with θ is the lowest and the inline forces of these cylinders are the lowest too. This findings reiterate earlier

conclusions (Chapter 5.3.3, Figure 68) that the lower force rise time would associate with lower peak force.

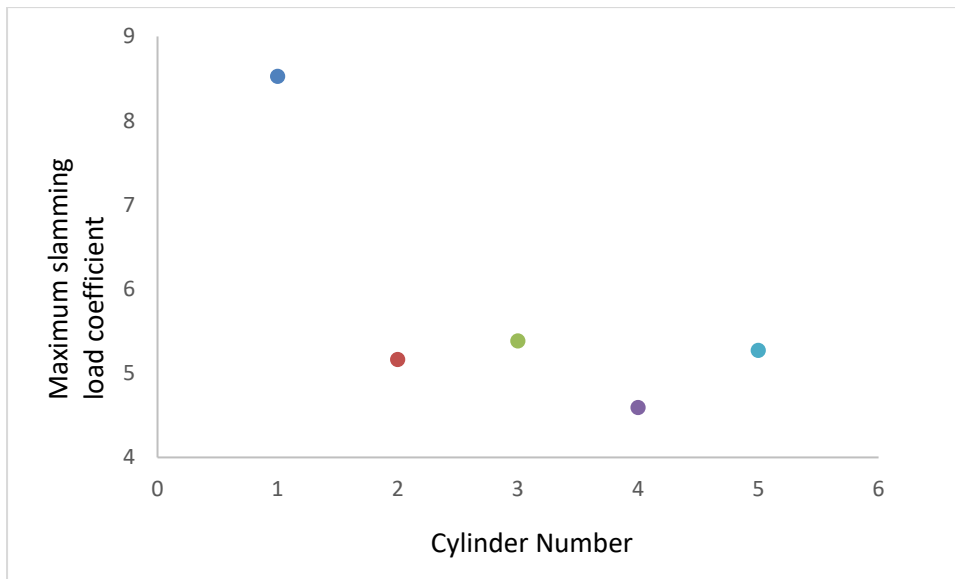


Figure 114 Maximum slamming load co-efficient for 5 cylinders, simulation case (1- square cylinder, 2- square cylinder with $\theta = 15\text{deg}$, 3- square cylinder with $\theta = 30\text{ deg}$, 4- square cylinder with $\theta = 45\text{ deg}$, 315mm circular cylinder)

Less for the square cylinder, cylinder 2 to 5 experienced a maximum slamming load ranging from 4.59 to 5.38. Showing similar traits with earlier experimental work (Figure 63), the square cylinder is shown to suffer the highest peak slamming coefficient. Interestingly, the square cylinders with varying angle of twist (θ) behaved similarly to that of a circular cylinder, with the maximum slamming load coefficient hovering close to one another. This could suggest that structures with a flat frontal plate would suffer the highest slamming load, in tandem with the experimental findings.

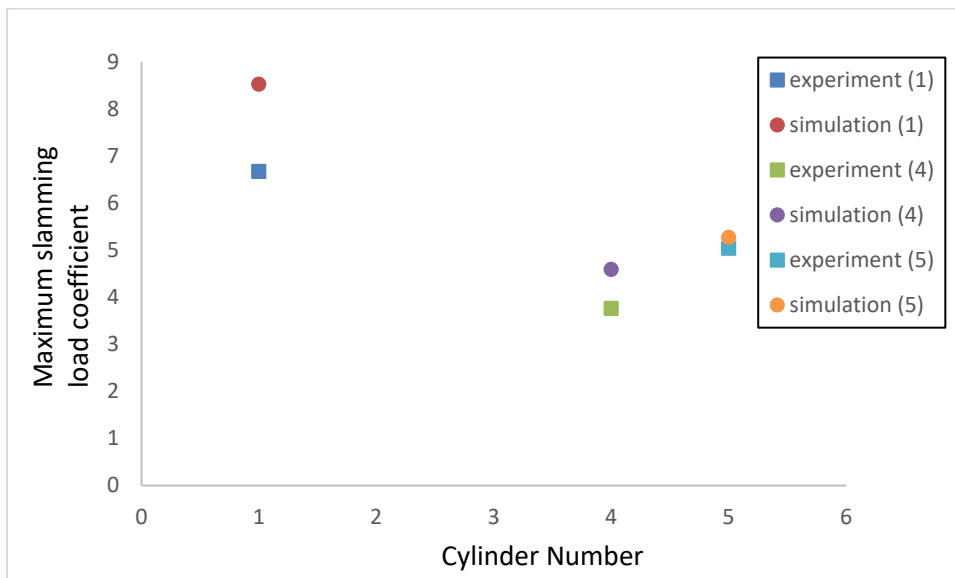


Figure 115 Maximum slamming load co-efficient for 3 cylinders, experimental & simulation case (1- square cylinder, 4- square cylinder with $\theta = 45\text{ deg}$, 315mm circular cylinder)

The simulation case (denoted by circular legend above), the slamming co-efficient seemed to be generally higher than the simulation case. However, the derived slamming load contributions does not seem to differ much (Figure 107). The higher slamming load coefficient obtained by the simulation case is most likely due to the slightly lower obtained wave kinematics (Figure 104).

Squaring the obtained wave kinematics by 2 (Equation 5) from both experimental and numerical work, that could explain the differential in the obtained slamming load coefficient between experimental and numerical solution. (If there is a kinematic deviation of 10% between experimental and numerical work, it would result in 19% deviation for the slamming load coefficient, due to the function of U^2)

Comparing between the diamond cylinder (square cylinder with $\theta = 45$ degree) and the square cylinder. Both experimental and numerical solution agreed that their ratio $\left(\frac{C_s(\text{diamond})}{C_s(\text{square})}\right)$ ranges 54% for the experimental case and 56% for the numerical solution. For the cylinder #5 (315mm circular cylinder), the maximum slamming coefficient for both numerical solution and experimental work have great agreement.

Both numerical and simulation work, for circular cylinders, square cylinders with angle of twist (θ), produces a maximum slamming load coefficient of less than $6.28, 2\pi$, inline with the limits set by past researchers for a 'traditional' circular cylinder ((Wagner, 1932) (Fabula, 1957) (R. Cointe, 1986) (Wienke, 2001)). However, for the square cylinder case, both the experimental and numerical solutions reported a maximum slamming load coefficient of above $6.28, 2\pi$. This means that the current design practice by class society, that assumes for a typical smooth circular cylinder, might not be applicable for a square cylinder case, (only in the event if the propagating plunging breaker hits at the structure in parallel axis, without any angle of twist (θ)).

7.6 Decaying

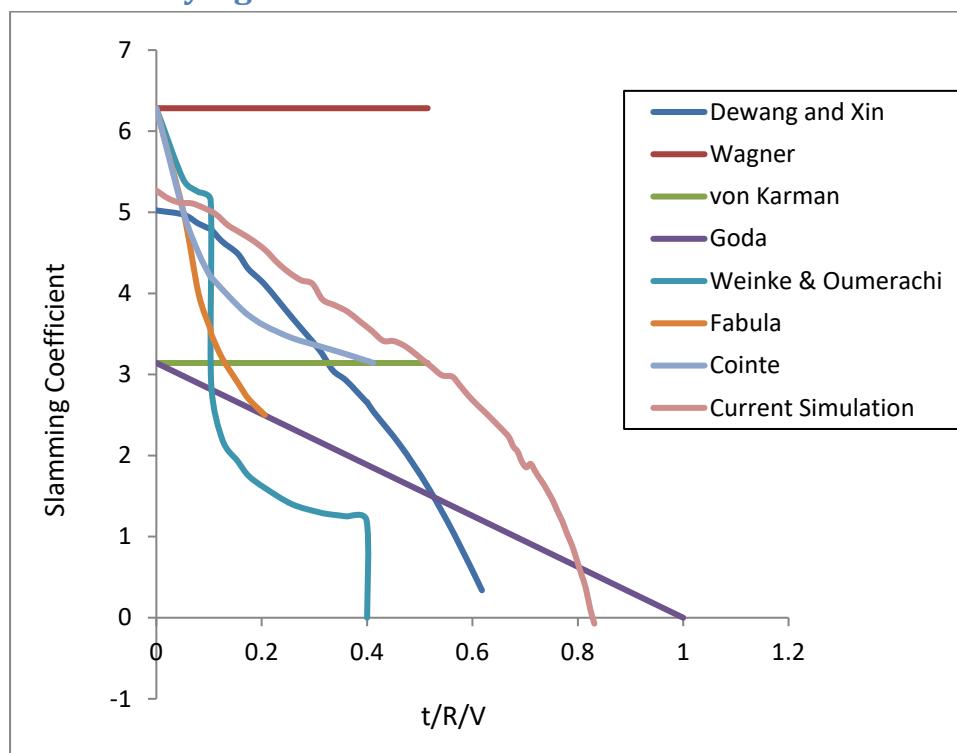


Figure 116 Comparison of time histories of the slamming coefficient (t = time, R = cylinder radius, V = velocity) [(von Karman, 1929) (Wienke, 2001) (Wagner, 1932) (Goda, 1966) (Fabula, 1957) (Cointe, 1989) (De Wang Chia, Laboratory Investigation of Slamming Load Contribution of Plunging Breaker, 2019)]

Earlier days researchers (von Karman, 1929) & (Wagner, 1932) focused only on the initial maximum slamming coefficient without focusing on the slamming coefficient time histories. Later on, researchers [(De Wang Chia, Laboratory Investigation of Slamming Load Contribution of Plunging

Breaker, 2019), (Cointe, 1989), (Goda, 1966) (Fabula, 1957)] tried to present the slamming load coefficient as a function of time, attempting to describe the slamming load coefficient decaying over time. Past researchers have attempted to describe the maximum slamming load coefficient upon impact, with values from π , 5.15 (Veritas D. N., 2010) and 2π . Figure 121 above showed a maximum slamming load upon initial contact at about 5.15, agreeing more with DNV classification guidelines (Veritas D. N., 2010).

Above simulation findings were compared with past researchers experimental findings. The simulation results noted a more linear slamming load coefficient decaying phenomenon, similar to that of Goda's findings. Whilst the earlier experimental work is done (De Wang Chia, Laboratory Investigation of Slamming Load Contribution of Plunging Breaker, 2019) has a closer fit to Cointe's initial time history description of the slamming load coefficient; $t/R/V < 0.5$, the simulation work deviates further from Cointe's finding and have a closer fit with earlier experimental work. However, comparing the experimental and numerical solution in this research, the numerical solution had a slightly gentler slope of decaying during the initial phase of post-slamming, $t/R/V \rightarrow 0.4$. Beyond $t/R/V$, the numerical solution had a parallel shape of decay as compared with (De Wang Chia, Laboratory Investigation of Slamming Load Contribution of Plunging Breaker, 2019).

8. Conclusion

After doing intensive literature review in the early year of the PhD project, few knowledge gaps were identified (as discussed in Chapter 2.7.5)

- 1) What would be a 'good' methodology to obtain the breaking wave kinematics?
- 2) How does offshore structures with different geometric cross sections contributes to the slamming load force or/and slamming load coefficient?
- 3) Could the geometric and kinematic breaking criteria be better calculated? Not using linear wave theory?
- 4) How would different breaking wave intensities affect the kinematics of breaking waves, and ultimately, if the breaking wave intensities play a crucial role in the slamming load coefficient?

With regards to the above identified design knowledge gaps, few hypothesis were made and experimental and numerical simulations were designed to answer the above questions

- 1) Different breaking wave intensities generated breaking waves with different kinematics profiles. The wave kinematics will be measured using both Lagrangian and Eulerian methods. What would be the variance between the 2 methods? Will the variance between the 2 method be affected by the stronger breaking wave intensities as previously described by (Cui Cheng, 2013) who did similar research work, but only limited to 'highly nonlinear, non-breaking waves'?
- 2) 3 cylinders with different geometrical cross sections were subjected to various plunging breakers. Previously as highlighted in the literature review (2.7.3), excluding the current PhD work/author, there is no researcher working on plunging breaking with different geometrical structures. What will be the impact on the slamming load contributions for these cylinders?
- 3) Predicting the onset of breaking waves. What would be the implications of the breaking criteria for different intensities of breaking wave?
- 4) How would the different cylinders slamming load coefficient behaves with stronger plunging breaker? A form of sensitivity test for the cylinders.

In the early stages of this research, Simulation and experimental work were carried out to attempt to create a plunging breaker. Early stages of research were focused on kinematic behaviour of plunging wave, geometric and kinematic breaking criteria for plunging wave. Plunging wave is a highly non-linear and dynamic phenomenon. Understanding its kinematic behaviour is the crux to many other underlying problems (kinematic breaking criterion, slamming load coefficient). Hence, there were attempts to understand the behaviour of the non-linear plunging breaker, and to associate its nonlinearity (breaking wave intensities) and its kinematics with a semi-empirical relation (De Wang C, 2018). Findings from the kinematics of plunging breakers, were applied to the geometric breaking criteria. During the literature review stage, there was concern regarding the use of a formula that describes the wave kinematics during breaking, as a constant behaviour (Equation 6). Instead of using the traditional linear method (via waveprobes) to estimate the crest-front steepness (ϵ), different methods were used to estimate the plunging wave kinematics, which in turn, multiply by the crest rise-time to obtain the accurate value of crest-front length.

Rigorous experimental and numerical works had been done to investigate the factors influencing plunging breaking impact loading on cylindrical structures. Cylinders with different geometrical cross-sections coupled with plunging breaking with various intensities have been generated to

investigate the impacts on the magnitude of the slamming load contribution due to initial plunging impact. It was suggested that using plunging breakers with even higher intensities (lower peak frequencies, f_p) is indeed associated with higher slamming load contribution output. However, due to the higher associated plunging wave kinematics, there is no distinctive relationship between a higher non-linear plunging breaker and the maximum slamming load coefficient.

Plunging breakers with 3 different maturities as defined by (Chan E.S L. Y., 1997) were then generated to impact on the same 5 cylinders; circular cylinder with varying radius, square cylinder and diamond cylinder. These 5 cylinders were also placed at a fixed location, and the 3 different plunging wave maturities were tweaked using different intended spatial location, but with the same cylindrical location. Agreeing with (Chan E.S L. Y., 1997), the transition phase of the plunging wave contributed the highest slamming load. Hence, much focus would be on the worse case plunging jet scenario; the transition phase. It was found that amongst the 5 cylinders tested, the square cylinder has the highest inline slamming load coefficient, followed by the circular cylinders and lastly the diamond cylinder. An interesting finding from the experimental work, the square cylinder had a maximum slamming load coefficient of $> 2\pi$, higher than the classification design guidelines. The experimental case also concluded a negative correlation amongst the contact area of the structure (parallel to the impact wave propagating direction) and the slamming load coefficient. This seems to suggest that the fullness of the structure will affect the capability of air entrapment during plunging impact. A higher fullness, like in the case of a flat plated wall equivalent; the square cylinder, would make it harder for the air entrainment between the plunging jet nose and the re-entry of the free surface, to escape during contact with the cylindrical structure, causing high-pressure air entrapment and giving rise to high slamming pressure/force.

The numerical solution, conducted using CFD- OpenFOAM, also yielded similar agreement with the experimental case. Numerical simulation was done for circular cylinder with 315mm diameter, square cylinder (with filleted corners, having aspect ratio R/D of 0.1) with an angle of twist ranging from 0 to 45 degrees, with 15 degree increment (with a 45 degree angle of twist the same as a diamond cylinder). Out of the 5 cylindrical cases, only the square cylinder yield a much higher maximum slamming load coefficient, even higher than the recommended design guidelines. Although no distinctive relations could be established from the twisting angle case ($\theta = 15, 30, 45$ degree), however it showed similar maximum slamming load coefficient with the circular cylinder cases. It is also having an agreement that having a non-flat contact plate, perpendicular with the plunging wave propagating direction, would ease on the air entrapment phenomenon during initial plunging breaking impact, reducing slamming impact loading.

The experimental and numerical simulation concluded that the geometrical cross section of the impacting structure would have significant impact on the slamming load coefficient as compared to the findings from using similar cross section geometry with different diameter. This concludes that the generic design guidelines should consider an expansion to include flat plate structures perpendicular to the breaking wave propagating direction; wall structures, square cylinder structures of offshore rigs.

With the above summary, we finally concluded the following novelties for this PhD project

- 1) A semi-empirical breaking wave kinematics is established, and is formulated as a function of breaking wave intensities non-dimensionalised parameter $\left(\frac{T_Z}{T_P}\right)$. In the event, whereby researchers do not have the luxury of having the time and resource consuming methodology

of video imagery processing A semi-empirical formula could be proposed in lieu of linear wave theory.

- 2) The use of Eulerian method to calculate breaking wave geometry would be under-estimating the breaking wave crest-front length, effectively giving a slightly inflated geometric breaking criterion. The use of Lagrangian wave kinematics (in the absent of video processing), would be a better substitute than using linear wave theory. (DW Chia, 2018)
- 3) The slamming load coefficient should be revised for offshore structures with square columns. A slamming load coefficient of 3π would be recommended for square columns. However, owing to the worse case scenario for circular cylinder structures is lower than the worse case scenario for a square cylinder, we recommend using the circular cylinder over the square cylinder for design purposes against breaking wave impact.
- 4) Earlier findings show a correlation between Area of waterplane coefficient and the slamming load co-efficient. We suggest a possible tweak to the current design guidelines to account for the effect of Area of waterplane coefficient

Future work could include exploring the effects of using different mediums (seawater) to create a plunging breaker to determine the effect on the slamming load contribution. Most experimental work conducted in the wave tank was done using freshwater (no thanks to the potential corrosion problems and environmental disposal problems associated with using seawater!). Freshwater by its own would have negligible differences for most other hydrodynamic problems that one may attempt to solve. However, for the case of plunging breaker, the magnitude of a slamming load contribution is widely dependant on the entrainment of bubbles during impact. There is an experimental work done (David E.S, 1999) to create breaking waves via 2 mediums; freshwater and seawater. David concluded that the use of the 2 mediums has an adverse effect on the generation of the bubbles and that breaking waves in seawater was found to be broken into multiples of smaller bubbles than its freshwater counterpart. David also investigated the impacts of breaking waves bubbles generation due to drop in temperature, and concluded that “a decrease in temperature from 20 degrees to 3 degree was found to increase bubble production in seawater by nearly 50%” - (David E.S, 1999). From this above literature survey, it is obvious that the plunging breaking slamming load could actually be further investigate to account both the type of mediums and the temperature of the mediums. It is possible to conduct CFD works with different mediums, by tweaking the kinematic viscosity. Potential future work could consider creating different maturity of plunging breaker coupled with different mediums and even temperatures, and possibly to derive with a semi-empirical solution with regards to the potential new findings.

9. Acknowledgements

I would like to thank my family and close friends who have either supported me in one way or another. To be able to have a chance to contribute to mankind in terms of advancing scientific researches is a great honour for me. I'm very honoured to have a great opportunity to be learning and researching under the strict guidance of Professor Longbin Tao, Associate Professor Arun Dev, Assistant Professor Xin Wang & Dr Yongchang Pu.

During the early years of this PhD, it was mentally and physically exhausting to be tasked with creating a deep-water plunging breaker via experimental work. Starting from scratch, reading through hundreds of academic papers, hoping in vain that some academicians did share more in-depth insights about creating a plunging breaker. Nonetheless, this journey has been challenging and fruitful. While it might be much easier to create a non-deep-water plunging breaker (simply via coastal effects), but creating a deep-water plunging breaker is a challenging task by itself.

There are days passing by, with me suffering from writer's block and insignificant progress, going back to square 1, it is frustrating and a norm. Also there are good days where you made a fair amount of exciting findings and progress. This had been a roller coaster journey.

Also, throughout these almost half-decade of researching, I've gained maturity in problem-solving skills, analytical skills and as well as reasoning skills, but at a cost of parts of my social life and maybe also 50% of my hair. Despite that, it is still a wonderful and fruitful part of a journey of my life.

Finally, I would also like to thank my current employer, Lloyd's Register Singapore Pte Ltd for being supportive whilst undertaking this PhD programme, and also Singapore Economical Development Board for co-funding my PhD. Special credits to Newcastle University Technical team of the hydrodynamics laboratory who had contributed to the strict integrity of engineering research works. A special tribute to the late Kieran Oliver, who been assisting me very much with the experimental set-ups during his stint as a Laboratory Technician. He is a very hardworking and energetic guy, well loved by everyone.

Bibliography

- A.H. Techet, A. M. (2005). High Speed PIV of Breaking Waves on Both Sides of the Air-Water Interface. *6th International Symposium on Particle Image Velocimetry*, (pp. 1-14). California.
- Babanin, A. C. (2007). Predicting the breaking onset of surface water waves. *Geophysical Research Letters*.
- Baldock T.E, S. C. (1996). A laboratory study of nonlinear surface waves on water. *Phil. Trans. R Soc. Lond.*, 649-676.
- Benjamin, T. B. (1967). The disintegration of wave trains in deep water. *Journal of Fluid Mechanics*.
- Bonmarin. (1989). Geometric properties of deep-water breaking waves. *Journal of Fluid Mechanics*, 405-433.
- Bredmose H, N. G. (2011). Breaking wave impacts on offshore wind turbine foundations: Focused wave groups and CFD. *29th Int Conf. on ocean, Offshore and Arctic Engineering OMAE2010*, . Shanghai, China: ASME.
- C.W. Hirt, B. N. (1981). Volume of Fluid (VOF) method for the dynamics of free boundaries. *J. Comput. Phys*, 201-225.
- Campbell, T. a. (1980). *Measurement of parameters affecting slamming - final report*. Southampton: Wolfson Marine Craft Unit Report No. 440, University of Southampton.
- Chan E.S, L. Y. (1997). Laboratory study of deep-water breaking waves. *Ocean Engineering, Vol 25*, 657-676.
- Chan E.S, W. M. (1988). Deep-water plunging wave pressures on a vertical plane wall. *Proc. R. Soc. Lond.*, 95-131.
- Chang K.A, L. P. (1998). Velocity, acceleration and vorticity under a breaking wave. *Physics Fluid*.
- Cointe, R. A.-L. (1989). Hydrodynamic impact analysis of a cylinder. *Journal of Offshore Mechanics and Arctic Engineering 109*, 237-243.
- Cui Cheng, Z. N.-C.-H. (2013). A study on Kinematics Characteristic of Freak Wave. *China Ocean Eng*, 391-402.
- Dalrymple. R.A, R. B. (2006). Numerical modelling of water waves with the SPH method. *Coastal Engineering*, 141-147.
- David E.S, B. D. (1999). Bubble shattering: Differences in bubble formation in fresh water and seawater. *Journal of Geophysical Research*, 3265-3275.
- De Wang C, T. L. (2018). Experimental research on kinematics of breaking waves. *Journal of Hydrodynamics*, 390-394.
- De Wang Chia, X. W. (2019). Laboratory Investigation of Slamming Load Contribution of Plunging Breaker. *The 14th International Symposium on Practical Design of Ships and Other Floating Structures* (pp. 1-15). Yokohama, Japan: PRADS.

- De Wang Chia, X. W. (2019). Slamming Force Contribution Due to Plunging Breakers on Circular, Square and Diamond Cylinders. Glasgow: ASME.
- Dean, D. (1984). *Water wave mechanics for engineers and scientist*.
- Duncan. (1983). The breaking and nonbreaking wave resistance of a two-dimensional hydrofoil. *Journal of Fluid Mechanics*.
- F.H. Harlow, J. W. (1965). Numerical calculation of time-dependent viscous incompressible flow of fluid with free surfaces. *Phys. Fluid* , 2182-2189.
- Fabula, A. (1957). Ellipse-Fitting Approximation of two-dimensional Normal Symmetric Impact of Rigid Bodies on Water. *Proceedings, Fifth Mid-western COnterence on Fluid dynamics*. Michigan: University of Michigan Press.
- Fenton, J. D. (1983). A fifth-Order Stokes Theory for Steady Waves. *Journal of Waterway, Port, Coastal and Ocean Engineering*, 216-234.
- G.I, T. (1971). The Scientific Papers of Geoffrey Ingram Taylor, Vol 4. *Mechanics of Fluids*.
- Gang Chen, C. K. (1999). Two-dimensional Navier-Stokes simulation of breaking waves. *Phys Fluids*.
- Goda, Y. H. (1966). Study of impulsive Breaking Wave Forces on Piles. *Report of Port and Harbor Research Institute*, 1-30.
- J. Wienke, H. O. (2005). Breaking wave impact force on a vertical and inclined slender pile-theoretical and large-scale model investigations. *Coastal Engineering*, 435-462.
- Johan Roenby, H. B. (2016). A computational method for sharp interface advection. *Royal Society Open Science*, 1-25.
- Kjeldsen. (1981). Kinematics of deep water breaking waves. *Offshore Technology Conference*.
- Kjeldsen, M. (1979). Breaking waves in deep water and resulting wave forces. *Offshore Technology Conference*.
- Kjeldsen, S. (1984). The experimental verification of numerical models of plunging breakers. *19th International COnterence on Coastal Engineering*.
- Le Méhauté, B. (1976). *An introduction to hydrodynamics and water waves*.
- Li Xiaoyi, A. M. (2010). Towards an efficient, high-fidelity methodology for liquid jet atomization computations. *American Institute of Aeronautics and Astronautics*.
- Longuet-Higgins MS, F. (1977). Theory of the almost-highest wave: The inner solution. *J. Acoust Soc. Am.*, 721-741.
- Longuet-Higgins MS, S. N. (1983). Measurement of breaking waves by a surface jump meter. *Journal of Geophysical Research*, 9823-9831.
- Longuet-Higgins, M. (1974). Breaking Waves - in deep or shallow water. *In Proc. 10th Conf. on Naval Hydrodynamics (Cambridge, MA)*, pp. 597-605.

- Longuet-Higgins, M. (1985). Accelerations in Steep Gravity Waves. *Journal of Physical Oceanography*, 1570-1579.
- Manual, S. P. (s.d.). Coastal Engineering Research Center, Department of the Army. Waterways Experiment Station,.
- McLean J.W, M. Y. (1981). Three dimensional instability of finite-amplitude water waves. *Physical Review Journal*, 817-820.
- Michael L Banner, X. T. (1998). On the determination of the onset of breaking for modulating surface gravity water waves. *J. Fluid Mech*, 107-137.
- My Ha Dao, L. W. (2016). Modelling physical wave tank with flap paddle and porous beach in OpenFOAM. *Journal of Oean Engineering* , 204-215.
- Niels Gjøøl Jacobsen, D. R. (2012). A wave generation toolbox for the open-source CFD library: OpenFoam (R). *International Journal for Numerical Methods in Fluids*.
- P.A Blackmore., P. H. (1984). Experiments on Full-Scale wave impact pressures. *Coastal Engineering*, 331-346.
- Perlin .M, H. J. (1996). An experimental study of deep water plunging breakers. *Physics of Fluids*, 2365-2374.
- R. Cointe, J. A. (1986). Hydrodynamic Impact Analysis of a Cylinder. *Journal of Offshore MEchanics and Arctic Engineering*, 237-243.
- Rapp, M. (1990). Laboratory measurements of deep water breaking waves. *Philosophical Transactions of the Royal Society*, 735-800.
- Schultz W.W, H. J. (1994). Potential energy in steep and breaking waves. *Journal of Fluid Mechanics*, 201-228.
- She.K. (1997). Experimental study of three0dimensional breaking wave kinematics. *Applied Ocean Research*, 329-343.
- Shemer L, S. H. (2013). On kinematics and dynamics of breaking water waves. *Procedia IUTAM*, 205-212.
- Snyder, K. (1983). *Surface Waves and Fluxes:Volume I - Current Theory*.
- SP, K. (1984). The experimental verification of numerical models of plunging breakers. *19th International Conference on Coastal Engineering*.
- Stansell. Paul, M. C. (2002). Experimental investigation of wave breaking criteria based on wave phase speeds. *Journal of Physical Oceanography*, 1269-1283.
- Stokes, G. (1880). On the theory of oscillatory waves. *Cambridge University Press*, 197-229.
- Tarik Sabuncu, S. C. (1981). *Hydrodynamics Coefficients for Vertical Circular Cylinders at Finite Depth*. Annapolis, MD, USA: US Naval Academy.
- Taylor, G. (1971). *The Scientific Papers of Geoffrey Ingram Taylor*. Mechanics of Fluids.

- Tian Z.G, P. M. (2010). Energy Dissipation in two-dimensional unsteady plunging breakers and an eddy viscosity model. *J. Fluid Mech*, 217-257.
- Veritas, D. (2011). RP-H103 Rules and standards.
- Veritas, D. N. (2010). *RP-C205 Environmental Conditions and Environmental Loads*. DNV.
- von Karman, T. (1929). *The impact on seaplane floats during landing*. National Advisory COmmittee for Aeronautics. Technical Notes, vol 321.
- Wagner, H. (1932). Uber Stoss-und Gleitvorgange an der Oberflache von Flussigkeiten. *Z. Angew. Math. Mech*, 193-215.
- Wienke, J. (2001). *Druckschlagbelastung auf schlanke zylindrische Bauwerke durch brechende Wellen-theoretische und grogmagst7bliche Laboruntersuchungen -PhD- thesis*,. TU Braunschweig, (in German).
- WK, M. (1982). The instability and breaking of deep-water waves. *Journal of Fluid Mechanics*, 163-85.
- Wu N.T, H. O. (1994). Numerical modelling of breaking wave impacts on a vertical wall. *Coastal Engineering*.
- Wu, Y. (2004). Laboratory measurements of limiting freak waves on currents. *Journal of Geophysical Research*.
- Xu Delun, H. P. (1986). Breaking of Wind-generated Waves. *Journal of Physical Oceanography*, 2172-2179.
- Yanfei Deng, J. Y. (2016). Freak wave forces on a vertical cylinder. *Coastal Engineering*, 9-18.
- Ying Tu, Z. C. (2017). A review of slamming load application to offshore wind turbines from an integrated perspective. *14th Deep Sea Offshore Wind R&D Conference, EERA Deep Wind*.
- Yuen, H. L. (1982). Nonlinear dynamics of deep-water gravity waves. *Advances in applied mechanics*, 153-180.
- Zhaoyuan Wang, J. Y. (2012). A new volume-of-fluid method with a constructed distance function on general structure grids. *Journal of Computational Physics* , 3703-3722.

Appendix

After spending first 9 months on literature reviews, two of Prof Chan's papers ((Chan E.S L. Y., 1997) (Chan E.S W. M., 1988)) and methodologies were chosen for the attempt to generate a plunging breaker. The aim of this chapter is to apply the knowledge gained from the literature review stage. Without an ability to replicate plunging breaker accurately, this PhD would have come to a halt. This would be a crucial bridge of this PhD.

In this experimental case, the superposition method (or sometimes also known as focusing method) was used. In Prof Chan's paper, this superposition method is further sub-divided into 3 methods; constant amplitude, constant steepness and constant spectra methods (the technicalities of these 3 were discussed in the Literature Review stage). In this chapter, the constant steepness method is used, because of the ability to create stronger plunging breaker, owing to this method's higher associated wave stability.

A.1 Experimental work in National University of Singapore

Towards the end of the first year of the candidature's PhD. In the vicinity of the NUS hydraulic lab, there are a total of four facilities; Ferrocement wave flume, long-strokes wave flume, coastal wave-current basin and an oscillatory water tunnel. This experimental work was carried out at the NUS long-stroke wave flume, having a dimension of 38m, 0.9m, 0.9m, (length, width and height respectively), using a piston-type wave-maker for the generation of waves. At this early stage of experimental work, no wave probes, load cell or hi-speed camera were used. However, for analysis purposes, the wave paddle was equipped with a motion sensor, transmitting the piston strokes displacement-time history back to the system.



Figure A1 – National University of Singapore Glass Wave Flume

Plunging breakers were generated at NUS, using the superposition of non-breaking regular waves consisting of arbitrary frequencies, using the constant steepness method. This constant steepness method involves using a fixed steepness value for each individual wave components, in this case a wave steepness (ak) value of 0.031416 were used; or a value of 0.01π . This value ($ak = 0.01\pi$) would equates to a 'wave-height to wave-length' ratio ($\frac{H}{\lambda} = 0.01$); assuming deep water airy wave theory. The 'wave-height to wave-length' ratio of 0.01, itself might seem impossible to generate a breaking wave. However, if one were to superposition dozens of regular waves, it would be possible to create a plunging breaker by superposition. The use of a low 'wave-height to wave-length' ratio, is deliberate, to ensure individual wave component stability and prevent any pre-mature breaking.

Initial attempt was made to generate breaking wave through the superposition of 10 regular waves with varying arbitrary frequencies, $0.56 \leq f \leq 1.1\text{Hz}$, having a step frequency ($\Delta f = 0.06\text{Hz}$)

Central frequency (f_c) = 0.83 Hz

Characteristic Wavelength (λ) based on central frequency = 2.14m

Characteristic phase speed (c) based on central frequency = 1.778m/s

After evaluating each wave component's wavelength and pre-determining the ak values, the maximum contributing wave amplitude a_n could be established. The amplitude could then be described as (Equation 13).

The value of wave amplitude is bounded by the space (x) and time domain (t). The location of breaking, (x_b) and the time of breaking, (t_b) should be set to the value of interest. An 'appropriate' value of (t_b) could only be established after (x_b) is defined. Given the length of tank is 38m, and there is a slope located at $x > 30\text{m}$ for the dispersion of the waves through shoaling effects, the upper limit of (x_b) is set at least 3 wavelengths away from $x = 30\text{m}$, to eliminate the risk of rebounding waves. However, the value of (x_b) shouldn't be set too near to the wave paddle such that, there isn't sufficient distance for the wave group to progress into a breaking wave.

Therefore, after taking into considerations the upper and lower limit of (x_b), the preferred (x_b) would be near the mid-length of the wave tank determined to be 12.7m. Next to determine the value of (t_b), it must not be at such a low value whereby, there is insufficient time allowed for the slowest wave in the wave package to reach the desired breaking location. If the time breaking (t_b) is too small, coupled with the slowest wave component in the wave packages, the slowest propagating wave components might not even reach the spatial focal point ($t_b * c < x_b$), resulting in loss in spectrum energy at the critical focal point.

Taking the phase speed, $c = \frac{\lambda}{T}$, the slowest wave would be in the highest frequency component of the wave package, $c = 1.3\text{m/s}$. Taking into consideration that the desired $x_b = 12.7\text{m}$, it would take about 12seconds, (excluding any phase lag) for the highest frequency wave to reach the desired breaking location. , the stroke paddle of the wave tank requires starting with relatively low motion. Therefore it is not advisable to pull the trigger on half dozens of wave within a couple of seconds. Hence, taking the low paddle motion and inputting some buffers for phase lag, t_b is defined as 18s.

Next, the phase shift of each individual wave components has to be determined. Phase shift could be adjusted by shifting the spatial domain ' kx ' or the time domain ' ωt '. But since there is only 1 wave paddle in the tank, the phase shift is adjusted by inputting a time lag to the existing wave paddle.

$$t_{lag,n} = \frac{\phi_n}{\omega_n} \quad (A1)$$

Recalling Equation 13 and attempting to set $\cos(k_n x_b - \omega_n t_b - \phi_n) = 1$, the time lag would be inputted in such a way that,

$$(k_n x_b - \omega_n t_b + \phi_n) = -2\pi * m; m = 0,1,2,3,4 \dots$$

$$(\phi_n) = (-k_n x_b + \omega_n t_b - 2\pi * m); m = 0,1,2,3,4 \dots$$

'm' value indicates the number of wave crest that has past x_b at the stipulated t_b for the individual wave component. (i.e. 'm' value of 0, would mean that at $x=x_b$, $t=t_b$, the individual wave component contributes its first wave crest)

After determining the value of the phase shift of each individual wave component, an excel spreadsheet is created for $0 < t < t_{max}$, with $t_{max} > t_b$, in this case, $t_{max} = 30sec$, with a small time step of 0.01s. The wave heights for all 10 waves are compiled for each time step, and these 10 wave heights would all combined into a final total surface elevation for each individual time step.

However, the wave tank has a zero initial condition, unlike the sea condition whereby waves started from the beginning of time. There is an important command to include in the pivot table. Due to the fact that at the wave tank, when $(k_n x - \omega_n t + \phi_n) > 0$, no waves are detected at the location of interest, due to the generated waves still lagging behind and yet to arrive at the desired location.

For example, looking at $x = 20m$, a wave having wave properties of $f = 0.74Hz$, $\omega = 4.65 \text{ rad/s}$, $k = 2.315 \text{ rad/m}$, would equate that the point of interest at $x = 20m$, is actually 46.3radian away from the wave paddle ($20m * 2.315 \text{ rad/m}$). For the wave paddle to generate waves to be detectable at $x = 20m$, or 46.3radians away, $\omega t > 46.3radians$, in this case, taking $\omega = 4.65 \text{ rad/s}$, $t > 9.96$ seconds for the wave to travel to the point of interest.

The wave height for each cell is inputted with an excel test function 'IF',

$$[\zeta_n * (\text{IF}(k_n x - \omega_n t + \phi_n) > 0, 0, \cos(k_n x - \omega_n t + \phi_n))] \quad (\text{A2})$$

The above Equation 28 command means that, if $(k_n x - \omega_n t + \phi_n) > 0$, then the input value would be 0, or else the input value would be $\zeta_n * \cos(k_n x - \omega_n t + \phi_n)$.

A.1.1 Strokes Signal Calculation

Even though, the wave maker that the candidate would be using in Newcastle University (maker: Edinburgh Designs), have an automated deduced strokes displacement-time history; whereby the user could input the desired wave spectrum or wave parameters, and the system would automatically calculate the required strokes output. However, the NUS wave maker, there is no such luxury for the users. This sub-chapter would give detailed insights about the generating of the Strokes displacement-time history signal.

As discussed in details about the physics behind the Strokes displacement for a piston type wave maker in (2.5 Generation of breaking waves). Recalling Equation A1, the surface elevation could be re-written as below

$$\zeta = [\zeta_n * \cos(-k_n x_b + \omega_n (t_b - t) - 2\pi * m)] \quad (\text{A3})$$

The above Equation A3 is consistent with past literature survey (Wu, 2004), except in the above formula, an additional term $(-2\pi * m)$ is added to account for the reduction of the phase shift, to allow more flexibility in shifting the individual wave components.

At this stage, the amplitude time history is derived for the wave paddle. However, a transfer function is needed to transfer the amplitude time history to stroke displacement time history.

Recalling Equation 15 and referring to Figure 6 H/S ratios for both Piston and Flap type wave-maker (Dean, 1984) Figure 6 for the inputs of a piston wave maker, the individual strokes-displacement time history contribution could be written as,

$$S_n = [\zeta_n * \cos(-\omega_n t + \phi_n)] * (S/H)_n \quad (A4)$$

From above Equation 30, summation of each individual Strokes displacement-time history would give Equation 16.

A.1.2 Strokes Signal Modification

Initial wave stroke displacement-time history signal produced, was a flop and failed to generate breaking wave. However, there are few limitations of the Strokes. There are kinematics limitations (maximum velocity and a maximum acceleration of the strokes), and as well as unable to ‘jump start’ as further detailed in the latter chapters.

Many researchers (Chan E.S L. Y., 1997), (Dean, 1984), (Wu, 2004), uses a cosine function to describe the surface elevation. It was based on an assumption that the wave paddle first generates a cosine wave at the instantaneous moment which the paddle is displaced forward, creating a wave crest at $x = 0m$.

Coupled with the earlier argument that, when $k_n x - \omega_n t + \phi_n > 0$, there would be no wave propagation at the chosen space and time. However as time approaches higher value, $\cos(k_n x - \omega_n t + \phi_n) \rightarrow -ve$. When the cosine term approaches 0 for the first time, it seems there would be a sharp rise of height elevation, cosine (0) = 1

The resulting strokes signal, which was calculated as a function of the wave height output would suffer an enormous velocity and acceleration value due to the sudden increase of height output within that small time step.

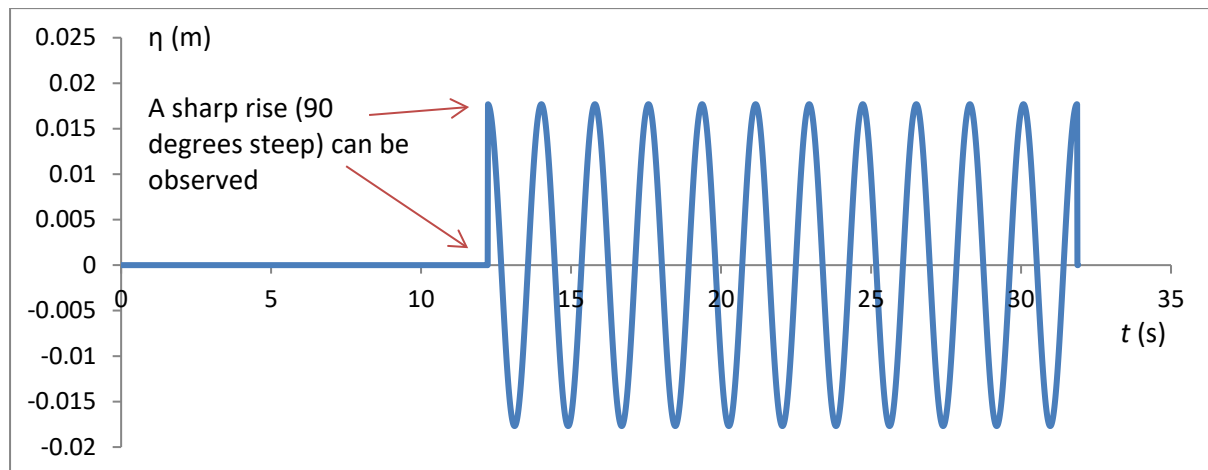


Figure A2 – Wave elevation time history of a regular wave using cosine function at $x_B = 12.7m$, analytical solution

As shown in above Figure A2, the analytical solution of using the cosine function would have expected a sudden sharp rise of the wave crest upon initial propagation of the regular wave. This is not realistic and feasible for the wave generation.

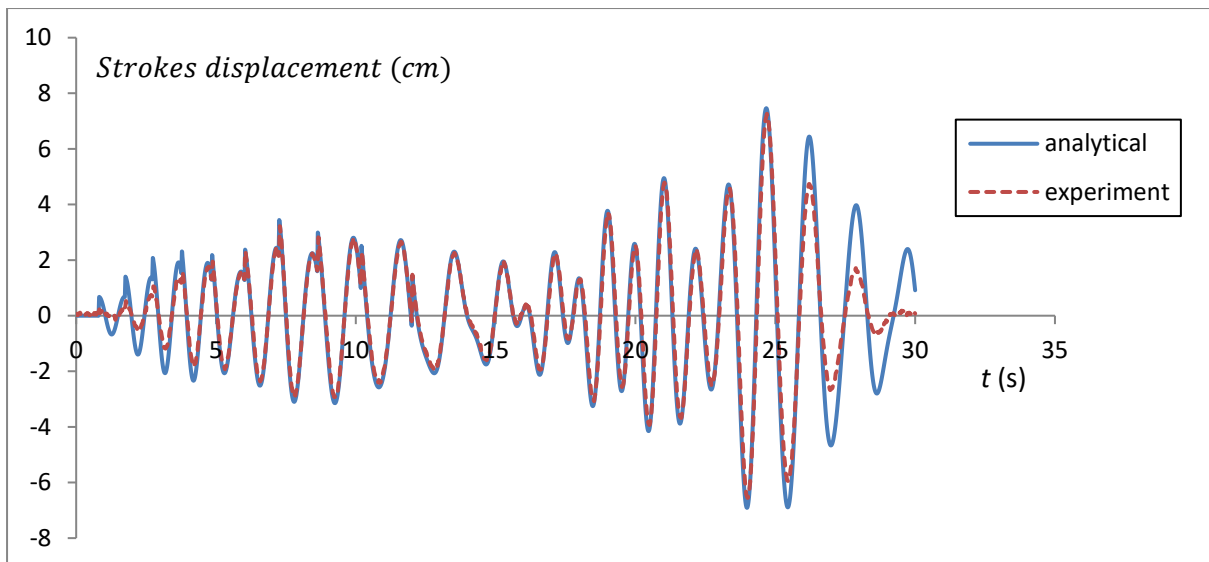


Figure A3 Comparing analytical input ex Experimental output for stroke displacement-time history

The 'analytical input' was the solution that was fed to the system for the stroke displacement-time history input; accordance to Equation A4. The maximum Strokes velocity of the wave maker is 0.77m/s and the suggested Strokes acceleration of less than g. The wave maker is also shown to have a 'slow start up', as it requires up to 5 seconds to attain a desired displacement of 2cm, and the wave maker also have a 'late rapid decay' in the last 5 seconds of the input signal (Figure 24). Due to the kinematic limitations of the wave maker, the wave maker is unable to reach some of the desired crest and trough values.

The 'slow start up' and 'late rapid decay' of the wave maker could be easily solved by inputting additional input time for just the high frequency low amplitude wave component at both ends of the graphs. However, the kinematic limitations of the wave maker are met due to the phenomenon attributed and shown in the above figure. Hence, an attempt was made to solve the above problem by changing the cosine function to a sine function. A sine function formula will start off the signal from 0, and eliminate the sudden amplitude spikes that the cosine term function experienced.

The cosine function formula does not accurately describe the wave phenomenon. Using a time step of 0.01s, a sudden elevation of 0.017m as shown in Figure A2 would have meant that the wave accelerated at an approximate 20g, and it is physically impossible. Also, it does strain to the wave maker by demanding an impossible feat of having an acceleration of 20g and also a stroke's velocity of 2.08m/s, well above the kinematic limitation of the piston wave maker.

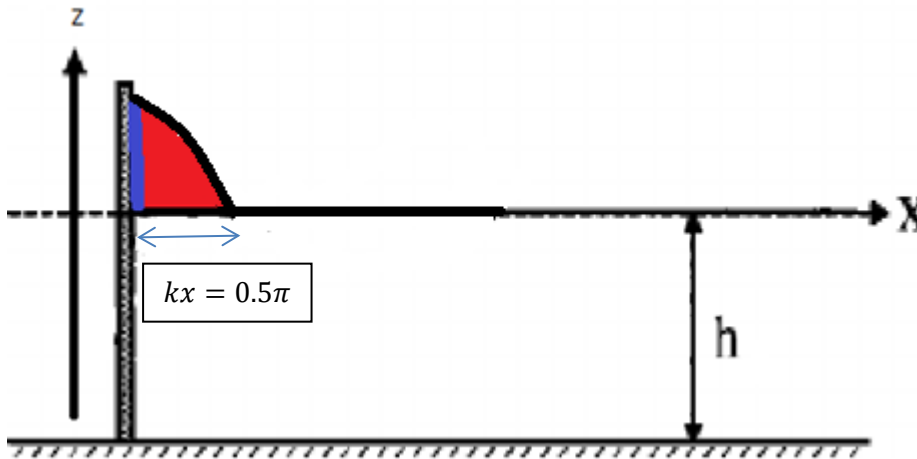


Figure A4 Wave generation using cosine terms (blue) and sine terms (red)

Previous cosine term, as shown in blue colour, only pictured the sharp crest approaching the point of interest (neglecting the red colour portion). Whereas the sine term function would consider the wave approaching at free surface level. The sine term function had also described how a wave propagates gradually from the free surface to the crest level, eliminating a sudden sharp spike (Figure A4).

In this research, a slight tweak to the cosine term was made. This is done by converting the cosine term to a sine term and deducting 0.5π (Equation A5).

$$\cos(kx - \omega t + \phi) = \sin(kx - \omega t + \phi - 0.5\pi) \quad (\text{A5})$$

Recalling Equation 13, the amplitude formula can be re-written as,

$$\sum \zeta = \sum [\zeta_n * \sin(k_n x - \omega_n t + \phi_n - 0.5\pi)] \quad (\text{A6})$$

The above-modified formula meant that the first wave would arrive when $(k_n x - \omega_n t + \phi_n - 0.5\pi)$ approaches 0. There is a subtraction of 0.5π to indicate that the wave actually propagates 0.5π faster than earlier estimation (as explained in Figure A4). On the right side of the equation, is the transfer function from a cosine term to sine term. Taking $\cos(k_n x - \omega_n t + \phi_n) = \sin(k_n x - \omega_n t + \phi_n + 0.5\pi)$.

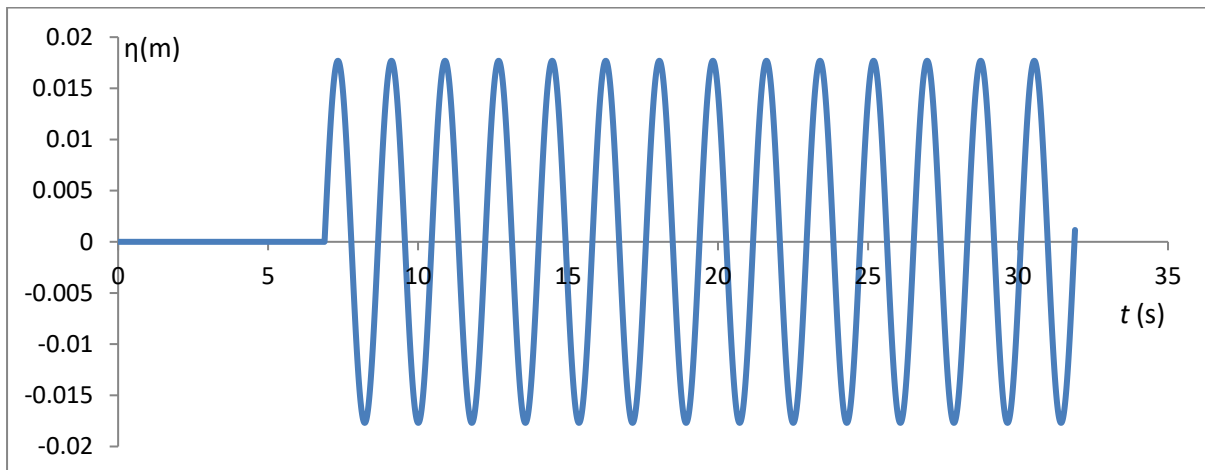


Figure A5 Wave elevation time history, using the sine function term, at $x_B = 12.7\text{m}$, analytical solution

After the conversion of the cosine term to sine, a gentle elevation could be observed, eliminating any sudden spike of elevation (Figure A5).

Table A1 Comparison of strokes displacement signal, before and after conversion

	Before conversion	After conversion
$\left(\frac{dS}{dt}\right)$	2.08m/s	0.155m/s
$\left(\frac{d^2S}{dt^2}\right)$	199m/s ²	5.95m/s ²

Before sign conversion, there is an expected strokes acceleration input of 20g, which is unrealistic. The maximum required strokes velocity input was 2m/s, this was more than double of the NUS wave tank maximum allowable strokes velocity. After conversion, the required strokes velocity of 0.155m/s is about 20% of the maximum strokes velocity (Table A1).

The new updated excel command for amplitude calculation would be written as,

$$[a_n * (IF(k_n x - \omega_n t - 0.5\pi) > 0, 0, \sin(k_n x - \omega_n t + \phi_n + 0.5\pi))] \quad (A7)$$

The above modified formula meant that the first wave would arrive when $(k_n x - \omega_n t + \phi_n - 0.5\pi)$ approaches 0. There is a subtraction of 0.5π to indicate that the wave actually propagates 0.5π faster than earlier estimation (Figure A1 & Figure A4). On the right side of the equation, is to describe the wave starting to propagate from the sea surface to the crest level, hence instead of -0.5π , a value of $+0.5\pi$ was used.

Recalling Equation A3, there was an additional term introduced, 'm'. A higher 'm' value would indicate the number of waves that propagate through the actual focal point before the focused wave. This term will allow further fine tuning of the wave signal. In general, the slower wave components will have a higher 'm' value, to allow the higher frequency and slower wave components to propagate first, and then allowing the faster wave components to superimpose with the slower wave at the intended focal point.

After inputting individual 'm' value and deducing the final phase shift of each individual wave component, recalling (Equation A3,A4,A6 & A7), the final strokes displacement-time history for the wave package could be established.

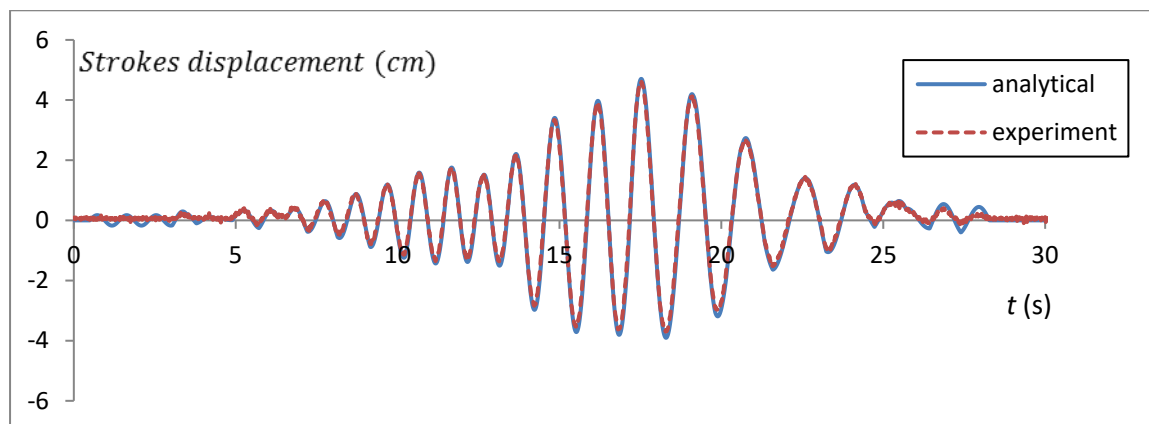


Figure A6 Comparing modified analytical input and experimental output for strokes displacement time history – after modification

The new modified strokes signal is comparable with the desired inputs as compared to the previous stroke signal (Figure A4). As compared to earlier signals, the maximum strokes displacement

required for the focused wave is lower at approximately 50mm, as compared to the previous requirement of 80mm. The adjustment of the 'm' values, or phase lag of the higher frequency waves, allowing these slow, shorter, propagating waves to be produced first by the wave maker. The initial 5 seconds of the strokes signals were dominated by the slow, high frequency waves, and even so, there were still discrepancies during the initial warm-up. However, these initial discrepancies doesn't affect the 'main body' signal for creating the plunging breaker. The strokes displacement-time history $5s < t < 25s$, had a much better fit as compared to the previous attempt and also resulting in lesser stress on the piston wave maker.

A.2 Post-processing

For non-breaking wave case

As explained in details in Chapter 4.5, this is a walk through of an example used to post process for a non-breaking wave case, to derive the drag coefficient and inertia coefficient (although it was noted that the acceleration values during a onset of slamming force is low, but post processing was still done to derive the C_m)

z= -50			z= -20			z= 10			z= 40			z= 70		
elevation	speed	F (N)												
74.27036	0.261323	13.07301	69.97866	0.22906	8.596314	80.97878	0.568513	6.347939	81.03398	0.422276	11.77762	82.78644	0.435592	11.7335
70.01148	0.262238	10.63293	86.29146	0.222077	13.20013	87.58453	0.45116	10.87976	80.92686	0.402581	10.96681	82.9553	0.42489	11.3504
75.42721	0.260424	11.31129	85.59639	0.230147	12.41254	85.01336	0.42115	8.614315	69.40862	0.35272	12.74214	81.75016	0.503361	12.4621
76.13507	0.267784	10.46624	60.07898	0.223329	6.356558	85.33925	0.41301	11.52698	80.83188	0.4411	10.10591	82.52618	0.438971	10.05674
77.56615	0.265262	10.37316	67.61998	0.232359	8.354841	83.73624	0.489004	8.516435	79.36265	0.421762	9.186684	83.38495	0.48972	10.79035
80.14199	0.276961	12.22894	84.79025	0.224899	13.22574	72.11956	0.456904	3.902636	75.84	0.399441	12.67306	82.32462	0.692076	12.40902
78.54135	0.268319	11.17334	84.44787	0.227245	12.52932	65.04716	0.473886	12.7365	81.10322	0.412278	11.04132	82.21388	0.445539	9.98467
81.49999	0.266251	12.21576	83.37866	0.245151	13.26853	77.45052	0.439095	6.130398	69.19182	0.511237	5.140077	80.55586	0.475243	12.83347
72.65631	0.278736	12.29488	74.59477	0.252188	9.773652	77.27997	0.539176	6.379012	80.69551	0.422397	10.80375	83.02824	0.504294	11.84991
77.01187	0.258198	10.89927	86.3147	0.26845	12.99894				79.23135	0.370225	9.847348			
76.24999	0.267477	11.52995	77.41967	0.231828	10.85751	79.39438	0.472433	8.337109	77.5994	0.420644	10.49304	82.39174	1.47	11.49668

N	H=	0.11 m
---	----	--------

amp (mm)	weight	u u
(-50.1 to -80)	1	0.044284
(-20.1 to -50)	1	0.071544
(-20 to 10)	1	0.053744
(10 to 40)	1	0.223193
(40 to 70)	1	0.176941
(70 to 100)	1	2.1609
		0.455101

Morrison's Equation	
0.5p =	500 kg/m3
D =	0.2 m
u u =	0.455101 m2/s2
Z =	0.18 m
	8.191819
cd =	1.301981

Figure A7 Post processing for drag component

Using strip theory, the cylinder in this example, $D = 200\text{mm}$ was used. For each elevation (z) 10 readings were taken (except for $z = 10\text{mm}$ and 70mm , where only 9 were used as it was discovered that one of the reading was corrupted). The kinematics of the non-breaking wave were extracted when acceleration is 0 or very close to 0. As previously explained, that's the moment when the force reading would be of drag component.

The blue box shows the $u|u|$ value in each Δz . And establishing the averaged $U|U|$ value (Figure 62, Equation 40). This compiled $u|u|$ would then be substituting back into the Morrison's Equation Drag Force (Equation 2); with the only unknown being the drag coefficient (C_D) (shown in red box in above figure).

The above was repeated for the acceleration/ F (inertia) component. However, the elevation point of interest, is only taken $-80\text{mm} < z < 0$; unlike the drag component where $-80\text{mm} < z < 100\text{mm}$.

Recalling Airy Wave Theory as below

$$\phi = \frac{\omega}{k} * a * \frac{\cosh(k(z+h))}{\sinh(kh)} * \sin(kx - \omega t) \quad (A8)$$

$$\eta = a * \cos(kx - \omega t) \quad (A9)$$

$$u = \omega * a * \frac{\cosh(k(z+h))}{\sinh(kh)} * \cos(kx - \omega t) \quad (A10)$$

$$\frac{du}{dt} = -\omega^2 * a * \frac{\cosh(k(z+h))}{\sinh(kh)} * \sin(kx - \omega t) \quad (A11)$$

According to A9, A10 and A11, the acceleration is at maximum, when velocity is 0 or surface elevation is or near 0. That explain why the elevation point of interest for maximum acceleration is as such $-80\text{mm} < z < 0$.

mass =	0.1m * 0.7854 * 0.2m * 0.2m * 1000	mass =	0.1m * 0.7854 * 0.315m * 0.315m * 1000	mass =	0.1m * 0.7854 * 0.4m * 0.4m * 1000
mass,200mm =	3.1416 kg	mass,315mm =	7.79 kg	mass,400=	12.57 kg
acc =	-1.4 m/s ²	acc =	-1.4 m/s ²	acc =	-2.4 m/s ²
Fi =	-5 N	Fi =	-10.2 N	Fi =	-26.96 N
Inertia co ,200=	1.136818	Inertia co 315=	0.935265	Inertia co 400=	0.893662
square mass =	3.965 kg	diamond mass =	3.965 kg		
acc =	-1.4 m/s ²	acc =	-1.4 m/s ²		
Fi =	-6.48 N	Fi =	-6.84 N		
Inertia co sq=	1.167357	Inertia co sq=	1.23221		

Figure A8 Post processing for inertia component

Recalling Equation 3, and with the derived acceleration, mass, and extracted Fi. The inertia coefficient could be derived.

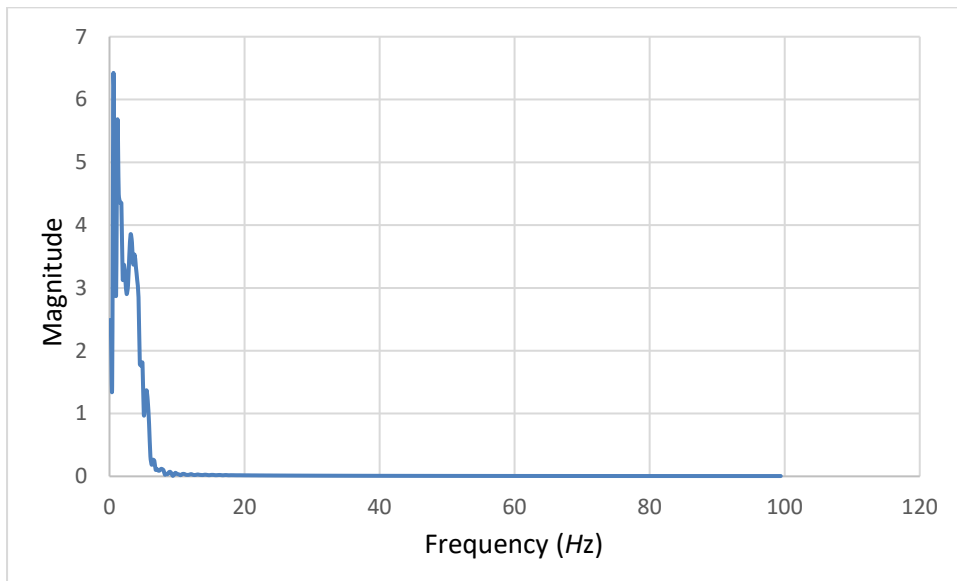


Figure A9 – FFT of square cylinder

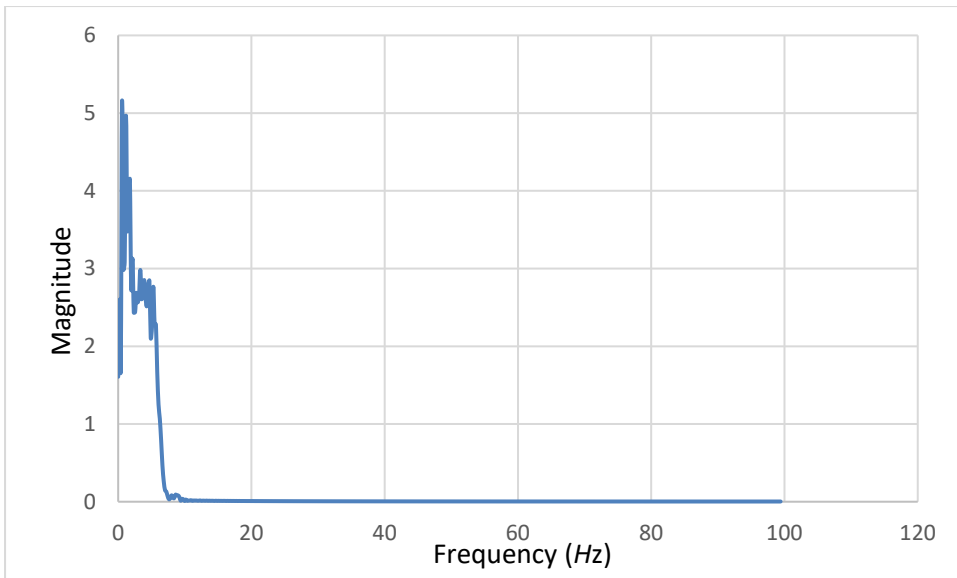


Figure A10 - FFT of diamond cylinder

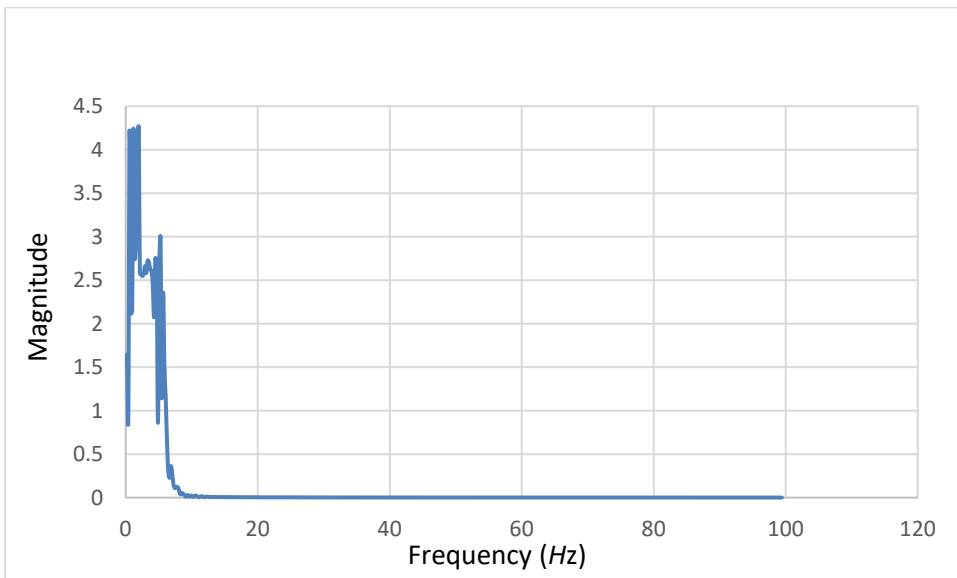


Figure A11 - FFT of 200mm circular cylinder

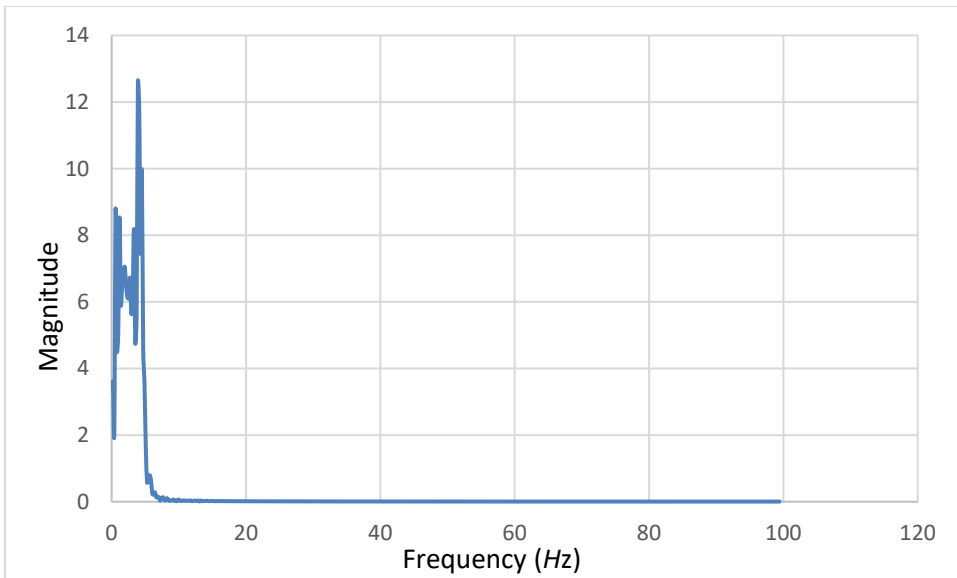


Figure A12 - FFT of 315mm circular cylinder

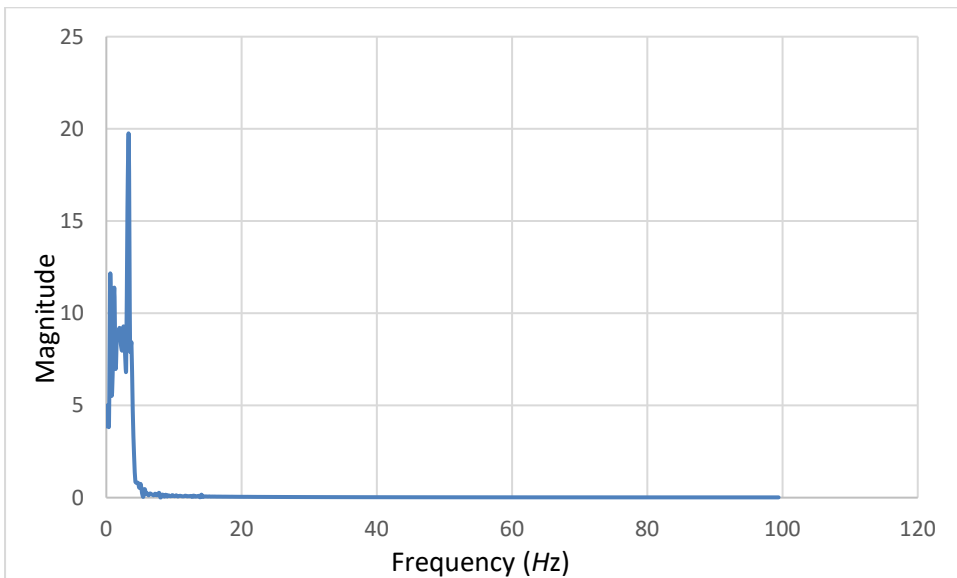


Figure A13 - FFT of 400mm circular cylinder